Episodic Accretion and Outflows in Young Stellar Objects & Near Infrared Instrumentation

A THESIS

Submitted to the
Tata Institute of Fundamental Research, Mumbai
for the degree of Doctor of Philosophy in Physics

by

JOE PHILIP NINAN

School of Natural Sciences
Tata Institute of Fundamental Research
Mumbai
August, 2016

Final Version Submitted in October, 2016

DECLARATION

This thesis is a presentation of my original research work. Wherever contributions of others are involved, every effort is made to indicate this clearly, with due reference to the literature, and acknowledgement of collaborative research and discussions.

The work was done under the guidance of Prof. D. K. Ojha, at the Tata Institute of Fundamental Research, Mumbai.

Joe Philip Ninan

In my capacity as supervisor of the candidate's thesis, I certify that the above statements are true to the best of my knowledge.

Prof. D. K. Ojha

Date:

Acknowledgements

I owe my deepest gratitude to my thesis advisor Prof. D. K. Ojha, for his guidance, discussions and constant encouragement, starting from my early days of undergraduate projects to the completion of my PhD. His dedication towards work was an invaluable source of inspiration to me at every stage of my research period. I am deeply grateful for all the extra effort he whole heartedly put in, to advise and guide me throughout this period at TIFR. I would also like to acknowledge Prof. S. K. Ghosh, for his extremely valuable guidance, and insightful discussions on various instrumentation projects I did.

I would like to express my deep gratitude to Savio and Milind, from whom I learned the art of astronomical instrumentation. The time spent with them at Ladakh during TIRSPEC project are the best memories from my PhD period. I would also like to thank Douglas, MKIR, for teaching me a lot on near-infrared instrumentation. Every discussion with him was insightful, fun, and productive.

I am indebted to Satheesha, Rajesh, Pradeep, Ganesh, Chandrakant, Shailesh, Sanjay, and Jeetendra for helping me in all the projects and IR group activities. The stay and work at Hanle, Ladakh, was both memorable and productive only because of the incredible hospitality and support we received from Angchuk, Sonam, and all the IIA team members at IAO, Ladakh. I would also like to thank Prof. Bhatt for the generous hospitality, as well as, help in conducting numerous nights of observation from CREST, IIA, Bangalore. Hundreds of nights of observation for the MFES program would not have been possible without the enthusiastic, talented support of Pramod, Kuppuswami, Venki, Rahul, Kiran, Lakshmi, Prabhu, and other operators at Hanle, who spent nights, losing out on sleep, clocking the allocated telescope time to its maximum use for me.

I am deeply indebted to Tapas, Kshitiz, and Blesson for all the help and discussions throughout the PhD period. I would like to express my sincere gratitude towards Dr. M. Puravankara, Prof. B. Mookerjea, Prof. A. Gopakumar, Prof. D. Narasimha, Prof. A. R. Rao, and Dr. S. Chandra for their interactions, guidance, and assistance on various occasions during the research period. I am indebted to Prof. H. M. Antia for teaching me various numerical method techniques, and helping me throughout my research projects. I am much obliged to Prof. Th. Henning for giving me a chance to visit MPIA, Heidelberg, and have many productive discussions with his colleagues at MPIA.

I cannot thank Ishan enough for all the profound discussions we had on a plethora of topics ranging from science to the human mind during our graduate school together. I am indebted to Rickmoy for giving me constant support, friendship and a memorable life during my stay at TIFR. I am deeply grateful to Rashmi, for showing me that there exists a wonderful universe even outside of TIFR.

I thank Harshant, Amit, and Prathyush for the inspiring times we had as roommates during the graduate school at TIFR. Their excitement and zeal towards physics was highly contagious and inspiring. I am indebted to my colleagues and fellow graduate students, Kuldeep, Debdutta, Sudip, Vikas, Jishnu, Ninad, Krishnendu, Nairit, Debjyoti, and all others for great discussions, enthusiasm, and an overall wonderful atmosphere at TIFR.

None of the research I did in this thesis would have been possible without the works of great coders of the Free Software Foundation, and other non-GNU free software. I relied extensively on them for doing my science. I am also deeply indebted to all the great engineers who built the excellent instruments I used for my observations. They are the real backstage heroes who push the frontiers of astronomy forward. I am grateful to the Government of India and my fellow citizens for funding my research in astronomy.

Finally and most importantly, I would like to thank my father, mother and my incredible sister for all the inspiration, guidance, support, encouragement, and love. I am forever indebted to them for their unconditional love, and sacrifices they have made to support me in doing whatever I wished to do.

Dedicated to Shri. H R Madhusudan, JNP, Bengaluru for introducing me to the excitement of experimental physics during REAP undergraduate program.

Contents

List of Figures

List of Tables

List of Abbreviations

FOV	**F**ield **O**f **V**iew
FWHM	**F**ull **W**idth **H**alf **M**aximum
GMRT	**G**iant **M**etrewave **R**adio **T**elescope
HCT	**H**imalayan **C**handra **T**elescope
HRS	**H**igh **R**esolution **S**pectrograph
IGO	**I**UCAA **G**irawali **O**bservatory
MFES	**M**onitoring of **F**Uors and **E**Xors **S**ources
SALT	**S**outhern **A**frican **L**arge **T**elescope
SUTR	**S**ample **U**p **T**he **R**amp
TIRCAM	**T**IFR Near **I**nfra**r**ed Imaging **Cam**era
TIRSPEC	**T**IFR Near **I**nfra**r**ed **Spec**trometer and Imager
YSO	**Y**oung **S**tellar **O**bject

Synopsis

1 Introduction & Motivation

Young low mass stars are formed by the fragmentation and gravitational collapse of cold dense molecular clouds. Due to their initial effective angular momentum, once the gas starts collapsing, they will form a central protostar with a rotating disc and envelope accretion system around it. The final mass this central pre-main sequence star will attain is decided by the efficiency of this disc-envelope accretion. While the overall stages of low mass star formation are known, the details of the physical processes that govern the evolution in each stage are poorly understood. In order to transport matter inward in a disc, it should lose its angular momentum. Molecular viscosities between radial layers in the disc are inadequate by orders of magnitude for transporting angular momentum. Turbulences can give rise to effective large viscosities which can result in the inward movement of matter from the outer disc to the inner disc. Outflows like disc winds are also capable of carrying away angular momentum by magnetic torquing. While all this complex accretion physics is going on, in parallel, planets also form in the disc by grain and pebble growth. The launching mechanism of the collimated outflows, accretion mechanism, angular momentum transport, grain growth for planet formation etc, are all still poorly understood. It is not yet clear whether protostars accrete matter continuously, however, several open puzzles in low mass star formation like the "Luminosity Problem" (mismatch between the observations and the statistically expected luminosity due to accretion from the disc to the star), or the periodic high density knots seen in the outflows of young stellar objects (YSOs), could be naturally explained if the protostars are assumed to be accreting episodically (Kenyon et al., 1990; Evans II et al., 2009; Plunkett et al., 2015). Such a sudden accretion outburst resulting in thermal heating of the disc can play an important role in planet formation (Stamatellos, Whitworth, and Hubber, 2011) and the overall chemistry of the protoplanetary disc. For example, they could explain silicate crystallisation (Ábrahám et al., 2009), formation of Calcium-Aluminium-rich Inclusions (CAIs) and Chondrules detected in comets (Connelly et al., 2012).

Observationally, over the last few decades, accretion from protoplanetary discs to young protostars has been found to be episodic in nature. These high accretion events occur after spending a long time in quiescence and they last for durations of a few months to a few years (known as EXors) to decades or longer (known as FUors). The accretion rate increases by a factor of 10 to 100 during this short period. Accretion outbursts are often serendipitously discovered when they brighten by 3 mag (EXors) to 5 mag (FUors) in the optical band. Detection of these outbursts is extremely rare due to their short duration in comparison to the $\sim$ 3 million years young

stars spend in the disc accretion stage. There are only about 18 of such confirmed sources which have been discovered so far. Analysis of the detection number statistics implies that every low mass star will undergo these outbursts repeatedly (approximately 50 times) during its formation stage (Scholz, Froebrich, and Wood, 2013). These episodic accretion events can significantly change the pre-main sequence isochrones used extensively for age and mass estimation (Baraffe, Vorobyov, and Chabrier, 2012). Even though various instability models have been proposed in the literature, the newly discovered FUors & EXors light curves show a much more complicated behaviour than predicted by the models (Audard et al., 2014).

If we assume the angular momentum taken away by the outflow to be equal to the angular momentum transferred from the accretion, a linear relation can be obtained between the outflow rate and the accretion rate (Konigl and Pudritz, 2000). Hence, almost all theoretical models of outflow driving mechanism predict the outflows to be proportional to the accretion rate (observations also confirm this relation). The large variability in the accretion rate (factor of 10 to 100) in a short time scale (a few years), makes FUors and EXors the best laboratories in the sky to understand various accretion and outflow related effects on protoplanetary discs and envelopes. They are also unique laboratories to test various outflow models by monitoring the simultaneous evolution of the outflow with respect to the accretion rate.

Hence, we started a long-term multi-wavelength monitoring program to characterise and study the FUors and EXors phenomena in detail. This long-term monitoring program was named *Monitoring FUors and EXors Sources* (MFES). Section 2 contains the methodology and multi-wavelength observations carried out in the study. Results from the study are presented in Section 3.

A significant fraction of these FUor and EXor objects chosen for the MFES program are heavily extinct due to the envelopes around them. In those sources, in the optical band, we could only detect the reflection nebula. In order to probe the central young star and the inner regions of the accretion disc, we needed to observe them in near-infrared and longer wavelengths. Initially, we started our near-infrared observations using the 512 $\times$ 512 HgCdTe array NIRCAM camera and 512 $\times$ 512 InSb array TIRCAM-II camera. Their small array size and lack of spectroscopic capability were a major limitation to the study. Hence, we decided to collaboratively develop a larger array (1024 $\times$ 1024) TIFR Near Infrared Spectrometer and Imager (TIRSPEC) with spectroscopic capability for the high altitude (4,500 m amsl) 2 m Himalayan *Chandra* Telescope (HCT), Hanle, India. My contribution to the instrumentation of TIRSPEC and a few other infrared instruments are summarised in Section 4.

During my doctoral work, I also released a few unified general purpose pipelines for the reduction of optical and near-infrared data (both imaging and spectroscopic) for the general user community of these instruments. Section 5 summarises the overall software design principle and capabilities of these pipelines. Finally, Section 6 concludes with the major results on outflow and accretion mechanisms in YSOs from our MFES program, and also the status of the instruments and software developed as part of this thesis work.

2 Methodology & Observations

Typical young solar mass pre-main sequence stars (like most of FUors & EXors) have temperatures of the order of ∼3000 K. They mostly emit in the optical bands. The innermost part of the accretion disc also reaches temperatures of similar order and typically dominates the radiation in the optical and near-infrared bands during an accretion outburst. The accretion shock plasma at the base of the accretion funnel on the surface of the central star strongly emits in the X-ray band. The remaining part of the disc and any left over envelope are the dominant emitters in the far-infrared band. Weak free-free emissions in radio are also expected from the small H II regions created by the shocks due to the central accretion or the outflows.

Since our aim is to study outflows and the inner disc environment, where the instability occurs during an accretion outburst, we decided to carry out long-term continuous monitoring of the optical and near-infrared fluxes from the sample of FUors and EXors which are currently undergoing outbursts. We started the monitoring project, MFES, using optical and near-infrared facilities in India and abroad. The following subsections briefly outline the motivations and the physics probed by our observations at different wavelengths.

2.1 Optical (3500 Å to 9000 Å)

During an accretion outburst in FUors and EXors, the optical continuum increases by a factor of 40 to 100. The energy output is completely dominated by the gravitational energy released from the inflow at the magnetosphere. Multi-band continuous photometric observations in U, B, V, R and I bands were carried out to track the evolution of the accretion, extinction, and periodic as well as non-periodic variations in the illumination by the central source. Along with the imaging observations, for the detailed kinematics as well as other physical environmental diagnostic measurements, we also carried out optical spectroscopic observations in the wavelength range 3500 to 9000 Å. Fluxes of various spectral lines gave an independent measure of the accretion rates, temperature, density etc. They also enabled us to track the evolution of outflow/wind from the innermost region at different accretion rates. The instruments we used for our optical observations are the HFOSC instrument on the 2 m HCT (Hanle, India), the IFOSC instrument on the 2 m IUCAA Girawali Observatory (IGO) Telescope (Pune, India) and the High Resolution Spectrograph (HRS) instrument on the 11 m South African Large Telescope (SALT) (Sutherland, South Africa).

2.2 Near-infrared (1 μm to 2.45 μm)

Near-infrared imaging and spectroscopic observations are also as important as optical since both the wavelength ranges are dominated by radiation from the inner instability region and magnetosphere. Unlike the optical wavelengths, the near-infrared wavelength is less affected by the extinction. Due to the heavy extinction of the central illuminating source, many of our sources in the MFES program were visible only in the near-infrared bands. Imaging in the near-infrared bands enabled us to do various colour-colour and colour-magnitude analyses. Near-infrared spectroscopy enabled us

to monitor magnetosphere accretion from He and H lines (Paschen and Bracket series), and also the evolution of the outburst disc environment using characteristic lines of FUors and EXors originating in the disc (eg: CO molecular band heads at 2.29 - 2.4 μm). The instruments we used for our near-infrared observations are TIRCAM-II on the 2 m IGO & the 1.2 m PRL telescope at Mount Abu (Rajasthan, India), and TIRSPEC & NIRCAM on the 2 m HCT.

2.3 Far-infrared (70 μm to 500 μm)

Since the far-infrared flux in YSOs is dominated by the extended outer disc and left over envelopes, the timescales of the variation in far-infrared flux are quite large in comparison to the optical and near-infrared wavelengths. Hence, we do not have to continuously monitor in far-infrared at the short timescales as we carried out our optical observations. We used multi-epoch far-infrared archival *Herschel* data to constrain the environment of FUors and EXors to estimate the envelope parameters, age, existence of outflow cavity etc.

2.4 Radio Continuum (1280 MHz)

The H II regions which can give rise to free-free emission in the radio band due to accretion or outflow shocks in young eruptive stars are very close to the detection limit of GMRT, India. We attempted to observe a selected sample of our sources using GMRT at 1280 MHz. However, we failed to detect our sources. Nonetheless, non-detection provided us upper limits on the Lyman continuum flux as well as the extent of H II regions around these sources which are currently undergoing outburst.

3 Intermediate FUors - EXors

For this thesis, among FUors and EXors in our MFES program, based on our preliminary analysis, we selected the most peculiar ones for a detailed study. Particularly, properties of V1647 Ori and V899 Mon seemed to fall at an intermediate region between the classical FUor and classical EXor properties. They had a mixture of spectroscopic signatures from both the families of outburst, and unlike classical FUors, they showed significant accretion variations over a timescale of a few years. Both of them also stopped their first accretion outburst abruptly to spend a short duration in quiescence and returned quickly to a long second outburst. This property alone makes these sources the ideal laboratories to test various disc instability models and accretion-outflow models. The first step of the study was to quantitatively characterise their outburst environments and detect any evolution at different phases of their outburst.

3.1 V899 Monoceros

In the Catalina Real-time Transient Survey (CRTS), V899 Mon (aka. IRAS 06068–0641) near the Monoceros R2 region, located 905 pc away (Lombardi, Alves, and Lada, 2011), was found to be suddenly undergoing an increase

in brightness. This discovery was first reported by Wils et al., (2009). We immediately started observing this source as part of our MFES program from 2009 November 30. The first step was the characterisation of the central pre-main sequence star. Using mid-infrared fluxes from the WISE survey, we obtained the mid-infrared slope of V899 Mon to be -0.5, which makes it a flat-spectrum source or an early Class II YSO. The increase in brightness during the outburst was 3 magnitude in the optical band. Since during an outburst, the flux is dominated by the accretion process, the colours representative of central sources can only be seen during its quiescent phase. Comparing all the colour combinations of U, B, V, R and I magnitudes from our observations during the quiescent period with Siess, Dufour, and Forestini, (2000) isochrone colours, we could constrain the mass of V899 Mon to be $\sim$ 2 $M_{\odot}$, and the extinction to the central source A_V to be $\sim$ 2.2 - 4 mag. These values were also found to be consistent with the estimates of extinction from near-infrared (J, H, K_S) colour-colour diagrams as well as the SED analysis. Far-infrared *Herschel* SPIRE and PACS images showed a heavy clump (mass $\sim 20\,M_{\odot}$) at the location of V899 Mon. From extinction estimates, we could conclude that the clump is not obscuring V899 Mon. However, the clump is thermally connected to V899 Mon, since we detect changes in far-infrared flux at two different phases of the V899 Mon's outburst. We concluded that it is either behind V899 Mon or we are seeing V899 Mon's optical light escaping through an outflow cavity. Spectral line profile shapes and high velocity component values in forbidden lines originating from jets also implied V899 Mon to be at a very low inclination angle. From these spectral line fluxes, we estimated the accretion rate, mass outflow rate, density and temperature in jets etc. Spectroscopically, V899 Mon showed a mixture of FUors as well as EXors signatures. While magnitude change and timescales were characteristics of EXors, higher level H atomic lines as well as CO lines were seen in absorption like in an FUor. Hence, V899 Mon clearly falls between the classical FUors and EXors.

During our monitoring period in 2010, V899 Mon suddenly increased its outflow strength and velocity to very large values ($>$ 800 km s^{-1}). We could also detect large variations in lines like O I λ7773 which measures turbulence in the disc during this period. Optical and even mid-infrared flux observations by the WISE telescope during this period showed significant fluctuations. By 2011, V899 Mon suddenly stopped its first outburst and transitioned to the quiescent phase. Surprisingly, just after one year in the quiescent phase, it returned to a second outburst phase. V899 Mon is still continuing its second outburst (until our recent observation in March 2016). As a first step, using the extinction law and spectral line flux changes, we ruled out the hypothesis that a temporary dust obscuration was the possible cause of dimming of V899 Mon (such events of dust obscuration are seen in UX Ori systems). We could conclude the quiescent phase to be a real period of reduced accretion, and during that phase, the accretion rates dropped by atleast a factor of 4. The evolution of the optical colours at different phases of transition showed the SED temperature of the optical flux was coolest during the transition phase (not at the quiescent phase!). This change in temperature was confirmed to be unrelated to the change in extinction by calculating the extinction invariant colour coefficients. Such a trend is consistent with what would be theoretically expected when the outburst originates in a disc cooler than the photosphere temperature (which

is seen during the quiescent phase). Hence, these measurements provide observational support for disc instability models of outburst. Our spectroscopic monitoring of V899 Mon's transition from the first outburst phase to the quiescent phase and back to the second outburst phase was at a temporal frequency which has not been possible in any other FUors or EXors. Hence, we could track the accretion and outflow evolutions at an unprecedented interval. Our spectra showed that the outflows, indicated by the P-Cygni profiles, completely disappeared when the source went from the first outburst phase to the quiescent phase. Outflows later reappeared gradually only after V899 Mon reached the peak of the second outburst. Overall, this is consistent with the theoretical outflow models which predict outflows to be proportional to the accretion rate. During our further monitoring in the second outburst, we detected significant decoupling in the instantaneous outflow strength to the accretion rate. We could detect high velocity episodic outflow variations in timescales as short as a week as shown in Figure 1.

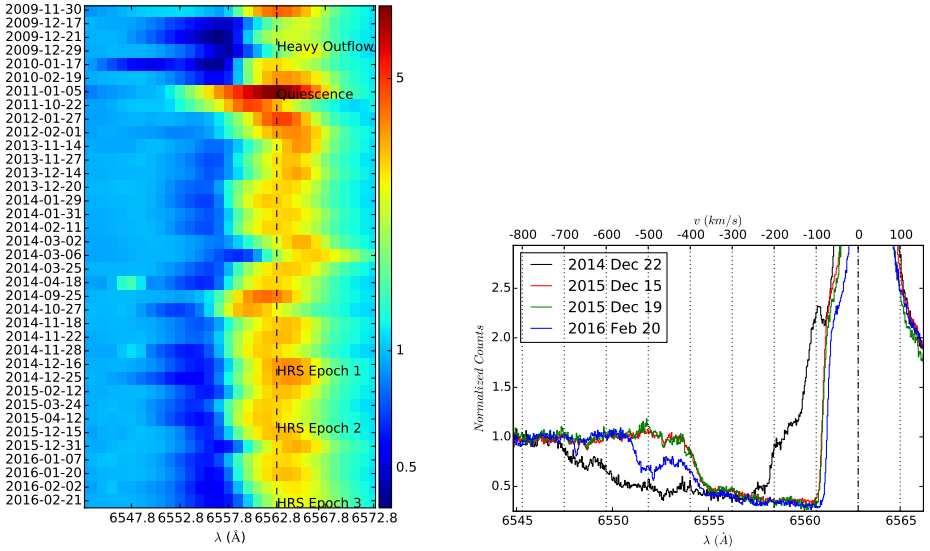

Medium Resolution Spectra

High Resolution Spectra

FIGURE 1: Outflow evolution traced in our medium resolution spectra (left figure) from 2009 to 2016 of the Hα line profile of V899 Mon. The main three epochs of HRS observations (shown on the right) are marked in the left figure. The variation in the extent of blue-shifted absorption shows the variation in peak velocity of the outflow at each epoch. The vertical dashed line is the center wavelength of the Hα line.

In order to study the evolution of these outflow components, we took high resolution (R$\sim$37000) optical spectra using the HRS instrument on the 11 m SALT at four different epochs. First, second, third and fourth observations were separated by a year, four days and two months respectively. We detected a change in velocity from -722 km s^{-1} in 2014 December to -425 km s^{-1} in 2015 December and to -550 km s^{-1} in 2016 February. Such large velocity changes, when the accretion rate remains fairly steady over these epochs, have never been seen in any YSOs. We did a detailed comparison analysis on possible outflow mechanisms proposed in literature by various

simulation groups and concluded that we might be seeing the signatures of magnetically driven polar winds predicted in magnetohydrodynamics simulations (see Section 3.3).

3.2 V1647 Orionis

V1647 Ori is located in the L1630 dark cloud of Orion, 400 pc away from us. It underwent a sudden outburst of ∼5 mag in the optical band in 2003 (McNeil, Reipurth, and Meech, 2004; Briceño et al., 2004) and illuminated a reflection nebula, now named as McNeil's nebula after its discoverer Jay McNeil. This is one of the extensively studied young eruptive stars in literature. V1647 Ori is a 0.4 Myr Classical T-Tauri star which has a disc of mass 0.05 $M_{\odot}$ and an inclination angle of $\sim 61^{o}$ (Acosta-Pulido et al., 2007a). Accretion rate of V1647 Ori has been 5×10^{-6} $M_{\odot}$ yr^{-1} during outburst phase and 5×10^{-7} $M_{\odot}$ yr^{-1} in quiescent phase (Acosta-Pulido et al., 2007a). Archival data shows ∼37 years prior to the 2003 outburst, i.e., in 1966, V1647 Ori had undergone a similar magnitude outburst, lasting somewhere between 5 and 20 months. What made this source very exciting is that after the source ended its 2003 outburst in 2006, within 2 years of quiescence it underwent a second outburst in 2008. It has been in an outburst state ever since (till our last observation in March 2016).

We started long-term continuous monitoring of the second outburst on 2008 September 14. To remove contamination from the strong non-uniform reflection nebula background, we developed a background interpolation based photometry and obtained accurate photometry of V1647 Ori observed in 110 nights spanning 5 years. We detected V1647 Ori to be undergoing a slow dimming at a rate of 0.04 mag yr^{-1} during its ongoing seemingly "plateau" shaped outburst phase. This rate is six times slower than the rate of dimming during the previous 2003 outburst. We could also detect a very interesting faster decline in the amount of light escaping via the cavity from accurate photometry of a knot in the reflection nebula. The V1647 Ori magnitudes also showed significant fluctuations in a timescale of a few days. At this rate of gradual dimming, scaling the duration of the first outburst, V1647 Ori will most likely remain in the outburst phase till ∼2020. By studying how the illumination on the reflection nebula has drifted over time, we could detect a consistent evolution in the circumstellar gas distribution between the 1966, 2003 and 2008 outbursts. The up and down movement of V899 Mon in the near-infrared colour-colour diagram along the reddening vector at different phases of the outbursts strongly hinted at a repeated dust sublimation of atleast A_V ∼5 mag between both the outbursts. We could detect forbidden [O I] λ6300 and [Fe II] λ7155 lines, which implies the existence of shock regions of T $\sim$ 9,000 - 11,000 K and n_e $\sim$ 10^5 -10^6 cm^{-3}, probably originating from jets. We could detect continuous strong outflows (∼350 km s^{-1}) formed near the magnetospheric accretion region in the P-Cygni profile of Hα line. Interestingly, we could also detect two short duration episodic winds with a H column density $\sim$ 3.4 $\times$ 10^{20} cm^{-2} in 2008 October and December (derived from the P Cygni profiles in Ca II IR triplet lines). Such episodic winds were detected for the first time in this family of objects, most likely driven by magnetic reconnection events.

3.3 Constraints on Physical Mechanism

Constraints from the short duration quiescence

Theoretical models that are available in the literature for explaining FUor/EXor outbursts can be broadly classified into three types. The first kind of model is purely a thermal instability model, initially proposed for dwarf nova systems and was later adapted for the FUors kind of outbursts (Bell and Lin, 1994). The second kind of model involves a binary companion or planet, which perturbs the disc, causing repeated sudden high accretion events (Bonnell and Bastien, 1992; Lodato and Clarke, 2004). The third kind invokes gravitational instability (GI) in the outer parts of the disc and also triggers magnetorotational instability (MRI) in the inner regions of the disc (Zhu et al., 2009, and references therein). In Bell and Lin, (1994) model, the thermal instability (or MRI in MRI based models) is triggered when the surface density in a region of the disc rises above a critical density (corresponding to a critical temperature). Due to the high effective viscosity, as a result of the eddies in instability, the disc will drain faster and it will go back to the quiescent phase when the surface density drops below another critical density. The viscous timescales determine the duration of the outburst and quiescent phases. Hence, to fill up the disc, it is fundamental for both the thermal instability and the MRI instability models to have a longer duration in the quiescent phase than in the outburst phase. This is in sharp contrast to the short duration quiescence seen in V1647 Ori ($\sim$ 2 years) and V899 Mon ($\sim$ 1 year) between their first and second outbursts. We did a quantitative analysis of the timescales in V1647 Ori based on the viscous alpha (α) disc model, and concluded none of the instability models which need the disc surface density to toggle between two critical densities can explain the light curve of V1647 Ori. This is so in the case of V899 Mon's light curve also. While for the large timescales (decades) of outbursts and quiescence, these instability models are valid, we need to look for other mechanisms which can pause the accretion for a short period without having to drain the disc below the critical density to explain the short period quiescence detected in V1647 Ori and V899 Mon. In case of V899 Mon, our spectroscopic observations showed heavy outflow activity just before V899 Mon transitioned to the quiescent phase. This is consistent with various disruptions due to magnetic funnel instabilities that can arise in magnetospheric accretion. Such instabilities can apply brakes to the accretion, since the discs still have surface density above the critical density, they can restart outburst immediately once the magnetic accretion funnel stabilizes. Hence, we proposed such instabilities seen in simulations are consistent, and could be the mechanism which can explain the short duration pauses in outburst.

Constraints from the episodic outflows

The large variations in the outflow velocity from V899 Mon at timescales as short as weeks could give a constraint on the outflow driving mechanism. Figure 2 shows the possible outflow mechanisms in a YSO from various simulation studies in literature. Each of these outflow wind mechanisms has characteristic stability timescales and outflow angles. Due to the likely low inclination angle (deduced from extinction, spectral line profile, etc.) of V899 Mon, outflows traced by the P-Cygni profile cannot be associated

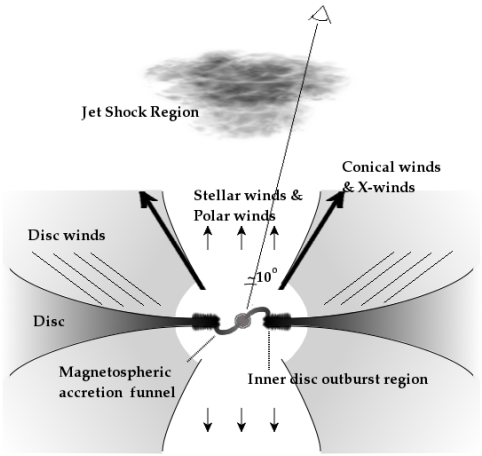

FIGURE 2: Schematic diagram of various outflow mechanisms which could be present in V899 Mon.

with disc winds, X-winds or other conical winds from the magnetosphere boundary. They can occult the line of sight and result in blue-shifted absorption only when the inclination angle is $\geq 30^o$. Typical stellar winds driven by radiation pressure along the polar axis were also found to be not variable enough to explain the large velocity changes like -722 km/s to -425 km/s. Due to the terminal velocity limit in these winds we could also rule out changes in optical depth to be the cause of apparent change in the outflow velocity detected in the P-Cygni profile. When the disc truncation radius due to the magnetosphere is outside the star-disc co-rotation radius, there can be magnetically accelerated winds in the polar direction, similar to the propeller regime high velocity outflow seen in fast rotating magnetospheres. After ruling out other mechanisms, we concluded that the most consistent mechanism which can give rise to such unstable, clumpy, short duration, high velocity winds are the magnetically accelerated polar winds seen in simulations by Kurosawa and Romanova, (2012). To our knowledge, V899 Mon has the most dynamically varying outflow strengths and velocity among YSOs observable in the optical band. Hence, we propose V899 Mon to be the most promising YSO to model and constrain various magnetospheric accretion and outflow simulations of YSOs.

Constraints on outburst frequency: A Hierarchical Bayesian model

The fundamental question regarding FUors and EXors is their role in star formation and the pre-main sequence evolution of YSOs. Do all young stars undergo these outbursts? What fraction of the final mass of a star is accumulated due to these outbursts? To answer these questions, their period of recurrent outbursts, age-period relation, etc. have to be understood. There have been some attempts to constrain these quantities by modelling occurrence of FUors events as simple binomial probability events (Scholz, Froebrich, and Wood, 2013; Hillenbrand and Findeisen, 2015). But, these models have a major limitation that they are modelling the probability of detection of outburst in a sample of YSOs observed at two different epochs. Hence, by design these models are restricted to use only a small set of multi-epoch surveys which are available.

The vast amount of photometric astronomical data are spread across many decades (and wavelengths) over the last century. I therefore modelled the whole process as a hierarchical Bayesian model, which gives enough freedom to make realistic models of multi-epoch, multi-wavelength astronomical observations. This will in future enable us to combine and use all the available archived photometric observations of the star forming regions (from VizieR and other observatory databases) to estimate the outburst frequency. The model being Bayesian also makes it straightforward to incorporate the probability distribution of the parameters from other observational methods like outflow knots, chemical abundance tracers of outburst, etc. It also enables us to predict how the constraints get better as more astronomical observations and data archives become available.

4 Near Infrared Instrumentation

Many of the sources in our MFES program are deeply embedded in the envelope. In the optical band, the central source is heavily extinct, and only the bright reflection nebula is typically visible around it. Hence, near-infrared observations are crucial for studying these deeply embedded sources. At the beginning of our project, the 512×512 HgCdTe array NIRCAM camera on the 2 m HCT was the only near-infrared imaging camera available to the general community in India. It had a small effective field of view (FoV) of 1.8 $\times$ 1.8 arcmin^2 which made it difficult to do accurate photometry using secondary standards in the field. For obtaining large FoV, TIFR IR lab first upgraded TIRCAM to TIRCAM-II by using a larger Raytheon InSb 512 $\times$ 512 pixel Focal Plane Array. My contribution to TIRCAM-II camera development was on the characterisation and calibration of the array and in the development of the data reduction pipeline. We could do imaging from J (1.2 μm) to L′ (3.6 μm) band. TIRCAM-II is currently being used with the 2 m IGO telescope, Pune. It is currently the only camera in the country which can do imaging upto L′ band.

4.1 TIRSPEC

One of the major goals of the MFES program is to track the evolution of accretion rate and outflows during different phases of the accretion outburst events. For measuring these quantities we needed to have spectroscopic observation of the line strengths of the near-infrared lines like Brγ, He I, etc. To meet this need, the TIFR Near Infrared Spectrometer and Imager (TIRSPEC) (Ojha et al., 2012) was conceived. It was developed in collaboration with M/s. Mauna Kea Infrared, LLC (MKIR), Hawaii, USA. TIRSPEC was designed for the side port of HCT, which enables us to do near simultaneous observations in both optical and near-infrared bands by switching the ports using a tertiary mirror. It was designed to have a FoV of 5 $\times$ 5 arcmin^2 in the imaging mode. We used multiple orders of a master grism and order sorters to obtain slit spectroscopy from 1 to 2.45 μm at a resolving power of $\sim$ 1200. Teledyne 1024 $\times$ 1024 pixel HAWAII-1 PACE array detector was used as the focal plane array. In the initial phase of the project, my contributions were on the software control and the wheel

mechanisms (as summarised below). We have one central Instrument Control Server, which coordinates the Mechanism Control Server, Array Control Server and the client GUI. The readouts from the array are done non-destructively by sample-up-the-ramp method at an optimal 3 μs per pixel rate in parallel from four quadrants of the detector. Hence, each exposure creates a 3-D data cube instead of a single readout image. This relatively new method of array readout enabled me to implement novel features like cosmic ray hit healing, saturation healing, non-linearity correction and non-linear bias voltage subtraction, before fitting straight line slopes to the data cube to generate the final image. These corrections significantly increased the dynamic range of images enabling us to take images of fields which contain both bright and faint stars simultaneously. For accurate photometry and spectroscopy, detector characterisations are very important. I quantitatively characterised the dark current, reset anomaly in HAWAII-I PACE array, effective read noise, gain, linear regime of individual pixels, detector persistence and fringe issue, bad, hot and cold pixels. Reset anomaly is a well known problem with HAWAII-1 PACE arrays, and from our noise statistic studies, I concluded that they are not thermal in origin and has features of a bias voltage non-linearly dropping with time after the last full detector reset. Spectral resolving power as a function of wavelength was estimated from narrow lines in the Argon spectrum. After thorough testing at TIFR, Mumbai, we transported the instrument to Hanle, and mounted it on HCT (4500 m abmsl) in June 2013. We obtained our first light on 21st June 2013. After the installation of the instrument, during the engineering calibration runs, from night sky observations, I characterised the instrument's plate scale, field of view, site's sky background and stability, field of view distortion, instrument flexure effects on slits and wavelength calibration, throughput, photometric as well as spectroscopic sensitivity, and finally, the colour equations for calibrating TIRSPEC magnitudes to the 2MASS magnitude system. We also conducted a few mechanism repairs to correct problems caused by the drop in liquid nitrogen boiling point due to low atmospheric pressure at the high altitude Hanle Observatory. We also updated the slit lengths in July 2014 to do larger dithering patterns.

I also developed observation tools to help the observers estimate various quantities like exposures, dither pattern, telescope shifts etc. A complete data reduction pipeline was also developed by me to reduce both imaging and spectroscopic near-infrared data. All the source codes (which are not under ITAR regulation) are released to the general astronomy community. The instrument was released to the general community from May 2014. It is right now heavily used by a wide astronomy community for science ranging from planetary sciences, to galactic star formation, to extra galactic studies. TIRSPEC was also extensively used for our MFES observational program.

4.2 TIFR Far-Infrared Balloon Telescope

The IR group at TIFR has been observing in the far-infrared (FIR) band (120 to 220 μm) using the TIFR 1-m FIR balloon borne telescope (Ghosh et al., 1988; Ghosh, 2010). To improve the pointing accuracy and aspect of the scan maps generated by the FIR telescope, I developed a wavelet based signal processing pipeline for the optical photo diode array signal, which is

generated as the telescope scans the sky for generating the FIR map. This optical image was then matched with the optical sky to correct for any systematic offset in telescope pointing. The FIR data are obtained from a Fabry-Perot Spectrometer which scans around the line of interest which is being observed. A general tool was developed to process this data and generate the map of the line strength and continuum separately. Using this, we generated [C II] 158 μm maps of nearby massive star forming regions which are now being used to study various heating and cooling mechanisms in photo dissociation regions in massive star forming regions.

5 Pipelines

MFES program being a long-term project spanning hundreds of nights from multiple instruments in optical and near-infrared bands, we needed to develop a systematic data reduction procedure and pipeline. Instead of a single purpose pipeline to reduce MFES data, the pipeline was designed to be useful to the general public for any of their science observations. Following were the major design philosophies followed in the development of the pipelines.

- Zero compromise on the reduction quality (with respect to manual reduction). Even if this means certain steps in reduction cannot be fully automated. For example, manual inspection of raw data to discard anything unusual was not automated.
- Minimise human interaction as much as possible.
- Unified interface for all the conceptually similar instruments. This helps astronomers to easily switch between instruments without having to learn a new pipeline each time.
- It should be usable by the general astronomy community who uses these instruments for studies different from the type of observations involved in MFES program.
- It should be modular, documented and re-factored enough to make it easy to add more instrument support to the pipeline as new instruments get commissioned in future.
- All codes are to be released to the public under GNU GPL 3+ license. Code structure should be reusable at a modular level to enable users to reuse them in their own programs or pipelines.

Pipelines were written by me in Python language to make use of the existing standard astronomy/science libraries like *astropy, numpy, scipy* and *pyraf*. All the codes are version controlled and hosted on Github and they are being constantly updated and improved as more and more users give feedback and suggestions. The algorithms of reduction are explained in the corresponding papers mentioned in the pipeline web page.

6 Conclusion

We carried out a long-term multi-wavelength monitoring of the FUors and EXors sources (MFES program) to characterise and understand the eruptive outburst phenomenon seen in YSOs. We did a detailed analysis of two of the most peculiar sources in the family of young eruptive sources, V899 Mon and V1647 Ori. They both showed a mixture of photometric and spectroscopic signatures of classical FUors as well as classical EXors; possibly indicating that the distribution of eruptive young variables form a continuous spectrum, not bimodal. We detected V899 Mon undergoing short term quiescence, and could monitor the simultaneous evolution of the accretion and the outflows. Our analysis of V899 Mon and V1647 Ori showed that the pure disc instability models cannot explain the short period quiescence seen in both of these objects. We proposed support for mechanisms which can temporarily pause magnetospheric accretion, without requiring the disc surface density to drop below a critical value (as required by various instability models). Our detection of heavily fluctuating high velocity outflows in V899 Mon prior to the transition strongly suggests instabilities in magnetospheric accretion. From our detection of large velocity fluctuations in the outflow from V899 Mon, we could constrain the outflow mechanism, and probably made the first detection of the polar winds driven by magnetic pressure similar to the winds in the propeller regime of a rotating magnetosphere.

For the study of heavily embedded sources in the MFES program, we also developed TIFR Near Infrared Imager and Spectrograph (TIRSPEC). After the detailed calibrations and performance analyses, the instrument was released to the public in May 2014, and it is heavily used by the astronomy community. Unified pipelines for data reduction of all the instruments used in the MFES program (optical and near-infrared, imager and spectrographs) were also written and released to the public under GNU GPL3+ license.

List of Publications

Thesis-Related Publications in Refereed Journals

1. 'A Bayesian Model for Constraining the FU Ori Outburst Frequency', **Ninan J.P.**, Ojha D.K. & Hillenbrand L. A., 2016b, (submitted in ApJ on 4^{th} August, 2016; under review)

2. 'Episodic High Velocity Outflows from V899 Mon: A Constraint On The Outflow Mechanisms', **Ninan J.P.**, Ojha, D.K., & Philip, N.S., 2016a, ApJ, 825, 65

3. 'V899 Mon: An Outbursting Protostar With Peculiar Light Curve And Its Transition Phases', **Ninan J.P.**, Ojha, D.K. et al., 2015, ApJ, 815, 4

4. 'TIRSPEC: TIFR Near Infrared Spectrometer and Imager', **Ninan J.P.**, Ojha, D.K. et al., 2014, Journal of Astronomical Instrumentation, 03, 1450006

5. 'Re-appearance of McNeil's nebula (V1647 Orionis) and its outburst environment', **Ninan J.P.**, Ojha D.K. et al., 2013, ApJ, 778, 116

6. 'TIRCAM2: The TIFR Near Infrared Imaging Camera', Naik M. B. et al., BASI, 2012

Thesis-Related Publications in Conference Proceedings

1. 'Probing the Structure and Kinematics of Outflows in Episodic Accretion of YSOs', SALT Science Conference 2015, PoS, SSC2015, 069

2. 'Second outburst phase of a young eruptive star V1647 Orionis (McNeil's nebula)', Astrochem2012, 1543, 1, 184-186, 2013, AIP Publishing.

3. 'Constraining models of accretion outbursts in low-mass YSOs' Ninan, J.P., Ojha, D.K., et al., 2013, ASI Conference Series, 9, 78.

4. 'The outburst and nature of young eruptive low mass stars in dark clouds', Ninan J.P., Ojha D.K. et al.,ASI Conference Series, 2012, Vol. 4, pp 1-8.

5. 'Post-outburst phase of LDN 1415 nebula (IRAS 04376+5413)', Pawade V. S. et al., ASI Conference Series, 2010, Vol. 1, pp 243-244

6. 'Second outburst phase of McNeil's nebula (V1647 Orionis)', Kaurav, S. S. et al., ASI Conference Series, 2010, Vol. 1, pp 237-238

Other Publications

1. 'Star formation activity in the neighbourhood of W-R 1503-160L star in the mid-infrared bubble N46', Dewangan L., Baug T., et al., 2016, ApJ, 826, 27

2. 'Near-Infrared Imaging of Barred Halo Dominated Low Surface Brightness Galaxies', Honey M., Das M., **Ninan J.P.**, et al., 2016, MNRAS, 461

3. 'Optical and NIR observations of the nearby type Ia supernova SN 2014J', Srivastav S., **Ninan J.P.**, et al., 2016, MNRAS, 457, 1000

4. 'A multi-wavelength study of star formation activity in the S235 complex', Dewangan L., Ojha D. K., et al., 2016, ApJ, 819, 66

5. 'Sh2-138: Physical environment around a small cluster of massive stars', Baug T, Ojha D.K., et al. 2015, MNRAS, 454(4): 4335-4356

6. 'Large-Scale Mapping of the Massive Star-Forming Region RCW38 in the [CII] and PAH Emission.', Kaneda, H. et al., 2013, A&A, 556, id. A92

Chapter 1

Introduction

The origin of our solar system has fascinated humanity from ancient times. Modern rigorous scientific studies to understand the formation of planets can be traced back to three centuries ago when Baffon (1749) first suggested that planets were formed via condensation of materials knocked out of the Sun by colliding comets. The current, well established theory of star and planet formation from the collapse of nebular clouds ('the nebular hypothesis') can be traced back to philosopher Immanuel Kant in 1755. It was Laplace, in 1796, who formalised this nebular hypothesis of the formation of a disc by the collapse of giant nebular clouds. He also refuted Baffon's idea, by arguing that if planets were formed by matter knocked out of the Sun, those material's Keplerian orbit would most likely crash them back in to the Sun. However, Laplace's nebular hypothesis could not explain why the angular momentum of the Sun, which consists of 99.8% mass of our solar system, has only 1% of the total angular momentum of our solar system[1]. Hence, the nebular hypothesis lost its popularity and was replaced by other competing models of two body interactions (which were in the same spirit of Baffon's theory). In the early half of the 20th century, various models in which material pulled out tidally from the Sun by other flyby stars, condense into planets were put forth separately by Chamberlin, Moulton and Jeans (1900s-20s). By the 1930s, many astronomers, mainly Jeffreys, Russel, and Spitzer, identified various issues with these models. For instance, the low probability of flybys by other stars, the difficulty in attaining large orbits for outer planets, and the inability of the hot gas to collapse into planets (ironically Spitzer used Jean's equilibrium criterion itself to demonstrate this!). The nebular hypothesis finally made a come back in the 1960s -70s in the form of protoplanetary disc models by the works of Lyttleton, McCrea, Safranov, etc. (see Woolfson, (1993) for a detailed historical summary).

Currently, it is well established that stars and planetary systems form by fragmentation and gravitational collapse of giant molecular clouds. The conservation of initial net angular momentum of the collapsing clouds in these stellar nurseries inevitably results in formation of a rotating accretion disc around the protostars[2]. With the advent of space-based infrared telescopes and ground-based sub-millimetre antennae over the last 3 decades,

[1] Even with the modern theories of angular momentum transport in protoplanetary discs, angular momentum still haunts our theories in more subtle ways like it did to Laplace three centuries ago!

[2] While it is also likely the case in high mass ($>2\ M_{\odot}$) stars, due to relatively poor observational evidence compared to low mass stars, the last word on the question of formation of accretion disc in high mass stars is not yet out.

astronomers have revolutionised the understanding of this crucial baby-stage of star and planet formation in deep stellar molecular cloud nurseries.

1.1 Life of a protoplanetary disc

The formation timescale of a protoplanetary disc is relatively very short ($\sim 10^4$ years). It is a function of the rotation rate of the central core as well as the free-fall time (Terebey, Shu, and Cassen, 1984). Since these parameters are sensitive to ambient conditions like the magnetic field strength, initial angular momentum, etc., it is quite likely that the initial masses and sizes of protoplanetary discs are spread over a large range of values. The heavily embedded initial cocoon phase, classified as Class 0, is not seen in optical or near-infrared wavelengths. Their observational studies started only recently after the development of technologies in the early 90s to probe them in the far-infrared and millimeter wavelengths. After Class 0, the protostar moves to Class I, Class II, and Class III stages[3] before entering the main-sequence life. They are classified based on the slope of spectral energy distribution (SED) in mid-infrared regime (Lada, 1987; Greene et al., 1994). Class I stage typically lasts for about $\sim$ 0.5 Myr. About 50% of the final main-sequence mass of the central star is accumulated by the early phase of Class I stage ($\sim$0.1 Myr). By the time the protostar with its circumstellar disc system enters the Class II stage, they slowly clear their circumstellar envelope cocoons and start becoming visible in the optical wavelengths. Meanwhile, the accretion of matter from the disc to the central star continues for the lifetime of the protoplanetary disc, which varies from 2 to 10 Myr (with a median of around 3 Myr). As the star becomes a Class III source, the accretion rates drop significantly (typically classified as weak-line T-Tauri stars). And finally, at a certain epoch, the disc suddenly vanishes in a short timescale. Discs in this clearing process are called transitional discs. The presence of mid-infrared flux excess at this stage, even when we do not see any significant near-infrared excess implies, the disc vanishes inside-out from the central source[4] (see review by Williams and Cieza, (2011) and references within). Figure 1.1 shows the summary of the formation stages of a protoplanetary disc system.

All the processes of planet formation and the growth of a central protostar have to finish in this short period of circumstellar accretion disc's existence (median lifetime of $\sim$3 Myr). The physical properties and the thermal state of the protoplanetary disc during its short period of existence determine the environment in which planets and stellar systems have to form. There is a complex radiative feedback in play here due to the self irradiation of the released accretion energy. This heating significantly affects the thermal and gravitational stability of the accretion disc, which in turn influences the accretion rate.

[3] Between Class I and Class II, there is also an intermediate class of sources known as flat spectrum sources. Their slope of mid-infrared SED falls between Class I and Class II.

[4] By mechanisms like photo-evaporation.

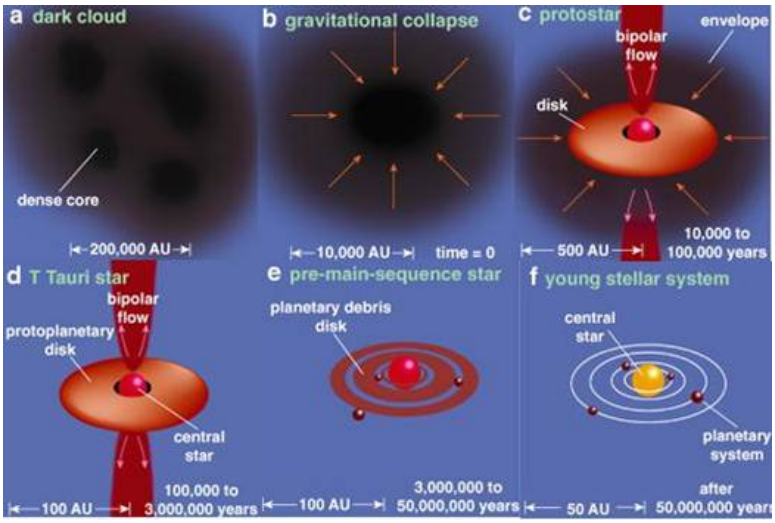

FIGURE 1.1: Stages and timescales in the formation of a star-planetary system from the collapse of giant molecular clouds. Image Courtesy: Thomas Greene, American Scientist, Jul-Aug 2001

1.2 Hints for episodic accretion

The crucial environmental parameters like the chemical composition, gravitational stability, thermal state, etc., of the protoplanetary disc are governed by the gravitational energy released from accretion. Hence, understanding the evolution of the accretion rate during the lifetime of a protoplanetary disc is imperative.

1.2.1 Luminosity problem

As mentioned in the previous section, half of the stellar mass is accreted in the first ~ 0.1 Myr. It implies that, for a 1 $M_\odot$ star, the average accretion rate during that period should be $\sim 5 \times 10^{-6}$ $M_\odot$ yr^{-1}, which will correspond to a mean accretion luminosity of about 25 $L_\odot$. This is much larger than the average observed luminosities of protostars from far-infrared surveys (Dunham et al., 2008). This famous problem in star formation is known as the "Luminosity problem" (Kenyon et al., 1990; Evans II et al., 2009). Even though the measurement of the accretion rates from the envelope to disc is not that robust, there is no significant indication of a mismatch between the expected and the observed accretion rates from the envelope to disc. This open problem can be solved if we envisage the hypothesis that the accretion from the disc does not occur at a constant rate, instead, it occurs in intermediate short period bursts of high accretion events. Since most of the sources we observe in a survey are statistically likely to be between these accretion bursts, we would possibly detect only the lower rates of accretion (Hartmann and Kenyon, 1996).

1.2.2 Calcium-aluminum-rich inclusions & Chondrules

In our own solar system, the thermal history of our protoplanetary disc is preserved in the chondrite meteorites. They contain complex millimeter to centimeter sized objects called calcium-aluminum-rich inclusions (CAIs) and Chondrules (see Figure 1.2). Radio dating of these objects show that they were formed recurrently during the lifetime of our historical protoplaneatry disc. CAIs can be formed only in high-temperature environments (>1300 K) and show signatures of recurrent re-melting. Chondrules were formed by getting flash heated to melting point and slowly cooled at slightly lower temperatures (<1000 K), recurrently over a timescale of ~ 3 Myr (Connelly et al., 2012). These temperatures and timescales are easily achieved in the inner part of the disc if the episodic accretion outburst hypothesis is true. Chondrules and CAIs once formed at the inner parts of the disc could get sprayed all over the outer regions of the disc via outflows (Shu, Shang, and Lee, 1996), or/and via radial diffusion along the midplane of the disc (Ciesla, 2007).

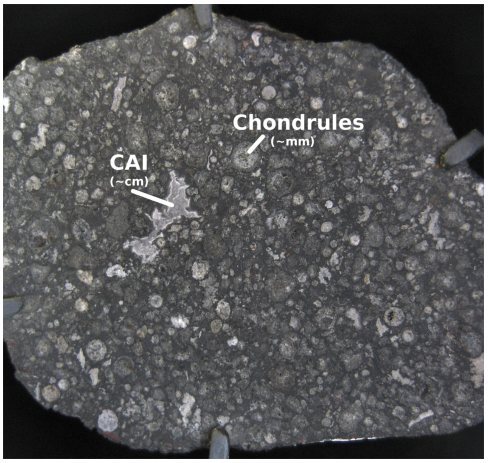

FIGURE 1.2: A slice of famous chondrite Allende meteorite which has CAIs and Chondrules embedded in it. Courtesy: Museum of Natural History, NY, USA

1.2.3 Outflows and the associated structures

Young stellar objects (YSOs) are also drivers of the spectacular, heavily collimated outflows and jets seen in star-forming regions (see Figure 1.3). When matter is accreted from the accretion disc, it also transfers angular momentum to the central star. If the angular momentum is not taken away from the system, a typical accreting classical T-Tauri star (CTTS) will reach break-up speed within the timescale of a million year. However, observationally CTTSs are found to be rotating only at $\sim$10% of the break-up speed (Herbst et al., 2007). Their rotation rate is also found to be almost constant throughout their disc accretion phase spanning a few million years (Irwin and Bouvier, 2009). Outflows from these objects are the most efficient way to take away the angular momentum from the star-disc system and prevent the star from spinning up. Hence, we expect the outflow to be proportional to the accretion rate. If that is the case, then one way to explain the dense

knots seen in the outflows (see Figure 1.3) are episodic events of high accretion. They could be the fossil evidence of accretion outbursts in the YSO's history (Dopita, 1978; Reipurth and Aspin, 1997; Ioannidis and Froebrich, 2012).

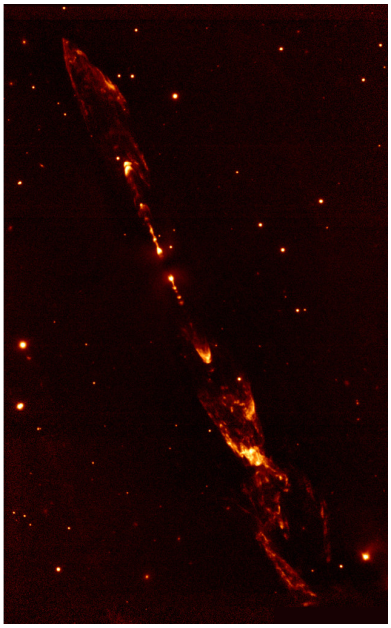

FIGURE 1.3: Near-infrared image of a spectacular, heavily collimated bipolar outflow, HH212. Knots are seen along the outflow. The central protostar driving the outflow is hidden by the disc due to its edge on view. Image Courtesy: Zinnecker, A. et al. 1997, Thomas Stanke, ESO

1.2.4 FUors and EXors Phenomenon

Observationally, some YSOs have been serendipitously discovered to undergo a sudden increase in brightness. Traditionally, on the basis of the light curve and spectrum, these accretion outbursts are classified as FUors (showing decades-long outbursts with 4–5 mag change in optical bands, and an absorption-line spectrum) and EXors (showing outbursts of a few months to years long with 2–3 mag change in optical bands, and an emission-line spectrum) (Herbig, 1977; Hartmann and Kenyon, 1996; Hartmann, 1998). Figure 1.4a shows the light curves of the three classical FUors, namely FU Ori, V1515 Cyg, and V1057 Cyg.

These sources were all spatially and kinematically associated with star forming regions. They showed reflection nebulae, significant infrared excess, CO band head absorptions in near infrared, different spectral types between optical and near infrared bands, etc. The widths of the emission lines as a function of wavelength were consistent with what we would expect from a bright accretion disc with a radial temperature gradient. These properties confirmed FUors to be YSOs with a luminous accretion disc, undergoing heavy rates of accretion (Hartmann, 1998). When FUors (EXors) undergo an outburst, its accretion rate increases by a factor of ~ 100 (~ 10), and hence, they are ideal candidates for the episodic outbursts which

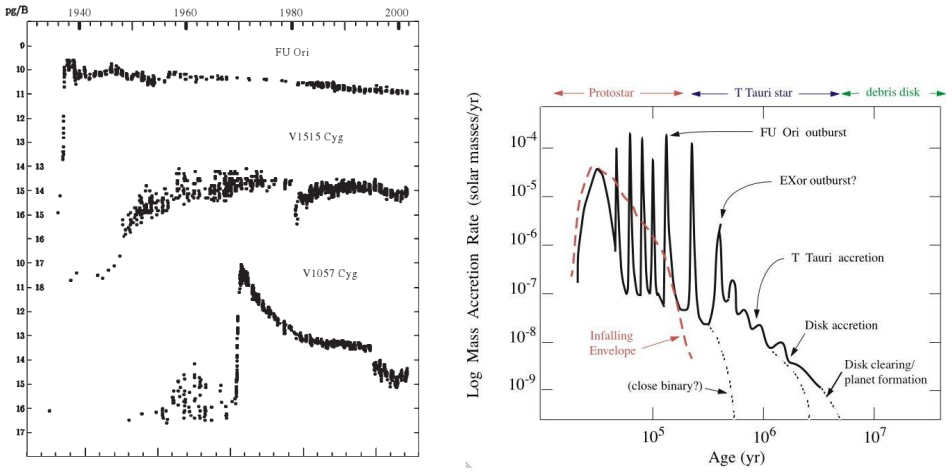

(a) (b)

FIGURE 1.4: a) Light curves of the three classical FUors (FU Ori, V1515 Cyg, and V1057 Cyg) showing a rapid rise to outburst by undergoing an increase in their optical magnitude by ∼5 mag. b) The plot shows the episodic accretion hypothesis during the formation of a YSO. The YSO will spend most of its time in quiescent phase, intermediately erupting to short duration accretion outbursts (FUors or EXors) multiple times in its pre-main sequence lifetime. Image Courtesy: (Hartmann, 2009)

could possibly solve all the open issues mentioned in previous subsections. Figure 1.4b shows the overall picture of this episodic accretion outburst hypothesis in the accretion history of a YSO. Due to the short timescales of outbursts in comparison to the millions-of-years timescale of star formation, these events are extremely rare, and less than two dozen confirmed FUor and EXor outbursts have been discovered so far (Audard et al., 2014).

1.3 Implications of episodic accretion

Motivation of This Thesis

As described in the previous section, the episodic accretion hypothesis can potentially solve the open issues in protoplanetary disc accretion. It will also have very significant implications in the star, planet, and comet formation as well. By comparing the silicate emission line before and after the outburst phase of EX Lup (a classical EX Or object), Ábrahám et al., (2009) showed the outburst event resulted in silicate crystallization. This shows the importance of this phenomenon in planet and comet formation. It is worthwhile to mention here that the formation of crystallised silicate in comets of our solar system is another poorly understood phenomenon. Thermal heating during the accretion events can make the protoplanetary discs stable from gravitational instabilities[5], which could negatively affect

[5]Condition for gravitational instability is given by the Toomre Q parameter being less than unity. $Q(R) = c\Omega/\pi G\Sigma$, where c is the speed of sound (proportional to square root of the temperature), Ω is the orbital angular velocity, and Σ is the disc surface density. Hence, at high temperatures the radius upto which the disc is gravitationally stable expands.

the fragmentation and formation of giant gas planets (Stamatellos, Whitworth, and Hubber, 2011). Another crucial factor which directly affects the planet formation is the expansion of the snow-lines during an accretion outburst. Planets are formed by grains getting stuck together and growing in size when they collide. An ice mantle (H_2O or CO ice) around the grains can make them sticky. Snow-line is the radius at which the temperature of the disc drops below the sublimation point of the corresponding ice. Only grains beyond this radius will have a significant ice mantle around them. Episodic accretion events in solar type stars can result in expansion of the snow-line radius from $\sim$5 AU to $\sim$40 AU, negatively affecting the formation of rocky planets within that radius (Cieza et al., 2016). Episodic accretion can also significantly change the pre-main-sequence isochrones in a Hertzsprung-Russell (HR) diagram, which is used extensively for initial mass function studies and age/mass estimation of YSOs (Hartmann, Zhu, and Calvet, 2011; Hosokawa, Offner, and Krumholz, 2011; Baraffe, Vorobyov, and Chabrier, 2012). From the number statistics of the discovered outbursts, it is estimated that every low-mass star undergoes $\sim$50 such short-duration outbursts during its formation stage (Scholz, Froebrich, and Wood, 2013). Hence, it is fundamentally necessary to understand and study the environment into which a protoplanetary disc system gets transformed to during accretion outbursts.

In Chapters 3 and 4 of this thesis, I present our results from the observational study of the environmental changes we discovered in two such outburst sources. The physical mechanism which is driving these episodic accretion events is not yet fully understood. In Chapter 5, I present the constraints we obtained which enabled us to rule out certain types of outburst mechanism models. We therefore proposed an observationally consistent mechanism for explaining the features of the light curves that we observed. The short timescale variations in the accretion rate of FUors and EXors make them unique laboratories to monitor the simultaneous evolution of the outflow with respect to the accretion rate. This enabled us to constrain, in Chapter 6, the outflow mechanism under way in these objects. And finally, the most crucial parameter for quantifying the effect of these outbursts on planet and star formation is their occurrence frequency. In Chapter 7, I present a hierarchical Bayesian model I developed for constraining, as well as comparing the outburst frequency across different classes of YSOs.

1.4 Monitoring of FUors and EXors (MFES) Program

Recognising the importance of the rare FUors and EXors phenomena in probing the environment and evolution of the protoplanetary discs, we started a long-term multi-wavelength monitoring program of all confirmed FUors and EXors. During the initial phase we had continuous monitoring of only two sources. We expanded this list significantly to include all observable northern hemisphere sources in 2008 (see Appendix A for the complete list of sources). During the period 2008 to 2016, we have observed for about 175 nights for this program using various optical and near-infrared telescopes. Details of observations and the data reduction procedures are discussed in Chapter 2.

For this thesis work, two of the most peculiar sources from our list, V899 Mon and V1647 Ori were selected for the detailed analysis. Results presented in this thesis are from these two sources.

1.5 Instrumentation (Part II)

In the MFES program, a significant fraction of our sources were heavily embedded, and we needed near-infrared observations to capture the photons escaping from the heavily extinct regions like the inner parts of the accretion disc and the magnetosphere. Part II of this thesis is on the near-infrared instrumentation work that I carried out to develop the instruments we used for this study. Chapter 8 contains the summary of the personal contributions to the development, repairs, upgrades, and final calibration of the TIFR Near Infrared Spectrometer and Imager (TIRSPEC). Chapter 9 describes my contributions to TIFR Near Infrared Imaging Camera -II (TIRCAM2) and 100 cm TIFR Far infrared Balloon-borne Telescope. Since the MFES program involved hundreds of nights of data from a wide variety of optical and near-infrared instruments, a few unified pipelines for all the instruments used in the MFES program were also developed. These pipelines are designed to be general enough for any kind of science observations and are easily adaptable for many similar instruments. In Chapter 10, the details and architecture of these data reduction pipelines are outlined.

Finally, the major results of the work presented in this thesis are summarised in Chapter 11.

Part I

Episodic Accretion and Outflows in Young Stellar Objects

Chapter 2

Observations & Data Reduction

Since the major goal of the MFES program is to study the inner part of the accretion disc, where the instability mechanism that results in episodic accretion occurs, most of our long-term monitoring was done in optical and near-infrared bands. However, we also observed our sources in longer far-infrared and radio wavelengths for constraining their environmental characteristics. For this thesis work, I have done a detailed study of two sources which were most peculiar in our MFES program, namely V899 Mon and V1647 Ori. In this chapter, we shall mainly describe the observations conducted as well as the procedures followed for the data reduction of these two sources.

2.1 Optical Photometry

During an FUori or EXori accretion outburst, the temperatures involved in the inner most part of the accretion disc are around $\sim$ 2000 - 3000 K. In these family of outbursts, the light curves in optical bands show maximal increase with respect to the longer wavelength light curves. Hence, to track any periodic as well as non-periodic variations in the flux from the central source, the detailed evolution of accretion rate, extinction, etc., we have to monitor the flux from these sources in the optical broad band filters.

Our long-term optical monitoring of V899 Mon started on 2009 November 30, and V1647 Ori on 2008 September 14. The observations were carried out using the 2 m Himalayan *Chandra* Telescope (HCT) at the Indian Astronomical Observatory, Hanle (Ladakh), belonging to the Indian Institute of Astrophysics (IIA), India, and the 2 m telescope at the IUCAA (Inter-University Centre for Astronomy and Astrophysics) Girawali Observatory (IGO), Girawali (Pune), India. For optical photometry, the central 2K $\times$ 2K CCD section of the Hanle Faint Object Spectrograph & Camera (HFOSC) with a pixel scale of 0.296$''$ was used on the HCT, and the 2K $\times$ 2K CCD of the IUCAA Faint Object Spectrograph & Camera (IFOSC) with a similar pixel scale of 0.3$''$ was used on the IGO. This gave us a field of view (FOV) of $\sim 10 \times 10$ arcmin^2 on both HCT and IGO. A detailed description of the instruments and telescopes is available at the IAO[1] and IGO[2] websites. V899 Mon's field $((\alpha, \delta)_{2000} = 06^h09^m19^s.28, -06^\circ41' 55'' .4)$ was observed in standard $UBVRI$ Bessel filters. We carried out observations for 69 nights, out of which 41 nights were observed through HCT and the remaining ones from IGO. The photometric observation log of V899 Mon is given in Table 2.1. V1647 Ori's field $((\alpha, \delta)_{2000} = 05^h46^m13^s.135, -00^\circ06'04''.82)$

[1] http://www.iiap.res.in/iao/hfosc.html

[2] http://www.iucaa.ernet.in/~itp/igoweb/igo_tele_and_inst.htm

was also observed with the same filters, and out of our total observation of 110 nights published in our 2013 paper (Ninan et al., 2013b), 84 nights were observed through HCT and 26 nights from IGO. The photometric observation log of V1647 Ori is given in Table 2.2.

TABLE 2.1: Observation log of V899 Mon

Date	JD	FWHM[a]	Filter(s)/Grism(s)	Instrument(s)
2009 Nov 30	2455166	1″.9	V,R,gr8	HFOSC
2009 Dec 04	2455170	3″.1	V,R,I	HFOSC
2009 Dec 16	2455182	1″.8	V,R,I	HFOSC
2009 Dec 17	2455183		gr7,gr8	HFOSC

[a] Measured average FWHM. This is a measure of the seeing.

Note: This table is published in its entirety in the electronic edition of Ninan et al., (2015). A portion is shown here for guidance regarding its form and content.

TABLE 2.2: Observation log of V1647 Ori

Date (UT)	JD	FWHM[†]	Filter(s)/grism(s)	Exposure time (in secs)
2008 Sep 14	2454724	1″.9	$V, R, I, gr8$	300, 480, 240, 2400
2008 Sep 15	2454724	1″.6	$gr8$	2400
2008 Sep 16	2454726	1″.5	V, R, I	600, 720, 240
2008 Sep 28	2454738	1″.1	V, R, I	240, 240, 180
2008 Oct 01	2454741	1″.2	V, R, I	120, 120, 90
2008 Oct 02	2454742	1″.2	$V, R, I, gr7$	240, 240, 180, 2400
2008 Oct 03	2454743	1″.5	$gr8$	2400

[†] Measured average FWHM. This is a measure of the seeing.

[††] Observed from IGO, all other nights are from HCT.

Note: This table is published in its entirety in the electronic edition of Ninan et al., (2013b). A portion is shown here for guidance regarding its form and content.

The standard photometric data reduction steps like bias subtraction, median flat-fielding, and finally aperture photometry of V899 Mon and V1647 Ori were done using our publicly released pipeline[3] for these instruments (see Chapter 10). Blank sky images in *I* band were used to create fringe templates by the MKFRINGECOR task in IRAF[4], which were later used to subtract the fringes that appeared in *I* band images taken from IGO.

Since V899 Mon source is quite bright and is not affected by any bright nebulosity, we used a 4 × full width half maximum (FWHM) aperture for optical photometry. The background sky was estimated from a ring outside the aperture radius with a width of 4.5″ .

[3] https://indiajoe.github.io/OpticalPhotoSpecPipeline/

[4] IRAF is distributed by the National Optical Astronomy Observatories, which are operated by the Association of Universities for Research in Astronomy, Inc., under contract with the National Science Foundation.

Point-spread function (PSF) photometry (using PSF and ALLSTAR tasks in the DAOPHOT package of IRAF) on V1647 Ori was not able to fully remove the nebular contamination. We found a strong correlation between fluctuation in magnitude of V1647 Ori and fluctuation in atmospheric seeing condition. This is because the contamination of flux from the nebula into V1647 Ori's aperture was a function of atmospheric seeing. So we generated a set of images by convolving each frame with two-dimensional Gaussian kernels of different standard deviation (using the IMFILTER.GAUSS task in IRAF) for simulating different atmospheric seeing conditions. We then recalculated the magnitudes by DAOPHOT, PSF, and ALLSTAR algorithms of IRAF for various atmospheric seeing conditions. The differential magnitudes obtained from each frame's set were interpolated to obtain magnitude at an atmospheric seeing of 1.18″, which was taken to be the interpolated seeing for all the nights, and was chosen to minimise the interpolation error. This method reduced our error bars in magnitude by a factor of two. Apart from the Gaussian convolution step, the PSF photometry steps were all the same as in Ojha et al., (2006).

Magnitudes of the whole McNeil's nebula and other objects in it like region C (near HH 22A) and region B defined by Briceño et al., (2004) in their Figure 2 (also see Figure 2.2) were measured by simple aperture photometry with an aperture radius of 80″ for nebula and 12″ for the regions C and B. For obtaining the flux, the aperture of objects like regions C and B was centered at the objects themselves.

Finally, the magnitude calibration was done by solving color transformation equations for each night using nearby Landolt's standard star fields (Landolt, 1992), and also using five and six secondary standard field stars in V899 Mon and V1647 Ori fields, respectively (see Figure 2.1 and 2.2). We identified these secondary standard stars based on the stability in their magnitude over the period of our observations.

2.2 NIR Photometry

Near-infrared (NIR) fluxes are also dominated by the energy released from heavy accretion. Unlike in optical bands, NIR bands are less affected by the extinction, and they can probe the extinct central source better than the optical bands. Due to the heavy extinction towards some of the sources in our MFES program, their central source was visible only in our NIR observations.

NIR photometric monitoring of our sources in J, H, and K / K_S bands was carried out using the HCT NIR camera (NIRCAM), the TIFR Near Infrared Spectrometer and Imager (TIRSPEC) mounted on HCT, and the TIFR Near Infrared Imaging Camera-II (TIRCAM2) mounted on the IGO telescope as well as the 1.2 m Physical Research Laboratory (PRL) Mount Abu telescope. NIRCAM has a 512×512 mercury cadmium telluride (HgCdTe) array, with a pixel size of 18 μm, which gives an FOV of $\sim 3.6 \times 3.6$ arcmin^2 on HCT. Filters used for observations were J (λ_{center}= 1.28 μm, $\Delta\lambda$= 0.28 μm), H (λ_{center}= 1.66 μm, $\Delta\lambda$= 0.33 μm), and K (λ_{center}= 2.22 μm, $\Delta\lambda$= 0.38 μm). Further details of the instrument are available at http://www.

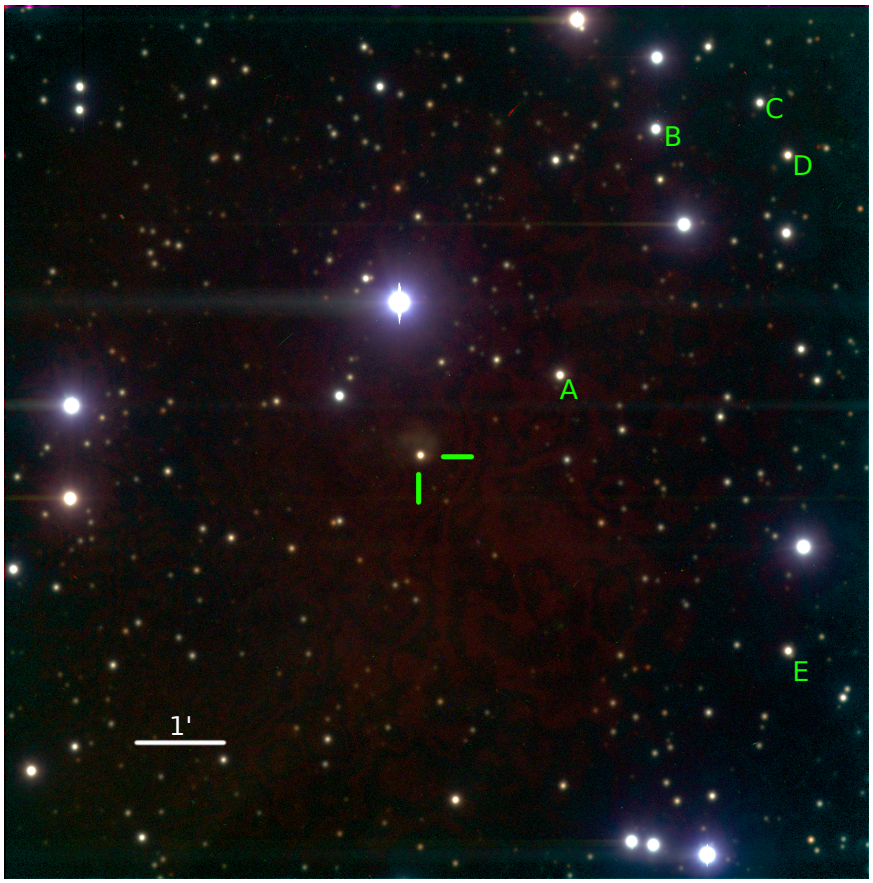

FIGURE 2.1: RGB color composite optical image of V899 Mon taken with HFOSC from HCT (V: blue; R: green; I: red) on 2011 January 2. V899 Mon was in its short-duration quiescent phase at this epoch. The FOV is $\sim 10 \times 10$ arcmin^2. North is up and east is to the left-hand side. Stars marked as A, B, C, D, and E are the secondary standard stars used for magnitude calibration. The location of V899 Mon is marked with two perpendicular lines at the middle.

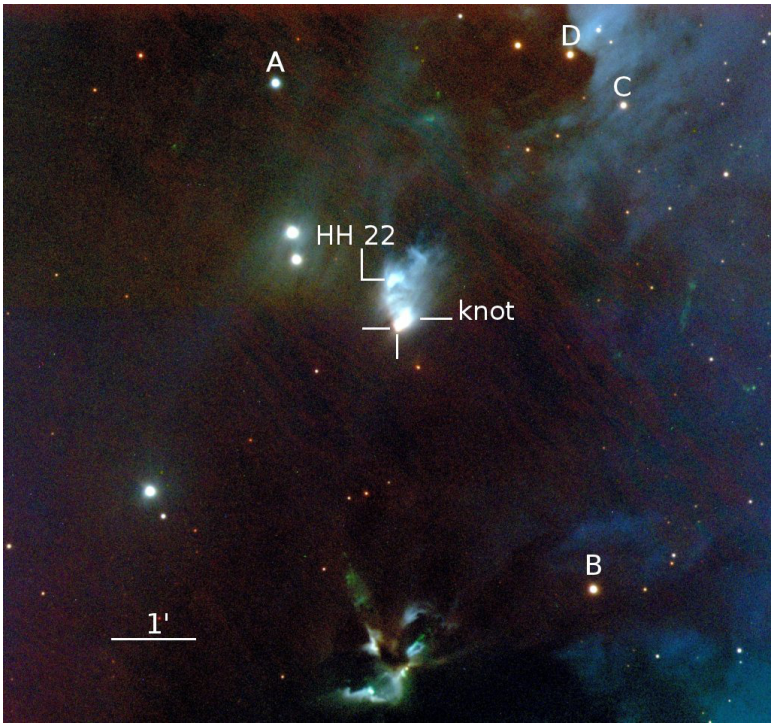

FIGURE 2.2: Color composite image of McNeil's nebula (V1647 Ori) region taken from IGO (V: blue; R: green; I: red) on 2010 February 13. FOV is $\sim 10 \times 10$ arcmin^2. North is up and east is to the left-hand side. Stars marked as A, B, C, and D are the secondary standard stars used for magnitude calibration. The location of V1647 Ori is marked at the center by two perpendicular lines. Region C, overlapping Herbig–Haro object HH 22A, is marked together. A knot in the southwestern section (region B) of the nebula is also marked. At 400 pc distance, the scale $1'$ corresponds to 24,000 AU.

iiap.res.in/iao/nir.html. TIRSPEC has a 1024×1024 Hawaii-1 PACE[5] (HgCdTe) array, with a pixel size of 18 μm, which gives an FOV of $\sim 5 \times 5$ arcmin^2 on HCT. Filters used for observations were J (λ_{center}= 1.25 μm, $\Delta\lambda$= 0.16 μm), H (λ_{center}= 1.635 μm, $\Delta\lambda$= 0.29 μm), and K_S (λ_{center}= 2.145 μm, $\Delta\lambda$= 0.31 μm) (Mauna Kea Observatories near-infrared filter system). Further details on TIRSPEC are available in Chapter 8 and Ninan et al., (2014) and Ojha et al., (2012). TIRCAM2 has a 512×512 indium antimonide (InSb) array with a pixel size of 27 μm. Filters used for observations were J (λ_{center}= 1.20 μm, $\Delta\lambda$= 0.36 μm), H (λ_{center}= 1.66 μm, $\Delta\lambda$= 0.30 μm), and K (λ_{center}= 2.19 μm, $\Delta\lambda$= 0.40 μm). More details on TIRCAM2 are available in Chapter 9 and Naik et al., (2012). The log of NIR observations of V899 Mon and V1647 Ori is listed in Table 2.1 and Table 2.2, respectively. For V899 Mon, we have photometric observations for a total of 25 nights in the NIR bands. Our first *JHK* observation was carried out during the peak of V899 Mon's first outburst on 2010 February 20, and the remaining observations were carried out during its current ongoing second outburst. For V1647 Ori, in the paper published in 2013 (Ninan et al., 2013b), we have a total of 14 nights of NIR photometric observations, with the first set of data taken during the quiescent phase in 2007, i.e. before its 2008 outburst.

NIR observations were carried out by the standard telescope dithering procedure. Five dither positions were observed. All the dithered object frames were median combined to generate master sky frames for NIRCAM and TIRCAM2. We combined twilight flats and all non-extended source frames observed during the same night to create accurate flats for each night. For NIRCAM and TIRCAM2, data reduction and final photometry were performed using the standard tasks in IRAF, while the TIRSPEC data were reduced using our TIRSPEC photometry pipeline (Ninan et al., 2014) (see Chapter 10). For aperture photometry we used an aperture of 3×FWHM and the background sky was estimated from an annular ring outside the aperture radius with a width of 4.5″. Magnitude calibration was done by solving color transformation equations for each night using Hunt's standard star fields AS 13 and AS 9 (Hunt et al., 1998), and the five field stars in case of V899 Mon (labeled in Figure 2.3) that we identified to have a stable magnitude and that are consistent with 2MASS[6] over the period of our observations. For V1647 Ori, on 2011 December 6, standard stars were not observed; hence, we used the magnitude of the nearby star (2MASS J05461162-0006279) measured on other nights for photometric calibration.

2.3 Medium-resolution Optical Spectroscopy

For detailed measurements of the kinematics of outflows as well as the environmental characteristics like temperature, density, etc. we need to study the time evolution in spectral lines.

Our medium-resolution ($R \sim 1000$) optical spectroscopic monitoring of V899 Mon started on 2009 November 30, and V1647 Ori on 2008 September 14. The spectroscopic observations were carried out using both HCT and

[5]HgCdTe Astronomy Wide Area Infrared Imager -1, Producible Alternative to CdTe for Epitaxy

[6]Two Micron All Sky Survey

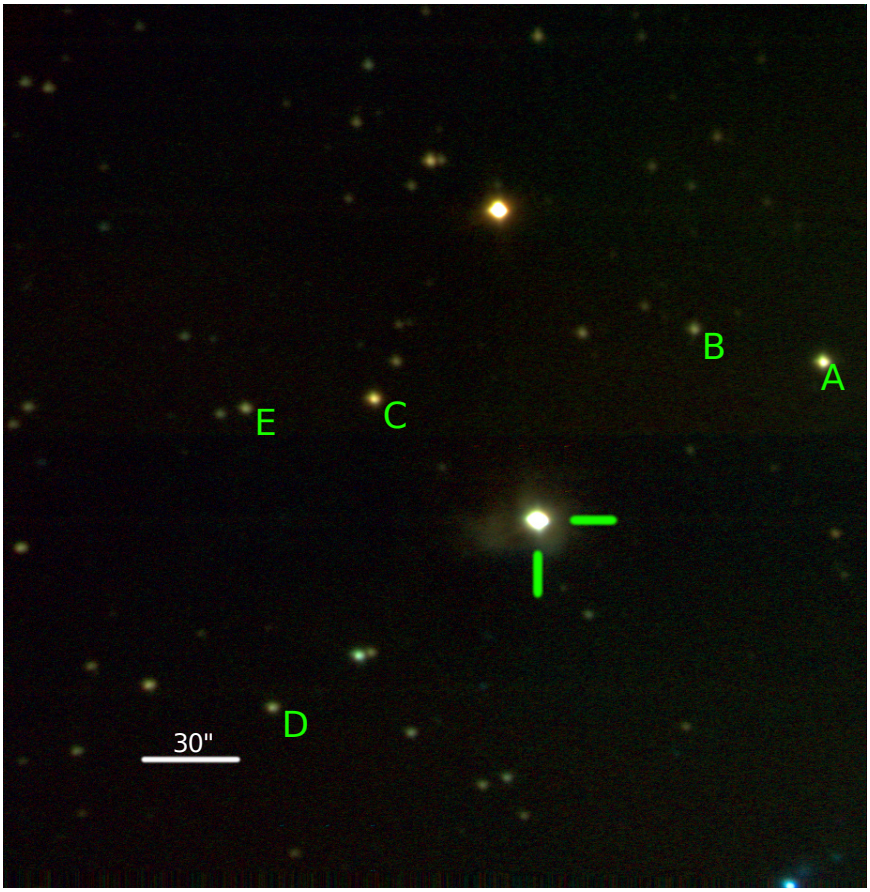

FIGURE 2.3: RGB color composite NIR image of V899 Mon taken with TIRSPEC from HCT (J: blue; H: green; K_S: red) on 2013 November 14. V899 Mon was in its second outburst phase at this epoch. The FOV is $\sim 5 \times 5$ arcmin^2. North is up and east is to the left-hand side. Stars marked as A, B, C, D, and E are the secondary standard stars used for magnitude calibration. The location of V899 Mon is marked with two perpendicular lines at the middle.

IGO. The full 2K $\times$ 4K section of the HFOSC CCD spectrograph was used for HCT observations, and the 2K $\times$ 2K IFOSC CCD spectrograph was used for IGO observations. These observations were done in the effective wavelength range of $3700 - 9000$ $\mathring{A}$, using grism 7 (center wavelength 5300 $\mathring{A}$) and grism 8 (center wavelength 7200 $\mathring{A}$). The spectral resolution obtained for grism 7 and grism 8 with the 150 μm slit at IGO and the 167 μm slit at HCT was $\sim$ 7 $\mathring{A}$. The log of spectroscopic observations of V899 Mon and V1647 Ori is listed in Table 2.1 and Table 2.2, respectively. For V899 Mon, we have 8 spectra from its first outburst phase, 4 from its short quiescent phase, and 30 from its ongoing second outburst phase. For V1647 Ori, in our 2013 paper Ninan et al., (2013b), we carried out spectroscopic observations for 35 nights through HCT and 24 nights from IGO, thus totaling 59 nights of spectroscopic observations of V1647 Ori's ongoing outburst.

Nebulosity contamination in the spectrum of V1647 Ori was minimised by keeping the slit in the east-west orientation. For wavelength calibration, we have used FeNe, FeAr, and HeCu lamps. Standard IRAF tasks like APALL and APSUM were used for spectral reduction using our publicly released PyRAF[7]-based pipeline developed for both HFOSC and IFOSC instruments (see Chapter 10).

2.4 High-resolution Optical Spectroscopy

We acquired multi-epoch high-resolution ($R \sim$ 37,000) spectra of V899 Mon during its second outburst phase on 2014 December 22, 2015 December 15, 19, and 2016 February 20, using the Southern African Large Telescope High Resolution Spectrograph (SALT-HRS) (Bramall et al., 2010). Both the red arm ($5490-8810$ $\mathring{A}$) and the blue arm ($3674-5490$ $\mathring{A}$) of the HRS instrument were used. For this medium-resolution instrument mode of HRS, it uses a 2.23″ fiber to collect light from the target source, and another fiber of the same diameter is used to sample a nearby patch of the sky. Apart from the target frames, ThAr arc lamp spectrum was also taken through the sky fiber for wavelength calibration. For tracing the aperture of target and sky fiber, we used bright quartz continuum flat taken through target fiber and sky fiber on nearby nights.

Since our total exposure was taken in a single readout, we had to carefully remove many cosmic rays hits in each frame. We used *Laplacian Cosmic Ray Identification* by Dokkum, (2001) to clean cosmic rays hits in the data frames. A reduction tool for SALT-HRS data was written and used to obtain wavelength calibrated, normalised spectrum (see section 10.3 in Chapter 10 for the reduction procedure I implemented in this tool).

The additive factor to translate observed velocities in the spectrum to heliocentric velocities was found to be 0.92 km s^{-1}, 4.22 km s^{-1}, 2.39 km s^{-1}, and -22.31 km s^{-1} for our four nights of observation using the *rvcorrect* task in IRAF.

[7] PyRAF is a product of the Space Telescope Science Institute, which is operated by AURA for NASA

2.5 NIR Spectroscopy

NIR (1.02 – 2.35 μm) spectroscopic monitoring of V899 Mon started on 2013 September 25 using TIRSPEC mounted on HCT. Depending on the seeing conditions, slits with 1.48″ or 1.97″ widths were used. Spectra were taken in at least two dithered positions inside the slit. Spectra of an argon lamp for wavelength calibration and a tungsten lamp for the continuum flat were also taken immediately after each observation without moving any of the filter wheels. For telluric line correction, bright NIR spectroscopic standard stars within a few degrees and similar airmasses were observed immediately after observing the source. The typical spectral resolution obtained in our spectra is R $\sim$ 1200. The log of spectroscopic observations of V899 Mon is listed in Table 2.1. It may be noted that all the 12 NIR spectral observations are taken during the current ongoing second outburst phase of V899 Mon.

NIR spectral data were reduced using the TIRSPEC pipeline (Ninan et al., 2014) (see Chapter 10). After wavelength calibration, the spectrum of V899 Mon was divided by a standard star spectrum to remove telluric lines and detector fringes seen in H and K orders' spectra. This continuum-corrected spectrum was scaled using the flux estimated from photometry to obtain the flux-calibrated spectrum. Since we do not have Y band photometry, we interpolated I band and J band λf_λ flux to Y band and used the interpolated flux to scale the Y band spectrum flux.

2.6 GMRT Radio Continuum Imaging

The detection of any free-free emission in radio band will provide estimates on the extent of the H II region due to accretion or outflow shocks, as well as the Lyman continuum flux. Continuum interferometric observation of V899 Mon at 1280 MHz with 33.3 MHz bandwidth was carried out on 2014 October 17 using the Giant Metrewave Radio Telescope (GMRT), Pune, India. GMRT consists of 30 dish antennae (each 45 m in diameter) in hybrid "Y" configuration (Swarup et al., 1991). Out of these, 25 antennae were online during our observation. The standard flux calibrator 3C 147 was observed for 15 minutes at the beginning and end of the observations. For phase calibration, the nearby Very Large Array calibrator 0607-085 was observed for 10 minutes after every 20 minutes of integration on V899 Mon. The total integration on the V899 Mon source was 4.5 hr.

CASAPY software was used for the data reduction. After careful iterative bad data flagging and gain calibration, we imaged the large FOV of 28′×28′ field by dividing the field into 128 w-projection planes using the *CLEAN* algorithm.

2.7 *Herschel* Far-infrared Photometry

The far-infrared flux in YSOs is dominated by extended outer disc and left over envelopes. Hence, they do not vary over short timescales like optical or NIR. But, far-infrared fluxes are very important for estimating the properties of the envelope, age, existence of outflow cavity, etc.

We obtained imaging observations of the V899 Mon region in SPIRE[8] 250, 350, and 500 μm and PACS[9] 70 and 160 μm from the *Herschel* data archive.[10] SPIRE data were available for two epochs, one on 2010 September 4 (Proposal ID: KPGT_fmotte_1) and another on 2013 March 16 (Proposal ID: OT1_rgutermu_1). PACS data of V899 Mon were only available in the later epoch. Data from both the epochs were reduced using the standard *Herschel*'s HIPE pipeline with the latest calibration file. For point-source aperture photometry of V899 Mon, we first tried the *sourceExtractorSussextractor* routine in HIPE on level 2 SPIRE data and the *multiplePointSourceAperturePhotometry* routine on PACS data. We also tried point-spread function (PSF) photometry using the *daophot* tool in IRAF. Since all these algorithms use an annular ring for background estimation and the background is highly non-uniform, the results were found to be very sensitive to aperture and background estimates. We finally estimated fluxes using *getsources* (Men'shchikov et al., 2012), which uses a linearly interpolated background estimate. These estimates were found to be consistent with the differential flux between two epochs (differential flux could be estimated more accurately since the subtracted image has a uniform background). The HIPE pipeline assumes a spectral energy distribution (SED) color, $\alpha = -1$ (where $F_\nu = \nu^\alpha$). The actual color α of V899 Mon was obtained from our flux estimates, and the corresponding color correction factor was applied to the flux values for obtaining color-corrected flux estimates.

2.8 WISE Photometry

We obtained imaging observations of the V899 Mon region in $W1$ (3.4 μm), $W2$ (4.6 μm), $W3$ (12 μm), and $W4$ (22 μm) bands from the *Wide-field Infrared Survey Explorer (WISE)* data archive (Wright et al., 2010). Photometric magnitude estimates were also available in the *WISE* all-sky catalog. $W1$ and $W2$ bands were observed at two epochs on 2010 March 17 and 2010 September 24, whereas $W3$ and $W4$ were observed only on 2010 March 17. Since $W1$ and $W2$ intensity maps looked severely saturated, we have used only $W3$ and $W4$ *WISE* catalog magnitudes for our study of V899 Mon.

For the study of our sources in the MFES program, we have also compiled other publicly available archival data of our source region at different epochs. Data were obtained from the following surveys and instruments:

[8] Spectral and Photometric Imaging Receiver

[9] Photoconductor Array Camera and Spectrometer

[10] *Herschel* is an ESA space observatory with science instruments provided by European-led Principal Investigator consortia and with important participation from NASA.

CRTS DR2[11], POSS survey[12], USNO-B catalog[13], IRAS survey[14], DENIS survey[15], 2MASS survey[16], AKARI[17], IRAC[18] and MIPS[19].

[11] Catalina Real-Time Transient Survey Data Release 2
[12] Palomar Observatory Sky Survey
[13] U.S. Naval Observatory B1.0 Catalog
[14] Infrared Astronomical Satellite, Survey
[15] Deep Near Infrared Survey of the Southern Sky
[16] Two Micron All-Sky Survey
[17] Akari All-Sky Survey Point Source Catalog
[18] Infrared Array Camera on Spitzer
[19] Multi-Band Imaging Photometer on Spitzer

Chapter 3

V899 Mon

A possible FUor-type eruption of V899 Mon (aka IRAS 06068-0641) located near the Monoceros R2 region (d$\sim$905 pc; Lombardi, Alves, and Lada, (2011)) was first discovered by the Catalina Real-time Transient Survey (CRTS) and reported by Wils et al., (2009). They announced the source as a FUor candidate based on the constant brightening it has been undergoing since 2005. The spectrum published by Wils et al., (2009) showed strong Hα and Ca II IR triplet lines, which identify the outbursting source as a YSO. In this chapter we present the results from our long-term monitoring of this very peculiar outburst source, during which we found the source undergoing transition from its first outburst phase to the quiescent phase, and finally returning to a second outburst phase within just a year of quiescent period. The results presented in this chapter are published in Ninan et al., (2015).

3.1 Photometric Results: Light Curves and Color Variations

An extended fan-shaped optical reflection nebula is typically seen around FUors. In the case of V899 Mon we detected only a small, faint, fan-shaped reflection nebula towards the north (see Figure 2.1). *U, B, V, R, I, J, H,* and K_S magnitudes of V899 Mon from our long-term continuous monitoring are listed in Table 3.1. Typical magnitude errors are less than 0.03 mag.

TABLE 3.1: Magnitudes of V899 Mon

JD	U	B	V	R	I	J	H	K_S
2455166			14.57	13.40				
2455170			14.22	13.10	12.08			
2455182			13.61	12.65	11.57			
2455186			13.51	12.37	11.37			

Note: Errors on *U, B, V, R* and *I* magnitudes are < 0.02 mag, TIRSPEC *J, H and* K_S magnitudes have errors < 0.02 mag, and TIRCAM2 and NIRCAM *J, H, K* magnitudes have errors < 0.06 mag.

Note: This table is published in its entirety in the electronic edition of Ninan et al., (2015). A portion is shown here for guidance regarding its form and content.

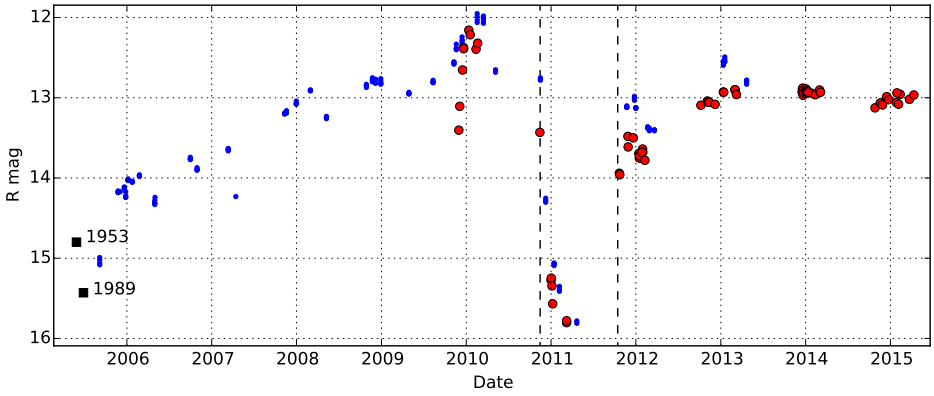

FIGURE 3.1: Light curve of V899 Mon showing its first outburst, short quiescent phase, and current ongoing second outburst phase. Red circles are R band magnitudes from our observations, and blue circles are CRTS magnitudes converted to R magnitudes. POSS-1 and POSS-2 epochs' R magnitudes are also shown for comparison as black squares.

The R band magnitude light curve is shown in Figure 3.1. Effective R band magnitudes[1] from the CRTS survey are superimposed in the same graph for displaying the complete picture of the initial rise of the first outburst. Images of the V899 Mon field observed on 1953 December 29, 1983 December 29, 1989 January 9, and 2000 February 8 are available from digitized POSS-1 and POSS-2 archives. Magnitudes at the two epochs (1953 and 1989) that used the R band filter are also shown in Figure 3.1. It should be noted that even though these magnitudes available in the USNO-B1.0 catalog are corrected for the non-standard bandpass filter used in the POSS-I survey, their variation seen between 1953 and 1989 might still be due to systematics in calibration.

Few other outburst sources like V1647 Ori, V582 Aur, and V2492 Cyg have also shown such a sudden brief transition to quiescent phase after reaching the peak of the first outburst (Ninan et al., 2013b; Semkov et al., 2013; Kóspál et al., 2013) (also see Chapter 4). The light curves of V582 Aur and V2492 Cyg were very unstable, but the light curve of V1647 Ori was very similar to V899 Mon in terms of the stability during the phase transitions.

One possible scenario that could explain the sudden dimming of the source in 2011 is occultation by a dust clump. By taking the dust size parameter R_V and change in extinction A_V as free parameters, we tried to fit the observed change in magnitudes of *V*, *R*, *I*, *J*, *H*, and K_S bands[2] between the first outburst and quiescent phases (i.e., 2.86, 2.90, 3.06, 2.96, 2.75, and

[1]CRTS DR2 V_{CSS} magnitudes of V899 Mon, were converted to effective R magnitude using color correction equation $V = V_{CSS} + 0.91 * (V - R)^2 + 0.04$ and $V - R = 1.11$. http://nesssi.cacr.caltech.edu/DataRelease/FAQ2.html#improve

[2]Even though we do not have NIR photometric measurements during the quiescent phase in 2011, our quiescent phase *I* band magnitude matches with the DENIS *I* magnitude observed on 1999 January 25, and DENIS *J* and *K* magnitudes of this epoch match with 2MASS *J* and K_S magnitudes observed in 1998. Hence, in this study we have taken 2MASS magnitudes as the quiescent phase *J*, *H*, and K_S magnitudes of the V899 Mon source.

2.36 Δ mag, respectively, in each band). Coefficients in Table 2 of Cardelli, Clayton, and Mathis, (1989) were used for calculation, and no positive value of R_V could fit the observed changes in magnitudes. Hence, we can safely conclude that the quiescent phase in 2011 was due to an actual break in the outburst, and it is not due to dust occultation. Even though we have not considered scattered excess blue light (like in UX Ori systems) in the above analysis, an almost similar magnitude drop ($\sim$ 2.8) in optical and NIR magnitudes to the pre-outburst phase makes it unlikely to be a case of dust obscuration. A stronger argument against the dust obscuration scenario comes from the observed variation in spectral line fluxes during this transition (see section 3.4). The relative flux changes observed in various spectral lines cannot be explained by a simple change in extinction.

Figure 3.2 shows the NIR $J-H/H-K$ color-color (CC) diagram. The position of V899 Mon in it shows no significant extinction to the source, and it falls on the classical T Tauri (CTT) locus. The positions in the CC diagram during first and second outbursts are also different from each other. But since we have only one NIR observation from the rapidly varying ending phase of the first outburst, it might not be a good representation of the NIR color of the first outburst.

The green squares measured during the 2013 - 2015 period of the second outburst show small movements along the reddening vector. Such short-period, small-amplitude fluctuations during the outburst phase are also seen in other FUor/EXor objects (Audard et al., 2014; Semkov et al., 2013; Ninan et al., 2013b). Unlike the quiescence in 2011, these short variations in the second outburst could be due to small dust clump occultations or minor fluctuations in the accretion. The NIR $J/J-K$ color-magnitude diagram (CMD) (see Figure 3.3) also indicates the general trend of V899 Mon getting redder (bluer) when it dims (brightens).

3.1.1 Outburst - quiescent transition phase

In contrast to existing FUor/EXor observations in the literature, we could carry out several observations of V899 Mon during its transition from outburst phase to quiescent phase and back. Figure 3.4 shows the V band magnitude light curve of the source, color-coded with $V-R$ color in the outer ring, and $V-I$ color at the center. These colors indicate that the object was reddest during the transition stages rather than during the outburst or quiescent phases. It could imply that the temperature of the extra flux component of the outburst was cooler at the beginning and it became hotter as the outburst reached its peak. Since the transition phase flux was cooler than the quiescent phase, outburst flux could not have initially originated on the surface of the hot central star; rather, it might have originated in the disk. This is the first direct observational evidence to support triggering of outbursts in the disk of FUors/EXors. The color change seen in this plot could be a combined effect of both change in extinction and change in temperature. Figure 3.5 shows the *V, R,* and *I* band light curves color-coded with an extinction invariant quantity. The y-intercept along the reddening vector in any CC diagrams, for example, $C_{VRI} = (V-R)-(R-I)*E(V-R)/E(R-I)$ (McGehee et al., 2004), is a weighted difference of two colors, which is invariant to change in extinction A_V. While it is not possible to completely

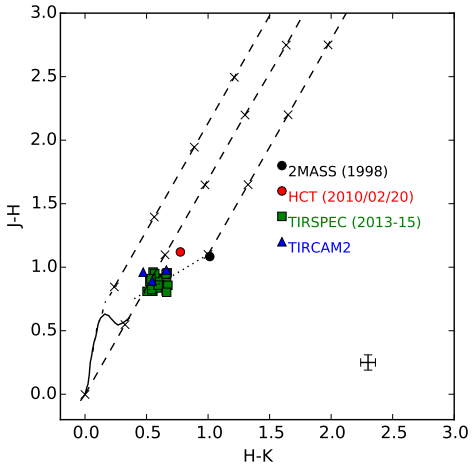

FIGURE 3.2: Positions of V899 Mon in the $J - H/H - K$ CC diagram during the quiescent phase (black circle), first outburst phase (red circle) and the second outburst phase (green squares and blue triangles). The solid curve shows the locus of field dwarfs, and the dot-dashed curve shows the locus of giants (Bessell and Brett, 1988). The dotted line represents the locus of classical T Tauri (CTT) stars (Meyer, Calvet, and Hillenbrand, 1997). The diagonal straight dashed lines show the reddening vectors (Rieke and Lebofsky, 1985), with crosses denoting an A_V difference of 5 mag. Typical error bars of each data point are shown in the bottom right corner.

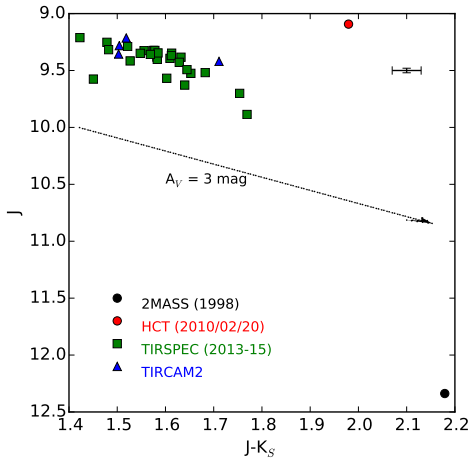

FIGURE 3.3: NIR $J/J - K$ color-magnitude diagram showing the movement of V899 Mon during its quiescent phase (black circle), first outburst phase (red circle), and second outburst phase (green squares and blue triangles). The arrow shows the reddening vector (Rieke and Lebofsky, 1985), which corresponds to an A_V of 3 mag. Typical error bars of each data point are shown in the top right corner.

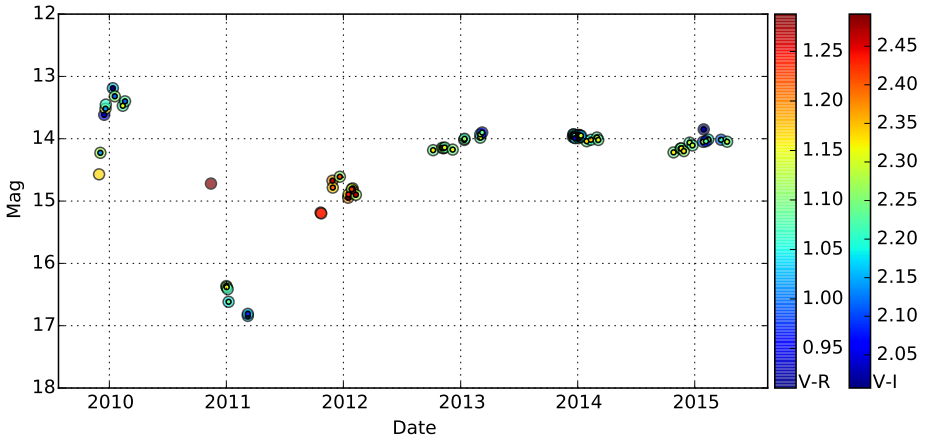

FIGURE 3.4: V band light curve of V899 Mon showing evolution of its $V-R$ and $V-I$ colors. The color of the outer ring shows $V-R$, and the color at the center shows $V-I$. We see that both the colors were reddest during the transition from the quiescent phase to the outburst phase.

separate out the degenerate SED slope change due to temperature and extinction change, any change in this extinction invariant color implies real change in the intrinsic SED slope (temperature). V899 Mon shows significant change in C_{VRI} between the end of the first outburst phase, quiescent phase, transition stage, and ongoing second outburst phase. Significant variation is also seen during the peak of the first outburst, implying that the temperatures of the source during those epochs were different than the ongoing second outburst. However, since C_{VRI} is a weighted difference between two colors and could not tell unambiguously whether the intrinsic slope of the SED became red or blue, Figure 3.5 only indicates change in the intrinsic slope of the SED (temperature). It does not clarify whether reddening of flux during the transition stage was due to temperature change alone or was due to the combined effect of a short-term increase in extinction and change in temperature.

3.2 Stellar Properties

V899 Mon was observed in $WISE$ 12 and 22 μm bands on 2010 March 17, within a month after our NIR observations in J, H, and K bands from HCT on 2010 February 20 (first outburst peak). We utilized them to estimate the conventional infrared logarithmic slope of the spectrum α (where $\lambda F_\lambda = \lambda^\alpha$) used for age classification of YSOs. During the peak outburst phase (2010 March), we obtained a slope $\alpha = -0.27$ between 2.16 and 11.56 μm and $\alpha = -0.51$ between 11.56 and 22 μm. These values classify V899 Mon as a flat-spectrum or an early Class II YSO (Greene et al., 1994) during its peak outburst phase.

$U-B$, $B-V$, $V-R$, and $R-I$ colors of Siess, Dufour, and Forestini, (2000) isochrones can be used to constrain photometrically the mass, age, and extinction of the source. This is done by finding a region in the mass, age, and extinction parameter space in which colors predicted by the Siess,

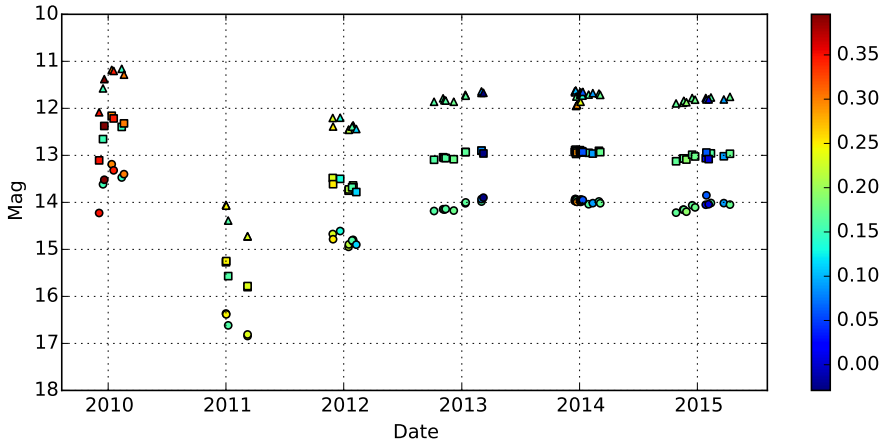

FIGURE 3.5: V, R, and I light curves of V899 Mon (circles, squares, and triangles, respectively), color-coded with the extinction-invariant color C_{VRI}.

Dufour, and Forestini, (2000) model are consistent with all the observed optical colors of V899 Mon. For this analysis, we sampled Siess, Dufour, and Forestini, (2000) isochrones in its valid age range 0.01–100 Myr and mass range 0.1–7 $M_\odot$ in log space. Nonuniform rectangular mass versus age grids were generated for each of the $U-B$, $B-V$, $V-R$, and $R-I$ colors by interpolating (using 2D Bi-spline) colors predicted by the Siess, Dufour, and Forestini, (2000) isochrones. $U-B$ and $B-V$ colors of V899 Mon during the second outburst and $V-R$ and $R-I$ quiescent phase colors were used for fixing the position of V899 Mon in this four-dimensional color space. The errors of the color estimates were taken to be 0.1 mag, which correspond to a symmetric 4D Gaussian in color space. The radial basis function (RBF) was used to calculate the distance to the source for each point in the mass–age grid. A contour was plotted for regions within 1σ distance from V899 Mon's position. These contours were repeatedly estimated for various values of A_V ranging from 0.5 to 8 mag (see Figure 3.6). As seen in the figure, $A_V < 2.2$ mag and $A_V > 4.0$ mag will make all Siess, Dufour, and Forestini, (2000) isochrone colors incompatible with V899 Mon and hence can be ruled out. Owing to the correlation between age and mass, we obtain tight constraints only for A_V from this analysis. Even though the analysis was done for all possible age ranges, since V899 Mon is a heavy disk accreting source, we expect its position inside contours to be only around the region where the age is $\sim$ 1 - 5 Myr.

Another independent way of estimating interstellar extinction is from photometry of field stars. The region around Monoceros R2 was studied in detail using 2MASS data by Lombardi, Alves, and Lada, (2011) (Figure 4 in their paper), and the extinction to the V899 Mon location is A_V = 2.6 mag. This value is consistent with our previous color space analysis.

Figure 3.7 shows the position of V899 Mon in the $V/V-I$ optical CMD during various epochs. Siess, Dufour, and Forestini, (2000) isochrones after correcting for extinction of A_V=2.6 mag are also overplotted. Since the major component of the outburst phase flux is nonstellar in origin, the closest

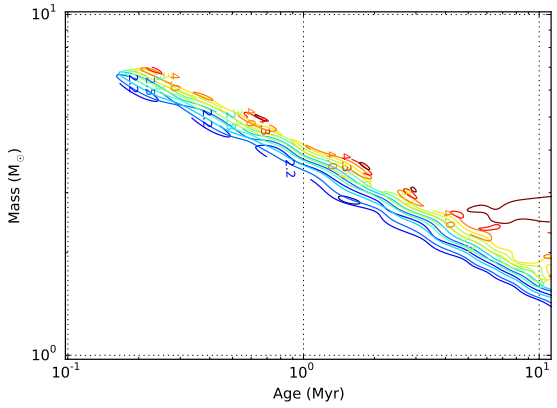

FIGURE 3.6: Contours showing 1σ constraints on mass and age of V899 Mon assuming Siess, Dufour, and Forestini, (2000) isochrones to be a valid model for V899 Mon in four-dimensional $U-B$, $B-V$, $V-R$, and $R-I$ color–color space. Contours corresponding to a range of admissible reddening values A_V are shown in different colors, and the corresponding A_V is labeled on the contours.

representation of the true position of V899 Mon might be its position during the quiescent phase. However, even the quiescent phase photometry suffers from scattered light. The scatter in the points on the CMD forbids the accurate estimation of age, but we get a rough estimate of the mass of the V899 Mon as 2 $M_\odot$. However, it should be noted that this estimate is sensitive to the estimated interstellar extinction value of A_V = 2.6 mag.

3.3 Spectral Energy Distribution

Available flux estimates of the V899 Mon over a wide wavelength range from optical to submillimeter were measured at random epochs. Since we had to use multi-wavelength data of nearby epochs for the construction of the SED, we chose the epoch near the peak of the first outburst (2010 February–March), during which maximum observations were available. For fitting YSO SED models, we used the online SED Fitter tool by Robitaille et al., (2007). Flux estimates from both *IRAS* and PACS show that the flux of V899 Mon starts rising in the 90 – 200 μm range after a gradual drop of SED in the mid-infrared region (see Figure 3.8). No SED models in Robitaille et al., (2007) could fit this double-peaked SED. Possible scenarios of such an SED are discussed in Section 3.3.1. To avoid the second far-infrared peak while fitting the SED of V899 Mon, we used all the flux estimates above 90 μm as upper limits. For constraining the SED better we also used 70 μm flux measured during the second outburst in 2013, but to account for the change in 70 μm flux between two outbursts, we used a 1 Jy error bar (which is consistent with the flux change we have seen in 250 μm SPIRE data from two epochs). Figure 3.8 (a) shows the SED fit obtained using *V, R, I, J, H, K_S, W1, W2, W3,* and *W4* fluxes from 2010 observations and PACS 70 μm flux from 2013 observations.

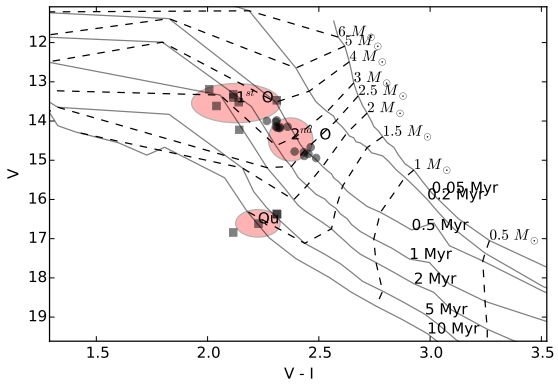

FIGURE 3.7: Optical $V/V-I$ color–magnitude diagram of V899 Mon during its first outburst (1^{st} O), second outburst (2^{nd} O), and quiescent (Qu) phases. Solid lines are Siess, Dufour, and Forestini, (2000) isochrones corresponding to 0.05, 0.2, 0.5, 1, 2, 5, and 10 Myr. Dashed lines are evolutionary tracks of masses 0.5, 1, 1.5, 2, 2.5, 3, 4, 5, and 6 $M_\odot$. An extinction correction for an A_V = 2.6 mag and a magnitude correction for a distance of 905 pc are applied to all isochrones.

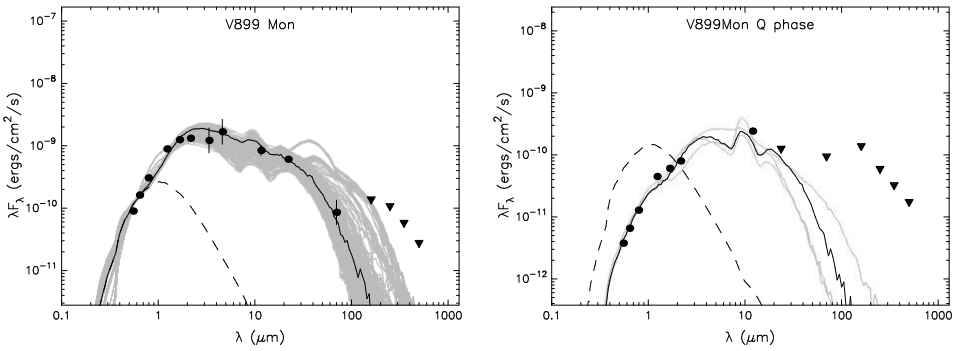

(a) First outburst (b) Quiescent phase

FIGURE 3.8: SED fit of V899 Mon (a) during its peak of the first outburst using *V, R, I, J, H,* K_S*, W1, W2, W3,* and *W4* fluxes from 2010 and PACS 70 μm flux from 2013, (b) during its quiescent phase using *V, R, I,* 2MASS *J, H,* K_S*,* and *IRAS 12* μm fluxes. MIPS1, PACS, and SPIRE fluxes were used only as upper limits. The filled circles represent the data points used for the fit, and filled triangles are upper limits. The solid black line is the best-fitted model, and the gray lines show subsequent good fits. The dashed gray line shows the stellar photosphere of V899 Mon in the best-fitted model (in the absence of circumstellar dust, but including interstellar extinction).

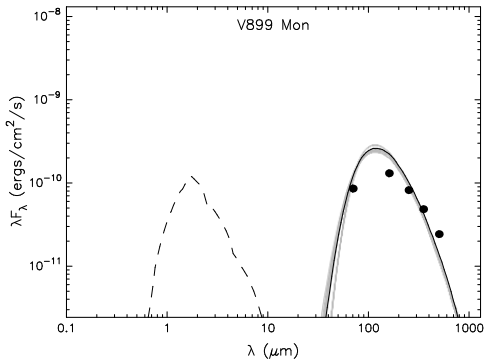

FIGURE 3.9: SED fit of V899 Mon during its second outburst phase using only *Herschel* PACS 70 and 160 μm, and SPIRE 250, 350, and 500 μm fluxes. The filled circles represent the data points used for the fit. The solid black line is the best-fitted model, and the gray lines show subsequent good fits. The dashed gray line shows the stellar photosphere of V899 Mon in the best-fitted model (in the absence of circumstellar dust, but including interstellar extinction).

For fitting the SED of V899 Mon's quiescent phase, we used flux estimates from different quiescent phase epochs. Figure 3.8 (b) shows the SED fit using *V, R, I,* 2MASS *J, H, K_S, and IRAS 12* μm fluxes. MIPS1 (24 μm), PACS (70, 160 μm), and SPIRE (250, 350, 500 μm) fluxes were used only as upper limits.

Treating far-infrared PACS and SPIRE fluxes of 2013 to be a separate independent clump, we also fitted the SED by taking these fluxes alone (see Figure 3.9 and section 3.3.2).

Stellar, disk, and envelope parameters obtained from all the three SED fittings are tabulated together in Table 3.2.

TABLE 3.2: SED fit results of V899 Mon

Parameter	Quiescence	1^{st} outburst	Far-IR alone
A_V (mag)	4.5 ±1.1	4.2 ±0.34	
distance (pc)	870 ±80	794 ±30	891 ±55
Age_* (Myr)	4.84 ±2.1	1.93 ±1.8	0.0073 ±.002
$Mass_*$ ($M_\odot$)	3.7 ±0.3	5.1 ±0.5	0.57 ±0.04
$\dot{M}_{envelope}$ ($M_\odot$)	0 ±5.7e-09	0 ±7.9e-08	24.7e-05 ±2.4e-05
$Mass_{Disk}$ ($M_\odot$)	1.2e-05 ±0.0179	1.4e-03 ±2.07e-03	0.048 ±0.008
$\dot{M}_{disk}$ ($M_\odot$/yr)	1.54e-10 ±4.9e-07	4.82e-09 ±7.6e-08	5.48e-07 ±2.7e-07
L_{total} ($L_\odot$)	162 ±79	419 ±168	8.55 ±1.54
$Mass_{env}$ ($M_\odot$)	8.13e-08 ±0.027	1.52e-05 ±0.07	23.43 ±2.0

Note: Median and standard deviation of the best fitted 20 models in each case.

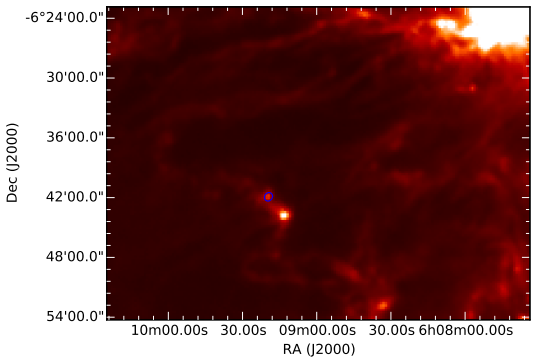

FIGURE 3.10: SPIRE 500 μm image of the V899 Mon field taken on 2013 March 16. The location of V899 Mon is marked with an ellipse to show the major and minor FWHM sizes determined for V899 Mon by the source extraction algorithm *getsources* (Men'shchikov et al., 2012). The brighter source IRAS 06068-0643, southwest of V899 Mon, is also a more embedded outburst source. The bright blob in the northwest corner of the image is the ionizing source in Monoceros R2.

3.3.1 70 μm dip in SED

The SED of V899 Mon shows a dip around 70 - 90 μm in both $IRAS$ and PACS data taken at two different epochs. This shape of the SED is very unusual and not seen in any other FUors/EXors. Objects with extended circumstellar envelopes typically show a smooth flat SED. We also do not see heavy extinction in optical bands as expected from a source surrounded by a large extended envelope. One possible scenario is that this object, instead of having a steady-state infall density distribution of the envelope, has a huge spherical cavity around it to a certain radius in the envelope. Significant optical light that we detect can be explained if our line of sight is along the opening created by the outflow.

Another possible geometric scenario is an envelope/clump with most of its mass behind V899 Mon. In the SPIRE 500 μm image (see Figure 3.10), we see that the bright blob marked with an ellipse at the position of V899 Mon is at the edge of a cloud, possibly being pushed back by the ionizing source of Monoceros R2.

3.3.2 Far-infrared component properties

Considering the far-infrared component part of the SED as a separate clump, we analyzed PACS-SPIRE data alone to obtain the characteristics of the clump. L_{bol} of the clump obtained by fitting the Robitaille et al., (2007) SED model for the far-infrared flux (> 70 μm) is ~ 8.6 $L_{\odot}$ (Table 3.2).

We have SPIRE 250, 350, and 500 μm observations at two epochs: during the peak of the first outburst on 2010 September 4, and later during the second outburst in 2013 March 6. PACS 70 and 160 μm observations were available only during the second epoch. Photometric flux values estimated for V899 Mon from PACS and SPIRE data are given in Table 3.3.

TABLE 3.3: Far-infrared fluxes of V899 Mon

Band	2010 Sep 14	2013 Mar 06	Δ flux
PACS 70 μm		2.01 Jy	
PACS 160 μm		7.02 Jy	
SPIRE 250 μm	9.02 Jy	6.86 Jy	2.86 Jy
SPIRE 350 μm	6.82 Jy	5.68 Jy	1.48 Jy
SPIRE 500 μm	4.65 Jy	4.06 Jy	0.33 Jy

Note: Δ flux between two epochs were estimated by aperture photometry on difference images using apertures 48″ ,60″ and 70″ for 250 μm, 350 μm and 500 μm respectively.

During the peak of the first outburst, fluxes were brighter than the second outburst by 2.8 Jy, 1.5 Jy, and 0.3 Jy in 250, 350, and 500 μm, respectively. V899 Mon was also optically brighter during the peak of the first outburst than the second outburst epoch by 0.75 magnitude (factor of 2) in R band. This implies that the far-infrared clump is heated by V899 Mon and is not spatially far from V899 Mon. We fitted the graybody model to SPIRE data from the two epochs (Figure 3.11) and estimated the mass to be 20 $M_\odot$ and temperature of the far-infrared clump to be 10.6 and 10.0 K at each epoch. This mass estimate is consistent with the envelope mass obtained from Robitaille et al., (2007) SED fitting (see Table 3.2). The graybody model was fitted using the following formulation:

$$S_\nu(\nu) = \frac{M(0.01(\frac{\nu}{1000GHz})^\beta)B(T,\nu)}{D^2} \tag{3.1}$$

where $S_\nu(\nu)$ is the observed flux density, M is the mass of the clump, $B(T,\nu)$ is the Planck's blackbody function for temperature T and frequency ν, D is the distance (taken to be 905 pc), and the dust opacity factor (κ_ν) was taken to be $0.01(\frac{\nu}{1000GHz})^\beta\ m^2kg^{-1}$, where β was fixed to be 2 (André et al., 2010).

To obtain a lower limit of A_V, we assumed that the entire mass M is in a uniform-density sphere of diameter $2R$ = 50″ (FWHM of the source in the SPIRE 500 μm image), and then the mass column density to the center of the sphere should be $3M/(4\pi R^2)$. Since most of the gas is molecular, we can equate this column density to N(H_2)$\mu_{H_2}m_H$, where N(H_2) is the H_2 column number density, μ_{H_2} is the mean molecular weight (taken to be 2.8), and m_H is the mass of hydrogen. Our mass estimate of 20 $M_\odot$ then corresponds to N(H_2) = 17.7×10^{21} molecules cm^{-2}. Using the relation $\langle N(H_2)/A_V\rangle = 0.95 \times 10^{21}$ molecules cm^{-2} mag^{-1} (Bolatto, Wolfire, and Leroy, 2013), we obtain an A_V of 18.6 mag to the center of the clump.

If we use PACS 160 μm flux also in the graybody fitting, then we obtain a mass of 12 $M_\odot$ and a temperature of 11.9 and 12.2 K for the far-infrared clumps at the two epochs. This mass corresponds to an A_V = 11.2 mag to the center of the uniform spherical clump. Both of these estimates are substantially higher than the actual A_V estimated from optical and NIR data. This implies that the heating source V899 Mon is not embedded at the center of this clump; it might be partially located on the front section of it (or any other geometry as discussed in Section 3.3.1). Even though the

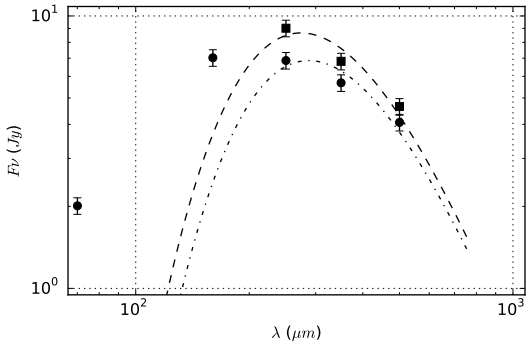

FIGURE 3.11: Graybody fit of V899 Mon's far-infrared SPIRE wavelength fluxes at two epochs. Filled squares are from the 2010 epoch during the peak of the first outburst, and filled circles are from 2013 during the second outburst. The dashed line is the graybody fit to the SPIRE data points of the first outburst in 2010, and the dot-dashed line is the fit to the SPIRE data points observed in 2013 during the second outburst. PACS data points of the second epoch are also shown, but were not used for the graybody fit.

mass estimate has some systematic uncertainties from the distance, dust opacity factor, and graybody model assumption, they are unlikely to cause a difference of 8 - 15 mag in the A_V value.

3.4 Spectroscopic Results

V899 Mon has a rich spectrum of emission and absorption lines in optical and NIR. Figure 3.12 shows the flux-calibrated optical and NIR spectra taken during the second outburst phase of the source. Our spectroscopic observations in optical cover the first outburst, transition, and quiescent phases, as well as the second outburst. The fluxes and equivalent widths of the detected lines at various epochs are tabulated in Table 3.4. The strong Ca II IR triplet emission lines in the spectrum confirm the V899 Mon source to be a YSO, and the detection of CO (2-0) and (3-1) bandhead absorption starting at 2.29 μm confirms this source to be an outburst family of FUors/EXors. These overtone bandhead lines are seen only in giants and FUors/EXors. In FUors/EXors they are believed to be forming in the accretion-heated inner regions of the disk, where temperature is in the range 2000 K $< T <$ 5000 K and density $n_H > 10^{10}$ cm^{-3} (Kóspál et al., 2011). One notable line not detected in the V899 Mon spectrum is Brγ at 2.16 μm. While Brγ is typically found in strong accreting T Tauri stars, it is not detected in many FUors.

3.4.1 Extinction estimates

To obtain de-reddened line fluxes, we need to know the extinction to the source. In Section 3.1 our NIR CC diagram does not show any significant extinction to the source. We also have an estimate of the interstellar extinction to the source to be A_V = 2.6 mag from Figure 4 in Lombardi, Alves,

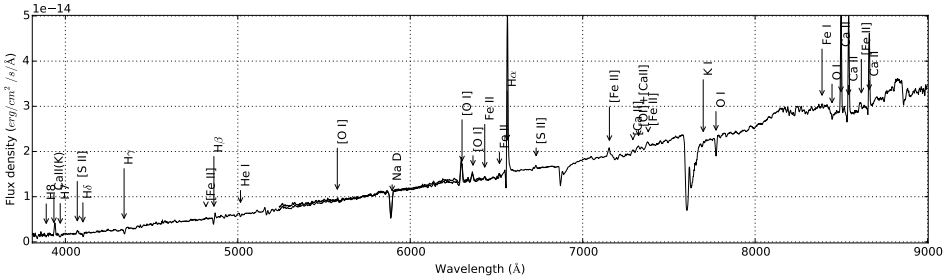

(a) optical

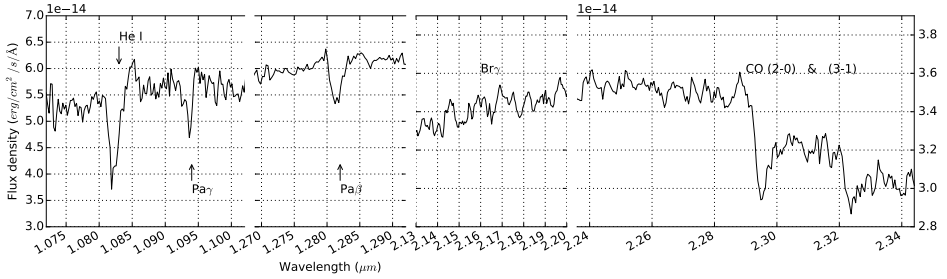

(b) NIR

FIGURE 3.12: Flux-calibrated optical and NIR spectra of V899 Mon during its second outburst. All spectra observed during the second outburst were median combined to improve signal-to-noise ratio. Identified lines in the spectra are labeled. The optical spectrum (a) is not corrected for atmospheric absorption lines. The absorption lines that are not labeled in the optical spectrum are atmospheric lines.

TABLE 3.4: Spectral line measurements of V899 Mon

Date	JD	Hα λ6562.8				Ca II λ8498	
		eqw (Å)	Flux (erg/cm^2/s)	eqw$_{abs}$ (Å)	Outflow Velocity (km/s)	eqw (Å)	Flux (erg/cm^2/s)
2009-11-30	2455166.33	-17.5	1.9e-13			-10.1	1.52e-13
2009-12-17	2455183.21	-6.88	1.38e-13	4.27	-254	-3.7	1.21e-13
2009-12-21	2455187.27	-7.77	1.83e-13	7.17	-199	-4.78	1.74e-13
2009-12-29	2455195.22	-6.82	1.69e-13	2.48	-263	-4.7	1.89e-13

Note: This table is published in its entirety in the electronic edition of Ninan et al., (2015). A portion is shown here for guidance regarding its form and content. Online version contains data of 28 lines.

and Lada, (2011). Hα (6563 Å) and Hβ (4861 Å) lines show an emission component in their P Cygni profile. If we assume an optically thin case B emission, the Balmer decrement ratio of the Hα/Hβ emission component should be in the range of 2.8 - 3 (Osterbrock and Ferland, 2006). Comparing this ratio with the ratios measured from our spectra, we obtained various estimates of A_V during outburst phase, ranging from 5.9 to 9.2 mag. Our Hβ profiles show a stronger absorption component than emission component; this might cause a significant underestimation of the Hβ flux, which was estimated by fitting a two-component Gaussian model to the line profile. This implies that the A_V estimate from the Balmer decrement is an overestimate. On the other hand, it is quite likely that the emission is not optically thin since it is believed to originate in the magnetospheric accretion column, which will make our estimate of A_V an underestimate. To be consistent with our other extinction estimates from the CC diagram and SED fitting in previous sections, we take A_V during the outburst phase to be 2.6 mag for the remaining spectral line calculations.

3.4.2 Accretion rate

Many of the spectral line fluxes originating near the magnetosphere have been found to correlate with the accretion luminosity. The correlation is empirically calibrated in the simple form: $log(L_{acc}/L_\odot) = a\ log(L_{line}/L_\odot) + b$. For estimating accretion luminosity from hydrogen Balmer series, He I, O I, Ca II IR triplet, Paβ, and Paδ lines, we used the coefficients a and b from Alcalá et al., (2014). The distance to V899 Mon was taken to be 905 pc, and the observed fluxes were corrected for an extinction of A_V = 2.6 mag. To estimate the accretion rate from the accretion luminosity, we assumed a mass and age of V899 Mon to be 2.5 M$_\odot$ and 1 Myr, respectively (consistent with the CMD). Stellar radius was then estimated to be 4 R$_\odot$ based on the isochrone for these values of mass and age (Siess, Dufour, and Forestini, 2000). Finally, using the formula $\dot{M}_{disk} = (L_{acc}R_*/GM)(1 - R_*/R_i)^{-1}$ (where disk inner radius $R_i \sim 5 \times R_*$;Gullbring et al., (1998)), we obtained accretion rates from various lines along the spectrum. No veiling correction was done for lines that are in absorption; hence, these accretion rate estimates can be slight underestimates. Figure 3.13 shows all the estimates

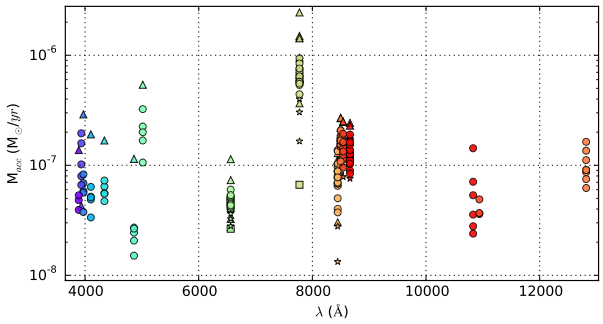

FIGURE 3.13: Accretion rates estimated from various lines from V899 Mon's optical and NIR spectra. Triangles show the first outburst phase, squares show the quiescent phase, stars show the transition phase, and circles show the second outburst phase. There is a significant difference in accretion rates estimated using different lines.

of accretion rates from various lines as a function of their wavelengths. Figure 3.14 shows the normalized accretion rates obtained from different lines at various epochs. A clear reduction in relative accretion, by at least a factor of 2 during quiescent phase with respect to the second outburst phase, is seen in all the accretion rates obtained from different lines.

3.4.3 Mass loss

Ratio of the mass loss to mass accretion in YSOs is a key parameter predicted by various jet launch mechanism models. The FUors/EXors family of objects gives us a direct observational constraint on this ratio. Based on the SED fit in Section 3.3, we obtained an L_{bol} of V899 Mon of $\sim$150 $L_\odot$ during the outburst phase. Using the relation between mass loss and L_{bol} in young HeBe and T Tauri stars, viz., $log(\dot{M}) = -8.6 + 0.7 \times log(L_{bol})$ by Nisini et al., (1995), we get an estimate of the mass outflow in V899 Mon to be $1{\times}10^{-7}$ $M_\odot yr^{-1}$. This rate is larger than typical T Tauri stars (10^{-8} $M_\odot yr^{-1}$) but less than classical FUors (10^{-5} $M_\odot yr^{-1}$) (Hartmann and Kenyon, 1996).

We could also directly measure the mass-loss rate from [O I] λ6300 flux using the relation *A8* of Hartigan, Edwards, and Ghandour, (1995). Mass outflow is directly proportional to the optically thin forbidden line emission fluxes originating in the outflow. The mass-loss estimate from [O I] λ6300 flux through a 2″ slit aperture, by assuming a distance of 905 pc and a typical sky plane component of the outflow velocity of 150 km s^{-1}, is $2.6{\times}10^{-7}$ $M_\odot yr^{-1}$.

We could not detect any significant change in these forbidden line fluxes during quiescence. Our 2″ slit aperture at 905 pc distance corresponds to a $2.7{\times}10^{11}$ km wide region. Even if we assume the sky plane velocity to be as large as 700 km s^{-1} (seen in P Cygni outflow), the gap in outflow due to one year of quiescence will be only $2.2{\times}10^{10}$ km, which is just 1/10 of the total aperture. Hence, our nondetection does not conclude whether the large-scale low-density outflow traced by forbidden lines was interrupted or remained uninterrupted during the quiescent phase.

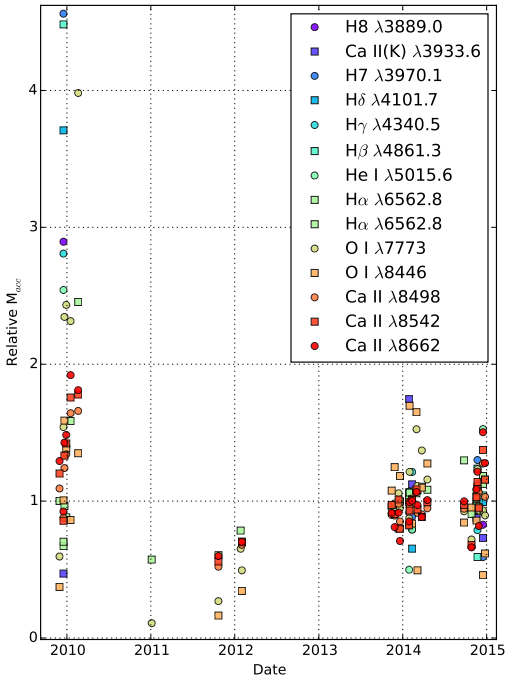

FIGURE 3.14: Relative change in accretion rates estimated from various lines during the transition from the first outburst phase to the quiescent phase and back to the second outburst phase.

3.4.4 Outflow Temperature and Density

Flux ratios of the optically thin forbidden emission lines provide a direct estimate of the density and temperature of the outflow region. For better signal-to-noise ratio, we estimated the average flux of the forbidden lines by combining all the second outburst phase spectra of V899 Mon. Flux ratio [S II] λ6716/λ6731 is a good tracer of density and is insensitive to temperature. Flux of the [S II] λ6731 line is 2.4$\times10^{-14}$ erg cm^{-2}s^{-1}, whereas the [S II] λ6716 line is not detected in our spectrum, so we estimate the upper limit to be $< 1\times10^{-14}$ erg cm^{-2}s^{-1}. The ratio [S II] λ6716/λ6731 < 0.45 implies that the electron density n_e is $> 10^4$ cm^{-3} (Figure 5.8 in Osterbrock and Ferland, (2006)). The ratio of [O I] λ5577/λ6300 in V899 Mon is ~ 0.09. For a range of temperature from 9000 to 20,000 K, this ratio is consistent with n_e ranging from 2×10^5 cm^{-3} to 4×10^6 cm^{-3} (Figure 6 in Hamann, (1994)).

Once we have a density constraint, we can now use other line ratios to estimate the temperature. For instance, using the formula 5.5 in Osterbrock and Ferland, (2006), for a density of $n_e = 2\times 10^5$ cm^{-3}, ratio [O I] (λ6300+λ6364)/λ5577 $\sim$ 15 gives an estimate of the temperature to be $\sim$ 8500 K. Density-insensitive line ratio [Ca II] λ7291 / [OI] λ6300 $\sim$ 0.1 in V899 Mon implies a temperature <9000 K (Figure 5 in Hamann, (1994)). But the line ratio [S II] λ6731 / [O I] λ6300 $\sim$ 0.08 implies a temperature $>$ 9000 K (Figure 5 in Hamann, (1994)). To be consistent with all these independent estimates, we shall take the temperature of the outflow to be $\sim$ 9000 K.

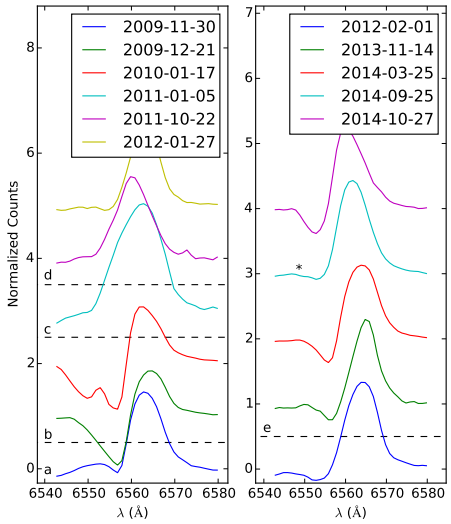

FIGURE 3.15: Selected sample of Hα emission line profiles from different phases of V899 Mon. (a) First outburst phase; (b) heavy outflow during the end of first outburst phase; (c) quiescent phase; (d) transition phase from quiescence phase to second outburst phase; (e) second outburst phase. The asterisk indicates a particular profile on 2014 September 25, when the P Cygni became very weak for a very short duration. The spectrum taken immediately after 1 month shown in the top of the right panel had a strong P Cygni profile.

3.4.5 Line profiles and variability

Hα λ6563 Almost all prominent lines in the spectrum showed variability during our period of observations. The line that showed the most dramatic changes in line profile is Hα, which has a strong P Cygni absorption component and is believed to be formed in a magnetospheric accretion funnel.

Figure 3.15 shows the evolution of the Hα P Cygni profile during its first outburst phase, quiescent phase, and the current ongoing second outburst phase. It is a selected representative sample of line profile plots from each epoch. The first spectrum published by Wils et al., (2009) shows no P Cygni profile in Hα. Our initial spectrum observed 13 days later during the peak of the first outburst shows a CI Tau profile typically seen in many T Tauri stars (Stahler and Palla, 2005). In subsequent spectra, the absorption component grows considerably, transforming the Hα line profile into a strong P Cygni profile (Figure 3.15). We also see complex structures in the absorption component of P Cygni in the spectrum taken on 2010 January 17. All these evolutions indicate that the outflow wind increased dramatically towards the end of first outburst. By the onset of the quiescent phase, the absorption component in P Cygni completely disappeared and the Hα showed a near-symmetric emission line. We also did not see any P Cygni profile when the source was undergoing transition from the quiescent phase to the second outburst phase. P Cygni profiles, much fainter in strength compared to the peak of the first outburst, only started appearing after the full onset of the second outburst. Even though during the second outburst the outflow P Cygni profile is more stable than during the last

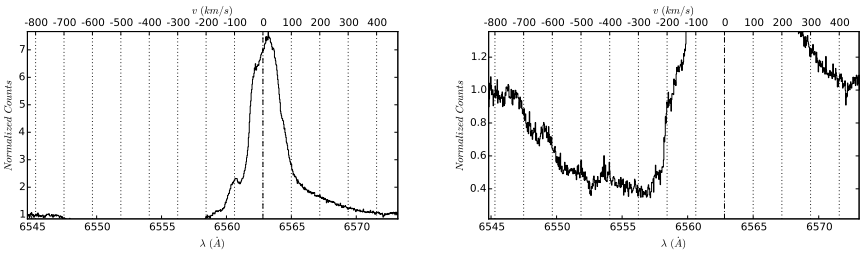

(a) Emission component (b) P Cygni absorption component

FIGURE 3.16: Hα (a) emission and (b) P Cygni absorption line profiles of V899 Mon observed on 2014 December 22 using SALT-HRS.

phase of the first outburst, the spectrum taken on 2014 September 25 shows only a very weak P Cygni in Hα. These delays and short pauses indicate a nonsteady nature in the outflows from FUors/EXors. Table 3.4 shows the fluxes and equivalent widths obtained by fitting a two-component Gaussian to the line profiles.

Our high-resolution spectrum ($R \sim$ 37,000) taken using SALT-HRS on 2014 December 22 resolves the Hα line and its multi-component profile. Figure 3.16 (a) shows the emission component of the Hα line profile, and Figure 3.16 (b) shows the absorption component in the spectrum taken using SALT-HRS. The redshifted part of the profile peaks at +18 km s^{-1} and has smooth wings with an extra broad component reaching up to a velocity of +420 km s^{-1} (Figure 3.16 (a)). On the other hand, the blue part of the profile shows complicated multicomponent velocity structures (Figure 3.16 (b)). The outflow absorption component extends up to -722 km s^{-1}. We could see structures in absorption at -648, -568, -460, -274, -153, -100, and -26 km s^{-1}.

These are typically associated with bulk motion within the outflowing gas (Stahler and Palla, 2005). To understand how the outflow components evolve, it will be interesting to study the evolution of these components in velocity time space by carrying out multiepoch high-resolution spectroscopic observations.

Forbidden lines [O I] λ6300, λ6363, [Fe II] λ7155 Another important tracer of outflow is the forbidden line [O I] at 6300.304 $\AA$. Our medium-resolution time evolution study does not show significant variation in this line, possibly owing to the fact that they originate in low-density jets/outflows. The SALT-HRS high-resolution spectrum shows a very interesting plateau profile for the [O I] λ6300 line (see Figure 3.17 for the resolved profile). Since we have not corrected our spectrum for telluric absorption, we shall not interpret the narrow absorption dips seen on the plateau structure. The profile has a strong redshifted emission at +25 km s^{-1} with an FWHM of 21 km s^{-1}. The emission in the blueshifted part extends up to $\sim$-450 km s^{-1}. Figure 3.18 shows the other two weaker forbidden lines [O I] λ6363 and [Fe II] λ7155 plotted over the [O I] λ6300 profile. We see an almost similar structure in [O I] λ6363, with a blueshifted emission extending up to -450 km s^{-1} and a narrow peak emission at +20 km s^{-1}. The [Fe II] λ7155 line also shows a very similar structure with a blue part extending up to $\sim$-500 km

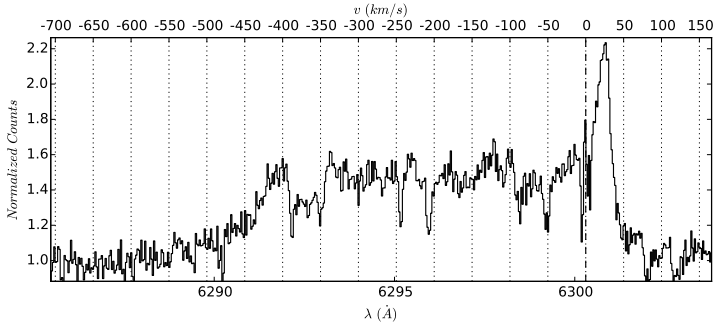

FIGURE 3.17: [O I] λ6300 emission line structure from V899 Mon observed on 2014 December 22 using SALT-HRS.

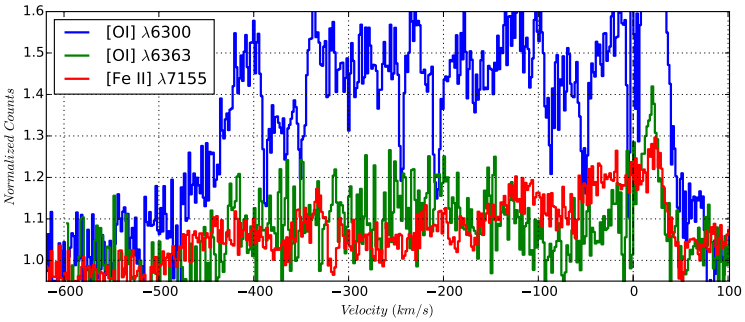

FIGURE 3.18: [O I] λ6363 and [Fe II] λ7155 emission line profile structures plotted over the [O I] λ6300 profile of V899 Mon observed on 2014 December 22 using SALT-HRS.

s^{-1} and a peak emission at $\sim$+22 km s^{-1}. Since the forbidden line emissions are optically thin, their flux is directly proportional to the column density of emitting species. The plateau profile implies almost equal column density in the blueshifted outflow with a velocity gradient in the jet. Since we are detecting only the velocity component of the jets along the line of sight, the gradient can be either due to actual change in the outflow velocity or due to the geometrical projection effect of the outflow. A cone-shaped outflow in the direction of the observer can give rise to different projected velocities from different radial regions of the cone. A time evolution study of these profiles will give insight into the structure of the outflow. The redshifted emission peak is more difficult to explain. This might be the rest velocity of the system, or originating from the envelope to disk infall shock regions on the surface of the disk, or from the tail part of a bipolar outflow that is moving away from us and emerging out of the region occulted by the disk in our line of sight.

Ca II IR triplet λ8498, λ8542, λ8662 Ca II IR triplet lines (8498.02 $\AA$, 8542.09 $\AA$, 8662.14 $\AA$) are believed to be originating inside and very near to the accretion column, resulting in their tight correlation with accretion rate (Muzerolle, Hartmann, and Calvet, 1998). Our continuous spectral monitoring shows that the P Cygni profile in Ca II IR triplet lines evolved similar to Hα. The outflow component got stronger toward the end of the first

outburst, then it completely disappeared during the quiescent phase, and finally reappeared after the full onset of the second outburst. As seen in typical T Tauri stars and FUors/EXors, the line ratios of Ca II IR triplet lines in the V899 Mon spectrum are found to be 1:1.01:0.77, representing an optically thick gas dominated by collisional decay. Unlike the emission components, the ratio of P Cygni absorption components of λ8542 and λ8662 measured from the high-resolution spectrum is 0.83:0.53 (= 1.57:1), which is more consistent with atomic transition strengths (1.8:1). This implies that the absorption components in outflow are optically thin. These values are surprisingly similar to the P Cygni profiles of Ca II IR triplet lines detected in the episodic winds of V1647 Ori (Ninan et al., 2013b). Following the same arguments as in Ninan et al., (2013b), we could estimate the Ca II column density in the outflow to be 3.4×10^{12} cm^{-2} and the hydrogen column density to be $N_H \sim 3.8 \times 10^{20}$ cm^{-2}.

Figure 3.19 shows the resolved profiles of Ca II IR triple lines. All the three triplet lines (λ8498.02, λ8542.09, λ8662.14) show an asymmetric triangular profile with a steeper slope on the red side and a shallower slope on the blue side. The peaks of these lines are redshifted by +18.7, +21.4, and +23.2 km s^{-1}, respectively. This increase in the redshift is also seen in the line center estimated by fitting a Gaussian profile to the lines. The σ of the fitted Gaussian for each line is 1.177, 1.229, and 1.186 $\AA$, respectively. The ratio of line widths of λ8498 and λ8542 is 0.96, which implies that λ8498 is $\sim$4% thinner than λ8542, as seen in many other T Tauri stars (Hamann and Persson, 1992), though there is no statistically significant evidence for the peak of the former line to be larger than the latter one. Hamann and Persson, (1992) attributed these ratios to substantial opacity broadening of λ8542 or to lower dispersion velocity in the deeper part of the region from where Ca II IR triple lines originate. The velocities of the smooth broadened emission profiles extend up to $\pm$150 km s^{-1}. Figure 3.20 shows the P Cygni absorption component in Ca II λ8542 and λ8662 lines. The absorption components are quite broad and extend up to $\sim$-470 km s^{-1} in both the lines. The absorption component in λ8662 shows a prominent structure that which extends only up to $\sim$-250 km s^{-1}.

O I λ7773, λ8446 The absorption component of O I triplet lines at 7773 $\AA$ (Figure 3.21), which is not seen in the photosphere of cool stars, is believed to be formed in T Tauri stars owing to warm gas in the envelope or hot photosphere above the disk, and it is an indicator of the turbulence (Hamann and Persson, 1992). The equivalent widths of this line in V899 Mon spectra show a very strong increase and then sudden decrease in strength just before the source went into the quiescent phase (see Figure 3.22). Owing to turbulence or disk rotational broadening of the O I triplet lines at 7771.94, 7774.17, and 7775.39 $\AA$, our high-resolution spectrum (see Figure 3.21) shows a blended Gaussian absorption profile with $\sigma = 2.43$ $\AA$ (FWHM = 220 km s^{-1}). The velocities originating from turbulence or disk rotation extend up to $\sim \pm$200 km s^{-1}.

Another O I triplet at λ8446 (containing 8446.25 $\AA$, 8446.36 $\AA$, 8446.76 $\AA$ triplet lines) is also seen in absorption in our SALT-HRS spectrum. These lines are also blended and have a combined FWHM = 174 km s^{-1}. The central position of the absorption line does not show any significant redshift and if present can be constrained to be $<$ 5 km s^{-1}. This implies that the

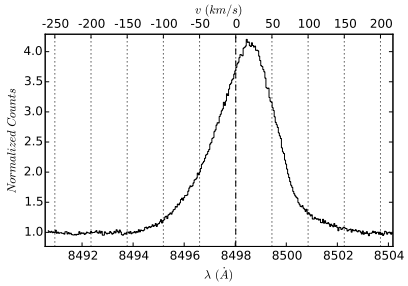

(a) λ8498

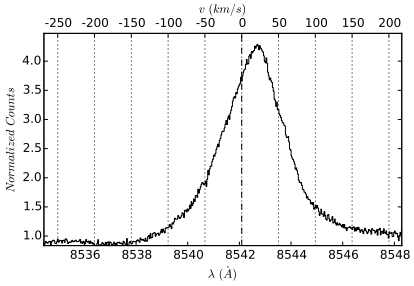

(b) λ8542

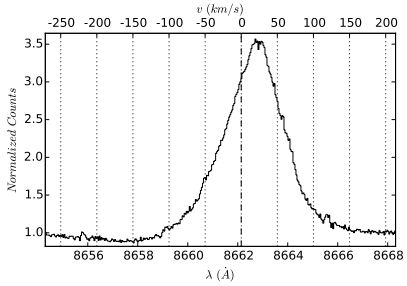

(c) λ8662

FIGURE 3.19: Ca II IR triplet emission line profiles of V899 Mon observed on 2014 December 22 using SALT-HRS.

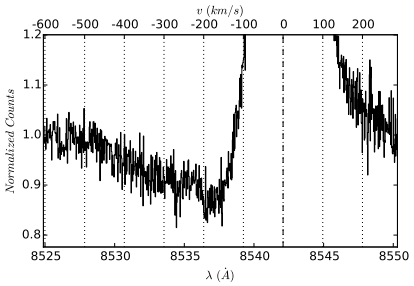

(a) λ8542

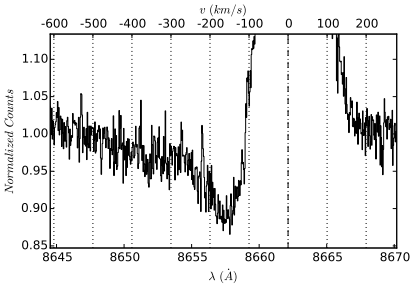

(b) λ8662

FIGURE 3.20: Ca II IR triplet P Cygni absorption line profile of V899 Mon observed on 2014 December 22 using SALT-HRS.

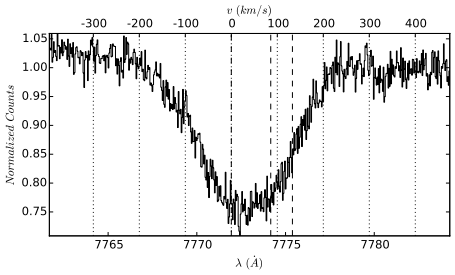

FIGURE 3.21: Blended O I λ7773 triplet absorption line profile of V899 Mon observed on 2014 December 22 using SALT-HRS. The vertical dashed lines mark the central positions of its triplet components at 7771.94, 7774.17, and 7775.39 $\mathring{A}$

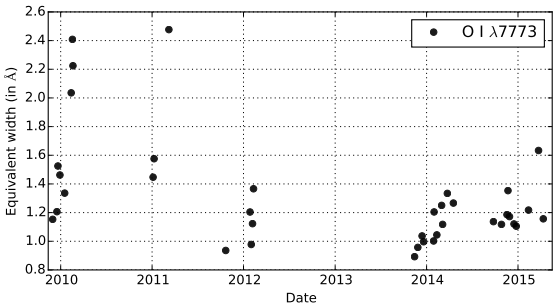

FIGURE 3.22: Evolution of equivalent width of O I λ7773 triplet, which traces the strength of turbulence in the disk of V899 Mon.

$\sim$+20 km s^{-1} (heliocentric velocity) redshift component seen in emission line profiles like the Ca II IR triplet and forbidden lines are not due to any uncorrected peculiar velocity of V899 Mon with respect to our Sun.

Fe I λ8514, λ8387, λ8689, λ8675 Many Fe I emission lines were detected in our medium-resolution optical spectrum. All these lines were also resolved in SALT-HRS spectrum. Fe I λ8514 is a blend of two lines at 8514.07 and 8515.11 $\mathring{A}$; their blended profile has an FWHM of 76 km s^{-1}. Fe I 8387.777 $\mathring{A}$ has a +26.5 km s^{-1} redshifted profile with an FWHM of 62.8 km s^{-1}, Fe I 8688.625 $\mathring{A}$ has a +26.74 km s^{-1} redshifted profile with an FWHM of 63.3 km s^{-1}, whereas a weaker Fe I 8674.746 $\mathring{A}$ line has a +40 km s^{-1} redshifted profile with an FWHM of 59.2 km s^{-1}. The redshifts in these lines are consistent with the redshifts we have measured in other resolved lines (for example, in Ca II IR triplet lines and forbidden lines).

3.5 Constraints from 1280 MHz Observation

V899 Mon was not detected in the 1280 MHz GMRT radio continuum map observed during its second outburst. The local background noise σ in the map after cleaning was $\sim$0.1 mJy. We could detect eight other point sources in the 28′ $\times$ 28′ FOV map centered at V899 Mon's position. For this study, we take a 5σ $\sim$0.5 mJy to be a strict upper limit on V899 Mon's 1280 MHz flux.

The ionizing flux from the magnetospheric accretion can create an H II region around the central source. Even though hydrogen Balmer lines detected in our optical spectra originate in the ionized region, since they are not optically thin, we cannot use them to constrain the extent of the H II region.

If we consider the H II region to be formed by a smooth, isothermal, and isotropic stellar outflow, from our mass outflow rate and velocity estimates, we can obtain the expected flux using the following formula (Moran, 1983).

$$S(\nu) = 1.3 \left(\frac{T_e}{10^4 K}\right)^{0.1} \left(\frac{\dot{M}}{10^{-6} M_\odot yr^{-1}}\right)^{4/3} \left(\frac{v}{10^2 km\ s^{-1}}\right)^{-4/3} \left(\frac{D}{kpc}\right)^{-2} \left(\frac{\nu}{GHz}\right)^{0.6} mJy$$

where $S(\nu)$ is the expected flux density, T_e is the electron temperature of the outflowing ionized wind, $\dot{M}$ is the mass outflow rate, v is the terminal velocity of outflow, D is the distance to V899 Mon, and ν is the frequency of observation. From our spectroscopic estimates of these quantities, we can substitute $\dot{M}$ = 0.26 $\times$ 10^{-6} $M_\odot yr^{-1}$, outflow velocity v = 1.5 $\times$ 10^2 km s^{-1} , T_e = 0.9 $\times$ 10^4 K, D = 0.905 kpc, and ν = 1.28 GHz. We obtain S(1.28 GHz) = 0.17 mJy, which is consistent with our observed upper limit of 0.5 mJy. Since the outflows we detected in the optical spectrum are unlikely to be an isotropic outflow, our predicted estimate of 0.17 mJy is also an upper limit.

Instead of considering a radial density profile due to outflow, since we have an estimate of density from forbidden optical lines, we can calculate an upper limit on the maximum size of a homogeneous, isotropic, spherical H II region around V899 Mon. For an H II region of radius R_s, using a spherical volume emission measure, we have the expression (Moran, 1983).

$$S(\nu) = 3.444 \times 10^{-83} \left(\frac{10^4 K}{T_e}\right)^{0.35} \left(\frac{1 GHz}{\nu}\right)^{0.1} \left(\frac{1 kpc}{D}\right)^2 \frac{4\pi R_s^3}{3} n_e^2$$

where the radius of the H II region R_s is in cm, and electron density n_e is per cm^3. Taking 0.5 mJy as an upper limit on $S(\nu)$ and $n_e \sim 1 \times 10^6 cm^{-3}$, we obtain $R_s < 20$ AU. Since the flux of the ionizing Lyman continuum inside an H II region is equal to the volume emission measure times the recombination rate, we have obtained the following relation for N_{Lyc},

$$N_{Lyc} = 7.5487 \times 10^{43} \times \left(\frac{S(\nu)}{mJy}\right) \left(\frac{T_e}{10^4 K}\right)^{-0.45} \left(\frac{\nu}{1 GHz}\right)^{0.1} \left(\frac{D}{1 kpc}\right)^2$$

Using our upper limit of $S(\nu)$, we obtain an upper limit on the Lyman continuum flux from V899 Mon to be $N_{Lyc} < 5 \times 10^{43}$ photons s^{-1}.

3.5.1 V899 Mon: FUor or EXor

The empirical classification between FUors and EXors is based on the similarity in observed properties with classical FUors (FU Ori, V1515 Cyg, etc.) and EXors (EX Lup, V1118 Ori, etc.). Audard et al., (2014) provide a detailed comparison of these objects from the literature. The ~3 mag change in the brightness of V899 Mon during its outburst is typical of the EXors family of outbursts. On the other hand, the duration of outbursts in V899 Mon, ~4 yr for the first outburst and greater than 3.5 yr for the ongoing second outburst, is significantly more than the typical duration EXors spend

in outburst (less than 1–3 yr). Unlike V899 Mon, EXors also remain in quiescence longer than the time they spend in the outburst phase. However, V899 Mon's outburst timescales are still much less than classical FUors.

Spectroscopically, classical FUors have all optical and NIR hydrogen lines in absorption, while EXors have those lines in emission. In the case of V899 Mon, Hα and a small component of Hβ are in emission, while all the other hydrogen lines in optical and NIR are in absorption. CO bandheads starting at 2.29 μm are also in absorption. Hence, spectroscopically also V899 Mon lies between classical FUors and EXors. The L_{bol} estimates of V899 Mon from SED are greater than that of typical EXors, and they are less than that of classical FUors. The mass accretion rate during outburst phase is typical of EXors and is an order less than that of classical FUors.

Many of the recently discovered outbursts like V1647 Ori, OO Ser, etc., also show such intermediate properties between the classical bimodal classification of FUors and EXors. Discovery of more such intermediate-type outburst sources like V899 Mon indicates that this family of episodic accretion outbursts probably has a "continuum" distribution and not bimodal.

3.6 Summary

In this chapter, we have presented the results from our long-term monitoring of V899 Mon from 2009 September to 2015 April. During this period, V899 Mon underwent transition from the first outburst phase to the quiescent phase and then back to the second outburst phase. The following are the key results of this chapter.

1. Optical and NIR spectroscopy of V899 Mon confirms it to be a member of the FUors/EXors family of outbursts.

2. We have estimated various stellar parameters of V899 Mon like mass, age and extinction, and outflow temperature and density.

3. At the end of 2010, V899 Mon abruptly ceased its first outburst phase and transitioned to the quiescent phase for a duration of little less than a year, immediately after which it returned to the second outburst.

4. Just before the break in the first outburst phase of V899 Mon, its spectra showed heavy outflow activity (indicated by a strong P Cygni) and increased turbulence.

5. The excess flux of the outburst initially had a cooler temperature than V899 Mon's photosphere and slowly became hotter as V899 Mon transitioned from the quiescent phase to the second outburst phase. This was seen in the change of $V-R$ and $V-I$ color of V899 Mon, which had reddest values during the intermediate transition period.

6. The outflows indicated by P Cygni profiles completely disappeared during the quiescent phase of V899 Mon and reappeared gradually only after V899 Mon reached the peak of the second outburst.

7. The high-resolution spectrum of the forbidden emission line profiles originating in outflows/jets shows blueshifted velocity components extending up to -500 km s^{-1}, while the outflows traced by Hα P Cygni

absorption profiles originating near the central star show complex multiple absorption components with velocities up to -722 km s^{-1}.

8. As expected from accretion outbursts, accretion rates estimated for V899 Mon from spectral lines show significant variation between first outburst, quiescent, and second outburst phases.

9. Since the A_V estimate from far-infrared is inconsistent with optical observations, V899 Mon is not embedded inside the far-infrared clump detected at its location. It is possible that our line of sight is through a cavity cleared out in the envelope. The clump is thermally influenced by the irradiation from V899 Mon since it showed variation in far-infrared flux between the first and the second outburst phases.

Chapter 4

V1647 Ori

Another recently discovered, peculiar, FUors/EXors object is V1647 Ori (V1647 Orionis), 400 pc away in the L1630 dark cloud of Orion. Unlike V899 Mon, this source is more extensively studied in literature. V1647 Ori underwent a sudden outburst of ~ 5 mag in the optical band in 2003 (McNeil, Reipurth, and Meech, 2004; Briceño et al., 2004) and illuminated a reflection nebula, now named as McNeil's nebula after its discoverer Jay McNeil. Reipurth and Aspin, (2004) reported 3 mag increase in the near-infrared (NIR) band and Andrews, Rothberg, and Simon, (2004) reported 25 times increase in 12 μm flux and no change in submillimeter flux of V1647 Ori during the outburst. Kastner et al., (2004) reported a 50 times increase in X-ray flux of V1647 Ori during the outburst and noted that the derived temperature of the plasma is too high for accretion alone to explain, hinting that magnetic reconnection events might be heating up the plasma. Based on the upper limit on radio continuum emission from McNeil's nebula at 1272 MHz from the Giant Metrewave Radio Telescope (GMRT), India, Vig et al., (2006) constrained the extent of the H II region corresponding to a temperature $\gtrsim$ 2500 K to be $\lesssim$ 26 AU. Spectroscopic studies showed strong Hα and Ca II IR triplet lines in emission (Briceño et al., 2004; Ojha et al., 2006). In the NIR region, strong CO bandheads (2.29 μm) and a Brγ line (2.16 μm; implying strong accretion) were detected in emission (Reipurth and Aspin, 2004; Vacca, Cushing, and Simon, 2004). The strong P-Cygni profile in Hα emission indicated wind-velocity ranging from 600 to 300 km s^{-1} (Ojha et al., 2006; Vacca, Cushing, and Simon, 2004). Abrahám et al., (2006) carried out AU-scale observations using the Very Large Telescope Interferometer/ Mid-Infrared interferometric Instrument (VLTI/MIDI). By fitting both spectral energy distribution (SED) and visibility values, they deduced a moderately flaring disc with temperature profile $T \sim r^{-0.53}$ (T(1AU) = 680 K) and mass $\sim 0.05 M_{\odot}$, with inner radius of 7 $R_{\odot}$ (0.03 AU) and outer radius of 100 AU. This temperature profile is shallower than the $T \sim r^{-0.75}$ canonical model (Pringle, 1981). They also reported that the mid-infrared emitting region at 10 μm has a size of ∼7 AU. Rettig et al., (2005) used the CO lines in the infrared (IR) band to measure the temperature of the inner accretion disc region, which was estimated to be $T \approx$ 2500 K.

Ojha et al., (2006) and Kospal et al., (2005) reported a sudden dimming and termination of the 2003 outburst in 2005 November. Thus, the 2003 outburst lasted for a total of ∼2 yr, and V1647 Ori returned to its pre-outburst phase in early 2006. Acosta-Pulido et al., (2007b) estimated the inclination angle of the disc to be 61° and also estimated the accretion rate to be $5 \times 10^{-6} M_{\odot}$ yr^{-1} during outburst and $5 \times 10^{-7} M_{\odot}$ yr^{-1} in the 2006 quiescent state. Aspin et al., (2006) reported that ∼37 yr prior to the 2003 outburst, i.e.,

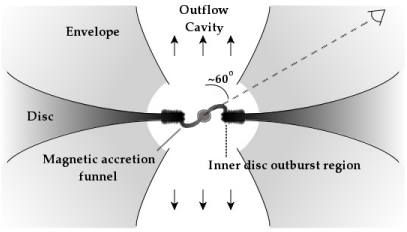

FIGURE 4.1: Cross section of V1647 Ori surroundings we know so far and the line-of-sight angle to the disc. Image is not drawn to scale.

in 1966, V1647 Ori had undergone a similar magnitude of outburst, lasting somewhere between 5 and 20 months.

Contrary to expected decades-long quiescense, V1647 Ori underwent a second outburst in 2008 after spending just two years in a quiescent state (Aspin et al., 2009). It brightened up to the same magnitude and had almost identical spectral features in optical and NIR bands as the first outburst. One striking difference was that the strong CO bandhead emission at 2.29 μm was absent in the second outburst (Aspin, 2011a). The X-ray flux with plasma temperature of 2-6 keV during both outbursts was postulated to be due to magnetic reconnection events in the disc-star magnetic field interaction (Teets et al., 2011, and references therein). Hamaguchi et al., (2012) normalised and combined both outbursts' data in X-ray and detected 1 day periodicity in the light curve, which they modeled with two accretion hot spots on the top and bottom hemispheres of the star rotating with 1 day period and inclination of $68°$. Figure 4.1 shows the overall cross-section picture of the surroundings of V1647 Ori we know so far.

In this chapter, we present the results from our more than four and a half years (2008 - 2013) of optical and NIR photometric and spectroscopic observations of the ongoing second outburst of V1647 Ori and the associated McNeil's nebula. The results presented in this chapter are published in Ninan et al., (2013b).

4.1 Photometric Results

Figure 2.2 shows the three-color composite image (V: blue; R: green; I: red) of the McNeil's nebula field (FOV $\sim 10 \times 10$ arcmin^2) obtained from IGO on 2010 February 13. Secondary standard stars used for flux calibration are marked as A, B, C, and D. The outburst source V1647 Ori, illuminating the nebula, is marked at the center. Region C, possibly unrelated to Herbig-Haro object, HH 22A, which is illuminated by V1647 Ori, is also marked. V1647 Ori had already reached its peak outburst phase before our first optical observation in 2008 September. Its light curve steadily continued in peak outburst flux ("high plateau") phase even until our last observation taken in 2013 March. However, our long-term continuous monitoring from 2008 September 14 to 2013 March 11 shows a slow but steady linear declining trend in the brightness of the source and nebula (Ninan et al., 2012). The

linear slopes and the error in estimates of slopes were obtained by simple linear regression by ordinary least-squares fitting. V, R, and I magnitudes of V1647 Ori and of region C, which is illuminated by V1647 Ori from its face-on angle of the disc, are listed in Table 4.1. Light curves of V1647 Ori in I and R bands clearly show a steady dimming (see Figure 4.2). During the first four and a half years of its second outburst, the brightness in I and R bands has decreased by ~ 0.2 mag. The rate of decline in magnitude of V1647 Ori is 0.036 ± 0.007 mag yr^{-1} in I band and 0.038 ± 0.007 mag yr^{-1} in R band. We do not see any statistically significant decline in V band magnitude of V1647 Ori. This could be due to the higher fraction of contamination of the nebula over V1647 Ori's aperture and slightly higher error in magnitudes due to faintness of the source in V band. These flux changes are along our direct line of sight at an angle of $\sim 30^{\circ}$ to the plane of the disc (Acosta-Pulido et al., 2007b). However, the flux measured along the cavity in perpendicular direction to the disc, which is reflected from region C, shows a dimming trend of 0.059 ± 0.005 mag yr^{-1} in I band, 0.051 ± 0.005 mag yr^{-1} in R band, and 0.060 ± 0.005 mag yr^{-1} in V band (see Figure 4.3). Hence, region C seems to be dimming faster than V1647 Ori. This could be either due to material inflow into cavity between region C and V1647 Ori as the outburst is progressing or due to a change in extinction along the cavity induced by slow dimming of V1647 Ori's brightness. During the first outburst in 2003, the linear dimming rate during the plateau stage was 0.24 mag yr^{-1} in R band (Fedele et al., 2007), which was ~ 6.3 times faster in magnitude scale than the present dimming rate in the second outburst. Just like in other T Tauri stars, we also see a lot of short time scale random variations in the source magnitude (peak-to-peak $\Delta V \simeq 0.35$ mag, $\Delta R \simeq 0.30$ mag, and $\Delta I \simeq 0.20$ mag), which could be due to density fluctuations in the infalling gas on to the star.

TABLE 4.1: Optical VRI photometry of V1647 Ori and region C

Julian Date	V1647 Ori			region C		
	V	R	I	V	R	I
2454724	19.08	17.06	14.98	15.59	14.99	14.36
2454726	19.11	17.11	15.04	15.57	14.98	14.36
2454738	19.00	17.04	14.99	15.59	15.06	14.36
2454741	19.04	17.05	15.02	15.59	14.98	14.33
2454742	19.09	17.09	15.04	15.55	15.02	14.39
2454745	19.12		15.02	15.60		14.30
2454751	19.26	17.08	15.02	15.50	15.02	14.20

†† Observed from IGO, all other nights are from HCT.

Note: Estimated error in magnitude of V1647 Ori is $\leq \pm0.05$ for V and $\leq \pm0.02$ for R and I. Estimated error in magnitude of region C is $\leq \pm0.02$ for V, R and I.

Note: This table is published in its entirety in the electronic edition of Ninan et al., (2013b). A portion is shown here for guidance regarding its form and content.

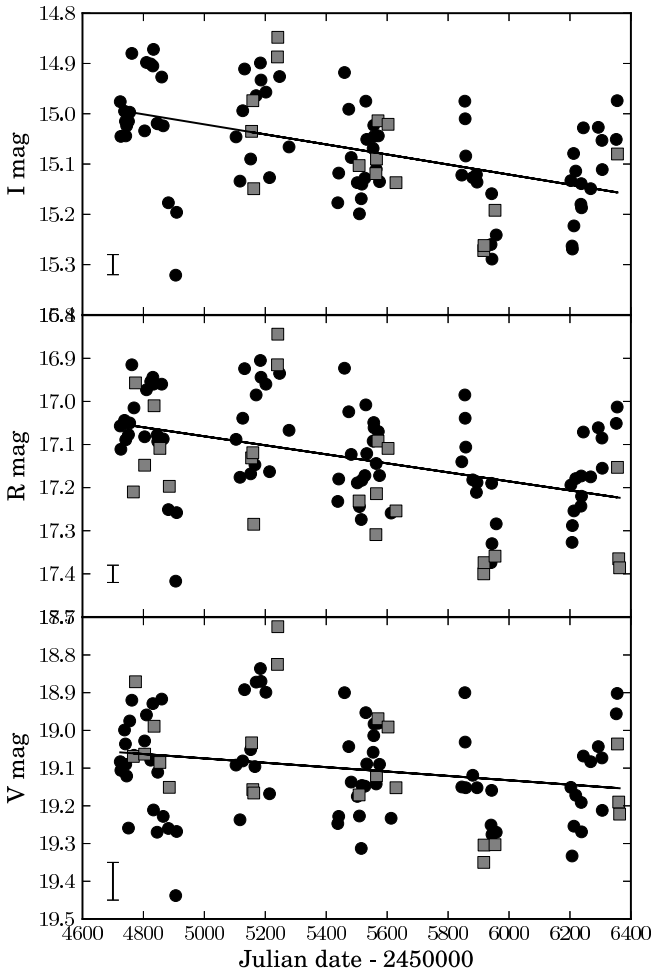

FIGURE 4.2: Magnitude variation of V1647 Ori in the *I*, *R*, and *V* band from 2008 September to 2013 March. Typical photometric error bar is given at the left bottom corner. The filled circles are from HCT, and filled squares are from IGO measurements. The rate of dimming in *I*, *R*, and *V* bands is 0.036 ± 0.007 mag yr^{-1}, 0.038 ± 0.007 mag yr^{-1}, and 0.021 ± 0.009 mag yr^{-1}, respectively.

Our light curve of V1647 Ori does not show any 56 day periodicity, which was reported by Acosta-Pulido et al., (2007b) during the first 2003 outburst. Based on the correlated reddening of flux during the minima of light curve, they proposed that periodicity was due to occultation of a dense clump in the accretion disc at a distance of 0.25 AU from the star. The peak-to-peak amplitude in *I* band was ∼0.3 mag in 2003. We have not detected this variability in the 2008 outburst, which implies that the dense clump might have gotten dissipated between the 2003 and 2008 outburst events. Our Lomb-Scargle periodogram analysis of magnitudes did not show any other statistically significant periodicity.

The optical magnitudes during the second outburst are almost similar to that of the first outburst in 2003. In fact, the first known outburst of V1647 Ori in 1966 (∼38 yr prior to 2003), reported by Aspin et al., (2006), also had similar magnitude to the present one, however, all three outbursts

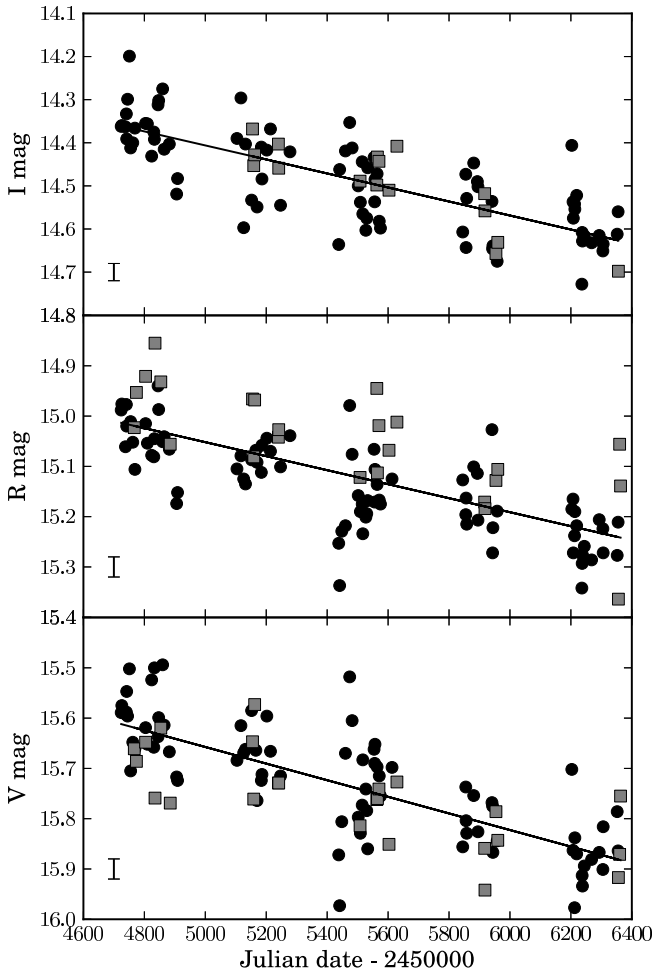

FIGURE 4.3: Magnitude variation of region C, illuminated by V1647 Ori, in the *I*, *R*, and *V* band from 2008 September to 2013 March. Typical photometric error bar is given at the left bottom corner. The filled circles are from HCT, and filled squares are from IGO measurements. The rate of dimming in *I*, *R*, and *V* bands is 0.059 ± 0.005 mag yr^{-1}, 0.051 ± 0.005 mag yr^{-1}, and 0.060 ± 0.005 mag yr^{-1}, respectively.

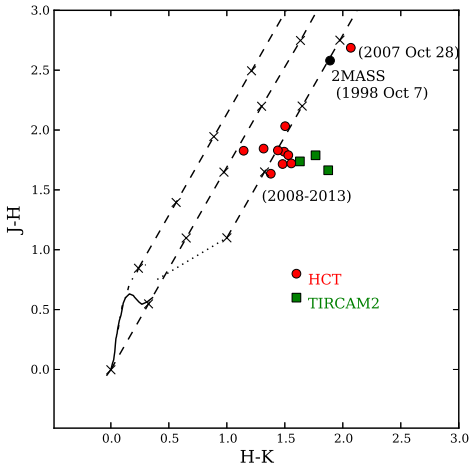

FIGURE 4.4: Movement of the position of V1647 Ori in the $J-H/H-K$ CC diagram from the quiescent phase in 2007 to the second outburst phase. The solid curve shows the locus of field dwarfs, and the dashed-dotted curve shows the locus of giants (Bessell and Brett, 1988). The dotted line represents the locus of CTT stars (Meyer, Calvet, and Hillenbrand, 1997). The diagonal straight dashed lines show the reddening vectors (Rieke and Lebofsky, 1985), with crosses denoting an A_V difference of 5 mag.

have different timescales. Implications of this fact on outburst model will be discussed in Chapter 5.

Our NIR *J*, *H*, and *K* magnitudes are listed in Table 4.2. Similar to the optical light curve, there is a faint dimming trend in NIR also. Venkata Raman et al., (2013), with more NIR data points, estimated the fading rate in *J* band to be 0.08 $\pm$0.02 mag yr^{-1}. The $J-H/H-K$ color-color (CC) diagram (Figure 4.4) shows the movement of V1647 Ori from the 2007 data point taken in quiescent phase to outburst state. It is similar to what was seen in the 2003 outburst. From the quiescent phase position in the CC diagram, V1647 Ori has moved towards the classical T Tauri (CTT) locus along the reddening vector and currently occupies the same position as in the 2003 outburst. The position of V1647 Ori in the CC diagram is consistent with a similar CC diagram published by Venkata Raman et al., (2013). This implies that the decrease in line of sight extinction during the outburst is the same as that seen during the 2003 outburst. Since our line-of-sight is through the envelope, it must be likely due to a reversible mechanism like dust sublimation in the inner region of the envelope during each outburst (Acosta-Pulido et al., 2007b; Mosoni et al., 2013; Aspin et al., 2009). Since the star is deeply embedded, we have reflections and dust emission effects also affecting the position of V1647 Ori in the CC diagram. So the extinction estimated from the CC diagram is not very reliable. Otherwise, we can see that the second outburst has cleared out circumstellar matter of $\delta A_V \sim 6 \pm 2$ mag. This is also consistent with the estimate of extinction change during first outburst by Mosoni et al., (2013), $\delta A_V \sim 4.5$ mag (see also Aspin, Beck, and Reipurth, (2008)).

TABLE 4.2: NIR J H K photometry of V1647 Ori

Date (UT)	J	H	K	Instrument
28-Oct-07	14.12	11.43	9.36	NIRCAM
19-Oct-08	10.64	9.01	7.63	NIRCAM
12-Jan-09	10.59	8.76	7.62	NIRCAM
12-Feb-09	11.04	9.01	7.51	NIRCAM
18-Feb-09	10.87	9.16	7.68	NIRCAM
23-Oct-09	10.71	8.89	7.40	NIRCAM
24-Oct-09	10.71	8.88	7.44	NIRCAM
20-Feb-10	10.75	8.96	7.43	NIRCAM
23-Mar-10	10.73	9.14		NIRCAM
18-Nov-11	10.75	8.90	7.58	NIRCAM
03-Dec-11	10.94	9.28	7.41	TIRCAM2
04-Dec-11	10.97	9.19	7.42	TIRCAM2
06-Dec-11	10.84	9.10	7.47	TIRCAM2
07-Nov-12	10.73	9.01	7.46	NIRCAM

Note: Estimated error in magnitude is $\leq \pm 0.1$ (K) and $\leq \pm 0.05$ (H and J).

4.2 Morphological Results

Between the 2003 and 2008 outbursts, McNeil's nebula does not have any significant morphological changes; however, the intensity distribution of the nebula has changed between the outbursts. Figure 4.5 shows the difference in R band flux along the nebula between 2011 and 2004. Images of similar atmospheric conditions were taken and scaled to match the brightness of V1647 Ori before subtracting the 2004 image from that of 2011. Brighter shade implies that the region is brighter in 2011 than 2004. We can see that region C is brighter in the second outburst than it was in 2004. This could be due to dust clearing up between the last two outbursts along the cavity seen in NIR in the region C direction (Ojha et al., 2005). Our photometric results show that region C is dimming faster than V1647 Ori, and one of the explanations for that could be material inflow into the cavity during the outburst. However, region C is relatively brighter in the 2008 outburst than in 2004 for the same brightness of V1647 Ori. This implies that the matter inflow to the cavity was not occurring during the quiescent phase between 2006 and 2008. This is also based on the implicit assumption that the extinction along the line-of-sight direction to V1647 Ori is the same between the 2003 and 2008 outbursts. The other significant change is in illumination of the south western knot (region B) of the nebula; its illumination seems to have shifted slightly towards the west. These illumination changes in the nebula imply a structural change in the circumstellar matter above the disc and cavity. A similar pattern and conclusion were also reported between the 1966, 2003, and 2008 outbursts by Aspin et al., (2006) and Aspin et al., (2009). Similar analysis of image pairs taken between 2008 and 2012 did not show any significant morphological changes. Our image pairs had a seeing of 1.6″. Hence, to check whether any change in illumination of nebula is occurring during the present outburst, we need images with seeing less than 1.6″.

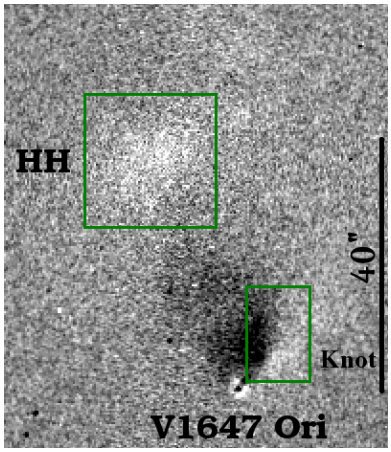

FIGURE 4.5: HCT *R* band image of 2011 minus 2004, after normalising with respect to the brightness of V1647 Ori. The images were chosen from the nights with the same atmospheric seeing and aligned using other field stars in the FOV. The bright portions show the regions that were relatively brighter in 2011, and dark portions show the regions that were relatively brighter in 2004. For example, region C shown in the upper box is brighter in 2011. Also note the change in illumination of south western knot region B marked by the lower box in the nebula. North is up and east is to the left-hand side.

4.3 Spectroscopic Results

V1647 Ori optical spectra show strong Hα (6563 $\AA$) emission and a Ca II IR triplet at 8498, 8542, and 8662 $\AA$ in emission. Other weak lines seen are Na D (5890+5896 $\AA$) and O I (7773 $\AA$) in absorption, and [O I] (6300 $\AA$), O I (8446 $\AA$), [Fe II] (7155 $\AA$) and Fe I (8388, 8514 $\AA$) in emission (see Figure 4.6). The equivalent widths of Hα, Ca II IR triplet lines, and O I (7773 $\AA$) are listed in Table 4.3.

4.3.1 Hα line

The strong Hα line in V1647 Ori shows a clear P Cygni profile, as well as substantial variations. Figure 4.7 shows the variations of Hα profiles during our four and a half years of observations. P Cygni profiles were more prominent in the early part of the outburst in 2008. To see the absorption component clearly, a Gaussian is fitted to the right wing of the profile in red color and the difference of the fit to actual spectra is plotted in green color. Figure 4.8 shows the outflow velocity and associated error bar of expanding wind from the blue-shifted absorption minima in the Hα profile. These blue-shifted absorption components were present in the 2003 outburst also and disappeared during the fading stage of the outburst (Ojha et al., 2006; Fedele et al., 2007). Figure 4.9 shows the variation in equivalent width (W_λ in $\AA$) of Hα emission. The calculation of W_λ was very sensitive to the weak continuum flux around λ6563 $\AA$, and the error estimate for each data point is $\sim \pm 3$ $\AA$. The W_λ of the 2008 outburst is in a similar range as that during the first outburst in 2003. Since Hα emission comes from the innermost

TABLE 4.3: Equivalent widths (in Å) of optical lines in V1647 Ori

JD	Hα	Ca II λ8498	Ca II λ8542	Ca II λ8662	OI λ7773
2454724	-36.35	-8.601	-8.758	-8.125	2.483
2454725	-35.1	-8.686	-9.1	-7.678	1.754
2454743	-36.52	-12.97	-13.35	-12.19	1.491
2454744	-28.62	-10.75	-10.86	-10.12	2.407
2454755	-32.84	-7.61	-7.621	-7.819	1.839

†† Observed from IGO, all other nights are from HCT.

Note: Estimated error in equivalent widths of Hα lines is $\sim \pm 3$ Å, error for Ca II IR triplet lines is $\sim \pm 0.5$ Åand the error for O I λ7773 lines is $\sim \pm 0.3$ Å.

Note: This table is published in its entirety in the electronic edition of Ninan et al., (2013b). A portion is shown here for guidance regarding its form and content.

accretion-powered hot zone, we can expect its strength to be proportional to the accretion rate. The optical photometric magnitude in the second outburst is similar to that of the first outburst, which implies that the continuum flux is almost of the same value. Hence, from the fact that W_λ is of similar value as in the first outburst, we can deduce that the accretion rate is also of the same order in both outbursts during its "high plateau"stage.

4.3.2 Ca II IR triplet lines

The plots of equivalent widths of Ca II IR triplet lines (8498, 8542, and 8662 $\mathring{A}$) are shown in Figure 4.10. We have much smaller error bars ($\pm 0.5\mathring{A}$) for the W_λ due to the higher continuum flux in these wavelengths. The Ca II IR triplet emission lines are seen to be in the ratio 1.07 ± 0.09:1.15 ± 0.1:1. This nearly equal ratio is due to optically thick gas with the collision decay rates larger than the effective radiative decay rates of upper states of Ca II lines. Such an environment is typically seen in many T Tauri stars. Optical thickness along with the non-detection of forbidden [Ca II] lines above noise, implies a number density of electrons of $\approx 10^{11}$ cm^{-3} (Hamann and Persson, 1992). For comparison with Figure 8 of Hamann and Persson, (1992), Figure 4.11 shows the scatter plot between the ratios of equivalent widths, $W_{\lambda 8498}/W_{\lambda 8542}$ and $W_{\lambda 8662}/W_{\lambda 8542}$, of our data, as well as previously published data from literature. The error bar in our new data (black squares) is ± 0.1. From the position of the 2007 data point (red diamond) taken during quiescent phase (Aspin, Beck, and Reipurth, 2008) in this scatter plot, Aspin, Beck, and Reipurth, (2008) and Aspin et al., (2009) had concluded that the optical density of the region emitting Ca II IR triplet lines changed significantly between outburst and quiescent phases. But since there is only one data point from quiescent phase and it is lying within the scatter of points from the ongoing outburst, it might be difficult to conclude that the change in ratios observed was actually due to V1647 Ori moving from quiescent phase to outburst phase. We could see a strong correlation between

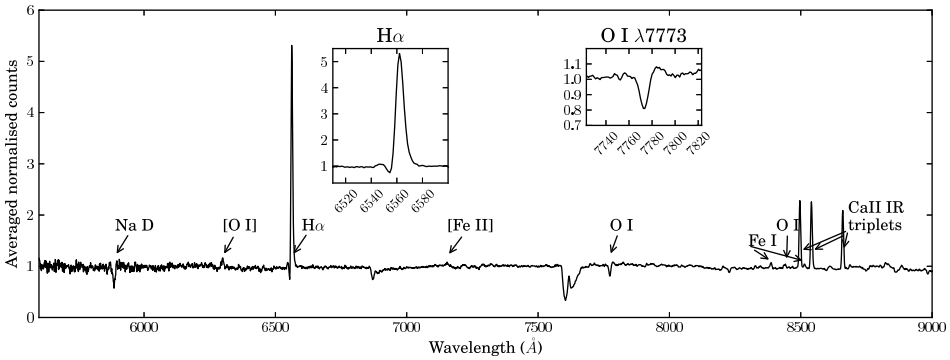

FIGURE 4.6: Spectral lines present in the spectrum of V1647 Ori are labeled above. To improve the signal-to-noise ratio, the normalised spectrum was obtained by weighted averaging of 33 HCT spectra taken over the outburst period 2008 September to 2013 March, each with an average exposure time of 40 minutes. The spectra are not corrected for atmospheric absorption lines. The absorption lines that are not labeled are atmospheric lines. Hα and O I λ7773 line profiles are shown more clearly in insets.

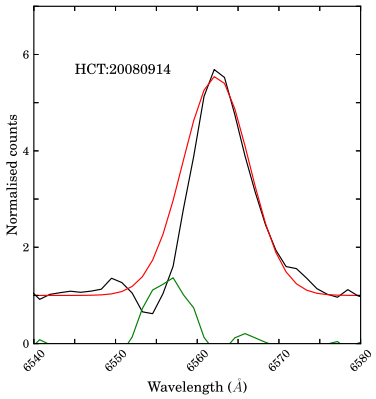

FIGURE 4.7: Variations of Hα profiles during our four-and-a-half-year observations. P Cygni profiles were more prominent in the early part of the outburst in 2008. A Gaussian is fitted to the right wing of the profile in red color, and the difference of that Gaussian fit to actual spectra is plotted in green color to see the absorption component clearly. Figure 4.7 with 70 other plots of remaining nights are available in the electronic edition of Ninan et al., (2013b).

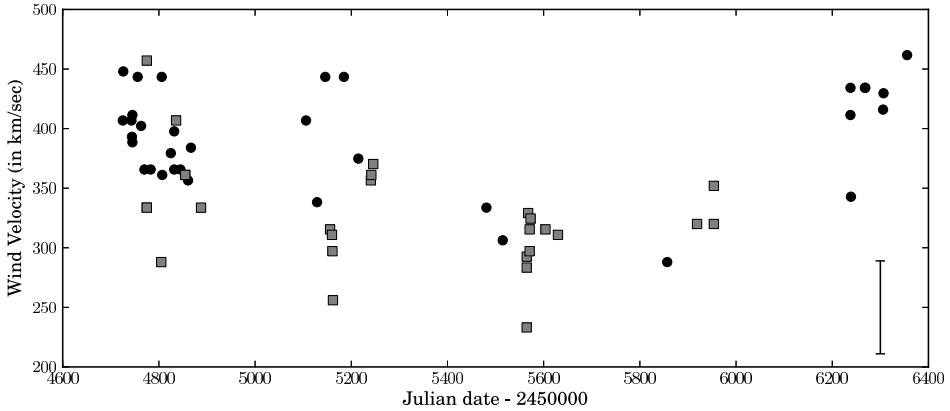

FIGURE 4.8: Velocity of expanding wind from the blue shifted absorption minima in the Hα P Cygni profile. The filled circles are from HCT, and gray filled squares are from IGO measurements. The error bar on the bottom right corner shows the typical ± 39 kms^{-1} error estimated for data points.

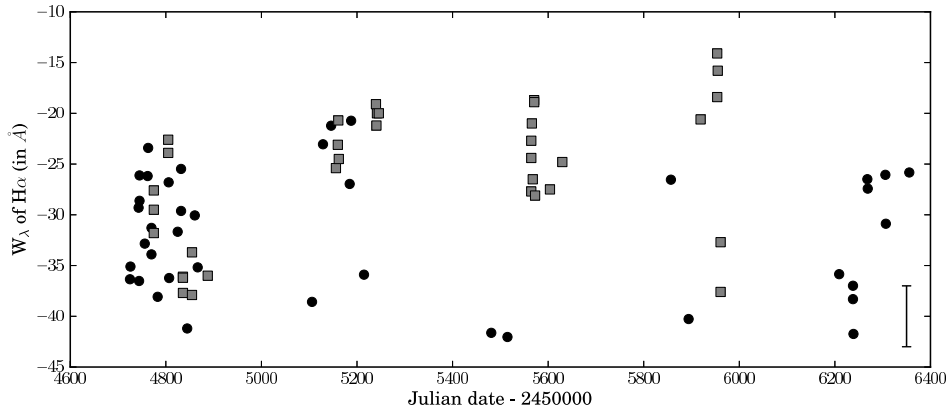

FIGURE 4.9: Variation in the equivalent width of Hα emission. The filled circles are from HCT, and filled gray squares are from IGO measurements. Each data point has an error bar of $\sim \pm 3\AA$. This error bar is shown at the right bottom corner.

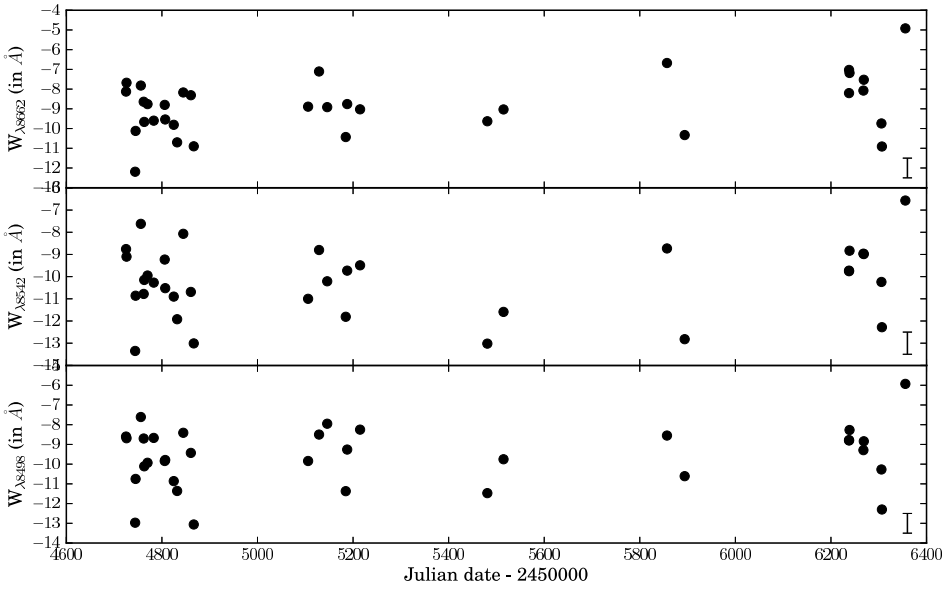

FIGURE 4.10: Variation in equivalent widths of Ca II IR triplet lines (8498, 8542, and 8662 $\AA$) during the outburst period 2008 September to 2013 March. All data points are from HCT measurement, and each point has an error bar of $\sim \pm 0.5\AA$. This error bar is shown at the right bottom corner. Due to limited spectral range in the IGO grism, Ca II triplet lines were not observed from IGO.

the equivalent widths (W_λ) of Ca II IR triplet lines (see Figure 4.12). The Pearson correlation coefficient (PCC) between both $W_{\lambda 8662}$ and $W_{\lambda 8498}$, and $W_{\lambda 8542}$ and $W_{\lambda 8498}$ is 0.88 with a two-tailed p value $\ll 0.0001$. This implies that the fluctuations in W_λ are not random statistical error. It could be due to fluctuations of continuum flux around $\lambda 8500\AA$. Peak-to-peak fluctuation of W_λ is $\sim 5\AA$, which means that if the flux from these lines is assumed to be constant, then the continuum flux has fluctuated by a factor of ~ 1.6, which in terms of the log scale of magnitude is ~ 0.5. This indeed matches with peak-to-peak fluctuation in *I* band magnitude during the entire period. We do not see any strong correlation between W_λ of the Hα line and Ca II IR triplets. However, it should be noted that the error bars in W_λ of Hα are much higher than those of Ca II IR lines due to low continuum flux around $\lambda 6563\AA$.

In the 2008 October 29 spectrum, we could clearly detect the P Cygni profile in Ca II IR triplet lines (Figure 4.13). The strengths of the absorption trough of the three lines were in the same pattern as that of T Tauri star WL 22 (Hamann and Persson, 1992), i.e., the pattern with strongest absorption in $\lambda 8542\AA$, then $\lambda 8662\AA$ and very weak in $\lambda 8498\AA$. The ratio of W_λ of the blue-shifted absorption between $\lambda 8542\AA$ and $\lambda 8662\AA$ is 0.76:0.45 = 1.69:1. This ratio is consistent within error bars with the 1.8:1 ratio of intensity from atomic transition strength of these lines. Hence, unlike the region producing emission lines, these absorption regions are optically thin. So by using the optically thin assumption, we can estimate the column density of Ca II by the formula (Spitzer, 1978):

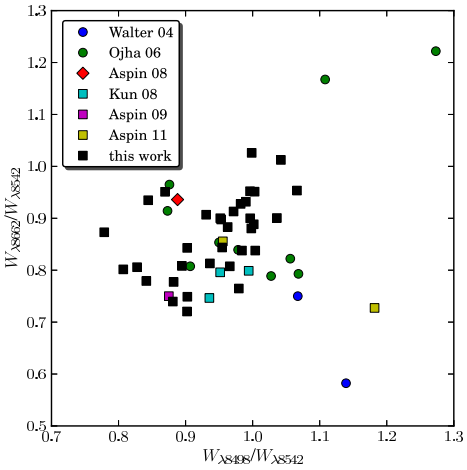

FIGURE 4.11: Ratio of Ca II IR triplet lines' equivalent widths, $W_{\lambda8498}/W_{\lambda8542}$ vs. $W_{\lambda8662}/W_{\lambda8542}$, of our data, as well as previously published data from the literature. 2003 outburst points are shown as circles (Walter et al., 2004; Ojha et al., 2006), 2008 outburst points are shown as squares (Kun, 2008; Aspin et al., 2009; Aspin, 2011b, and This work), and the 2007 quiescent phase point is shown as a diamond (Aspin, Beck, and Reipurth, 2008). The typical error bar on our new data (black squares) is $\sim \pm 0.1$.

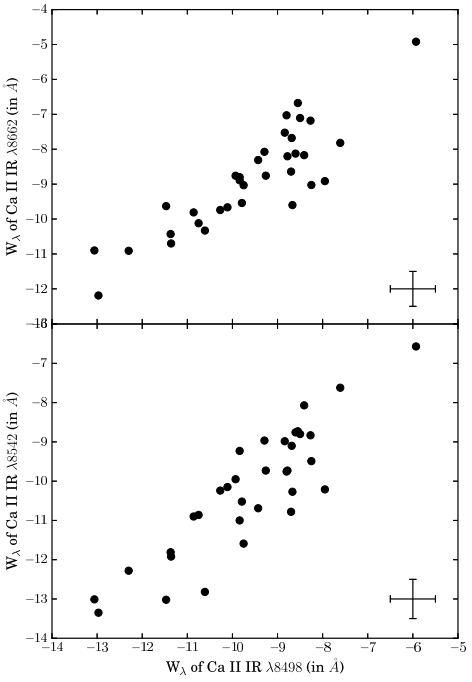

FIGURE 4.12: Strong correlation between the equivalent widths of Ca II IR triplet lines. Typical error bar is given at the right bottom corner. The Pearson correlation coefficient (PCC) between both $W_{\lambda8662}$ and $W_{\lambda8498}$, and $W_{\lambda8542}$ and $W_{\lambda8498}$ is 0.88 with a two-tailed p value $\ll 0.0001$.

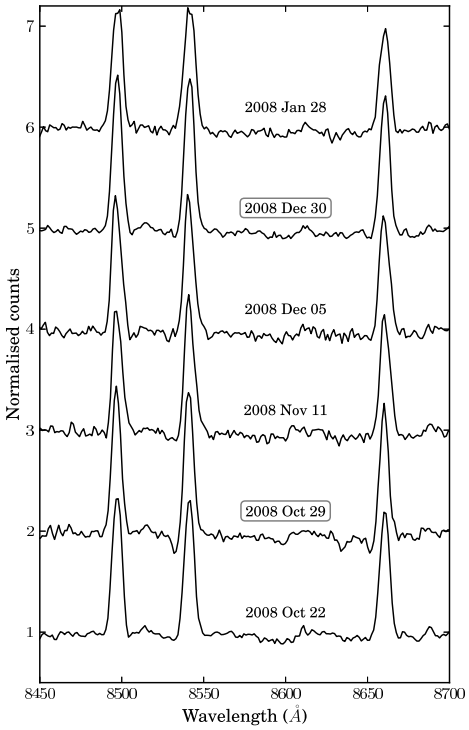

FIGURE 4.13: Spectrum of V1647 Ori taken on 2008 October 29 showing a clear P Cygni profile in Ca II IR triplet lines. A similar but fainter profile was once more detected in 2008 December 30. None of the other nights' spectra showed this profile. For comparison, available nearby nights' spectra are also plotted.

$$N_{CaII} = 1.1 \times 10^{20} \times \frac{\mathring{A}}{\lambda}^2 \frac{1}{f_{lu}} \frac{W_\lambda}{\mathring{A}} \text{ cm}^{-2} ,$$

where the oscillator strength f_{lu} for the lines 8542 and 8662 $\mathring{A}$ are 0.39355 and 0.21478 respectively, taken from Merle et al., (2011). Substituting the W_λ, wavelength and oscillator strength for both lines, we get the column density (N_{CaII}) as 2.9×10^{12} cm^{-2} and 3×10^{12} cm^{-2}, respectively. This is the column density of Ca II atoms in this small duration of outflow wind. Assuming reasonable estimates of temperature T = 2600K (disc temperature estimated by Rettig et al., (2005)) and pressure P = 1 Pascal (typical pressure in solar winds), the fraction of ionisation using Saha's formula is ≈ 0.004. Hence, dividing by this fraction, we obtain the column density of Ca atoms in the gas blob to be $\approx 7.5 \times 10^{14}$ cm^{-2}. Assuming solar metallicity, we obtained the column density of hydrogen (H) in the outflowing gas blob as $\approx 3.4 \times 10^{20}$ cm^{-2}. From the Doppler shift of the absorption minima, we also obtained a wind velocity of 313 ± 10 km s^{-1} (in the $\lambda 8542 \mathring{A}$ line) and 303 ± 10 km s^{-1} (in the $\lambda 8662 \mathring{A}$ line). We also detected a faint P Cygni profile in the $\lambda 8542 \mathring{A}$ line on 2008 December 30, with a blue shifted velocity of 329 ± 10 km s^{-1}. Apart from these two episodic events, none of our other spectra show any detectable P Cygni profile. The episodic nature of these two winds implies they are magnetic reconnection driven winds rather than pressure driven steady winds.

Even though our medium-resolution spectra cannot be used to study

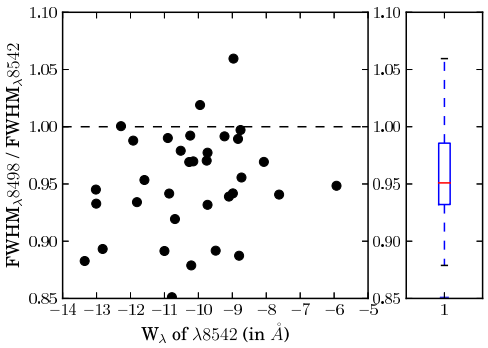

FIGURE 4.14: Scatter plot of the ratio of the widths of 8498 and 8542 $\AA$ vs. equivalent width of the line $8542\AA$. Most of the points lie below 1.0 in Y-axis. Box and whisker plot of the distribution is also plotted on the right side. This shows that the $8498\AA$ line is slightly narrower than the $8542\AA$ line.

line widths, since the Ca II IR triplets are near by, we could do relative comparison of the widths of the Ca II IR triplet lines, where width is taken to be the FWHM of the Gaussian fit of the continuum normalised profile. Since this quantity is the FWHM of the Gaussian profile that we get after the convolution of instrument response on the actual line, it is not the FWHM of the line. However, since the lines are very close and the instrumental convolution is common, the wider line will give a wider FWHM after convolution. Figure 4.14 shows a scatter plot of the ratio of the widths of $\lambda8498$ $\AA$ and $\lambda8542$ $\AA$ versus the equivalent width of the line $\lambda8542$ $\AA$. Most of the points lie below 1.0 in the ratio axis. Using the 'test statistic' for mean with 34 data points, we could reject null hypothesis *H_o: The mean of the ratio is 1*, with 6σ confidence. This shows that the $\lambda8498\AA$ line is slightly narrower than the $\lambda8542\AA$ line. A similar trend is seen in most of the T Tauri stars (Hamann and Persson, 1992). Apart from showing this skewness, since our spectra are of only medium resolution, we cannot quantify the narrowness of the line. This narrowness of the optically thinner line $\lambda8498\AA$ could be explained by either substantial opacity broadening in $\lambda8542\AA$ (since 1:9 is the ratio of atomic line strength) or lower dispersion velocity in the inner part of the region of Ca II IR emission (Hamann and Persson, 1992).

Our period search in the equivalent width (W_λ) of Ca II IR triplet lines found six faint periodicities in all three lines in the range of 1–100 days with $\sim 2\sigma$ confidence level in amplitude. The possible periodicities and confidence were estimated by the Lomb-Scargle periodogram along with Monte Carlo simulation. The possible periods are 3.39, 8.09, 27.94, 30.8, 40.77, and 45.81 days. Since the amplitudes are only of 2σ confidence level, they can be confirmed only with more observations. Figure set 4.15 shows the folded data of the entire four-and-a-half-year observations and the statistical significance of the amplitudes. The amplitude of the least-squares fitted cosine function is ~ 1. If this periodicity is due to change in the continuum flux, the corresponding amplitude of magnitude change we expect in logarithmatic I band magnitude is ~ 0.1. This is not much above our error in magnitude estimate, so the fact that we do not see similar periodicity in I band magnitude does not rule out the cause of change in W_λ as change in continuum flux. We also do not see any corresponding significant periodicity in

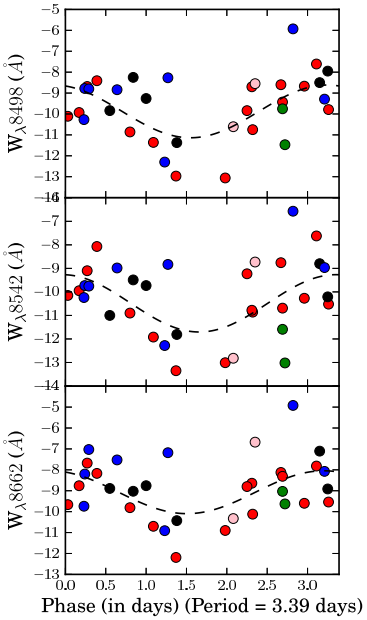

FIGURE 4.15: Folded phase plot of the W_λ of Ca II IR triplet lines λ8498, λ8542, and λ8662 (in $\AA$), and *I* band magnitude. The folding is done over the entire four and a half years of data. The red, black, green, pink, and blue circles correspond to data of 2008, 2009, 2010, 2011, and 2012 winter observations, respectively. The amplitudes (in $\AA$) of the three lines in each folded plot are as follows. For a period of 3.39 days:- 1.26 $\pm$ 0.69, 1.22 $\pm$ 0.75, 1.03 $\pm$ 0.67; for a period of 8.09 days:- 1.13 $\pm$ 0.70, 1.33 $\pm$ 0.71, 1.17 $\pm$ 0.65; for a period of 27.94 days:- 1.13 $\pm$ 0.72, 1.11 $\pm$ 0.79, 1.14 $\pm$ 0.67; for a period of 30.8 days:- 1.26 $\pm$ 0.61, 1.25 $\pm$ 0.63, 0.98 $\pm$ 0.58; for a period of 40.77 days:- 1.26 $\pm$ 0.65, 1.42 $\pm$ 0.58, 1.18 $\pm$ 0.59; for a period of 45.81 days:- 0.95 $\pm$ 0.76, 1.29 $\pm$ 0.74, 1.10 $\pm$ 0.68. *Figures 4.15.2 - 4.15.6 are available in the electronic edition of Ninan et al., (2013b).*

W_λ of Hα.

Aspin, Beck, and Reipurth, (2008) took the spectrum of V1647 Ori during the quiescent phase in 2007 February. The W_λ of both Ca II IR triplet lines and Hα were $\sim$ 3.3 times the present value. Aspin and Reipurth, (2009) had used the ratio of W_λ of Hα between the 2003 outburst and quiescent phase to estimate change in accretion rate. Similarly, since the continuum flux changed by a factor of $\sim$ 40 between the quiescent and 2008 outburst phase, we can estimate that the change in the line flux of both sets of lines is by a factor of $\sim$ 10. This agrees with the change in accretion rate. Thus, the origin of Ca II IR triplet lines is directly connected to the accretion rate just like Hα. This is in agreement with the finding of tight correlation between Ca II IR line flux and accretion rate in T Tauri stars by Muzerolle, Hartmann, and Calvet, (1998), which suggests that the origin of these lines is in the magnetospheric infall zone. The similar value of W_λ of Ca II IR lines with that of 2003 also strengthens the claim that the accretion rate on to the star from the inner disc was the same during both outbursts.

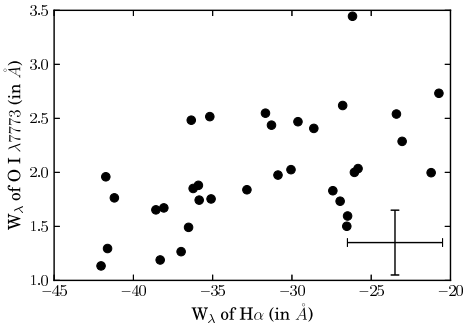

FIGURE 4.16: Correlation between equivalent width of Hα and O I $\lambda 7773 \AA$. Typical error bar is given at the right bottom corner. PCC is 0.54 with a two-tailed p value of 0.001. The weak anti-correlation could be due to a positive correlation between the Hα and red shifted emission component that is filling the absorption component in the O I $\lambda 7773 \AA$ profile. Bootstrap analysis gave a 95% confidence range of PCC of [0.29, 0.72].

4.3.3 Oxygen lines

The most prominent oxygen line is O I 7773 $\AA$ in absorption; however, weak O I 8446 $\AA$ line is also detected in emission. We should be careful in interpreting the W_λ of the O I $\lambda 7773$ $\AA$ absorption line because the profile shape of the line seems to be a combination of the red shifted emission component and more stronger blue shifted absorption component (see Figure 4.6). A weak anti-correlation is seen between Hα and O I $\lambda 7773 \AA$ (see Figure 4.16). Correlation had PCC = 0.54, with a two tailed p value of 0.001. This anti-correlation in W_λ of O I 7773 $\AA$ and Hα could be due to positive correlation between emission component of O I $\lambda 7773 \AA$ filling in the absorption dip and Hα. Since O I $\lambda 7773 \AA$ cannot be formed in the photosphere of cool stars, the absorption component is due to warm gas in the envelope or hot photosphere above the disc, while the emission component might be due to the hot gas region from which Hα is also being emitted. Ojha et al., (2006) reported a decreasing trend in the W_λ of O I $\lambda 7773 \AA$ from the beginning until the end of the 2003 outburst, which was interpreted to be a possible decrease in turbulence in the outer envelope during the outburst period. We do not see such a trend in the 2008 outburst, but the values of W_λ in the 2008 outburst remain the same as that during the second half of the 2003 outburst. A slight decrease of W_λ in the later part of the 2003 outburst observed on 2005 September 8, as reported by Ojha et al., (2006), in contrast to the increase of W_λ of other lines, could be due to an increase in the W_λ of the O I $\lambda 7773 \AA$ emission component.

4.3.4 Forbidden lines

We detected [O I] (6300$\AA$) and [Fe II] (7155$\AA$) forbidden line emissions in V1647 Ori's spectra. The presence of [O I] $\lambda 6300 \AA$ and [Fe II] $\lambda 7155 \AA$ implies shock regions probably originating from jets. This combined with non-detection of the [S II] (6731$\AA$) line above our noise level, implies that

the shock region has temperature $T \approx 9000 - 11000$K and electron number density $\approx 10^5 - 10^6$ cm^{-3} (Hamann, 1994). We see significant variations in the strengths of the forbidden lines [O I] and [Fe II]; however, the lines are too faint in our individual spectra to quantify statistically. During the fading stage of the 2003 outburst in 2006 January, when the bright continuum flux decreased, Fedele et al., (2007) were also able to detect various strong forbidden line emissions, namely [O I] $\lambda\lambda 6300\mathring{A}, 6363\mathring{A}$, [S II] $\lambda\lambda 6717\mathring{A}, 6731\mathring{A}$ and [Fe II] $\lambda 7172\mathring{A}$.

4.4 Summary

In this chapter, we have presented the results from our four and a half years of continuous monitoring of V1647 Ori in its second outburst phase starting from 2008. Following are the key results of this chapter.

1. V1647 Ori is still in outburst "plateau" stage, at similar magnitude to the 2003 outburst in optical and NIR bands. It is undergoing a slow dimming at a rate of 0.04 mag yr^{-1}, which is six times slower than the rate during the 2003 outburst. The magnitude shows significant short-timescale ($\sim$1 day) variations.

2. Morphological studies on illumination of the nebula show a consistent change in the circumstellar gas distribution between 2008, 2003, and 1966 outbursts.

3. P Cygni profiles in Hα emission lines show outflowing wind velocities of $\sim$350 km s^{-1}. Apart from the continuous wind we also detected short-duration episodic winds driven by magnetic reconnection events twice, with H column density $\approx 3.4 \times 10^{20}$ cm^{-2} from P Cygni profiles in Ca II IR triplet lines in 2008 October and December. From Ca II IR triplet and Hα line strengths, the accretion rate was found to be the same as that during the 2003 outburst and is $\sim$10 times more than the quiescent phase.

4. We could not detect the 56 day periodicity seen in the 2003 outburst.

5. Detection of the forbidden [O I] $\lambda 6300$ and [Fe II] $\lambda 7155$ lines implies shock regions of $T \approx 9000-11000$K and $n_e \approx 10^5-10^6$ cm^{-3}, probably originating from jets.

Chapter 5

Constraints on Outburst Mechanisms

In this chapter I outline the implications and constraints we obtain on the physical mechanism behind the outburst phenomenon. By analysing the time scales, as well as the evolution in spectral lines at various phases of V1647 Ori and V899 Mon, we could rule out certain theoretical models and propose possible scenarios. The results presented in this chapter are published in Ninan et al., (2013b) and Ninan et al., (2015).

5.1 Theoretical models

Theoretical models that are available in the literature for explaining FUor/EXor outbursts can be broadly classified into three types. The first kind of model is purely a thermal instability model, initially proposed for dwarf nova systems and was later adapted for the FUors kind of outbursts (Bell and Lin, 1994). The second kind of model involves a binary companion or planet, which perturbs the disc, causing repeated sudden high-accretion events (Bonnell and Bastien, 1992; Lodato and Clarke, 2004). The third kind involves mainly gravitational instability (GI) triggering magnetorotational instability (MRI) (Zhu et al., 2009, and references therein). The Bell and Lin, (1994) model (hereafter BL94) is a purely thermal instability model. The cyclic behaviour in all the instability models (thermal instability or MRI) can be explained by the equilibrium S curve in the disc surface density versus temperature plane (see Figure 5.1).

In BL94, the thermal instability (or MRI in MRI based models) is triggered when the surface density at a region in the disc rises above a critical density (corresponding to a critical temperature). The critical temperature in the thermal instability model is the temperature at which hydrogen ionises. As hydrogen ionises, the sudden increase in opacity due to free electrons will reduce the radiation escaping from the disc, pushing the equilibrium temperature to very high values. This is represented by the up arrow (A $\rightarrow$ B) in the Figure 5.1. In case of MRI models, the critical temperature is the temperature at which MRI instability kicks in. This is typically taken to be the temperature of dust sublimation in Zhu et al., (2009). Due to the high effective viscosity, as a result of the eddies in instability, the disc will drain faster and it will go back to the quiescent phase when the surface density drops below another critical density (C $\rightarrow$ D in Figure 5.1).

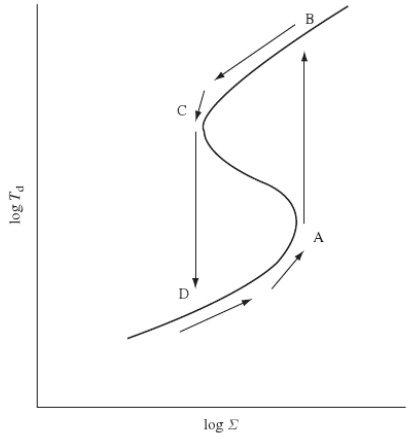

FIGURE 5.1: The equilibrium S curve in the disc surface density (Σ) versus temperature (T_d) plane of an accretion disc obtained by balancing the energy released in the disc with the energy radiated out.

5.2 Time scales of an outburst

The viscous time scales determine duration of outbursts (B $\rightarrow$ C) and quiescent phase (D $\rightarrow$ A). The inner region at a radius r during outburst will deplete below the critical surface density in viscous time scale $\tau_{\rm visc} = r^2/\nu$. Based on α prescription of viscosity, $\nu = \alpha c_s H$, where c_s is the isothermal sound speed, $H \approx c_s/\Omega$ is the disc thickness, Ω is orbital angular velocity at radius r, and α (< 1) is a dimensionless parameter (see Figure 5.2). Substituting, we get the relation :
$\tau_{\rm visc} = \frac{r^2\Omega}{\alpha c_s^2} = \frac{1}{\alpha\Omega}(\frac{r}{H})^2$.

5.2.1 Case study with V1647 Ori

Let $v_R \approx r/\tau_{\rm visc} \approx \nu/r$ be the effective inward radial velocity component of gas in the inner accretion disc. Then the mass infall rate at radius R is $\dot{M} = -2\pi R\Sigma v_R$, where Σ is the surface density of the disc at that radius. Substituting v_R, ν, and H in the above equation of $\dot{M}$, we get
$\dot{M} \approx 2\pi\Sigma\alpha c_s^2/\Omega$.
The timescale of transition between outburst and quiescent phases is much smaller than the viscous timescale. Hence, Σ will remain constant, and Ω will also remain constant at a given R, which leaves only the term αc_s^2 to explain the change by a factor of $\sim$10 in inner disc accretion rate to V1647 Ori between the outburst and quiescent phases. Since the square of isothermal speed of sound $c_s^2 = R_g T/\mu$ (where R_g is the gas constant, T is temperature, and μ is mean molecular weight), the temperature change by a factor of 10 between the phases at the trigger of thermal instability (Zhu et al., (2009), Appendix B, their Figure 14) alone will cause a net change in accretion rate by a factor of 10. Hence, at least in the inner region of the disc, α can change only by a multiplicative factor of order 1 to remain consistent with the observed change in accretion rate.

In BL94, assuming the mass infall rate to the inner disc region $\dot{M}_{\rm in}$ = constant, the α determines the timescales and the ratio $\alpha_{\rm outburst}/\alpha_{\rm quiescent}$ is

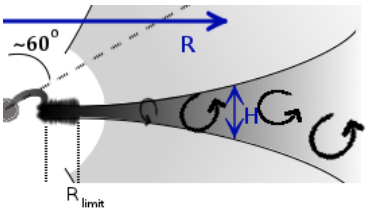

FIGURE 5.2: Cross section of an α disc. R is the radial distance from the star, and H is the thickness of the disc, which flares up as the radius R increases. $R_{\rm limit}$ is the radius up to which the outburst extends. We are looking into the system at $\sim 60^\circ$ along the dashed line drawn in the figure. In the α disc model, the viscosity is due to large turbulent eddies. The speed of eddies is upper bounded by the velocity of sound (c_s) because any supersonic flow will get dissipated by shock. The size of eddies is also upper bounded by the thickness (H) of the disc. Thus, taking α to be a free parameter < 1, we get the viscosity in the disc as $\nu = \alpha c_s H$. The orbital velocity is taken to be Keplerian in our problem.

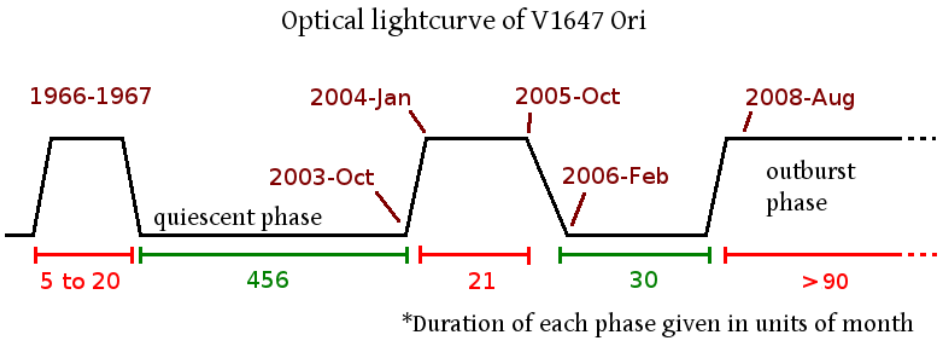

FIGURE 5.3: Optical light-curve history of V1647 Ori. The duration of each outburst and quiescent period is marked in units of months. The X-axis of the image is not drawn to scale.

proportional to the ratio of time in quiescent phase to time in outburst phase (BL94; Table 2). Figure 5.3 shows the schematic of the light curve of V1647 Ori in optical band that we know till now. The photometric magnitudes and overall SED during the quiescent phase in 2007 match with pre-2003 outburst data (Aspin, Beck, and Reipurth, 2008). The drop in accretion rate during quiescence with respect to the outburst phase was by a factor of 10[1].

Let α_{o1}, α_{o2}, and α_{o3} represent the three outburst phase α values and α_{q1} and α_{q2} represent the two quiescent phase α values. If we assume $\dot{M}_{\rm in}$= constant in BL94, from the ratio of periods, we get the following relations: $\alpha_{o1} = (22\text{–}89)k\alpha_{q1}$, $\alpha_{o2} = 21k\alpha_{q1}$, $\alpha_{o3} < 9k\alpha_{q1}$, and $\alpha_{o3} < 0.6k\alpha_{q2}$, where k

[1]Even though accretion rate had fallen by a factor of 10 during quiescent phase, it was still of the order of 10^{-6} $M_\odot {\rm yr}^{-1}$. Based on this, Aspin et al., (2009) had suggested that the 2003 outburst might not have actually terminated in 2006. Since we do not have a good estimate of the pre-outburst accretion rate, we shall consider this sudden drop in accretion rate by a factor of 10 as a drop from outburst state to quiescent phase in outburst models.

is just the proportionality constant corresponding to the constant $\dot{M}_{\rm in}$.
We also get $\alpha_{o2} = (0.23\text{–}0.95)\alpha_{o1}$, $\alpha_{o3} < 0.4\alpha_{o2}$, and $\alpha_{q2} = 15\alpha_{q1}$.
This is a very huge variation in α parameter. However, our accretion estimates, during the 2003 as well as 2008 outbursts, show that the accretion rate of matter onto the star from the inner disc was quite stable at $\sim$10 times the rate in quiescent phase. Thus, the α parameter should not be varying as much as we estimated; especially the relation $\alpha_{o3} < k0.6\alpha_{q2}$ is impossible from the fact that viscosity has to be more in outburst phase than quiescent phase. These unrealistic α values we obtained are what we should have expected from the following simple physical argument. Since the effective viscosity of the disk is lower during the quiescent phase than the outburst phase, the surface density increases more slowly during the quiescence than the rate at which it drained during the last outburst phase. When the first outburst stopped, if the disk density had drained below the critical density, then it has to spend more time in the subsequent quiescent phase to replenish the disk before undergoing a second outburst.

One way to save the instability model is to consider the possibility that the assumption $\dot{M}_{\rm in}$= constant in BL94 is not true. An increase in $\dot{M}_{\rm in}$ can decrease the draining rate of the inner disc and can account for a longer duration of the outburst period. It can also explain the six times slower rate of dimming in the magnitude of the V1647 Ori during its plateau stage in the present outburst compared to the 2003 outburst.

By letting $\dot{M}_{\rm in}$ be a variable and substituting $R_{\rm limit}$ to be the radius up to which instability extends, to constrain parameters, we compared the viscous timescale
$\tau_{\rm visc} = R^2_{\rm limit}/\nu \approx R^2_{\rm limit}\Omega/\alpha c_s^2$
between the 2003 and 2008 outbursts. The instability triggering temperature at the boundary has to be the same for both outbursts, so the speed of sound c_s will be the same. Parameter α can also be taken to be the same during both outbursts based on our previous conclusion. Now the only free variable parameter that determines the timescale is $R_{\rm limit}$. Substituting Keplerian $\Omega \propto R^{-\frac{3}{2}}$, we finally obtain the relation for the viscous timescale in terms of $R_{\rm limit}$ to be $\tau_{\rm visc} \propto R^{\frac{1}{2}}_{\rm limit}$.

BL94 gives the radius up to which instability extends to
$R_{\rm limit} = 20R_\odot(\frac{\dot{M}_{\rm in}}{3\times10^{-6}M_\odot yr^{-1}})^{\frac{1}{3}}(\frac{M_*}{M_\odot})^{\frac{1}{3}}(\frac{T_{\rm eff}}{2000})^{-\frac{4}{3}} \propto \dot{M}^{\frac{1}{3}}_{\rm in}$
Substituting this proportionality, we get $\tau_{\rm visc} \propto \dot{M}^{\frac{1}{6}}_{\rm in}$.
Thus, the ratios of mass infall rate from outer to inner disc during each outburst are related to the duration of outburst by the relation
$\frac{\dot{M}_{\rm in_{2008}}}{\dot{M}_{\rm in_{2003}}} > (\frac{90}{21})^6 \approx 6000.$
Thus, the infall of gas from outer to inner disc during the 2008 outburst is at least 6000 times (three orders) more than that during the 2003 outburst.

The model presented by Zhu, Hartmann, and Gammie, (2010) includes an MRI instability contribution to viscosity parameter if the temperature of the disc goes above the MRI triggering temperature (T_M) and also includes an effective viscosity contribution from GI beyond the radius given by Toomre's instability parameter Q. The relation between $R_{\rm limit}$ and $\dot{M}$ in this model is $R_{\rm limit} \propto \dot{M}^{\frac{2}{9}}$.
Thus, $\tau_{\rm visc} \propto \dot{M}^{\frac{1}{9}}_{\rm in}$, and hence $\frac{\dot{M}_{\rm in_{2008}}}{\dot{M}_{\rm in_{2003}}} > (\frac{90}{21})^9 \approx 480000.$

Therefore, the infall of gas from outer to inner disc during the 2008 outburst is at least 480000 times (five orders) more than that during the 2003 outburst. This estimate is two orders more than BL94. It should be kept in mind that the viscosity timescale gives only an order-of-magnitude estimate of the duration of outburst. For a comparison of actual simulated duration of outburst and viscous timescale see Table 1 in Zhu, Hartmann, and Gammie, (2010). If the present outburst continues for a larger period, $\frac{\dot{M}_{\rm in_{2008}}}{\dot{M}_{\rm in_{2003}}}$ will further increase.

Such a large order of magnitude change in the $\dot{M}_{\rm in}$ is impossible in a smooth viscous disc. The only way to explain the large ratio of $\dot{M}_{\rm in}$, is that there was a dip in mass inflow to near zero in 2003. The change in inflow of material from outer to inner disc could be due to many possibilities like MRI, GI, or planet perturbation[2]. For example, a gap in the disc could have resulted in the sudden ending of the 2003 outburst. This gap or low-density region has to be near the typical $R_{\rm limit}$ predicted by each model, i.e., $\sim$1 AU.

In our 2013 paper (Ninan et al., 2013b), we estimated the change in photometric magnitudes between 2003 and 2008 outburst phase due to predicted change in radius $R_{\rm limit}$, we modelled a disc with temperature profile given by outburst accretion rate inside $R_{\rm limit}$ and quiescent accretion rate outside $R_{\rm limit}$. The magnitude variations in optical I and NIR J bands were found to be less than 1 mag for variation of $R_{\rm limit}$ by a factor of six[3]. Mosoni et al., (2013) reported an increase in visibility of the resolved interferometric study of V1647 Ori using VLTI/MIDI observations in the 8–13 μm range during the early stage of fading in the 2003 outburst (between 2005 March and 2005 September). Apart from the possible scenarios discussed by Mosoni et al., (2013), it could also be explained by the relative increase in contribution in total flux from the extended outburst disc when the central star's accretion slowed down. A similar VLTI/MIDI visibility study of the ongoing 2008 outburst will give more input to constrain $R_{\rm limit}$ and outburst models.

The scenario is very similar in V899 Mon. The quiescent period was only less than a year in case of V899 Mon, and, just like in the case of V1647 Ori, it cannot have replenished its disc to fuel the ongoing long second outburst.

5.2.2 Rise times in V1647 Ori and V899 Mon

The rise times of an outburst is determined by the speed at which the instability spreads over the inner disc. Typically, if the instability is triggered from an outside annulus, the increased inflow of gas from that annulus to the inner annulus will quickly trigger instability inside as well. As a result the instability will propagate faster towards the inside. In the case of V1647 Ori, the rise times in both the outbursts were similar and fast. This can be explained by an outside-in triggering of the instability from outer radius (Bell and Lin, 1994). In the case of V899 Mon, the average rate of change in magnitude during the onset of first outburst was 0.038 mag month^{-1} ; on the other hand, during the onset of second outburst it was faster than

[2]The smooth surface density assumptions of the disc were anyway in doubt since the clump in the disc at 0.27 AU disappeared in our second outburst observations.

[3]This factor has now become 18 by April 2016

0.15 mag month^{-1} . This difference implies that the timescales of the mechanisms that triggered the first and second outbursts are different.

5.3 Cause of break in the first outburst

The break in the first outburst we have seen in V1647 Ori, as well as in V899 Mon is not a rare case. V582 Aur (FUor source) also showed multiple, very brief quiescences during the ongoing outburst (Semkov et al., 2013). As we have seen in the previous section calculations, this cannot be explained by purely thermal instability models. In order to explain these short-duration breaks in outbursts, we need to look for mechanisms during an outburst that can pause the accretion for a short duration before the disk gets critically drained. In such scenarios, the outburst can re-initiate as soon as the mechanism that was pausing the accretion disappears.

Before V899 Mon transitioned to the quiescent phase, its spectroscopic observations showed an increase in the outflow activity (Section 3.4). Later the strong P Cygni profiles of outflow suddenly vanished as the object entered the quiescent phase. Since outflows are believed to be driven by magnetic fields, it is possible that some magnetic-field-related mechanism is responsible for abruptly pausing the accretion during the active outburst phase. Spectral line fluxes that are proportional to accretion, as well as the continuum flux of V899 Mon, increased suddenly during this short duration before the quiescence. In the final optical spectrum taken before the source transitioned from its first outburst phase to quiescent phase, we detected a sudden increase in equivalent width of the OI λ7773 absorption line (an indicator of turbulence). They are indicative of highly turbulent activity around the V899 Mon source just before it transitioned to quiescent phase. Even in the case of V1647 Ori, our observations detected a variety of episodic events like sudden short-duration winds with hydrogen column density $\approx 3.4 \times 10^{20}$ cm^{-2}, fluctuations in Hα flux, etc. The variations in Hα flux could have their origin in some magnetic phenomena in the accretion funnel. However, unlike V899 Mon, we do not have any spectroscopic observation of V1647 Ori during its ending phase of the first outburst.

Accretion in low-mass YSOs is generally accepted to be via magnetospheric accretion funnels from disk to star. A large rate of accretion can provide a negative feedback in many ways. There are various semianalytic and numerical simulation studies in the literature on instabilities that can break and restart magnetospheric accretion (Kulkarni and Romanova, 2008; Orlando et al., 2011; Blinova, Romanova, and Lovelace, 2015). For instance, the accretion can stop if the inner truncation radius of the disk moves outside the co-rotation radius (D'Angelo and Spruit, 2010). In another scenario, the differential rotation between the inner accretion disk and the star can lead to inflation of the funnel, resulting in field lines opening and reconnecting, reducing accretion flow while enhancing outflow (Bouvier et al., 2003). These kinds of breaking mechanisms have the extra advantage that they can easily explain how a second outburst can restart without having to replenish the depleted disk within the short quiescent phase. Some other FUor sources like FU Ori, V1515 Cyg, and V2493 Cyg also show a short-duration dip in their light curves after they attained the initial peak of their

outburst. All of them seem to indicate a complex negative feedback loop in magnetospheric accretion.

It is interesting to note that both V899 Mon and V1647 Ori spent a shorter duration in the first outburst compared to their ongoing second outbursts. The reason for the second outburst being more stable than the first outburst could be because of the change in the inner disk's physical parameters by the heating or the draining of the disk during the first outburst (such as the extent of the interaction region between magnetosphere and inner disk, their coupling, inner radius of the disk, etc.). In the case of V1647 Ori, from the stability in the phase of the X-ray accretion spot, Hamaguchi et al., (2012) had shown that the location of the spot of the accretion column shock on the star did not change significantly between the first and second outbursts. Hence, if the quiescent phase of V1647 Ori was also due to disruption in magnetic funnel accretion, at least the base of the magnetic funnel on the star surface was not completely disrupted.

5.4 Summary

In this chapter, we did a detailed timescale analysis of various instability models to explain the timescales we observed in V899 Mon and V1647 Ori. Even though we do not have a direct observational evidence to support increased magnetic activity, the outflow and turbulence signatures in the spectrum and continuum flux are consistent with instability in the magnetic accretion funnel, and the timescales are strongly inconsistent with any other instability models that depend on critical disk surface densities to switch the outburst on and off.

Chapter 6

Constraints on Outflow Mechanims

Outflows from young stellar objects are the most efficient way to take away the angular momentum from the star-disc system and prevent the star from spinning up while it undergoes accretion from the disc. If we assume the angular momentum removed by the outflow to be equal to the angular momentum transferred from the accretion, one can obtain a linear relation between the outflow rate and the accretion rate (Konigl and Pudritz, 2000). Hence, almost all theoretical models predict the outflows to be proportional to the accretion rate (they are also consistent with the observationally estimated proportionality factor $\sim$0.1).

EXor and FUor outbursts occur for a short duration (few years to decades) and many of them have associated outflows detected. Hence, they provide a unique laboratory to monitor the simultaneous evolution of the outflow with respect to the accretion rate. The rich optical spectrum of these sources enables us to estimate the accretion rate from the flux of a certain set of emission lines, and the outflows originating in the innermost region of the accretion disc via P-Cygni line profiles. Previously, among other young eruptive stars, a reduction in the P-Cygni outflow absorption has been seen in V2492 Cyg when the source dimmed for a very short duration in 2010 (Aspin, 2011b). However, variable extinction plays a major role in the light curve of this source (Hillenbrand et al., 2013). Hence, the correlation between the outflow and the accretion is difficult to conclude. Small scale variations in the outflow strength and velocity were also reported in V2493 Cyg during its rise to outburst phase by Lee et al., (2015).

Our first discovery of episodic short duration winds was in V1647 Ori (see 4.13 in Chapter 4). It had a time scale of a few days, and for a system at 61° inclination angle, this implied they are magnetic reconnection driven winds rather than pressure driven steady winds.

In the family of young eruptive stars, V899 Mon showed the most dynamic changes in outflow with respect to accretion when the source transitioned from its first outburst in 2010 to a short one year quiescence in 2011 and then back to its ongoing second outburst in 2012 (see Chapter 3). Apart from the detection of the complete disappearance of outflow P-Cygni profiles for a long duration when the accretion rate dropped to the quiescent level, we could also detect significant short timescale decoupling between the outflow wind strengths and the accretion rates. Non-correlated variability between accretion and wind indicators is also seen in Class I protostars (Connelley and Greene, 2014). Overall, there seems to be a complex relationship between accretion and the wind in short time and length scales.

To study the outflow mechanism in V899 Mon, we decided to do a multi-epoch high resolution study of the outflows from V899 Mon (see Chapter 2). In this Chapter, we report the evolution in the line profiles, and the outflow components. We will compare and discuss various possible theoretical outflow mechanisms which could explain the observed episodic outflow events. And finally, we will conclude in the end with the most-likely scenario of magnetic pressure driven polar stellar winds. These direct multi-epoch observations of young eruptive stars provide measurements which can be directly compared with the theoretical magnetohydrodynamic (MHD) simulations of the magnetospheric accretion and outflows. The results presented in this chapter are published in Ninan, Ojha, and Philip, (2016).

6.1 Outflow Evolution

6.1.1 Forbidden Lines

Figure 6.1 shows the change in the profile structure of the forbidden lines [O I] λ6300, λ6363 and [Fe II] λ7155. The blue-shifted high velocity ($\sim$ -475 km s^{-1}) components of these three line profiles have similar velocity structure and are believed to be formed from shocks in the jet, away from the central star. Over a timescale of one year, between 2014 December and 2015 December, we could detect a drop in the medium velocity plateau component with respect to the maximum velocity component in [O I] λ6300. We do not see any significant short timescale variation between 2015 December 15, 19 and 2016 February 20 spectra. A hydromagnetic jet collimated by the toroidal magnetic fields does not spread sideways as fast as an ordinary hydrodynamic jet when it encounters a jet shock (Konigl and Pudritz, 2000). Thus the evolution of the relative column density of various projected velocity components (obtained from these blue-shifted forbidden line profiles), in principle, contain information to differentiate between the type of jets. However, such an analysis is beyond the scope of this thesis. We shall use only the maximum velocity from these shock lines to infer the inclination angle and the terminal velocity in Section 6.2.

6.1.2 Hα, Hβ & Ca II IR triplet lines

Figure 6.2 shows the evolution in the blue-shifted absorption due to the outflow in Hα line profile between 2014 December, 2015 December and 2016 February. The very high velocity component (extending up to -722 km s^{-1}) in Hα present during 2014 December disappeared in both the 2015 December spectra. 2016 February 20 profile shows re-emergence of a high velocity component in outflow extending up to -550 km s^{-1}. Figure 6.3 shows this high velocity component in the Hβ profile plotted over the Hα profile. If the high velocity clump was optically thin, the ratio of the equivalent widths would have been equal to the ratio of the oscillator strength (0.6407 for Hα and 0.1193 for Hβ) times line wavelength. However, the Hβ profile has same equivalent width as Hα, hence the high velocity clump is optically thick. The shallower depth of this high velocity outflow absorption with respect to the lower velocity absorption implies the high velocity winds are

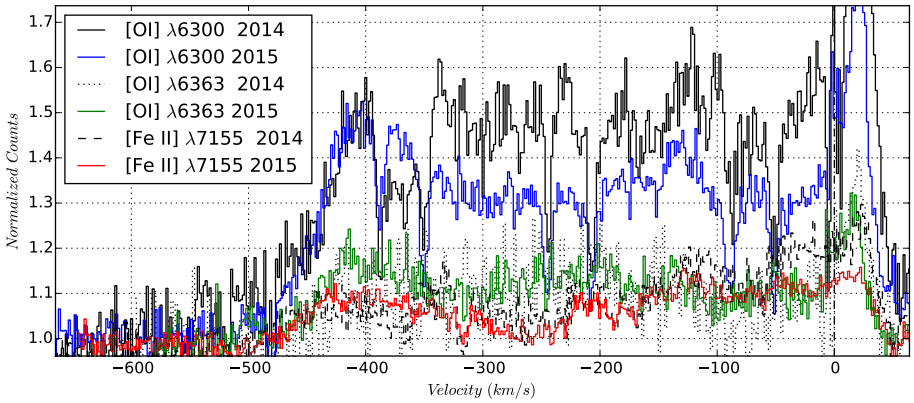

FIGURE 6.1: Evolution between 2014 December and 2015 December of the forbidden line profiles originating in the shock from V899 Mon. The high velocity components in the shock extend up to $\sim$ -475 km s^{-1}. The profiles do not show any significant variation between 2015 December and 2016 February, hence they are not plotted here.

hotter at optical depth $\tau \sim 2/3$. Hence, its density and/or temperature are different from the low velocity outflow components.

We did not detect any significant change in the outflow structure in a timescale of 4 days between 2015 December 15 and 19. Even though we could not resolve the detailed structures, very high velocity episodic outflow components have also been previously detected at various epochs (especially at the end of the first outburst) in our medium resolution spectra (Chapter 3). We used our new medium resolution spectra of the second outburst to obtain the typical timescales of the variation in outflow. Figure 6.4 shows the large variation in outflow velocity component detected in all of our medium resolution spectra. The velocity plotted in Figure 6.4(b) (upper panel) corresponds to 95% drop in the blue-shifted absorption profile from the continuum level during the second outburst. It shows significant velocity variations in timescales as short as a few days. Hence, the large variation we detected in the high resolution spectra was the norm during the ongoing second outburst. As far as we know, such high velocity changes have never been reported in this family of heavily disc accreting young objects. The bottom panel of Figure 6.4(b) shows a scatter plot of the rate of change in the outflow velocity versus the change in the outflow velocity. This scatter plot distribution, which contains information regarding both the magnitude as well as the rate of change in the outflow velocity, could be used to quantitatively match a similar scatter plot distribution of the outflow velocity fluctuations in MHD simulations.

Outflow signatures are also seen in the high resolution P-Cygni profiles of Ca II IR triplet lines (Figure 6.5). These absorption components are optically thin; interestingly, they did not show any high velocity wind component which was seen in the Hα profile during 2014 December or 2016 February. The Ca II IR triplet line λ8498 is least affected by the blue-shifted absorption from outflow. Hence, we did the line bisector analysis on the emission line profile of λ8498. Figure 6.6 shows the line bisectors obtained at various epochs. Since the Ca II IR triplet emission lines of V899 Mon are

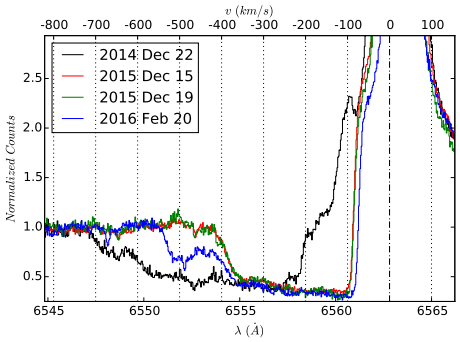

FIGURE 6.2: Outflow evolution between 2014 December 22, 2015 December 15, 2015 December 19, and 2016 February 20 of the Hα line profile from the magnetosphere of V899 Mon. All profiles are shifted to heliocentric velocity (by 0.92 km s^{-1}, 4.22 km s^{-1}, 2.39 km s^{-1} and -22.31 km s^{-1} respectively).

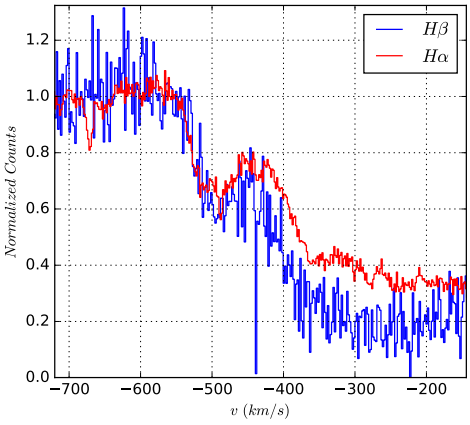

FIGURE 6.3: High velocity outflow component in 2016 February spectrum seen in both Hα and Hβ normalized line profiles of V899 Mon. Despite their different oscillator strengths, equivalent width of both Hβ and Hα of the high velocity component at -500 km s^{-1} (which appeared in 2016 February) show that even the high velocity outflow's H lines are saturated.

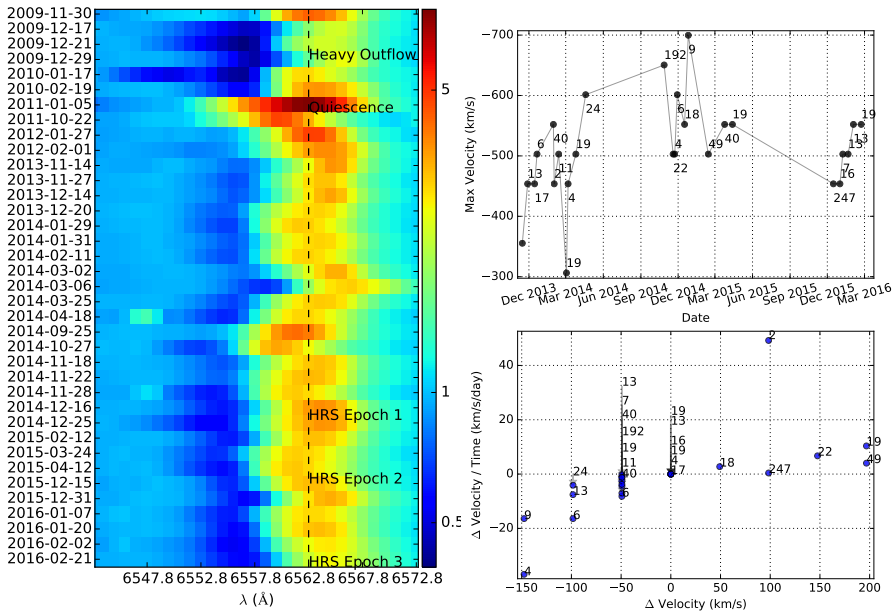

(a) (b)

FIGURE 6.4: Outflow evolution traced in our medium resolution spectra from 2009 to 2016 of the Hα line profile. (a) The three epochs of HRS observations are marked in the map. The color scale is in log scale. The variation in the extent of blue-shifted absorption shows the variation in peak velocity of the outflow at each epoch. The vertical dashed line is the center wavelength of the Hα line. (b) The time evolution in the outflow velocity at 95% drop from the continuum in absorption profile from the spectra taken during the ongoing second outburst. The numbers marked at each point show the number of days passed to the previous observational data. The plot at the bottom shows the scatter plot between the floor rate of change in the outflow velocity (obtained by dividing velocity change with the number of days between the consecutive observations) with respect to the change in the outflow velocity. This distribution represents both the magnitude and the timescales of the fluctuations in velocity.

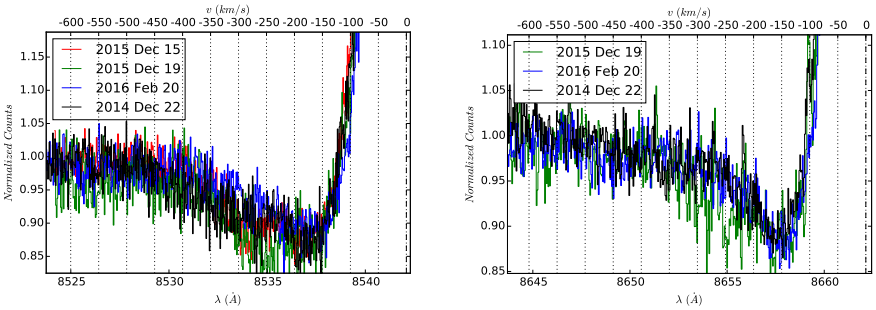

(a) λ8542 (b) λ8662

FIGURE 6.5: Outflow evolution between 2014 December, 2015 December and 2016 February traced by Ca II IR triplet P-Cygni absorption line profiles of V899 Mon. We do not see any significant variation in these optically thin absorption profiles.

optically thick, the line center becomes optically thick at an outer radius region than the line wings, which become optically thick in a region more deeper and closer to the central source. The fitted line bisector shows a clear increasing blue-shift in the velocity of the gas from the regions closer to the central source. There is a significant difference between 2014 December and 2015 December spectra. This could be due to a combined effect of change in optical depth and/or velocity change.

6.2 Possible Outflow Mechanisms

Figure 6.7 shows the various outflow mechanisms which could operate in a young stellar object undergoing accretion from the disc via magnetospheric accretion. Disc winds are driven by magneto-centrifugal forces along poloidal magnetic field lines if they are tilted by more than 30^o by the Blandford & Payne mechanism (Blandford and Payne, 1982). Centrifugally driven X-winds can arise from the inner disc region if the inner disc truncation happens at the co-rotation radius of the magnetosphere (Shu et al., 1994). Magnetic pressure driven conical winds can also arise from the inner disc-magnetosphere boundary irrespective of the truncation radius (Romanova et al., 2009; Lii, Romanova, and Lovelace, 2012). Along the polar direction, one can have radiatively driven stellar winds, as well as magnetic pressure driven winds, like in the case of Poynting jet in propeller regime (Lovelace et al., 2002; Ustyugova et al., 2006) when the magnetosphere is rotating fast enough. All the above mentioned outflow mechanisms have their own characteristic velocity, outflow angle, as well as stability timescale. In this section we shall analyze each mechanism in the light of the episodic outflow velocity changes seen in V899 Mon.

Since the estimated mass of V899 Mon is in the range of 1.5 – 3.7 $M_\odot$ (Chapter 3), it lies outside the upper boundary of low mass stars. Whether there is enough magnetic field strength to have a magnetospheric accretion for these mass ranges is a debated topic in literature. Even though V899 Mon seems to have a higher mass than typical low mass T-Tauri stars, optical and near-infrared spectra as well as radio continuum flux indicate it to be a low mass star rather than typical high mass stars like Herbig Ae

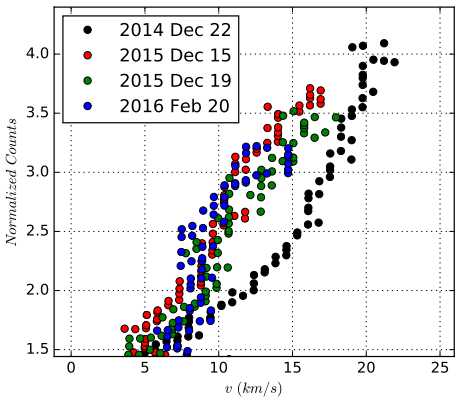

FIGURE 6.6: Evolution in the line bisector of the optically thick Ca II IR triplet λ8498 emission line. This line is least affected by the absorption from outflow. Each of the color points are the bisectors of the corresponding night's line profile. Since the line bisector is taken on an optically thick emission line, the y-axis corresponds to the normalized flux counts of the line profile. The extreme flat wings of the profile in the range 1 – 1.5 is discarded from the bisector analysis due to the large uncertainties in the bisector values.

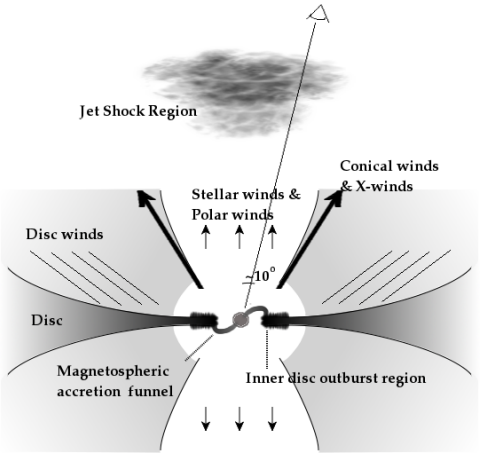

FIGURE 6.7: Schematic diagram of various outflow mechanisms which could be present in V899 Mon (see the text).

(Chapter 3). This factor, along with its relatively low mass accretion rate compared to FUor (the rate is about the same order as of V1647 Ori, which is known to have a magnetospheric accretion) makes magnetospheric accretion a reasonable scenario for V899 Mon.

The inclination angle of the source is crucial to estimate the contribution of each type of outflow on the final P-Cygni profile seen in Hα and Ca II IR triplet lines. V899 Mon is most-likely to be at a very low inclination angle and is seen almost face-on for the following reasons. The optical extinction ($A_V \sim 2.6$ mag) to the source is very small compared to what could be expected from its mid-infrared and far-infrared fluxes, and this could be the case if we are viewing V899 Mon through the low density outflow cavity (Chapter 3). Since the cavity opening angles can be quite large, the constraint on inclination angle is quite wide. The maximum velocity in the blue-shifted high velocity component of the forbidden lines (Figure 6.1) originating in the jet shocks has been shown to correlate with the inclination angle by Appenzeller and Bertout, (2013). The large velocity $\sim$ -475 km s^{-1} seen in V899 Mon would thus imply a very low inclination angle according to Figure 3 in Appenzeller and Bertout, (2013). It should be noted that V899 Mon's velocity falls outside the region of their correlation plot by $\sim$ 100 km s^{-1}. However, the velocity seen in V899 Mon is still within the velocities expected from T-Tauri stars. Hence, it is likely to obey the same correlation, and we could constrain the inclination angle to be low for V899 Mon. The near symmetric profiles of Hα and Ca II IR triplet lines during the quiescent period in 2011 of V899 Mon are also consistent with the low inclination angle line profiles modeled by Kurosawa and Romanova, (2012). Finally, the Hα P-Cygni profile shape in the ongoing outburst phase in 2015 December 15 and 19 is very similar to a pre-FUor, V1331 Cyg, which is known to be at a very low inclination angle. Hence, the most consistent picture is obtained when the inclination angle to V899 Mon is taken to be small ($\sim 10^o$).

Disc winds, X-winds and Conical winds can result in blue-shifted absorption only when they occult our line of sight to the central magnetosphere. They can be in the line of sight when the inclination angle is larger than the opening angle of these winds ($\gtrsim 30^o$) (Kurosawa and Romanova, 2012). If the inclination angle of V899 Mon is small, these winds cannot produce the absorption component in P-Cygni profiles. However, in principle, one can still obtain a P-Cygni profile from these high inclination angle winds, if the disc's continuum radiation is much larger than that of the central star. The typical ratio between the disc continuum and central star flux required for this is about a factor of 100 (as shown by Tambovtseva, Grinin, and Weigelt, (2014)). The change in the net flux from V899 Mon system between outburst and quiescence is only about a factor of 15 (ΔR mag = 2.9), hence this is very unlikely to be the case of V899 Mon. Moreover, considering the projection angle of these winds, the actual de-projected velocity of the winds will have to be unrealistically high.

Even if we consider the scenario where the inclination angle to V899 Mon is large, the centrifugally driven winds like X-wind and disc winds will have a characteristic velocity proportional to the Keplerian orbital velocity at the base of the wind. Since the Keplerian velocity is proportional to $R^{-0.5}$, the detected change in the outflow velocity from -722 km s^{-1} to -425 km s^{-1} would imply a change in radius of the base of the outflow by a factor of 3. These outflow mechanisms are also relatively stable over

long timescales. Other mechanisms like conical winds also typically cannot result in such high velocity winds detected in V899 Mon (Kurosawa and Romanova, 2012). Magnetospheric ejection winds driven by the inflation and re-connection of magnetospheric field lines to the disc have a strong episodic nature. However, its terminal velocity is again limited by the gravitational escape speed similar to X-winds (Zanni and Ferreira, 2013). Hence, if V899 Mon's inclination angle is large, among various possible outflow mechanisms, wide angle conical winds in propeller regime is the most likely outflow mechanism. These winds have difficulty in attaining the observed high velocities, but the timescales of the stability in these winds are consistent with our observations (Ustyugova et al., 2006; Romanova et al., 2009).

The high resolution P-Cygni profile structure in Hα line of V899 Mon during 2015 December was strikingly similar to that of V1331 Cyg, whose inclination angle is known to be small (Petrov et al., 2014). Petrov et al., (2014) could obtain a good fit to this profile in V1331 Cyg using a radiative transfer model including stellar wind. While a stellar wind inside the polar opening angle can explain the profile structure seen in 2015 December, we should also be able to explain both the variation in the outflow strength as well as outflow velocity seen over the timescale of weeks in V899 Mon. Even though the outflow strength dropped below the detection limit when the accretion rate dropped during the 2011 quiescence, in the ongoing second outburst, we do not see any significant causal connection between the variations in outflow strength and the accretion (estimated from emission line strengths). Smaller changes in outflow velocity ($\sim$ 50 to 100 km s^{-1}) could be explained as the traced velocity at the corresponding radius where the accelerating wind gets optically thick. Change in opening angle due to magnetic field strength variation in the magnetosphere will result in change in density of the outflow and thereby the radius at which wind gets optically thick (Petrov et al., 2014). However, this change in apparent outflow velocity has an obvious upper limit of terminal velocity. So we need to look for some other mechanisms to explain the very high velocity ($>$-722 km s^{-1}) episodic outflows detected in 2014 December and other epochs during the ongoing outburst. The change in outflow strength can also be caused by any change in the fraction of accreting matter which gets redirected in the polar direction as an accretion powered stellar wind. Recent simulations by Ustyugova et al., (2006), Romanova et al., (2009), and Kurosawa and Romanova, (2012) have shown that it is possible to have magnetic pressure driven polar winds which redirect matter from the upper part of the magnetospheric accretion funnel flow. They are similar to the propeller regime high velocity outflow in the polar direction seen in a fast rotating magnetosphere which has a disc truncation radius outside the co-rotation radius. Such a regime is possible in young Class I stellar sources which are typically found to rotate with a period of a few days. The acceleration to high velocities like 500–1000 km s^{-1} occurs only very near to the magnetosphere where the magnetic pressure dominates and these winds later slow down as they move farther away. Their velocity is sensitive to the accretion rate and the outflow density, and their episodic nature with a timescale of a few weeks seen in simulations (Romanova et al., 2009; Ustyugova et al., 2006) are also consistent with our observations. It should be noted that Kurosawa and Romanova, (2012) did not obtain any significant contribution from these polar

winds to the blue-shifted P-Cygni absorption. The polar wind outflow rate was only about 10^{-10} $M_\odot$ yr^{-1} in their MHD simulations. Stellar winds were also not included in their model. This low density of polar outflow did not result in any significant absorption. However, Romanova et al., (2009) showed the polar high velocity jets can have up to 10% of the conical wind mass flux. The total mass outflow from V899 Mon is $\sim 10^{-7}$ $M_\odot$ yr^{-1} (Chapter 3), hence it is possible to have mass outflow up to $\sim 10^{-8}$ $M_\odot$ yr^{-1} in the polar axial winds; which is sufficient to produce blue-shifted absorption in Hα profile. Presence of stellar wind could also further increase the mass flux along polar winds (Romanova et al., 2009). The outflow mechanism in these simulations of the high velocity clumpy episodic outflows along the polar direction is the most observationally consistent mechanism which can explain the fluctuating high velocity winds seen in V899 Mon.

6.3 Summary

Our multi-epoch high resolution spectroscopic observations of the outflow traced by the P-Cygni profile in V899 Mon show change in velocity from -722 km s^{-1} in 2014 December to -425 km s^{-1} in 2015 December and to -550 km s^{-1} in 2016 February. We do not detect any significant variation in the outflow profile over a time scale of 4 days between 2015 December 15 and 19. However, our more frequently sampled medium resolution spectra show high velocity episodic outflow variations in the timescale as short as a week at other epochs of the ongoing outburst. In the likely scenario where V899 Mon is seen at a low inclination angle to our line of sight, the most consistent mechanism which can give rise to such unstable, clumpy, short duration high velocity winds are magnetically accelerated polar winds seen in simulations by Kurosawa and Romanova, (2012) and Romanova et al., (2009). The highly variable nature of outflow strength and velocities make V899 Mon the most dynamic source which can be used to model and constrain the time evolution in various magnetohydrodynamic simulations of the magnetospheric accretion and outflow in young stellar objects.

Chapter 7

Bayesian Model to Constrain Outburst Frequency

The frequency and the amplitude of the sudden heating of the protoplanetary discs by these episodic accretion outbursts can have significant effect on planet formation (Stamatellos, Whitworth, and Hubber, 2011) and the overall chemistry of the protoplanetary disc. Rapid accretion events would also significantly change the pre-main sequence isochrones used extensively for age and mass estimation of the YSOs (Hartmann, Zhu, and Calvet, 2011; Hosokawa, Offner, and Krumholz, 2011; Baraffe, Vorobyov, and Chabrier, 2012). Hence, the frequency of these accretion outburst events is crucial to model the effects of outbursts on the star-disc system. These outbursts are presently understood in the framework of effective viscosity changes in the disc, caused by the different instabilities which could arise in an accretion disc (Bonnell and Bastien, 1992; Bell and Lin, 1994; Clarke and Syer, 1996; Kley and Lin, 1999; Armitage, Livio, and Pringle, 2001; Vorobyov and Basu, 2005; Boley et al., 2006; Zhu et al., 2009). However, the frequency of outbursts is not constrained by these models. In fact, any empirical estimate of the frequency of outbursts will be a valuable input for these models.

It should be noted that, due to the small sample size of the discovered outbursts, it is not yet clear whether such an episodic accretion outburst is the norm in all YSOs or if they are seen only in certain specific populations. While the episodic accretion outbursts have been observed in both embedded, typically Class I, and optically visible Class II YSOs, there is no clear trend on how the outburst frequency evolves as a function of the age, or the disc mass.

There have been various attempts in the literature to model the detected number of outbursts to constrain the recurrence period of outbursts[1]. The basic idea of all these attempts was to take the ratio of the number of YSOs undergoing outburst to the total number of YSOs. Depending on how accurately the numerator and the denominator were estimated, the constraint on the period of outbursts is spread over 2 orders of magnitude (see section 3.1 of Hillenbrand and Findeisen, (2015) for a detailed discussion of various attempts in the literature).

In this chapter, we propose a Bayesian approach to the period estimation problem. Our model enables us to incorporate all available archived

[1]Episodic accretion is at the best only quasiperiodic. However, since the timescales between consecutive outbursts are large, periodic models are a good approximation. In this chapter, we would be using the term outburst period to represent the time interval between outbursts in spite of their expected quasiperiodic nature.

photometric observations of star-forming regions into any specific simulation. It also enables us to answer more detailed questions about the universality of the outburst phenomenon, or dependence on age, cluster properties, and environment. In section 7.1 we outline the merits of a Bayesian approach to this problem over the frequentist approach of the binomial model. In order to incorporate multi-epoch, multi-wavelength data, we need a flexible and general data representation format, and this is described in section 7.2. Our Bayesian model is explained in section 7.3; we start with a simple case, and then we expand the complexity of the model step by step. In section 7.4 we list the major caveats to data interpretation using our model. We summarise in section 7.5 by briefly discussing the major results. We have publicly released our code that simulates the data set and then fits the Bayesian model.

7.1 Merits of a Bayesian Model

The traditional frequentist approach to the problem of estimating the outburst period is to model the number of detected outbursts in a sample of YSOs as a random sampling from a binomial distribution of a certain outburst rate (Scholz, Froebrich, and Wood, 2013; Hillenbrand and Findeisen, 2015). In this model, for an outburst rate of $r\ star^{-1}\ year^{-1}$, while considering a two epoch survey with sample size N_{YSO} and a time gap Δt, the average expected number of outbursts in the sample is $r\Delta t\ N_{YSO}$. In the following sub-sections, we briefly outline the advantages of the Bayesian model over this frequentist approach.

7.1.1 Applicability in short duration outbursts

For the above mentioned representation of the outburst period (the interval between outbursts) for a rate parameter to be valid, the assumption $r\ \Delta t << 1$ should be true, i.e., there should be only a maximum of one outburst during the entire period of observation (Δt). Hence, the model cannot be used to study the short period outbursts like EXors, where the period is comparable to or smaller than the survey time gap, since the events would be missed and the Binomial model will become invalid if $r\ \Delta t > 1$. Recently discovered eruptive variables seem to indicate that there is a continuum of sources between classical EXors and FUors (see review by Audard et al., (2014) and demonstration in Kraus et al., (2016) of a 30 year duration for the outburst of V346 Nor, long considered an FU Ori star). Hence, it is desirable to have a model which is equally applicable to all ranges of periods. Bayesian models can be built without the above constraints. Starting with the input parameters, if a model can be build to calculate or simulate the output observational data, then, when the actual observed data is available, the Bayes theorem can be used to obtain the posterior probability of the parameters of the model. In our Bayesian model, we have not used the rate representation of the period. Instead, we represent the actual YSO light curves as an ideal rectangular waveform, where the high state represents the outburst phase and the low state represents the quiescent phase. There is no limitation on the period of repeated outbursts which this model

can fit. Hence, the same model can be used to study all ranges of periodic outbursts seen in eruptive variables. This capability is also important to make quantitative comparisons across different classes and age groups which could potentially have different periods for outbursts.

7.1.2 Multi-epoch observational data

Over the last century, there have been many photometric observations and surveys of YSOs in different wavelengths. Each survey has a unique number of YSOs, time span of the observations of the same field with same equipment (this is Δt), and a cadence which is often irregular especially for the ground-based surveys. In the binomial model, since the rate parameter is the combined product of the outburst rate r and Δt, one has to fit separately each sample of YSOs observed in a certain time interval Δt. In a scenario where we have random time intervals of observations for each YSO in the collection of photometric surveys, we do not have a single Δt for a large enough data subset to fit the rate parameter separately. This is the major limitation in using the binomial model to fit all the archival data available from various old as well as the new multi-wavelength surveys.

However, in our Bayesian model, we can naturally incorporate any number of available observations and simultaneously take advantage of both recent, deep, short cadence surveys (like *WISE*, *Spitzer*, *ASAS*, *PTF*, *PanSTARRS*, *ATLAS* etc.), as well as old static surveys (like *POSS*, *2MASS*, *SDSS*, etc.). Incorporating all the available data sets will provide much tighter constraints on the parameters like the period of outbursts we want to estimate.

7.1.3 Incorporating constraints from other methods

Bayesian models can easily incorporate constraints on the parameters from other considerations (for example, the period estimates obtained from the knots in outflows, or ranges of likely estimates required to explain the "Luminosity Problem" in YSOs, envelope temperature, etc.). They can be incorporated into the model as prior probabilities of the parameters we are trying to estimate. In the binomial model, there is no direct way to incorporate such extra prior beliefs on the parameters.

7.1.4 Simple interpretation of the results

The output from the Bayesian model is the probability distribution of the parameter values. Given the observational data, a Bayesian model re-allocates the credibility of values each parameter could take across possibilities. This probability distribution can be summarized by Bayesian credible intervals. Conceptually, the 95% in a 95% frequentist confidence interval represents the probability of that interval to contain the true period, while the 95% in a 95% Bayesian credible interval represents the probability of the true period to fall within that interval. Hence, Bayesian credible intervals are easier and more intuitive to visualize than the traditional frequentist confidence intervals.

7.1.5 Power to compare between classes

The true advantage of our Bayesian model is its power in statistical comparison between different clusters and classes (e.g., SED type or stellar mass range or wavelength of observation) of YSOs. Instead of fitting models separately for individual classes, hierarchical Bayesian models and the Bayesian networks can provide better constraint by simultaneously fitting across various classes. This is especially important when a few classes have small samples to provide independent constraint. A hierarchical model pools the information from across the classes to give better constraints for the lesser-sampled classes. In the specific context of our YSO problem, these models will allow us to constrain and compare any significant variation in the outburst periods across different categories of YSOs and physically associated clusters.

7.1.6 Predictive power of the model

Hillenbrand and Findeisen, (2015) did a detailed power analysis of the binomial model. Similarly, to do the power analysis of our Bayesian model, we can simulate an observational data set, and try to estimate the input parameters and their credible intervals. After fitting the Bayesian network using the presently available data, we can make predictions for future large telescopes and surveys using the same network.

7.2 Representation of the Data (D)

In this section, we describe the representation of the multi-epoch, multi-wavelength data which is the input to the model for fitting. Observed raw data are the flux or magnitude measurements at two or more epochs. The outburst phenomenon we are modeling has a well defined change in magnitude ΔM (e.g., 2–3 mag in case of EXors, and 4–5 mag in case of FUors). If the magnitude never changed beyond this ΔM during the entire duration of the observations, we have no way of knowing whether the star is in the outburst phase (represented by the integer 1) or in the quiescent phase (represented by the integer 0). Hence, we denote each observation of that star to be in an unknown state (represented by an integer larger than 1). If we detect a source to have transitioned to an outburst phase at a certain epoch, we denote all the previous quiescent states as low states (represented by 0) and the outburst epoch states as high states (represented by 1). Thus, each star in the sample with multiple epoch of observations (D_i) is represented by a list of integers corresponding to each epoch. For example, [2,2,2,2] is a star which did not change its magnitude beyond the range of normal young star variability in all the four epochs of observation. [0,0,1,1] is a star which was found to be in outburst in the third epoch. And [1,0,0] is a star which was found to have transitioned to quiescence in the second epoch. Each entry in this sequence of the states also has a corresponding observation time stamp. For some YSOs, data from very different wavelengths might also be available in literature, for example, mid-infrared *Spitzer* and *WISE* surveys. It is not always possible to compare these fluxes directly with optical fluxes, to decide whether the source underwent a transition or not. Hence,

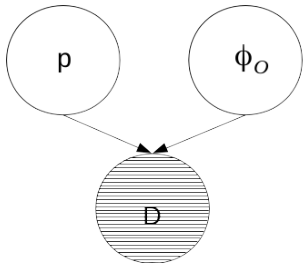

FIGURE 7.1: The basic single period, single outburst phase model. Node p is the period, ϕ_O is the outburst phase, and D is the observed data.

we represent them as a new unknown state by an integer larger than 2, say for instance 3.

This structure of data is designed to be general enough to represent all the multi-epoch, multi-wavelength observations of YSOs available in the literature. The photometric errors (normally <0.1 mag) and the quiescent state photometric variability (typically <0.2 mag) are assumed to be much less than the threshold change in the magnitude (ΔM) which defines the outburst.

7.3 Bayesian Models

In this section we present our Bayesian models. We start with the simplest model and expand the model step by step for more general cases depending on the data.

7.3.1 The simplest model

The simplest model is where all the stars in the sample are modeled to have one unknown period and a fixed duration of outbursts. This forms the lowest level in the Bayesian network model (see Figure 7.1).

For applying the Bayes theorem, we first calculate the likelihood function $P(D_i \mid p, \phi_O)$. This is the probability of obtaining the observed data D_i, given a period p and an outburst phase ϕ_O (explained below). This calculation is the heart of our model.

For a given period p, without losing generality, we represent epochs of the observation in a phase diagram. We assign 0 phase to the beginning of the quiescence and ϕ_O is taken to be the phase at which the source transitions from the quiescence to the outburst phase. Figure 7.2 shows one period in the light curve of a star undergoing outburst. The time axis is transformed to phase from 0 to 1 of a given period p (Phase = Time/Period mod 1). This model has only two parameters, namely the period (p) and an outburst phase (ϕ_O). The duty cycle of the outburst in this model is 1-ϕ_O.

We now calculate the likelihood. For each star's data D_i, the first epoch of the observation in the phase curve (Figure 7.2) is equally likely to be anywhere in the interval 0 to 1. We denote that unknown initial phase as ϕ_1. Phases of subsequent epochs are given by adding the differential phase (of time difference) to the initial phase, i.e., ϕ_2 = ϕ_1 + (Epoch$_2$ - Epoch$_1$)/Period mod 1.

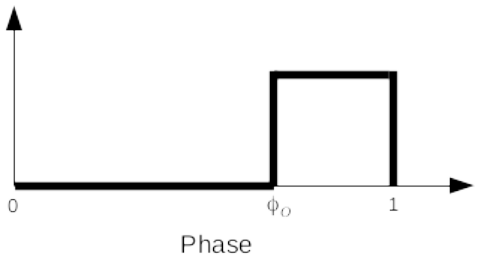

FIGURE 7.2: Single period light curve of a star. Time axis is transformed to phase from 0 to 1 of a given period p (Phase = Time/Period mod 1).

Each new epoch of observation of a star gives a new constraint on the interval in which ϕ_1 lies. By taking an intersection of all the constraints from each epoch on the interval ϕ_1 belongs, we obtain the final sub-intervals which contain the ϕ_1 of that source in the phase space 0 to 1. Since the first epoch of the observation is a uniform random draw from this sub-interval in the phase space 0 to 1, the total size of the final interval is equal to the probability of the observation of that particular multi-epoch data, i.e., likelihood $P(D_i \mid p, \phi_O)$. Due to the calculation of intersections of intervals in a phase circle, we cannot write an analytic expression for the likelihood. We implemented this likelihood calculation numerically in Python using open interval sets of *SymPy* module. For obtaining the likelihood of observation of all the observed stars in the sample (D), i.e., $P(D \mid p, \phi_O)$, we multiply all the independent individual probabilities together. $P(D \mid p, \phi_O) = \Pi_i P(D_i \mid p, \phi_O)$

Prior

In Bayes formula, the posterior probability distributions of the parameters are estimated by taking the product of likelihood with prior probability distributions, i.e., $P(p, \phi_O \mid D) \propto P(D \mid p, \phi_O) \times Prior(p, \phi_O)$. Prior probability distribution is our prior belief on the values the parameters could take. We could take a completely non-informative prior, where we consider all values of period to be equally likely. In the case of FUors, the most skeptic prior belief of the period range can be taken to be 5×10^2 to 1×10^6 years (section 3.1 in Hillenbrand and Findeisen, (2015)). In this chapter, we have taken our prior probability distribution to be a uniform distribution in this wide range. Defining reasonably constraining priors also has the practical benefit of making Markov-chain Monte Carlo (MCMC) sampling faster and efficient.

Predictive Power of the Model

The predictive power of our model was analyzed by simulating many instances of possible observational data for various hypothetical outburst periods, and calculating the probability density function of the period. To simulate the data set, which mimics the observation, we generated N number of random initial phases (ϕ_1) for N number of stars. The time epochs

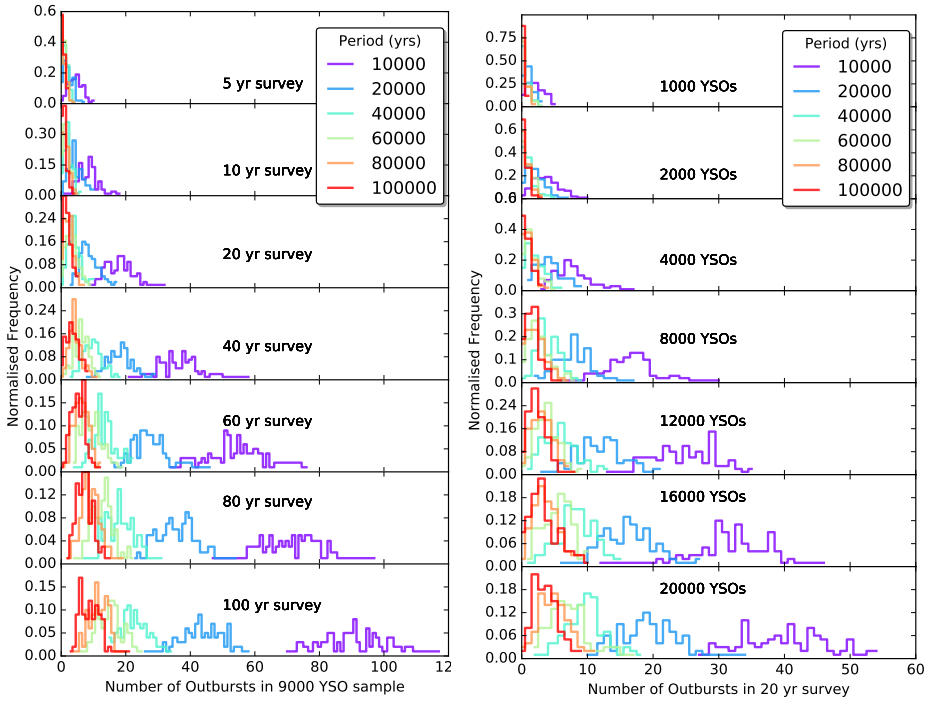

(a) (b)

FIGURE 7.3: a) Frequency distribution of the number of outbursts occurring in a simulation of a two epoch survey containing a sample of 9000 YSOs. b) Similar histograms of the number of outbursts occurring for a 20 year survey gap with varying number of YSOs in the sample. True outburst period corresponding to each histogram is shown in the color legend. Longer periods need longer time baselines and/or larger YSO samples in order be measurable.

of observations were then converted to phase differences using the true period assumed in each simulation. Comparing these phase values of each epoch with the model outburst phase (ϕ_O), we generated the light curves in the format explained in section 7.2.

Figure 7.3a shows the histograms of the number of outbursts occurring in a simulation of a two epoch survey containing a sample of N = 9000 YSOs. Figure 7.3b shows similar histograms of the outbursts over 20 years with varying number of YSOs in the survey sample. When the total duration of the simulated survey is shorter than the duration of the outburst, the number of epochs of observation in the survey is not relevant to the calculation, so the two-epoch scenario is sufficient.

For this single period model, we could directly calculate the posterior probability distribution by evaluating the likelihood function for a grid of periods using the phase interval intersection method mentioned in the section 7.3.1. However, in order to conduct simulations of more extended models mentioned in the sections below, where direct likelihood calculations become difficult, we implemented Monte Carlo based posterior probability calculation using *PyMC3* Python module.

MCMC chains were run separately for each simulated observational data. After the MCMC chain has converged, we plotted the histogram of

the samples in the chain to obtain the posterior probability density distribution (PPDD) of the period p. We could summarize the PPDD from each simulation using the highest density interval (HDI). 95% HDI is the shortest Bayesian credible interval which includes 95% posterior probability of the estimated quantity. For each observational data set, corresponding to a certain hypothetical period of outburst, gap between the epoch of surveys, and the number of YSOs in the survey we calculate one 95% HDI to represent the estimated posterior probability density of outburst period. Figure 7.4a shows the color bands obtained by connecting together the 95% HDI of the estimated posterior probability density of the outburst period. Each color represents a hypothetical true period in the simulation (in the range 10^4 to 10^5 years, shown in legend of the plots). The x-axis (5 to 100 yrs) is the time gap between the two observations in a two epoch survey of a sample of 9000 YSOs. As expected, the HDI of the estimated period becomes better separated and constrained as the survey time gap increases. Figure 7.4b shows similar HDI bands of different colors corresponding to different hypothetical periods assumed in the simulation. Here the X-axis is the number of YSOs in the simulation. The time gap between two epochs of survey is fixed to be 20 years. As expected, the HDI gets better constrained as the number of YSOs in the sample increases for the 20 year time gap survey. The HDIs plotted in both the figures are median values of the HDIs estimated from all the instances of simulated observational data.

The outburst phase (ϕ_O) parameter has no effect on the detected number of outbursts when the observation time cadences are smaller than the outburst duration. Hence, it cannot be constrained unless we have observations spanning a duration longer than the outburst duration. For the calculations shown above, the outburst phase was taken to be ϕ_O = 0.99, i.e., 1% of the time was spent in the outburst state during one period (duty cycle). When the outburst period is only 10,000 years, a 1% duty cycle implies an outburst duration of 100 years, then the cadence of a 100 year gap survey is comparable to the outburst duration. Hence, if we do not have any intermediate epoch observations, we are under-sampling the light curve, and this could result in artifacts similar to aliasing. This effect is clearly seen in the sudden drop in the lower bound of the HDI of 10,000 year band for the 100 year survey (see Figure 7.4 a; bottom right corner). However, this is not an issue in realistic scenarios. The degeneracy allowing smaller periods to replicate the observation will be removed by any intermediate observation of those YSOs during the 100 year gap. For the sake of simplicity in presentation, the simulations shown here are for two epoch surveys, however, the model has no restriction in adding any number of observational epochs in to the data sample.

As a function of the parameter ϕ_O, this model also provides us an estimate on the number of sources which are right now undergoing an outburst (outbursts which we cannot directly detect from lightcurve observations since they have not undergone any transition).

7.3.2 Expanding the Bayesian network

The model described in the previous section can be easily extended to incorporate a range in the period and/or the outburst duty cycle among various

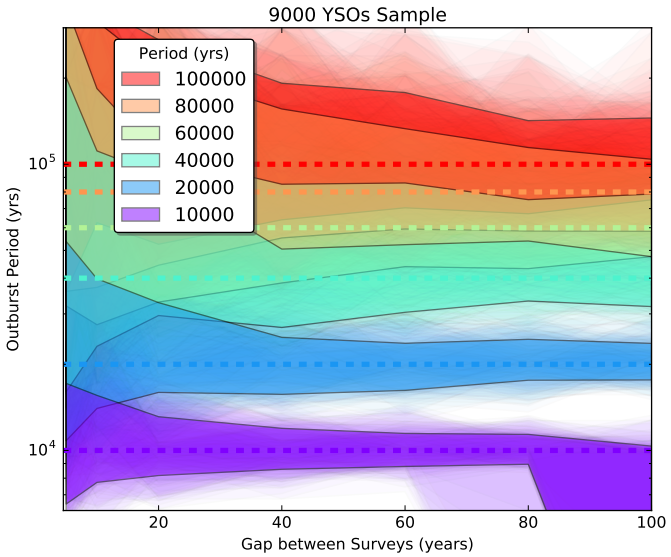

(a)

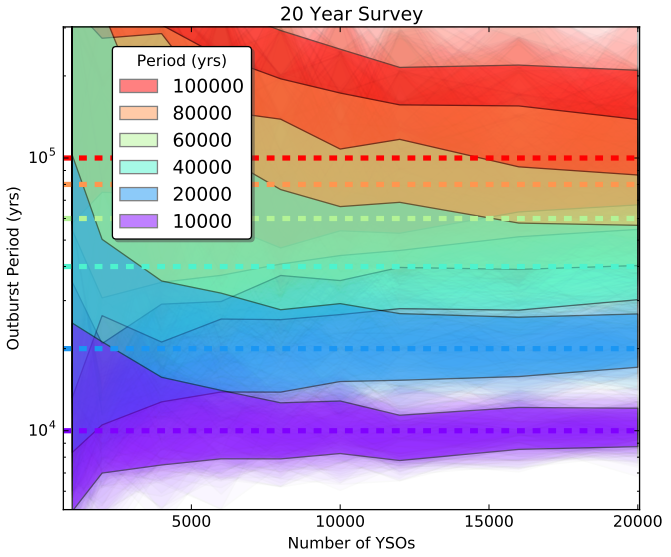

(b)

FIGURE 7.4: a) The evolution of the median 95% highest density interval (HDI) of the inferred period from all the simulated data sets as a function of different time gaps between multiple epoch observations. True periods used in simulations are shown in the corresponding color legend. b) The evolution of the HDI of the inferred period for an increasing number of YSOs in the sample of a 20 year time gap survey. The HDIs plotted in both the figures are median of the HDIs estimated from all the instances of simulated observational data. The individual HDI estimates are also shown in the background as fainter bands. The HDIs of long outburst periods ($> 5 \times 10^4$ yrs) gets well separated only in long baseline surveys or in surveys containing large number of YSOs.

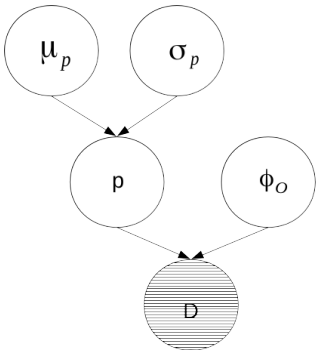

FIGURE 7.5: Added node μ_p is the mean of the normal distribution of the period p, and the node σ_p is the standard deviation of that normal distribution.

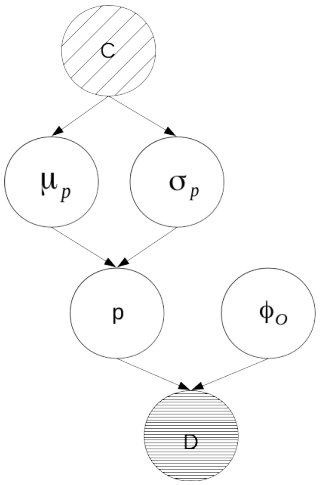

FIGURE 7.6: Added node C represents the probability of the object belonging to each class. Here class could be age classes or clusters.

populations of YSOs. Figure 7.5 shows the extension of the Bayesian network to incorporate different periods among different stars in a cluster or extended sample. The conditional probability table for the period node p is a univariate Gaussian. $P(p \mid \mu_p, \sigma_p) = N(\mu_p, \sigma_p)$, where μ_p is the mean period and σ_p is the standard deviation of the periods in the sample.

One of the major astronomical questions we want to address using our model is whether there is any significant variation in the distribution of the period between different classes of YSOs, or across the YSOs from spatially different clusters of different ages. For this, we add another class node as parent to the μ_p and σ_p which can denote the class each star belongs to.

Figure 7.6 illustrates the full Bayesian network with class C node added. $P(\mu_p \mid C)$, the probability distribution of the mean period when given the input class node value, i.e., the conditional probability table for the μ_p node, is obtained by fitting the data.

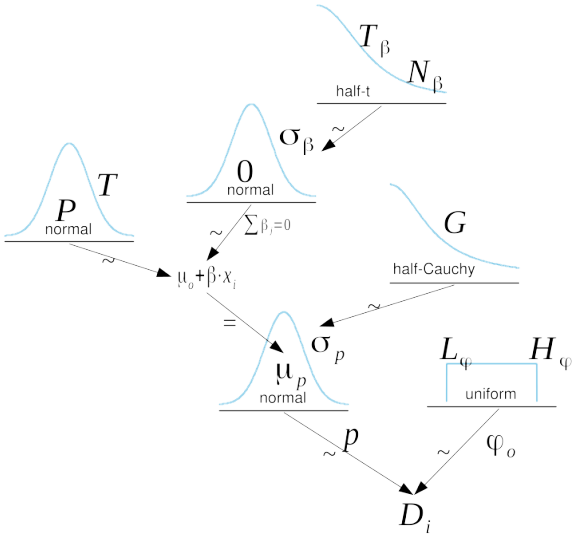

FIGURE 7.7: Kruschke style diagram of the hierarchical Bayesian ANOVA to quantify any significant difference in the mean of the period between various classes of YSOs.

7.3.3 Bayesian ANOVA model

In order to quantify our belief on any significant variation in the period among different classes of YSOs, we modeled a Bayesian version of classical ANOVA (analysis of variance) (Kruschke, 2014). We represent the membership of each star in a class (such as SED type, stellar mass, observation wavelength, cluster, etc.) by a vector x_j. This has dimension equal to the number of categories with the classes. For example, a YSO belonging to the age Class 0 will be represented as (1,0,0), Class I as (0,1,0) and Class II as (0,0,1). We write the mean period of the star belonging to j^{th} class as $\mu_{pi} = \mu_o + \sum_j \beta_j x_j$, where μ_o is the overall mean period, β_j is the amount by which the mean μ_p changes for the class j, and x_j is the vector representing the class the star belongs to. To constrain the sum of the variations from the mean to be zero, we also add the extra condition $\sum_j \beta_j = 0$. The basic structure of this hierarchical model of the Bayesian version of ANOVA is represented by a Kruschke style diagram in Figure 7.7.

Each node in the model is implemented by the corresponding standard distribution function in our *PyMC3* implementation of the model. While the model we have presented here can be easily expanded to a more complicated model, the constraints become weaker as the number of parameters in the model increases. Hence, the complexity of the model has to be decided based on the available data for fitting.

7.3.4 Example simulation

To demonstrate an example of a comparison analysis between multiple classes of YSOs with possibly different periods, in this section we present a multi-class, multi-epoch data simulation. For our fictitious data, we consider a sample of 1000 Class 0, 3000 Class I, and 10,000 Class II YSOs. Since the mid-infrared surveys that have completely characterized the infrared

Light curve	Class 0	Class I	Class II
[0,1]	2	1	
[1,0]	1	1	
[2,2]	997	2998	
[2,2,2]			5000
[0,1,1,1]			1
[1,1,1,0]			1
[1,1,0,0]			1
[2,2,2,2]			4997

TABLE 7.1: Outburst simulation of Class 0, Class I & Class II YSOs

spectral energy distributions and hence classes of YSOs in nearby molecular clouds are only a decade old (Gutermuth et al., 2009; Megeath et al., 2012), let us consider we have two epochs of observations, with a 10 year gap, of our Class 0 and Class I sources. Since Class II sources could also be detected in the 2MASS survey, we have their observations at time gaps of 0, 10 and 20 years. If we consider half of our Class II sources (i.e., 5000 YSOs) were also visible in the optical, then we have observations of those YSOs taken approximately 50 years ago in the last *POSS* survey, or in other optical survey archives.

To simulate a possible observational light curve data set, we arbitrarily take the period of FU Ori type outburst to be 10^4, 3×10^4, and 3×10^5 years for Class 0, Class I, and Class II YSOs, respectively. Using the same procedure mentioned in section 7.3.1, we generate a possible observational data set summarised in Table 7.1.

Our model consists of a hyper-parameter mean period μ_p, which is the mean period across the three classes. zd_p is a vector of three random delta values with mean 0, which when added to μ_p gives the three periods p_0, p_1, and p_2 for Class 0, Class I, and Class II, respectively. Outburst phase ϕ_O was kept fixed at 0.9 in the phase space. Figure 7.8 shows the posterior probability distribution of each of the variables and their trace from the MCMC chain.

As expected, the true periods of each of the classes we used for simulation of the data fall within the posterior probability curves estimated for each period. As we mentioned in section 7.1, Bayesian posterior probability distributions are simple to interpret, and can easily be used to calculate the probability of various comparisons across the classes. For instance, by taking the area of the curve below 0 in the histogram of the difference between any two period traces, we obtain the probability of one being less than the other. In this case, we can quantify that $p_0 < p_1$ with a probability 0.98, $p_1 < p_2$ with a probability 0.97, and $p_0 < p_2$ with a probability 1.

One major advantage of hierarchical Bayesian models like this, is the pooling of information across the groups. For instance, in this example, if the data available for the Class I group is poor, the model can still obtain a good constraint on its period by pooling information from the periods across other classes.

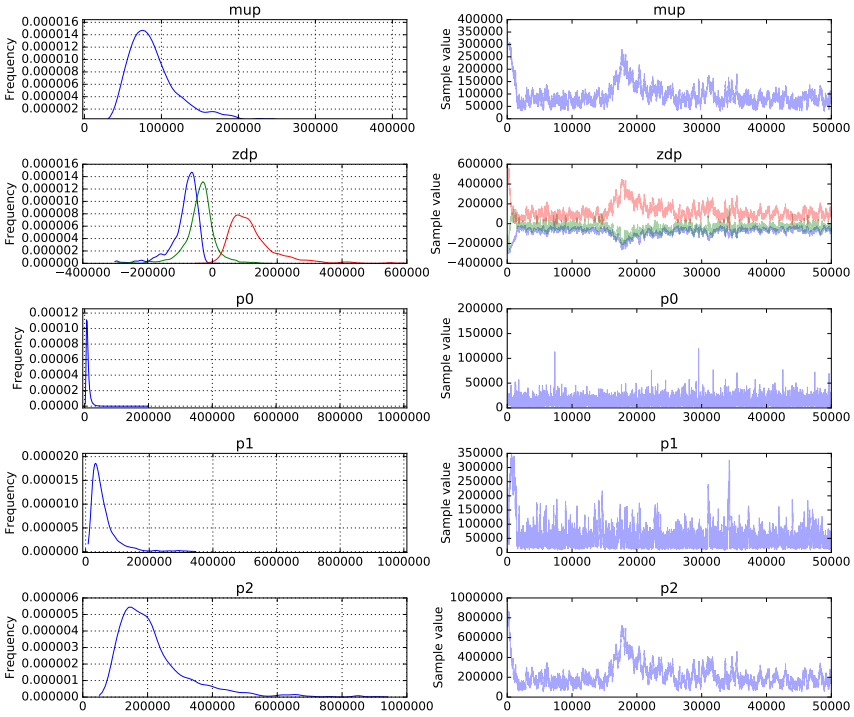

FIGURE 7.8: Histogram (left) and trace (right) of the MCMC sampling of the main variables in our YSO model with three classes. The first row is of the mean period μ_p. The blue, green and red curves in the second row are of the deviations from μ_p of p_0, p_1, and p_2 respectively. The last three rows are of the variables p_0, p_1, and p_2. The histograms on the left represent the posterior probability distributions (PPD), and the traces are shown on the right to convey the quality of convergence in the MCMC run. The PPDs of p_0, p_1, and p_2 show the difference between the outburst periods of Class 0, Class I and Class II YSOs are extractable from the simulation.

7.4 Caveats

In this section, we point out the caveats of the Bayesian model approach to fitting outburst event frequencies in an observational data set.

7.4.1 Non periodicity of the outbursts

It is not likely that the outbursts are strongly periodic or even quasiperiodic (Zhu, Hartmann, and Gammie, 2010; Vorobyov and Basu, 2010). This randomness factor is especially important when the observational cadence is of comparable timescale to the average outburst frequency. In such cases, it is important to have hyper-parameters for the period to model its randomness in a sample (as shown in Figure 7.5). One short period object in a sample of long period objects is enough to completely break a simple single period model. Hence, depending on the data, one should add more layers to the hierarchical Bayesian model. This unavoidably increases the complexity of the model, and will loosen the constraints.

7.4.2 Very slow decay to quiescence

Various disc instability models predict a sharp transition from quiescent to outburst state and also in some scenarios from outburst to quiescence (see Figure 7 in Audard et al., (2014) for a compilation of different models). This was the motivation for adopting a tophat waveform for the model (see Figure 7.2). It is clear from the symmetry of this waveform used in the model that when the period of the outburst is much larger than the typical observational cadence, the probability of seeing a star transforming from an outburst to a quiescence is the same as seeing it transforming from quiescence to an outburst phase. Surprisingly, all the classical FUors which are reported so far in the literature, are those detected to be transforming from the quiescence to the outburst. The other half is unknown in the literature from lightcurve analysis even though they should be there somewhere in the same data archives. Hence, if tophat waveform model is true, then our model implies that there is a correction by a factor of 2 to the estimate of the total number of FUors in the literature. On the other hand, if that is not the case[2], then the rectangular tophat waveform model is not a good representation of the light curve. One can easily update this model to a *sawtooth* pulse waveform to represent such a scenario of slow decay to quiescence. One can identify whether this is representative of the true case, by looking for any statistically significant difference between the number of stars undergoing outbursts to the number of stars transitioning to the quiescent phase in the same data set for a long enough duration survey. Both of these quantities will be statistically similar in case of the sharp transition model. If there are significantly fewer sources undergoing transition to the quiescence than to the outburst, then a *sawtooth* waveform model is implied.

[2] V1057 Cyg is one example among the classical FUors which does not have a tophat shaped flat plateau and a sharp decline in the light curve.

7.4.3 Sampling bias in data

Data included in the modeling have to be carefully vetted to prevent any sampling bias. As in any model fitting, all the estimates of the parameters are strictly representative of only the data sample used. Hence, the data chosen should be a good representation of the sample of YSOs we are trying to model. Selection bias can also occur if the YSO samples are included from the images which are observed after knowing that those regions contain outburst sources. This could result in an over estimation of the outburst rate. This bias can be avoided by making sure all the YSO samples in the data sets are taken from observations not related to any outburst observations. Once a YSO is included in the data sample from an unbiased survey, if more data is found to be observed of the region at a later or an earlier epoch[3], we can still consider those data points in the light curves of the sample of YSOs already included in our data set. In short, no *new* sources should be included from an image which was observed knowing there is an outburst object in the field.

7.5 Summary

In this chapter, we have presented a framework for a powerful, flexible hierarchical Bayesian model which can be used to constrain the period of FUors and EXors outbursts using all the available photometric data. Currently, all the FUors in the literature are those detected transitioning to an outburst phase from their quiescence. If the outburst to quiescence transition timescale of FUors is similar to the quiescence to outburst transition timescale, then our model predicts existing archival data to contain statistically same number of FUors transitioning to quiescence. Using simulations, we have shown that reasonable constraints can be obtained by already existing archival observations of YSOs spread over the last century. Future wide-field telescope surveys such as *ZTF* (Zwicky Transient Factory) and *LSST* (Large Synoptic Survey Telescope) will provide more data to constrain variations in the periods across different classes and clusters of YSOs.

The code for fitting our Bayesian models are publicly released under GNU GPLv3+. Documentation and latest version of the source codes are maintained at `https://github.com/indiajoe/OutburstEstimator`.

[3] which could be because an outburst was reported in that region

Part II

Near Infrared Instrumentation

Chapter 8

TIRSPEC

We started our MFES program using the optical imagers and spectrometers available in the country. However, many of the sources in our program are deeply embedded in their envelope. In the optical band, the central source is heavily extinct, and only a bright reflection nebula is generally visible around it. Hence, near-infrared observations were crucial for studying the inner accretion disc regions of these deeply embedded sources. In order to obtain dynamical measurements of the outflows and the accretion rate in our sources, we had to carry out spectroscopic monitoring of accretion and outflow sensitive spectral lines in the near-infrared wavelengths. At the same time, there was no publicly available near-infrared spectrograph for astronomers in the country. The need was felt for a near-infrared spectrometer, which could be used with one of the 2 m class telescopes available in India. To meet this need, the TIFR Near Infrared Spectrometer and Imager (TIRSPEC) (Ojha et al., 2012) was conceived. Aim of this instrument was to provide capability to do spectroscopy in the 1.0 to 2.5 μm band with a medium spectral resolving power of $\sim$1200. It was designed to be used on one of the side ports of the 2 m HCT at Hanle (Ladakh) (4500 m amsl, Figure 8.1), along with the existing optical Hanle Faint Object Spectrograph and Camera on the main port, to allow for near simultaneous observations in the optical and near-infrared bands.

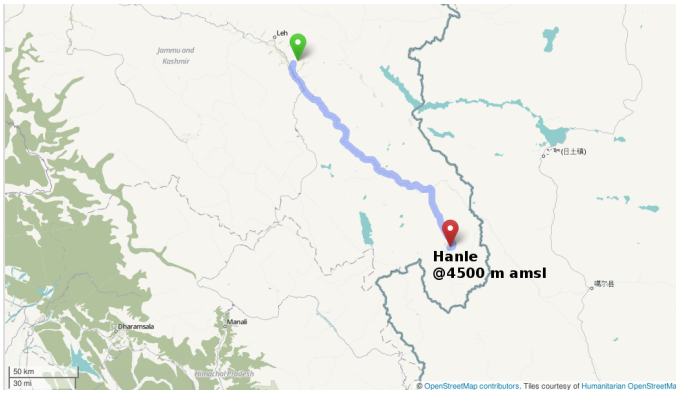

FIGURE 8.1: Location of 2 m HCT in Indian Astronomical Observatory, Hanle, India (78.9641 E, 32.77944 N, 4500 m amsl). Image Courtesy: Open Street Map

TIRSPEC was developed in collaboration with M/s. Mauna Kea Infrared, LLC (MKIR), Hawaii, USA, to provide both imaging as well as spectroscopic capabilities in the 1.0 to 2.5 μm near-infrared wavelength range and was designed around a Teledyne 1024 $\times$ 1024 pixel HAWAII-1 PACE

array detector as the focal plane array. When mounted on the side port of the 2 m HCT, the field of view (FoV) in the imaging mode is $307'' \times 307''$ with a plate scale of $0.3''$/pixel, while in the spectroscopic mode it covers a wavelength range from 1.0 to 2.5 μm with a spectral resolving power of $\sim$1200. The first light for this instrument on the HCT was observed on June 21, 2013 and after the characterization and engineering observational runs, the TIRSPEC was released to the worldwide astronomical community for science observations from May 1, 2014.

In this chapter, I describe the technical details of TIRSPEC (Section 8.1), and also the characterization and performance analysis I did before releasing the instrument to the users for scientific observations (Section 8.2). I also present the performance analysis of TIRSPEC as related to the Hanle telescope site and some samples of the science observations conducted during the engineering runs (Section 8.3). I conclude with the present status of the instrument in Section 8.5. The work presented in this chapter is published in Ninan et al., (2014).

8.1 Instrument Overview

8.1.1 Structure

The TIRSPEC has an overall envelope size of 481 mm (width) $\times$ 600 mm (length) $\times$ 500 mm (height). The cryostat is designed as a double bath-tub which allows all the vacuum penetrations to be from the top plate of the cryostat. Figure 8.2 shows an exploded view of the cryostat with the outer cube providing the vacuum jacket. The optical bench is mounted within

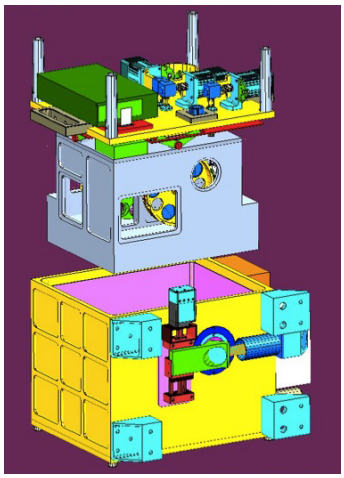

FIGURE 8.2: Exploded front view of the TIRSPEC cryostat. The yellow tub and top plate are the outer vacuum jacket. The pink color shields are floating radiation shields. The grey enclosure is the LN2 cooled enclosure which houses the optics.

the liquid Nitrogen (LN2) cooled enclosure which hangs inside the outer vacuum jacket from 4 rigid fiber-glass V-trusses connected to the top plate. Thermally insulated mirror finished floating shields line the inner side of the vacuum jacket to provide good radiation shielding and to improve LN2

hold time. The LN2 tank can hold about 8.6 liters of LN2 which provides a hold time of more than 36 hours at the observatory site. The array controller electronics and the power supply for the motors and electronics are mounted on one side of the cryostat. The three motors for the slit wheel and the two filter wheels are mounted on the outer side of the top plate and are coupled to the filter and slit wheels through right angled gears and ferrofluidic vacuum feed-throughs. A calibration lamp assembly provides for spectral line calibration of the spectrometer using an argon lamp with a movable plane mirror which can be moved in and out of the optical path using an Animatics SmartMotor and linear stage arrangement. The calibration box also hosts a tungsten lamp for continuum flats with an integrating sphere.

8.1.2 Optics

TIRSPEC's optics were designed to be used on the side port of the 2 m HCT to provide an image scale of 0.3″/pixel covering a FoV of 307" x 307". Figure 8.3 shows the layout of the optics. The f/9.2 beam from HCT enters

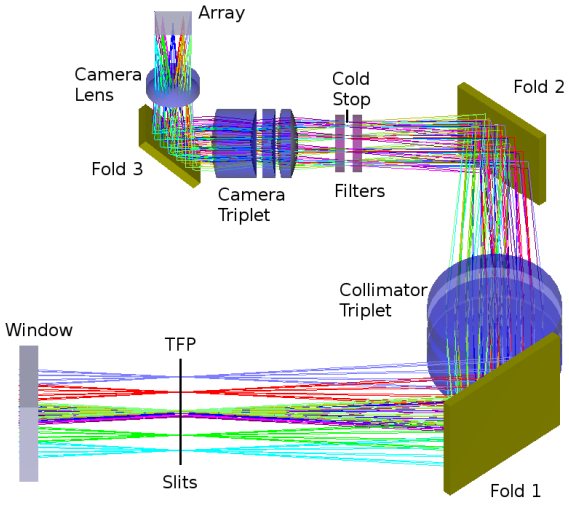

FIGURE 8.3: TIRSPEC's folded optics design.

the instrument via the CaF_2 window. At the telescope focal plane (TFP) there is a 11 position slit wheel which has 5 short slits (50″ length)[1] and 5 long slits (300″ length) with slit widths of 0.9″, 1.48″, 1.97″, 2.96″ and 7.92″, as well as one open position for the imaging mode. A collimator system consisting of a BaF_2-LiF-BaF_2 lens triplet is used to obtain a good quality achromatic image of the telescope aperture at the cold stop which is sandwiched between two 12 position filter wheels. The first filter wheel has broad band filters (J, H, K_s) and order sorter filters (Y, J, H, K) and two cross dispersing grisms (HK and YJ). The second filter wheel has seven narrow band filters, one grism, a block for taking dark images and an open position. Table 8.1 lists the details of the imaging filters and Figure 8.4 shows the transmission curves of all the available imaging and order sorter filters.

[1]During the initial installation we had used 10″ slits, but it was found to be inadequate for proper sky subtraction. Hence, during our second repair mission we upgraded the slits to 50″ .

The collimated beam is then imaged on to the focal plane array detector using a BaF_2-LiF-$ZnSe$ triplet lens and a BaF_2 singlet lens. To fit the entire optics inside the LN2 cooled enclosure, the optical path is folded at three locations using gold coated fused silica plane mirrors.

The focal plane array used in TIRSPEC is a HAWAII-1 PACE Array[2], manufactured by *Teledyne Scientific & Imaging, LLC, USA*. It is a 1024 x 1024 array, with a pixel size of 18 μm square and has a cutoff wavelength of 2.5 μm. The array has HgCdTe detector layer on top and a silicon readout layer below which contains readout amplifiers and associated circuits. Both the layers are connected by indium bumps at each pixel (Hodapp et al., 1996; Rieke, 2007). The array has four quadrants which are read out simultaneously. Read out starts from the bottom left corner pixel to the top right corner pixel of each quadrant at a rate of 3 μs/pixel. The detector is operated at a temperature of 76-77 degrees K at Hanle (Ladakh).

TABLE 8.1: Imaging filters of TIRSPEC.

Filter	Band pass (μm)
J	1.17 - 1.33
H	1.49 - 1.78
K_s	1.99 - 2.30
Methane off	1.584 (3.6 %)
[Fe II]	1.645 (1.6 %)
Methane on	1.654 (4.0 %)
H2 (1-0) S(1)	2.1239 (2.0 %)
Br γ	2.166 (0.98 %)
K-Cont	2.273 (1.73 %)
CO (2-0)	2.287 (1.33 %)

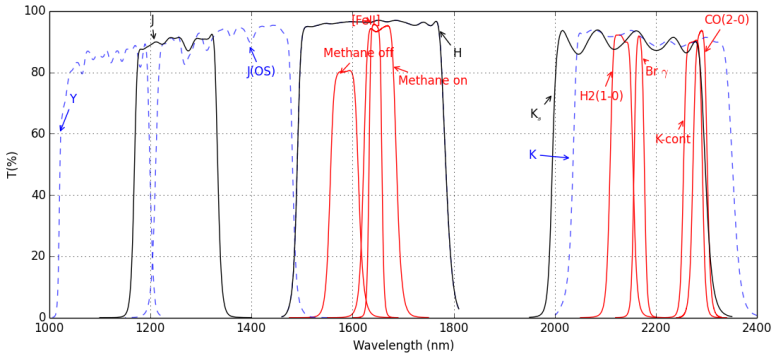

FIGURE 8.4: Transmittance curves of various filters on TIRSPEC. The black curves are the broad band J, H and K_s filters, the red curves are the narrow bands, and the blue dashed curves are the order sorters for spectroscopy.

[2]HgCdTe Astronomy Wide Area Infrared Imager - 1, Producible Alternative to CdTe for Epitaxy

Spectroscopy using TIRSPEC can be done using the single order mode or the cross dispersed mode. In both modes, a *YJHK* grism is positioned in the second filter wheel. This grism has a groove width of 12.4 μm and a prism angle of 21.9^o which disperses *Y*, *J*, *H* and *K* in its 6th, 5th, 4th and 3rd orders respectively. To obtain the spectrum of each order separately, in the single order mode, the corresponding order sorter filter is positioned in the first filter wheel which blocks the other orders.

In the cross dispersed mode, we can simultaneously obtain spectra in two orders. Two modes are provided which cover the *Y* and *J* windows or the *H* and *K* windows. This is accomplished by positioning the *YJHK* grism in one filter wheel and a cross dispersing grism in the second wheel. The cross dispersing grism is mounted 90 degrees rotated with respect to the *YJHK* grism and has a custom order sorter filter that covers both orders. The first order dispersion of the *YJ* cross dispersed grism with groove width of 6.2 μm and a prism angle of 8^o is used to obtain cross dispersed *Y* and *J* spectrum. Similarly, the first order dispersion of the *HK* cross dispersed grism with groove width of 15.4 μm and prism angle of 5^o is used to obtain cross dispersed *H* and *K* spectrum. All the grisms are directly ruled grisms. Table 8.2 shows the wavelengths covered in each mode.

TABLE 8.2: Wavelength coverage in different spectroscopy modes.

Spectroscopy Order	Wavelength Range (μm)
Y	1.02 - 1.20
J	1.21 - 1.48
H	1.49 - 1.78
K	2.04 - 2.35
*YJ**	1.02 - 1.49
*HK**	1.50 - 1.84 & 1.95 - 2.45

* *YJ* and *HK* are cross dispersed modes.

Note: 1.84 to 1.95 μm is not part of the spectrum in *HK* due to their dispersion being outside the physical dimensions of the detector array.

8.1.3 Electronics and Control systems

The HAWAII-1 PACE array is controlled by an *ARC Gen III array controller* (also known as Leach Controller or SDSU Controller) from *Astronomical Research Cameras, Inc. (ARC), San Diego, USA*. The array is mounted on a Fanout Board inside the cryostat. The image data is sent to the *ARC-46: 8-Channel IR Video Processor* in the array controller box mounted at the side of the TIRSPEC cryostat where it is amplified and digitized. The *ARC-32 CCD and IR Clock Driver Board* provides the clocks to the array and the controller boards. The *ARC-22: 250 MHz Fiber Optic Timing Board, Gen III* generates the waveforms as well as communicates with a PCI (Peripheral Component Interconnect) interface board, the *ARC-64: 250 MHz PCI Interface board, Gen III* mounted in the TIRSPEC control computer, via a duplex fiber optic cable link which transfers data and commands between the computer and the

array controller box. The cryostat and array temperatures are monitored using a *Lakeshore temperature controller Model 335*.

The slit wheel, filter wheels and calibration box mirror are moved using independent SmartMotors manufactured by *Animatics Corporation, Milpitas, USA*. The motors are controlled through a standard Ethernet interface. The slit wheel and filter wheels have a spring loaded detent mechanism with a thin film Hall sensor to detect the position of the wheel.

8.1.4 Software

The TIRSPEC instrument is controlled from the TIRSPEC control computer using the main control software. The TIRSPEC control computer is connected to two independent networks with one being used to communicate with the observatory network for remote access, and the other being used to communicate with the TIRSPEC components which includes the Animatics SmartMotors and the TIRSPEC power control switches. The overall structure of the instrument control software is shown in Figure 8.5.

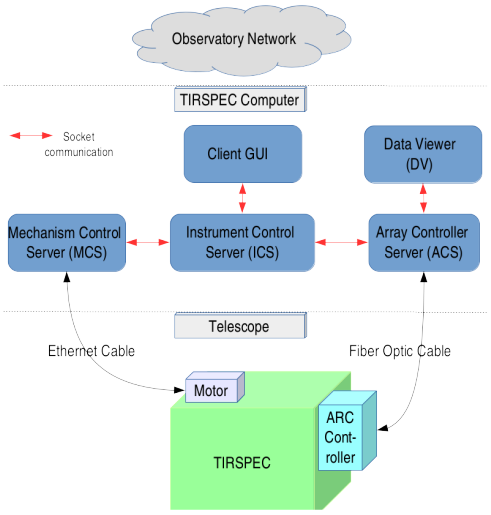

FIGURE 8.5: Overall structure of TIRSPEC instrument control software

The Instrument Control Server (ICS) software is the central server which controls all the other servers. It communicates with the other servers via UNIX style sockets. The ICS receives commands from the client graphical user interface (GUI) as well as returns instrument status to the GUI. When the client requests a particular filter to be in position, the ICS receives the command from the GUI and, if it is a valid command, it sends the instruction to the Mechanism Control Server (MCS). The MCS talks via the Ethernet link with the corresponding Animatics SmartMotor which turns the filter wheel to the desired position. When the client requests an exposure of a specified integration time, the ICS receives the command, and if the system is ready, it sends the instruction to the Array Controller Server (ACS). The ACS talks via the ARC application programming interface (API) to the ARC controller. The ARC device drivers and API are highly customized versions of the standard code provided by *Astronomical Research Cameras,*

Inc. Once the CPU receives an interrupt from the PCI board after the data is fully written to the system memory, ACS generates a FITS[3] image from the raw data and saves it to the hard-disk in standard FITS format. It also sends the data via a socket to the quick look viewer software DV[4]. DV has tools to do basic image arithmetic as well as quick measurements to check image quality.

Readout mode and image generation

When an exposure is not being taken, the array is continuously reset globally. At the beginning of any exposure, the reset pulse is stopped and the detector is read out non-destructively. The detector can be read out in various modes. For optimal results, the sample-up-the-ramp (SUTR) readout mode has been chosen as the default mode. The pixels are read at a rate of 3 μs per pixel and since all four quadrants of the detector are read out simultaneously, it takes 0.9 seconds to complete one full read out of the array. For an integration time I, the actual exposure time is automatically adjusted to the nearest multiple of 0.9 second and the actual integration time used is written to the header of the data file. A total of $I/0.9$ non-destructive readouts of the cumulative counts in the array pixels are executed during the duration of the exposure. Thus, the raw data for each exposure is a data cube with the pixels on the two axes and time on the third axis. The flux in each pixel is then calculated by fitting a slope by linear regression to this SUTR readout data cube along the time axis. Due to the reset anomaly discussed later in Section 8.2.2, one needs to subtract the dark readout cube from the image data cube before linear slope fitting. The SUTR readout technique gives us unique capabilities to recover data from cosmic ray (CR) hits and saturation.

Cosmic ray hit healing

HCT at Hanle (4500 m amsl) is prone to much higher CR hits than lower altitude observatories. Since the SUTR readout has time resolved data, the readout counts before and after a CR hit can be used to retrieve the slope of the flux at that pixel. Figure 8.6 shows the typical SUTR readout generally seen for a CR hit. The sudden jump in the ramp can be detected using a digital filter shown in the inset of Figure 8.6. This filter is created by convolution of a first difference filter and a Mexican hat filter. After identifying the CR hit location, the slope in linear sections of the SUTR data is estimated and averaged (weighted by the error in slope of each section).

Saturation healing

Another advantage in using the SUTR readout is that saturated pixels can be selectively discarded. This is especially useful when observing fields which have both bright and faint stars. The flux is estimated using only the readouts during the linear regime of the pixels containing bright saturating stars, while for the remaining pixels, the entire data is used. This effectively increases the dynamic range of the detector beyond the actual well depth.

[3]Flexible Image Transport System
[4]Data Viewer by NASA Infrared Telescope Facility (IRTF), Hawaii, USA

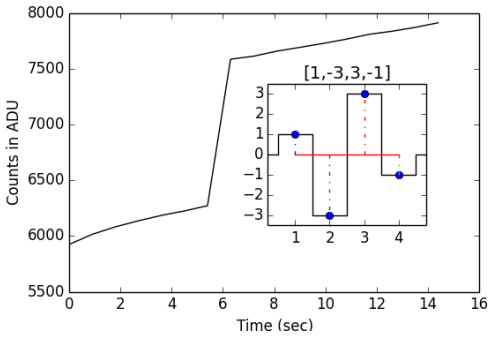

FIGURE 8.6: CR hit between the 5^{th} and 6^{th} seconds during an SUTR readout exposure. The inset shows the digital filter used to detect these events.

Non-linearity correction

From SUTR readout data we have estimated the non-linearity correction coefficients for each pixel, which can be applied to reconstruct the data beyond 1% non-linearity. This has not been done by default to any of the data. In general, all the data beyond the linear regime is discarded before fitting the slope.

8.2 Characterization and Performance

8.2.1 Dark current

Dark current noise determines the sensitivity limit we can attain in the spectroscopy mode. Unlike the imaging mode, the noise in a faint star continuum signal is dominated by dark current and effective readout noise. Dark current is measured by reading out the array cooled to 77 K (normal operating temperature) with the cold block filter in the second filter wheel.

The measured dark current has an exponential fall off at the beginning of the exposure. This high value at the beginning is due to the reset anomaly of the detector and is not due to high dark current. The reset anomaly is discussed in more detail in Section 8.2.2. Hence, the actual dark current of the instrument is estimated only after the detector output has stabilized. A straight line fit to the readout values after skipping the first 27 sec of data from the start of the exposure up to 100 sec gave a dark current value of 0.032 ADU/sec. This multiplied by gain (see Section 8.2.4) gives us an estimate of the dark current $\sim$ 0.19 e^-/sec. This value matches with estimates of dark current by others on similar HAWAII-1 PACE 1k x 1k Array (Acosta-Pulido, Dominguez-Tagle, and Manchado, 2003). Stability of dark current over a time scale of one night was tested to decide the number of dark frame readouts needed to be taken during each night. It was found that it would be enough to take a few sets of dark frame readouts at the beginning and end of each night.

8.2.2 Reset Anomaly

The HAWAII-1 PACE array has been known to have a non-linear behaviour immediately after the detector is reset (Finger et al., 2000; Acosta-Pulido, Dominguez-Tagle, and Manchado, 2003). In spite of resetting at the same frequency as the readout, to reduce the effects of the reset anomaly as suggested by Riopel et al., (2004), we still see the reset anomaly in our readouts. The green curve in Figure 8.7 shows the non-linear output obtained in the dark readout due to the reset anomaly. Since this is a strong function of

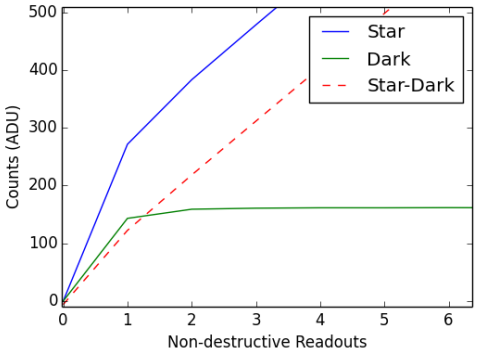

FIGURE 8.7: The linear slope in sample-up-the-ramp (SUTR) readout. Blue curve shows the readout of a pixel exposed to star and green line shows the dark readout. Red dashed line is the linear readout which is recovered after subtracting the non-linear dark in image data cube.

the time that has elapsed since the reset at the beginning of exposure, we get a vertical gradient in the raw image frames in each of the quadrants as shown in Figure 8.8. One solution to this anomaly is to take long exposures

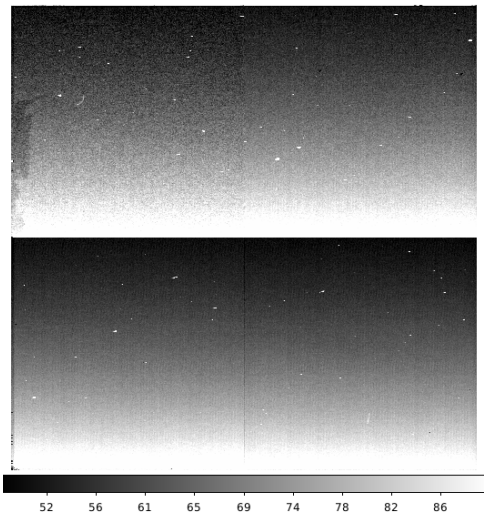

FIGURE 8.8: The vertical gradient in each quadrant of the raw image due to the reset anomaly in a 4 sec dark exposure. This gradient in the raw image can be removed fully by dark subtraction.

and discard the first few readouts. But, this cannot be done for imaging in the *H* and *K* bands or for bright stars due to saturation. Hence, it is crucial to decouple this non-linear readout portion to obtain the true linear slope corresponding to the flux. This non-linear behaviour was found to be an additive effect, and can be subtracted out to obtain the linear curve corresponding to the actual flux falling on the detector. Figure 8.7 shows the linear curve (red dashed line) recovered after subtracting the dark readout (green curve) from the raw readout curve (blue curve). Finger et al., (2000) had also shown this additive nature of the reset anomaly.

To study the noise statistics of these large counts obtained at the initial seconds of the exposure, multiple dark SUTR readouts were taken and the dark current versus the variance were plotted. If the large counts obtained in the initial seconds of the exposure are due to dark current, we expect a Poisson noise variance in them. Figure 8.9 shows the counts versus the variance. Blue dots are points corresponding to pixels from a good 100x100 subarray of pixels with origin at (400,400) of the full array. The red squares correspond to the mean of the blue points corresponding to each set of readouts. The plot shows the red points are almost constant and do not increase linearly with the counts. The green dashed line shows the expected increase in variance if the counts had Poissonian statistics, as a function of the counts. This implies that the reset anomaly does not have any significant contribution in the final noise of the data if we just discard the first few readouts (see Section 8.1.4).

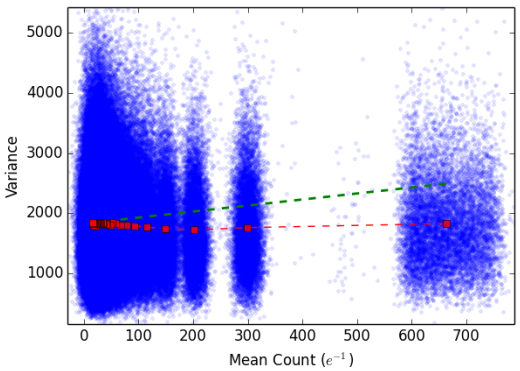

FIGURE 8.9: Variance versus mean counts. The green dashed line shows the expected increase if the counts are of Poissonian statistics like dark current, and the red squares represent the measured variance obtained by averaging of the blue points, each representing pixels in a 100 x 100 subarray with origin at (400,400) in the full array.

8.2.3 Readout Noise

Readout noise mainly comes from the amplifier noise in the electronics circuits. These were found to be uncorrelated in our 0.9 sec readout time interval of each pixel during an exposure. Since dark current was found to be very small compared to the readout noise after 27 sec of integration, we used the difference of consecutive frames in SUTR readout of a dark frame,

to estimate $\sqrt{2}$ times readout noise. The readout noise was found to be different for each quadrant. Figure 8.10 shows the histogram of readout noise for single readout of different pixels in the array. The mean readout noise

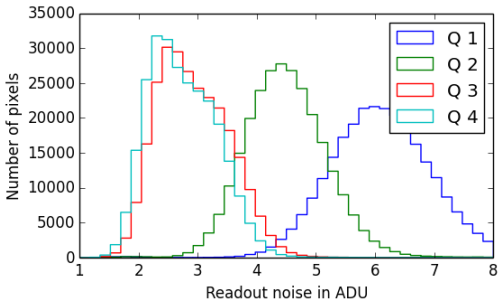

FIGURE 8.10: Histogram of readout noise for single read out in the array. The four histograms correspond to the four quadrants in the array.

for single readout for each quadrant is 6.1, 4.5, 2.9 and 2.8 ADU, with an average value of 4.1 ADU (i.e. ~ 25 e$^-$) for the full array. It should be noted that this value is the readout noise for a single readout, hence readout noise contribution in the flux estimate is usually much less than this, and it is a function of the number of readouts in a single exposure and flux. Detailed treatment of error contribution of readout noise in flux calculation in SUTR (line-fitting) mode is available in Robberto, (2007).

8.2.4 Gain

Gain is the multiplicative factor which converts ADU counts obtained from the detector array to electrons. This is crucial to estimate the actual photon counts obtained to estimate photon noise. For measuring the gain, we took multiple exposures of different exposure times with the array exposed to the telescope enclosure with the *K* filter. Since the thermal flux from the telescope is stable over the short duration of our exposures, these images are purely photon noise limited. For each pixel we calculated the slope of ADU flux counts versus variance. Since photon noise follows Poisson statistics, actual electron counts versus variance will have a unity slope. Hence, the multiplicative gain factor was calculated by taking the inverse of the slope in ADU counts versus variance plot. Figure 8.11 shows the histogram of the gain obtained for each pixel in the array. The median gain of the detector was found to be $\sim 6\ e^-/\text{ADU}$.

8.2.5 Saturation level (Linear range)

Unlike optical CCDs, near-infrared detectors have strong non-linearity near the saturation level of the pixels. Each pixel saturates and deviates from the linear regime at slightly different counts. Using the SUTR readout data, we estimated the upper limit of the linear regime for each pixel separately. The median saturation point of the pixels was found to be at ~16000 ADU, subtracting the median bias level of ~5700 ADU, gives us an effective well depth of $\sim$ 10300 ADU ($\sim$ 61800e^-). By default, all the data in the non-linear regime are discarded, but we have added a provision in the data

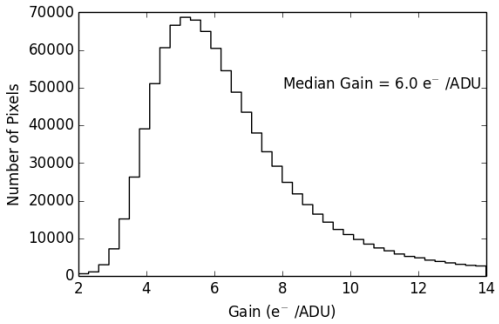

FIGURE 8.11: The histogram of ADU to e^- gain of each pixel in the array.

reduction software for users to do non-linearity correction in the non-linear regime and save the corrected data if needed (see Sections 8.1.4 and 8.4).

8.2.6 Bad, Hot and Cold pixels

Bad pixels are defined to be those pixels in the array which deviate more than 8σ from the median value in the image obtained by dividing two flats taken in high and low incidence flux. This set includes all the pixels whose gain is varying with time or are completely dead. In our detector array, most of such pixels are along the edges. The percentage of the bad pixels in the array is 0.1%. Apart from this, during some of the nights, the vertical single strip of pixels at column position 512 (at the border of the quadrants) was also found to have a varying gain. Hence, we avoid objects falling on that column during our observations.

Hot pixels are defined to be pixels which have counts more than 8σ above the median value in a dark readout of 100 sec. Their fraction was found to be 2.3% (most of them are located at the four quadrant corners heated by the glow from the nearby readout transistor). Similarly, cold pixels (pixels which have counts less than 8σ below median value in dark) fraction was found to be 0.07%. It is to be noted that only a subset of cold and hot pixels are actually bad pixels, which need to be masked, and the remaining can be corrected by flat fielding and dark subtraction. For robustness of all the above calculations, standard deviation σ was estimated from the median absolute deviation.

8.2.7 Spectral resolving power

The reciprocal linear dispersion of TIRSPEC in spectroscopy mode is $\sim$4.7 $\mathring{A}$/pixel. The effective spectral resolving power of the spectra in each order was estimated by finding full-width-half-maximum (FWHM) of argon lamp lines through the narrow slit of 0.9" width. Figure 8.12 shows the median $\lambda/\Delta\lambda$ spectral resolving power along the slit obtained from argon lines as a function of wavelength.

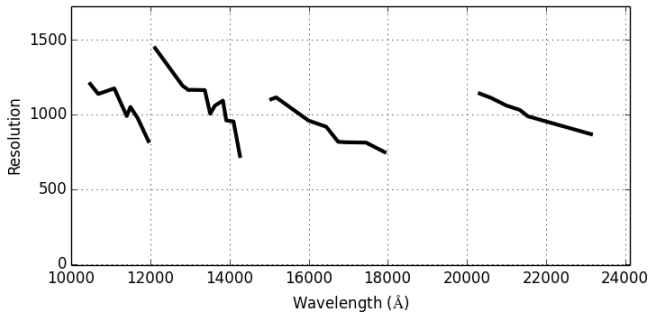

FIGURE 8.12: Median spectral resolving power measured as a function of wavelength from the argon lamp spectrum.

8.2.8 Fringe issue

Spectra in *K* band show fringes in the detector. HAWAII-1 PACE arrays are known to have this issue due to interference in the sapphire substrate on which the HgCdTe detector material is grown (Hodapp et al., 1996). Figure 8.13 shows the normalized strength of fringes seen in *K* band of 0.9" slit spectrum. The fringe pattern was found to be stable and its Fourier transform gave a typical wavelength scale equivalent to $\sim$ 36 $\mathring{A}$ in dispersed spectrum. Since this is close to our typical stellar line widths, it is not safe to use any Fourier transform based fringe removal technique. However, since the fringes are stable, it can be removed by normalizing with contemporaneous flat and standard star spectra taken at the same position along the slit.

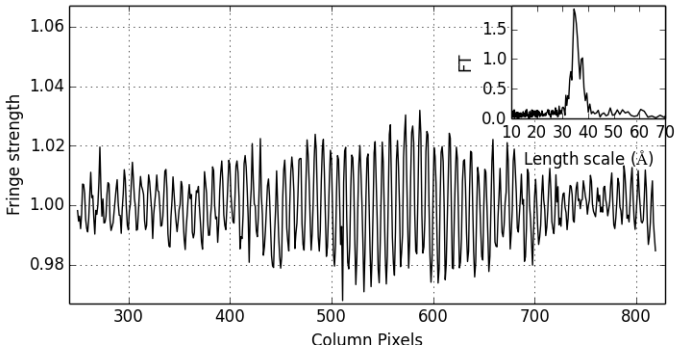

FIGURE 8.13: Normalized fringe pattern seen in *K* band spectrum. Fourier transform of the fringe pattern (shown in inset) gave the spatial size of fringes to be $\sim$36 $\mathring{A}$.

8.2.9 Persistence issue

HAWAII-I PACE array detectors are known to have strong persistence and this leaves a slowly decaying persistence image if exposed to very bright light. The time scale for decay of the persistence image is a function of the strength of bright light which caused persistence. A shift of 23 pixels perpendicular to the dispersion direction in the position of the spectrum by the

grism in TIRSPEC avoids the spectrum from overlapping on the persistence of bright star image taken for centering the star in the slit.

8.3 Performance on HCT

8.3.1 Plate Scale and Field of View

We matched 2MASS coordinates of stars in the selected near-infrared standard star fields catalog (Hunt et al., 1998) to the pixel coordinates in the TIRSPEC image. The WCS submodule in Astropy[5] and optimize submodule in Scipy[6] was used to fit the world coordinate parameters by least square minimization. The plate scale of TIRSPEC images obtained is 0.30 arcsec/pixel. With the measured plate scale, we obtain a FoV of 307 $\times$ 307 arcsec^2 ($\sim$ 5 $\times$ 5 arcmin^2) for the 1024$\times$1024 array.

8.3.2 Sky background

In near-infrared, where the sky is almost 800 times brighter than in the optical, the faint magnitude limit in the imaging mode is limited by photon noise from the sky background. To estimate the sky brightness at HCT, we observed near-infrared standard star fields from Hunt et al., (1998) on various nights. The sky brightness in H and K bands was found to vary depending on the humidity during the nights. This is expected, since the major contribution of flux in the H band comes from water and OH telluric lines. The median values of sky brightness obtained in good night conditions are the following: J = 16.14 mag/arcsec^2, H = 13.70 mag/arcsec^2, K_s = 13.35 mag/arcsec^2 and K = 13.20 mag/arcsec^2. These are comparable to other good sites like Mauna Kea (4145 m amsl) and Paranal (2635 m amsl).

The other important related parameter is the time scale of variation in sky brightness. This determines how fast one should observe separate sky frames, to subtract from object frames (especially while observing diffuse/extended emission regions). Time scales also vary considerably from night to night. To obtain typical time scales, we monitored the sky brightness of one region continuously in intervals of 17 seconds. Figure 8.14 shows the auto-correlation of sky brightness in the J, H and K_s filters. The e-folding time scale in auto-correlation is $\sim$600 sec in the H and K_s bands at HCT site, whereas the time scale is longer in the J band.

8.3.3 Throughput of the entire system

The throughput of the entire system was measured by counting the total flux from standard stars over an area of 4 times the FWHM of their profile. The image mode throughput percentage is 16 $\pm$ 5 %, 20 $\pm$ 5% and 20 $\pm$ 5% for the J, H and K_s bands respectively. This percentage corresponds to the net throughput and it includes the atmosphere, telescope mirrors, instrument optics and quantum efficiency (QE) of the detector. These values are consistent with our initial theoretical estimate of throughput. Spectral throughput is difficult to measure by this method, because of the difficulty in placing the star at the exact center of the slit every time. However, we

[5] Astropy Collaboration et al., (2013)

[6] Scipy is a standard package for scientific computing with Python (Oliphant, 2007)

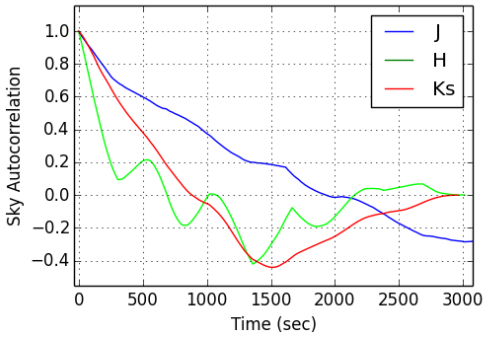

FIGURE 8.14: Blue, green and red curves show the auto-correlation of the J, H and K_s sky brightness respectively. The e-folding time scale gives the typical time scale in which sky brightness varies at the HCT site.

have a theoretical estimate of the spectral throughput to be 30%, which does not include the QE of the detector and the slit losses.

While the cross dispersed mode of spectroscopy has the huge advantage of simultaneously taking two orders of spectrum and even slightly extended wavelength coverage at the 2.4 μm end, there is a trade off in the net throughput between the single order and the cross dispersed modes due to the additional grism. Figure 8.15 shows the measured fractional throughput of the cross dispersed mode relative to the single order mode. This was obtained by taking the ratio of the continuum tungsten lamp spectra in the single and cross dispersed modes through the same slit.

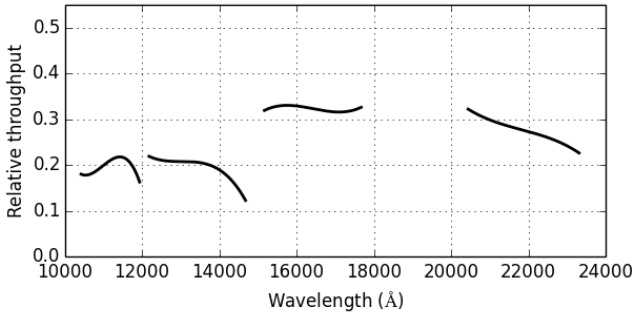

FIGURE 8.15: Four curves showing throughput in the cross dispersed mode normalised with respect to the corresponding single order mode in each band. This fractional reduction in net throughput is due to the additional grism used in the cross dispersed mode.

8.3.4 Photometric sensitivity

The estimate of the limiting magnitude depends on the seeing conditions. During our instrument calibration nights, FWHM of the star profile was never below 1.4" in the K_s band. To estimate the photometric sensitivity, we observed crowded standard star fields (Hunt et al., 1998) and obtained

the estimated magnitude versus magnitude error plot. Figure 8.16 shows the J, H and K_s magnitudes versus their magnitude errors obtained for the sources in the AS 40 field (Hunt et al., 1998) for 170 sec of exposure at 40^o elevation on a night with seeing of 1.8". The photometry was carried out with an aperture of radius 1 FWHM.

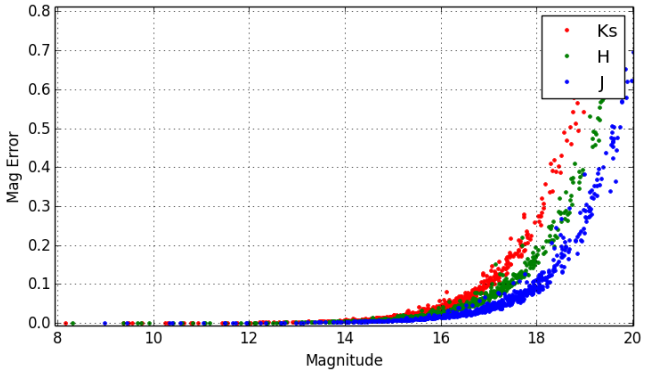

FIGURE 8.16: J, H and K_s magnitudes versus magnitude errors plot for the sources in the AS 40 field, taken with 170 sec of total exposure. The photometry was carried out with an aperture of radius 1 FWHM.

Figure 8.17 shows the exposure time required for 0.1 mag error (10%) photometry for various star magnitudes on a typical night. It is generated by calculating the signal-to-noise (S/N) ratio for slope fitting (Robberto, 2007) and integrating the entire S/N ratio contribution for a given Gaussian star profile of FWHM=1.6" and photometric aperture of radius 1 FWHM.

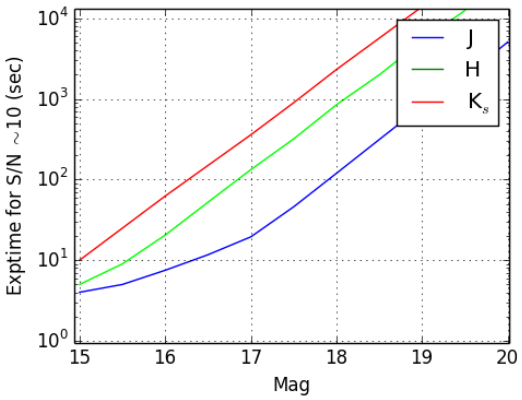

FIGURE 8.17: Exposure time required for 0.1 mag error (10%) photometry versus star magnitudes in the J, H and K_s bands.

Exposure time calculator

The S/N ratio calculation in the SUTR readout is slightly more complicated than simple double-correlated readouts. We have made an exposure time

calculator for TIRSPEC, which first creates a model star profile based on seeing conditions, star magnitude, sky brightness and zero point magnitude of TIRSPEC. The S/N ratio for a set of aperture radii is then numerically calculated using gain, readout noise and number of non-destructive readouts in the exposure using the error propagation formula of the SUTR mode (see Robberto, (2007) for the equations). Figure 8.18 shows the screenshot of this tool.

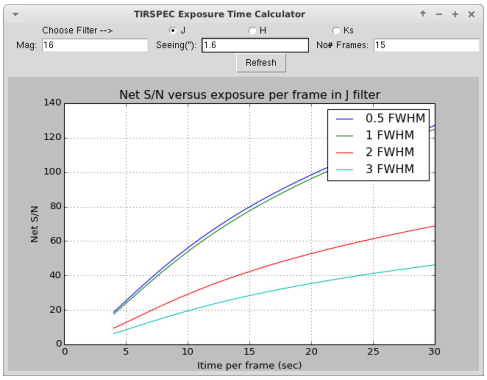

FIGURE 8.18: Screenshot of the S/N ratio estimator. Various curves show the S/N ratio that can be obtained for corresponding photometry aperture radius as a function of exposure time per frame.

8.3.5 Spectroscopic sensitivity

Attainable spectroscopic sensitivity for different magnitudes were estimated by taking spectra of faint stars. Figure 8.19 shows various estimates of exposure time required for a continuum S/N $\sim$ 10 in single order mode. It is quite sensitive to the FWHM of the star profile as well as the accuracy in centering of the star inside the slit. We have found that spectra of stars upto 12 mag in the *J*, *H* and *K* bands can be obtained under typical (1.6" seeing) night conditions.

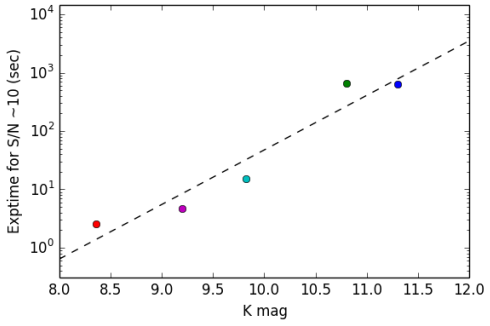

FIGURE 8.19: Various estimates of exposure time required in single order mode for S/N $\sim$10 in continuum in the *K* band versus *K* band magnitude of the source on typical nights observed from HCT site.

8.3.6 Color equations

For accurate (1%) broad band photometry, we need to correct for the filter response with stars of different color. Coefficients of 1^{st} order color equations were obtained by fitting a straight line to magnitude zero points of standard stars with a wide range of colors. To establish the color equations, we have observed the color ranges from 0.45 to 2.5 for *J*-K_s, 0.35 to 1.76 for *J*-*H*, and 0.06 to 2.83 for *H*-K_s. To improve the statistics, we simultaneously fitted the slopes of many standard star fields, letting the airmass correction term free to vary from one field to another. Standard star fields were taken from Hunt et al., (1998) and red standard stars from Persson et al., (1998). The color correction equations obtained for TIRSPEC at HCT site for calibrating to 2MASS magnitudes are the following.

$$\begin{aligned}
J-K &= 0.97 \pm 0.03 * (j-k) &&+\beta_{JK} \\
K-k &= 0.11 \pm 0.03 * (J-K) &&+\beta_{Kk} \\
J-H &= 1.00 \pm 0.05 * (j-h) &&+\beta_{JH} \\
J-j &= 0.12 \pm 0.04 * (J-H) &&+\beta_{Jj} \\
H-K &= 0.82 \pm 0.07 * (h-k) &&+\beta_{HK} \\
K-k &= 0.07 \pm 0.03 * (H-K) &&+\beta_{Kk}
\end{aligned} \tag{8.1}$$

8.3.7 Field of View distortions

To measure any distortions in the FoV, we used the coordinates of 2MASS sources in a crowded field observed with TIRSPEC. After matching the coordinates of stars in the TIRSPEC image with the 2MASS field, we used the geomap tool in IRAF[7] to obtain second order transformation coefficients to quantify FoV distortion. A third degree general polynomial fit was also done to study the FoV distortions. Figure 8.20 shows the measured deviation from linear FoV in the array plane. The units are in arcsec. Significant FoV distortions are found only towards the edge of the array.

8.3.8 Sample Images and Spectra

During the engineering runs, to test the scientific capabilities of the instrument, we observed various astrophysical sources in imaging as well as in spectroscopy modes. The objects observed range from star-forming regions, transient sources like young low mass star eruptive variables, novae (Ninan et al., 2013a), supernovae (Srivastav et al., 2016) and Wolf Rayet stars to objects like white dwarfs, our solar system planets, and stars from various positions in the main sequence Hertzsprung-Russell diagram. Figure 8.21 shows color composite images created from the *J*, *H* and K_s images of some of the sources observed with TIRSPEC. Figure 8.22 shows the near-infrared spectra obtained from various kinds of sources taken with TIRSPEC.

[7]IRAF is distributed by the National Optical Astronomy Observatory, which is operated by the Association of Universities for Research in Astronomy, Inc., under cooperative agreement with the National Science Foundation.

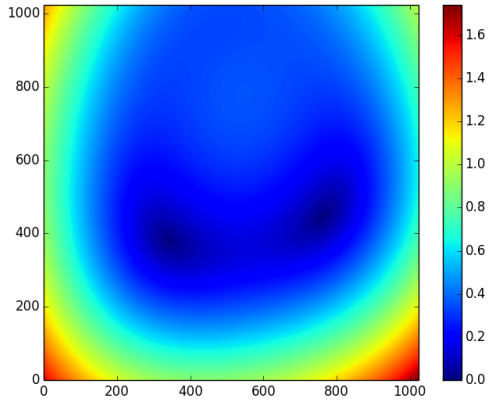

FIGURE 8.20: The colour map shows the magnitude of deviation from the linear estimate of FoV in units of arcsec.

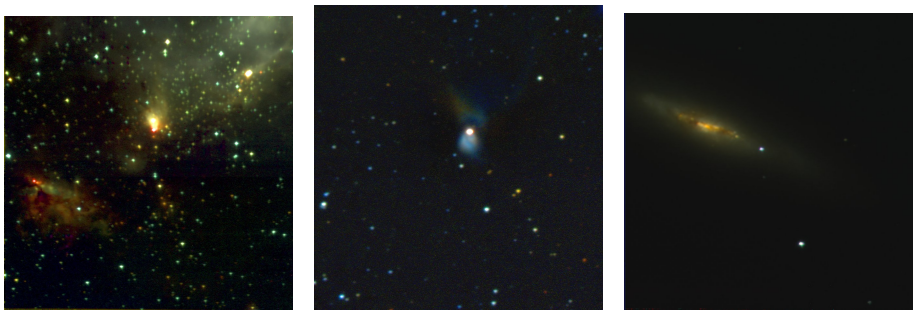

FIGURE 8.21: Various RGB color composite images generated using TIRSPEC J (blue), H (green) and K_s (red) images. On the left is NGC 7538 (star-forming region), at the middle is V2494 Cyg (FU Ors family of outburst source), and on the right is SN2014J (Supernova in M82).

8.4 Data Reduction Tool

I have developed a data reduction tool for analysis of TIRSPEC data to automate most of the steps in the near-infrared data reduction, without compromising on the quality of the reduced data. This semi-automated pipeline requires human guidance only in tasks like flagging good and bad frames, choosing sources of interest for photometry, etc. This tool is specially designed for multi-epoch observations, where many nights of data of a particular source have to be reduced together. See Section 10.1 in Chapter 10 for more details on the TIRSPEC near-infrared pipeline. The latest version of source codes (under GNU GPLv3+ license) are regularly updated on the instrument website[8].

[8] http://web.tifr.res.in/~daa/tirspec/

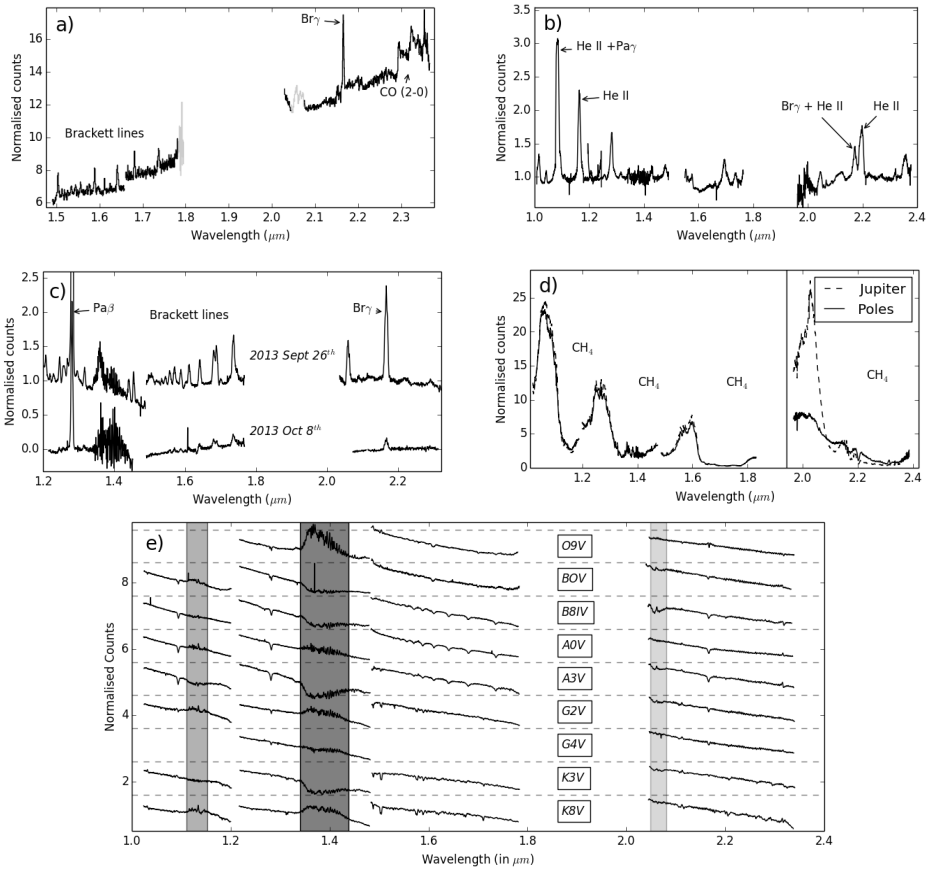

FIGURE 8.22: Sample of the near-infrared spectra taken with TIRSPEC. a) PV Cep (FU Ori kind of outburst source with outflow jets), b) WR 6 (Wolf Rayet star), c) Nova Del 2013 (near-infrared Spectral evolution of Nova), d) Spectrum of Jupiter and its poles (*K* band spectrum is scaled for clarity), e) Stellar Spectra of various main-sequence spectral type stars.

8.5 Status

8.5.1 Upgrades and Repairs

Soon after the installation of the instrument at the Hanle site, the filter wheels got stuck. We identified the problem to be an excessive contraction of the aluminium holders which hold the steel ball bearings of the rotating gear that turns the filter wheels. This was caused due to the lower LN2 boiling temperature at 4500 amsl altitude atmospheric pressure. In our first repair mission, we made a clean room in Leh and widened the holder to the required radius, before replacing the damaged ball bearings.

During the first few months of operation, we noticed slippage in the filter wheel positions. After extensive trouble shooting using the Hall sensor readings, we identified the worm pin in the gear which was causing the issue. It was rectified in a second repair mission to Hanle. We also replaced our short 10″ slits with 50″ slits for better sky subtraction during this mission.

During the dry, cold, 2013 Himalayan winter at Hanle, the moving stage of the calibration mirror failed. This was also repaired in the second repair and upgrade mission.

8.5.2 Current Status

After successful characterization and performance analysis runs on the telescope, TIRSPEC was officially released to the astronomy community for science observations from May 1, 2014. It is currently being used heavily by various astronomers in India and abroad. Several refereed papers have already been published using TIRSPEC data in the fields ranging from study of nearby local star formation regions to novae and extra-galactic astronomy. For my observations of the sources in the MFES program, as discussed in the Part I of this thesis, TIRSPEC was extensively used as the main near-infrared imaging and spectroscopy instrument.

Chapter 9

TIRCAM2 & TIFR Far-Infrared Balloon-borne Telescope

Apart from the TIRSPEC, two other major instrument projects which I worked on during my doctoral thesis work were TIFR Near Infrared Imaging Camera - II (TIRCAM2) and 100 cm TIFR Far-Infrared Balloon-borne Telescope. In this chapter, I present my contributions to both these instruments.

9.1 TIRCAM2

The Infrared Astronomy Group at TIFR had developed a near infrared imaging camera, named TIRCAM1 (TIFR Near Infrared Imaging Camera - I), for astronomical imaging applications. It was based on a SBRC[1] InSb focal plane array (FPA) (58 $\times$ 62 pixels), sensitive between 1 and 5.5 μm. Astronomical observations with TIRCAM1 were regularly carried out during 2001 - 2006 at the f/13 Cassegrain focus of the Mount Abu 1.2 m telescope belonging to Physical Research Laboratory (PRL), India. The TIRCAM1 system and related work have been described in Ghosh and Naik, (1993), Ojha et al., (2002), Ojha et al., (2003), and Ojha et al., (2006).

In 2007, TIRCAM1 was upgraded to TIRCAM2 with the aim of introducing a larger format detector array. The TIRCAM2 uses a Raytheon InSb FPA (Aladdin III Quadrant 512$\times$512 pixels), with a pixel size of 27 μm square, and an f/9 re-imaging lens system. The quantum efficiency of this new array is more than 80% from 1 to 5.5 μm. The TIRCAM2 system has seven filters and one block disk. The FPA operates at 35 K and is cooled by a closed cycle cooler. After the upgrade, I worked on the detector calibration, optimal observation strategy, as well as on the data reduction procedures for TIRCAM2. The observation tests and calibrations were conducted at 1.2 m Mount Abu PRL Telescope and 2 m IUCAA Girawali Observatory (IGO) Telescope, Pune. Figure 9.1 shows the TIRCAM2 system mounted at the direct port of the IGO telescope. My contributions presented in this chapter on TIRCAM2 are published as a section in the TIRCAM2 instrumentation paper, Naik et al., (2012).

9.1.1 Optimal observation strategy

The InSb array is sensitive upto 5.5 μm. This puts a much stronger requirement to optimise the data acquisition in the high background radiation regime. By similar analysis procedure done for TIRSPEC, the dark current

[1] Santa Barbara Research Center

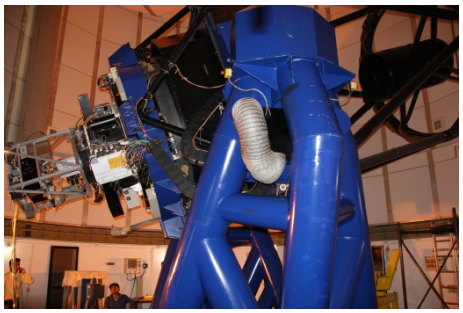

FIGURE 9.1: Observational setup of TIRCAM2 at the 2 m IGO telescope

and readout noise of TIRCAM2 FPA was measured at the IGO site. Dark current was 12 e^-/sec and the readout noise was ∼30 electrons, which is comparable to the datasheet value of 10 to 50 electrons noise for the FPA.

We observed several bright infrared standard sources, the Trapezium cluster in the Orion region, eruptive variables from our MFES program like V1647 Ori, V899 Mon, etc., and a few galaxies in the J (1.20 μm), H (1.66 μm), K (2.19 μm) and nbL (3.59 μm) bands during the observational runs in 2011 – 2012. The typical seeing was 1 - 2 arcsec during the observations. We obtained several dithered exposures of the targets in each of the NIR bands. Typical integration times per frame were 10, 0.2, 0.2 and 0.02 s in the J, H, K and nbL bands, respectively.

9.1.2 Data Reduction

The images obtained by TIRCAM2 were written in FITS format and were processed with IDL, Python and IRAF scripts. Observations were carried out in 5-point dither pattern. We also obtained several dithered sky frames close to the target position in each NIR band. Overall, the NIR images went through the standard pipeline reduction procedures like electronic gain correction, bad pixel masking & correction, dark/sky-subtraction, flat-fielding, co-adding images, and magnitude calculation. A stable, but non-uniform illumination was found in the TIRCAM2 images. These were removed by subtracting blank sky images before the flat fielding step. Instrumental magnitudes were extracted using the iraf *daophot/phot* and *apphot/phot* tasks. Photometric calibration was done from the observations made on the same nights, of the United Kingdom Infrared Telescope (UKIRT) standard stars, at airmasses close to that of the target observations.

9.1.3 Performance

Fig. 9.2 shows a few sample images (*clockwise from top left*: Trapezium cluster in the J-band and in the K-band, NGC 5866 lenticular galaxy, McNeil's nebula, NGC 4567 & NGC 4568 twin galaxies and BS 2943 star) taken with TIRCAM2 using the 2 m IGO telescope.

Limiting Magnitudes

The limiting magnitude obtained from the analysis of the Trapezium cluster field is 16.3 (T_{int} ∼ 1050s) and 14.5 mag (T_{int} ∼ 164s) in the J and K bands,

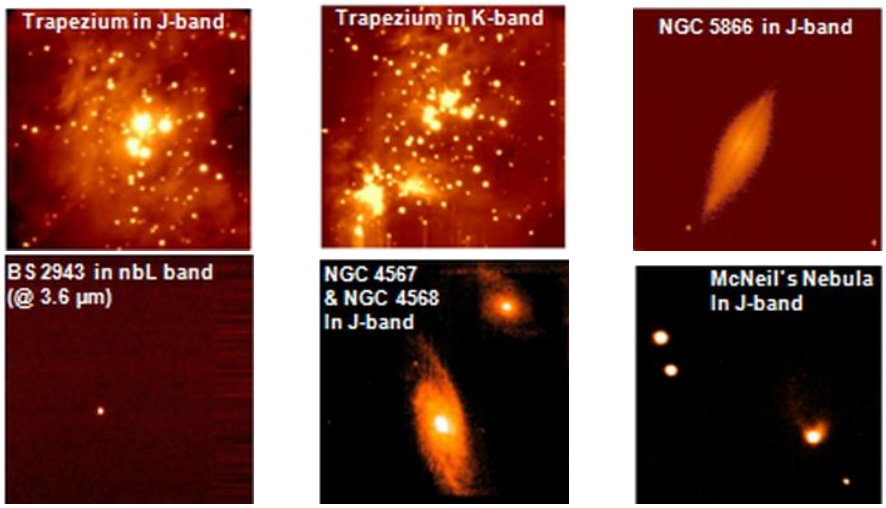

FIGURE 9.2: A few sample images (∼2.3 arcmin x 2.3 arcmin) taken using TIRCAM2 mounted on the 2 m IGO telescope.

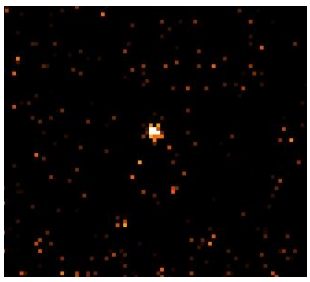

FIGURE 9.3: The faintest star (BS 2721) observed in the nbL-band with a total integration time of 0.5s. Its L-band magnitude is 4.08.

respectively. In the nbL-band, the faintest object we observed was BS 2721 from the IGO on 2011 February 17, having an L-band magnitude of 4.08 ($T_{int} \sim 0.5$s). Fig. 9.3 shows the image obtained by combining 25 dithered frames. Typical integration time per frame was 0.02s.

Assuming a similar sky condition, we estimated the limiting magnitude in the nbL-band for a longer exposure time. The limiting magnitude was taken to be the magnitude of the star which has its peak of flux profile at 5σ level above background, where σ is the background noise. From our BS 2721 image we obtained a sky σ of ~ 0.40 ADUs for a 0.1s dithered frame. Combining 5 such frames reduced the σ to ≈ 0.16 ADUs. As expected, this is indeed reducing as $\sqrt{N}$. Assuming the same sky condition, we estimated the flux ratio of a limiting magnitude star with respect to BS 2721. Combining this with the $\frac{1}{\sqrt{t}}$ fall of the background standard deviation σ, we get the limiting magnitude $M_{limit} = 4.08 + 0.828 + 1.25 \log t$. Note that, this is valid for the same atmospheric condition as of 2011 February 17 at IGO (FWHM $\sim$ 1 arcsec). Using the above formula, if we observe for 1 hour then the expected limiting magnitude comes out to be 9.3 in the nbL-band. Fig. 9.4 shows the plot of limiting magnitude in the nbL-band *versus* total exposure time.

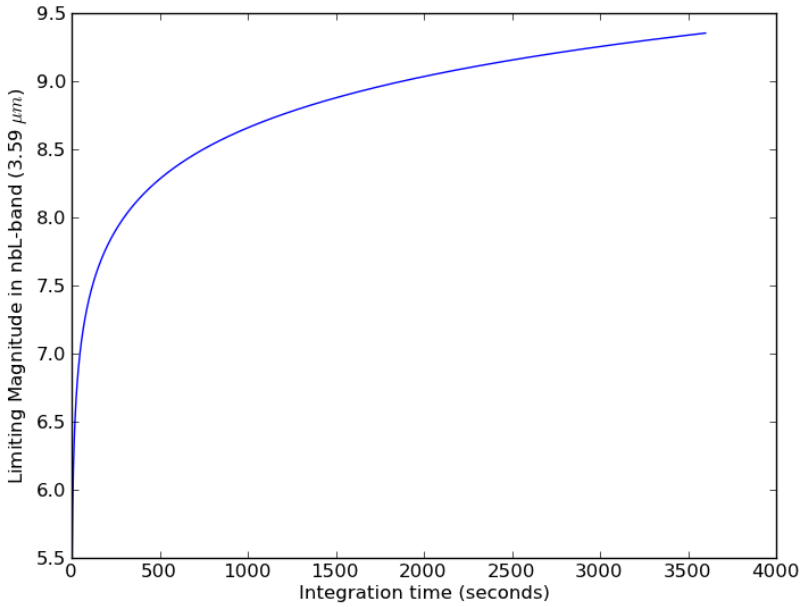

FIGURE 9.4: The limiting magnitude with 5σ detection criteria in the nbL-band (3.59 μm) as a function of exposure time in seconds. The atmospheric conditions are assumed to be similar to 2011 February 17 at IGO.

Our limiting magnitude is determined by the background σ. If the background flux reduces by X magnitude then the limiting magnitude will increase by $\frac{X}{2}$ magnitude.

Linearity in nbL-band

To check the linearity of counts in the nbL-band, we took the data of those nights where 3 or more standard sources were observed. Fig. 9.5 shows the plot of instrumental magnitudes calculated using log of ADUs/sec *versus* standard L-band magnitudes from the UKIRT. The plot shows that our array is linear in this regime.

It is interesting to compare the *Spitzer*-IRAC values of saturation limit in the 3.6 μm band. For a frame time of 2s, the point source saturation limit in the IRAC 3.6 μm band is < 7.92 mag. TIRCAM2 can therefore be used to observe the range of magnitudes brighter than the saturation limit of the *Spitzer*-IRAC.

9.1.4 Summary (TIRCAM2)

The upgradation of the near infrared camera TIRCAM2 to utilize a 512×512 InSb array and additional narrow-band filters for use at the focal plane of Indian 2 m class telescopes was successful. The systems were tested and the observing runs of TIRCAM2 at the IUCAA 2 m telescope at Girawali and PRL 1.2 m telescope at Gurusikhar were quite successful. We could observe sources in the nbL-band ($\sim$ 3.59 μm) from the Girawali (altitude $\sim$1000 m) and Gurusikhar (altitude $\sim$1722 m) sites. Our estimate of the limiting magnitude shows that TIRCAM2 can be used to observe the bright magnitude

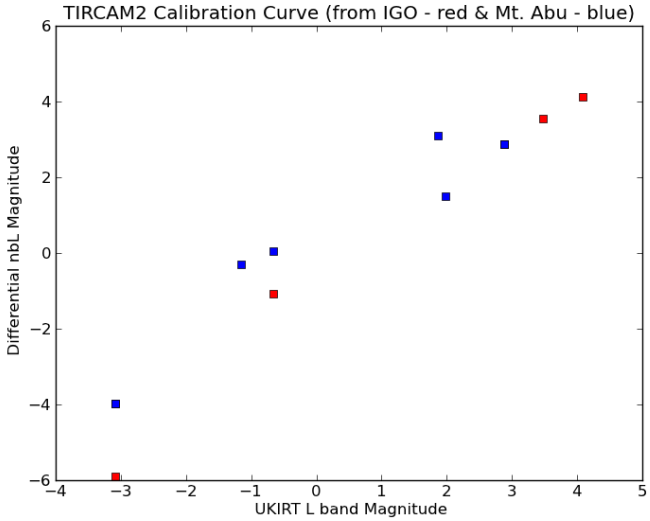

FIGURE 9.5: Instrumental magnitudes from log of ADUs/sec *versus* actual L-band magnitudes from UKIRT, showing linearity of TIRCAM2 in the nbL-band (red squares – IGO data, blue squares – Mount Abu data).

range at 3.6 μm below *Spitzer-IRAC* saturation limit. After calibration, TIRCAM2 was used for our MFES program described in Part I of this thesis. This is the only imaging camera available in the country which can observe upto nbL-band in NIR. Recently, we shifted TIRCAM2 to India's largest ground-based telescope, 3.6 m Devasthal Optical Telescope (DOT), Nainital. TIRCAM2 is currently mounted on the primary port of 3.6 m DOT. From our calculations, we expect a factor of 2 improvement in the signal-to-noise ratio, and hence, an improvement in the limiting magnitude by 0.75 mag on DOT.

9.2 TIFR Far-Infrared Balloon-borne Telescope

Balloon-borne far-infrared (FIR) observations were initiated at TIFR in the early 1970s. Balloon & Telescope designing, manufacturing, and flights are conducted from TIFR Balloon Facility at Hyderabad, India. Early telescopes were relatively small in size. The 100 cm TIFR FIR balloon-borne telescope (T100) currently used had its first flight in 1983. Over the last 3 decades, it has undergone many upgrades and has conducted FIR observations from 120 to 220 μm wavebands (Ghosh et al., 1988; Ghosh, 2010). The back-end instrument currently used on this telscope is a scanning Fabry Perot Spectrometer (FPS), tuned to map the most dominant cooling emission line of [C II] at 158 μm.

Since the FIR sky background varies quite fast (even at $\sim$30 km altitude), this telescope during its initial phases was mostly observed in the sky chopped mode by wobbling the secondary mirror. However, more sensitive observations can be done in the fast spectral scan mode using FPS where sky chopping is not done. In the following sections, I present the algorithm developed for generation of optical and FIR maps in un-chopped mode of observation.

9.2.1 Optical map generation

In order to obtain greater accuracy in pointing and aspect of the telescope, there is an array of photo diodes at the focal plane of the telescope, which can map an optical image of an offset field of view. This offset is well calibrated. Hence, this optical map can be used to correct the aspect of the FIR map. However, in the un-chopped mode of observation, since there is no chopping of the optical signal, it is too noisy to be directly used for generating an optical map. In the following subsections, I outline a wavelet-based signal processing step that I have designed to filter out noise from the unchopped noisy photo diode signals.

The PDA Signal

The photo diode array (PDA) consists of 8 photo diodes placed in a line. Each photo diode gives an independent time series output proportional to the amount of optical light imaged on to it. The raw output signal is negatively correlated to the flux. We measure a dip in the voltage signal as a star enters the field of view (FoV) of the diode and the signal rises back when the star exits the FoV. Figure 9.6 shows the typical signal we obtain from a photo diode as a bright star enters and leaves the FoV of the photo diode when the telescope scans the sky. Some of the photo diodes were found to be faulty and their signals had to be discarded. As the telescope executes the raster scan of a region in the sky, the same star can enter the field of a photo diode multiple times during each elevation scan (see Figure 9.6). All of these multiple dips in the time series data will get associated with a single star once we fold the time series data to fill a matrix of sky image using the telemetry information from the telescope.

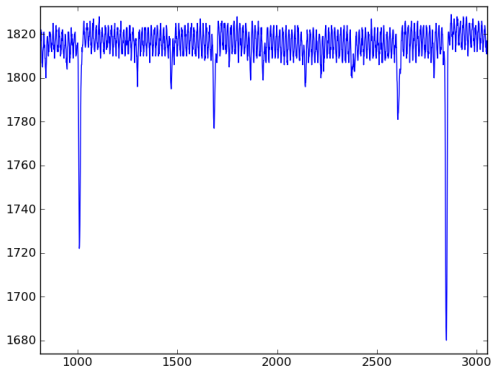

FIGURE 9.6: Sample raw signal from a photo diode as a bright star enters and leaves the array multiple times during the telescope scans.

Unlike the signal from a bright star shown in Figure 9.6, signals from most of the stars are only slightly above the noise level. We need to filter out the noise to generate a clear optical map of the sky. In the following subsections, I explain the algorithm designed for this noise removal. All the processes are done offline. This is currently incorporated into the existing data analysis pipeline of the telescope.

Signal Processing

The filtering was designed to be done in two sequential stages (see Figure 9.7). In the first stage, we use a finite response band pass filter to remove easily separable high frequency noise and low frequency bias fluctuations. To remove noise from the regions where there are no stars, in the second stage we further refine the filtering using wavelet decomposition. This reduces the background noise in the final optical map.

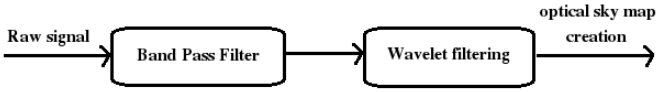

FIGURE 9.7: The raw signal is first passed through a band pass filter and its output is further processed by a wavelet filter. The final clean signal is used by the later stages of the pipeline to generate an optical map of the sky.

Band Pass Filter

In the first stage, the high frequency noise and low frequency bias shifts are easily removed by a band pass filter. The filter is designed to have its high frequency cut off low enough to remove maximum amount of high frequency noise without affecting the star light signals. Similarly, the low frequency cut off is kept high enough to remove maximum low frequency fluctuations in signal without affecting star signals. A finite impulse response filter was designed using *scipy.signal.firwin2*[2] task. The designed bandpass filter is represented by the following 32 filter coefficients.

[6.11690260e-05, -1.73726203e-04, -6.92609440e-04, -1.69394736e-03, -3.20690168e-03, -4.84671557e-03, -5.65165527e-03, -4.12661487e-03, 1.44407175e-03, 1.24589456e-02, 2.93909828e-02, 5.13268588e-02, 7.58569138e-02, 9.94196437e-02, 1.18052519e-01, 1.28351336e-01, 1.28351336e-01, 1.18052519e-01, 9.94196437e-02, 7.58569138e-02, 5.13268588e-02, 2.93909828e-02, 1.24589456e-02, 1.44407175e-03, -4.12661487e-03, -5.65165527e-03, -4.84671557e-03, -3.20690168e-03, -1.69394736e-03, -6.92609440e-04, -1.73726203e-04, 6.11690260e-05]

To make sure this stage does not introduce any filter delays, we pass the signal twice, once forward and then backwards through this filter.

In this simple band pass filter, we do not utilise any temporal information to adaptively remove noise. In the next stage, we do a wavelet decomposition, and utilise the information across the frequency spectrum to remove noise adaptively at each epoch in the data stream.

Wavelet filtering

The output of the bandpass filter from the previous stage is taken as input to this stage. Wavelet decomposition of a signal is fundamentally the same as

[2] *firwin2* is for designing finite impulse response filters in the *signal* submodule of *Scipy*

separating out the components of the signal into different frequency bands using a bank of band pass filters. The shape of the band pass filter is decided by the *mother wavelet* we choose for wavelet decomposition. It is usually good to choose a standard, orthogonal mother wavelet which resembles the signal we are searching for. Then, the convolution of the wavelet with the signal will provide maximum correlation value. Since our stellar signals look like gaussian dips in the time series data, we chose to use *symlets 4*[3] wavelet. Figure 9.8 shows the *symlets 4* mother wavelet we used for detecting dips in our signal.

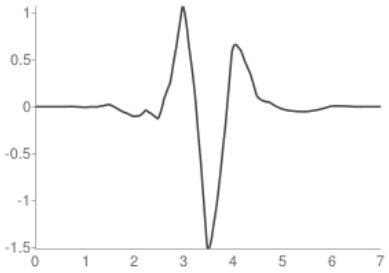

FIGURE 9.8: The mother wavelet chosen to detect gaussian dips in signal: symlets 4.

Wavelet decomposition, basically creates a filter bank of band pass filters by scaling this mother wavelet. Figure 9.9 shows the filter bank analogy of wavelet decomposition. The low pass (LP) output is recursively split into two, by another set of low and high pass filter pairs created by scaling the mother wavelet.

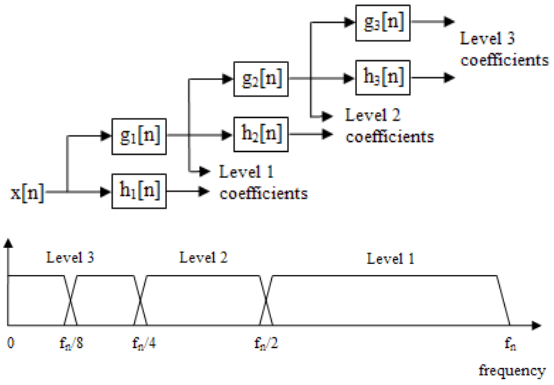

FIGURE 9.9: In the filter bank analogy of wavelet decomposition, the low pass filter output of the signal is recursively passed through more pairs of high pass (h) and low pass (g) filters, and they generate the wavelet transform coefficients at each level. The final frequency band decomposition is as shown in the diagram below. The exact shape of each band pass is decided by the mother wavelet. Image courtesy: Wikipedia

[3] http://wavelets.pybytes.com/wavelet/sym4/

When we do a Stationary Wavelet Transform (SWT)[4] of the signal, we will get a set of coefficients for each of the high pass (HP) output shown in Figure 9.9. Hence, for a 1-dimensional input signal we will have N sets of 1-dimensional coefficients forming a 2-dimensional Spectrogram. The value of N is decided by the level upto which the recursive band pass filtering is done in the filter banks (i.e., the number of decomposition steps in SWT). SWT has more redundancy than the discrete wavelet transform (DWT), but it gives us more freedom to change the coefficients without affecting the inverse reconstruction of the filtered signal. Even though DWT is not redundant like SWT, due to the down sampling[5] of the band pass outputs, we cannot independently change the coefficients without affecting the proper reconstruction of the signal.

Figure 9.10 shows a typical SWT spectrogram of our PDA signal. The X axis of the spectrogram is time, and Y axis shows the frequency bands (highest frequency at the bottom and lowest frequency at the top). The color map represents the absolute value of the coefficients. The vertical white patches across various filter bands are the epochs when a star entered the field of view.

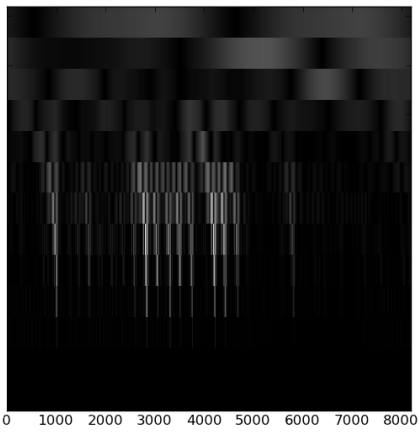

FIGURE 9.10: The spectrogram of the output signal from the bandpass filter of a region containing many bright stars. X axis is time. Each row in Y axis is coefficients from different high band pass levels in SWT decomposition. The bright regions are where signal from the star is present.

A few of the lower most and higher most bands which do not contain any information are directly set to zero.

The algorithm described below is designed to remove the noise from epochs without star signal.

1. Start processing from the lowest frequency band coefficients and proceed to higher frequency band coefficients (i.e., top to bottom rows in the spectrogram).

[4]SWT is also known by other names like Undecimated Wavelet Transform (UWT), Redundant Wavelet Transform, etc.

[5]this affects the time translation invariance of the coefficients.

2. Partition the row of coefficients along the time axis into blocks with a partition size equal to the size of the reconstruction filter of that level.
3. For each block, check whether the standard deviation in the coefficients of the block is above a certain threshold (1.5 times) of the standard deviation in any of the blocks on both sides.
4. If yes, then check whether the blocks in the coefficients of previous (atleast 3) lower frequency band levels at that epoch were also significant.
5. If yes, we identify this block as star signal and proceed to the next block.
6. If any of the previous conditions are not satisfied, it is taken to be a *no star region* and the coefficients in that block are all set to zero.

This algorithm is pictorially shown in Figure 9.11.

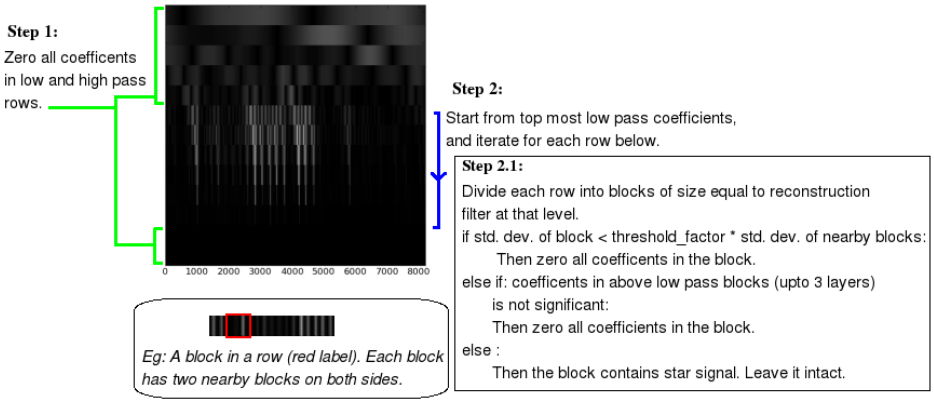

FIGURE 9.11: The wavelet filtering algorithm to remove noise from regions without star signal.

The final output of this algorithm will be a spectrogram with all the coefficients of the regions without signal from star are set to zero. Figure 9.12 shows the spectrogram after zeroing the coefficients using this algorithm.

The output spectrogram is then finally converted back to 1-dimensional signal by inverse stationary wavelet transform (ISWT) with the same mother wavelet. This gives us the final noise free PDA time series signal to be used for the optical sky map generation. Optionally, we can also put a cut off to threshold only the significant star signals while generating the final map. Figure 9.13 shows an optical map generated by successful implementation of this algorithm. The stars in the field were identified, and their calculated centroid was used to correct the aspect of the FIR map.

9.2.2 FIR map generation using Fabry-Perot spectrometer

An FPS tuned to 158 μm [C II] line designed at ISAS[6], Japan was used with the T100 telescope. Details of the instrument setup is described in Mookerjea et al., (2003).

[6]Institute of Space and Astronautical Science

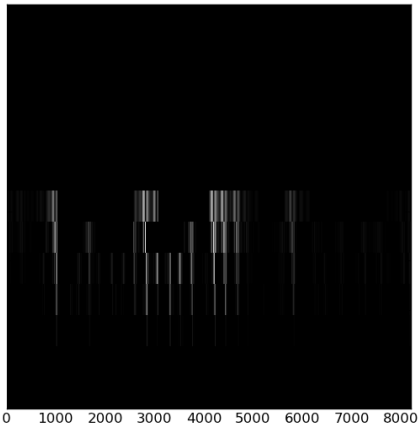

FIGURE 9.12: Output spectrogram of the input raw spectrogram shown in Figure 9.10 obtained by the context aware zeroing of regions without star signal.

The signal

In the un-chopped mode of observation, the scan of a wavelength window around 158 μm is carried out at a much higher speed than the spatial scan speed of the telescope. This enables us to complete, on an average, atleast one full scan of the spectral window before telescope pointing shifts to the next pixel area in the raster scan. There is no sky chopping by the secondary mirror in this mode of observation. In the following subsection, I briefly outline the FIR map generation algorithm I wrote for the un-chopped mode of observation.

FIR map generation algorithm

The telemetry of the telescope system is used to bin and tag the output of the FPS into a 2-D grid of points with a pixel size of 0.5 arcmin. The encoder reading of the wavelength scan is pre-processed by matching with the triangular waveform of the control signal. This is used to separate the upscan signal from the down scan of the FPS. Due to the hysteresis involved in the wavelength scan cycle, the upscan data is processed separately from the down scan data. At the final stage, after calibration, we merge the two FIR maps from both the scans.

After removing any outliers due to any packet corruption during the downlink of the data, a moving average baseline of the spectral window is generated using the signal from regions along the edges of the raster scan. This generation of background template is done iteratively to use only the regions which do not have [C II] line emission.

Once these moving average background templates are generated, background is subtracted from all the data points using the nearest neighbour background template. The FPS's resolution is much poorer than the width of [C II] line emission, hence a Lorentzian profile is taken as a good model for the instrument profile.

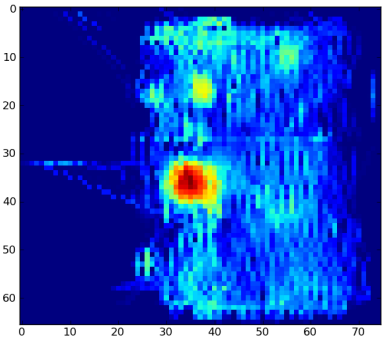

FIGURE 9.13: Sample result: an optical map generated using the wavelet filtering algorithm. The X and Y coordinates are in pixels (0.5 arcmin/pixel) in elevation and cross elevation axis. Centroid of the stars from this optical map is used to correct the aspect of the FIR map.

The center and width of the Lorentzian profile is taken to be a shared single free parameter for all the pixels in the map. The line strength, and the continuum are independent parameters for each pixel. This constrained model is then fitted to all the background subtracted data simultaneously.

The above algorithm was implemented with enough modularity to allow for flexible line models with various constraints. Once the map is generated for up and down scans separately, they are merged together to obtain a single map and a world coordinate system (wcs) calibration is applied.

Final flux calibration is done using the peak count measured from Saturn observation taken during the same flight. Figure 9.14 shows the FIR maps generated for two star-forming regions, NGC 2024 and RCW 36, using this map generation algorithm.

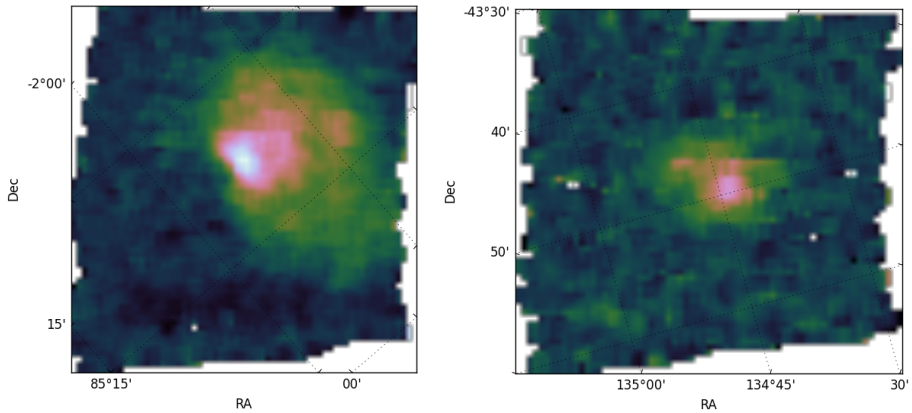

FIGURE 9.14: 158 μm [C II] line flux maps of star forming regions, NGC 2024 (left) and RCW 36 (right), generated using the FPS data reduction algorithm.

Chapter 10

Data Pipelines

The observations for our long-term MFES program were spread over hundreds of nights using various optical as well as near-infrared instruments (see Chapter 2). For studying the long-term time variability of our sources, it was important to have a consistent reduction procedure for data from all the nights. Over a period, an automated pipeline also reduces the time required to be spent on data reduction for doing science.

Since the quality of reduction is crucial for our science, the key philosophy in the design of the pipeline is not to compromise on the quality of data reduction, even if that means compromising on the ability of full scale automation. For instance, the complex, yet crucial step of visual inspection of raw data to discard anything unusual has not been automated. On the other hand, reducing human inputs is vital for making the code less susceptible to human errors, and to save time via automation. Hence, the pipeline was designed to minimise the human input whenever we have a good algorithm without compromising on the reduction quality.

The pipeline was also designed to be general enough for use by other users of the instrument. As a by-product of this work, I released a general pipeline for all these instruments for use of the general astronomy community. In order to reduce the overheads in learning reduction of data from new instruments, while switching between multiple instruments, the interface of the pipelines was designed to be similar. By re-factoring the implementation of fundamental data reduction procedures to be independent of the instrument, we isolated the instrument specific processing steps from the common fundamental steps. Thus, multiple instruments could be incorporated into the same pipeline. In the following sections, I outline the basic steps in the near-infrared and optical data reduction pipelines that were developed.

10.1 TIRSPEC Pipeline

The TIRSPEC, mounted on the side port of the 2 m HCT, is a near-infrared spectrometer and imager (see Chapter 8). TIRSPEC and the telescope are controlled remotely by the observer from The Centre for Research & Education in Science & Technology (CREST), Hosakote, IIA, Bangalore (India) via a satellite link. In one typical night of observation, the SUTR[1] data acquisition mode in which TIRSPEC is operated, can generate upto 50 GB of raw data. With the existing satellite link bandwidth, it is not possible to download all the raw data to the control room in Bangalore on the same

[1]Sample up-the-ramp

day. Hence, we had to separate our TIRSPEC data reduction pipeline into two parts. The first part, which generates the dark subtracted slope images, is run automatically at the HCT site itself, on the TIRSPEC server. The second part, which does the remaining data reduction, is run by the instrument user.

10.1.1 Slope image generation

The slope image generation is the first part of the pipeline which is run on the TIRSPEC computer server at Hanle. Figure 10.1 shows the block diagram of the stages in this part of the pipeline. It logs file creation, generates cosmic ray (CR) hit healed dark averages, does intelligent pixel masking to recover from saturation or reset anomaly, dark subtraction and final slope fitting (see Section 8.1.4 for more details on these algorithms). This fully automated stage is run at the end of each night's observation. The data that is received by the observer at the Bangalore control room contains the dark-subtracted slope images. Two log files which are generated are also provided to the observer. One contains the log messages of the image generation pipeline, and other contains a summary of all observations done during that night.

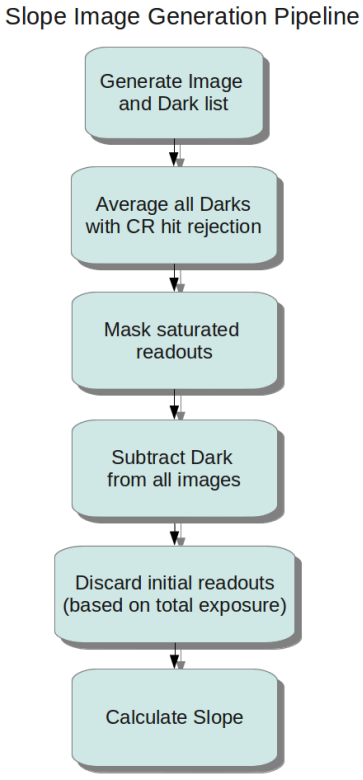

FIGURE 10.1: Block diagram of the Slope image generation stage of the TIRSPEC pipeline. This part is fully automated and runs on the TIRSPEC server at Hanle.

This part of the pipeline also includes various routines for non-linearity correction, CR hit removal, etc. If the user wants to work on the raw SUTR data and reprocess it, the modular design ensures the same code can be imported as a module in an interactive Python terminal to separately use the collection of routines. Documentation is incorporated inside the source code itself.

10.1.2 Near-infrared Photometry & Spectroscopy

The second part of the pipeline which does photometry or spectroscopy data reduction is run by the user. This stage is controlled by a configuration file, which the user can configure to execute a photometry or a spectroscopy pipeline. Figure 10.2 shows the block diagrams of this second stage of the pipeline. The first five blocks which include steps like identifying the targets, visual inspection of data quality, combining of the same dither positions (which are automatically identified), flat correction, and bad pixel interpolation are common to both the photometry and spectroscopy pipelines. In Figure 10.2, the blocks which have a human face smiley represent blocks that need some human supervision. All the blocks are independent and can also be run separately. The meta data for the pipeline is passed on from one block to the next block via standard human readable text files. This provides more control on the flow of the pipeline to advanced users, if they want to interrupt and intervene in the execution.

Photometry procedure

The sixth block onwards in Figure 10.2 a) are specific to photometry. The combined multiple dithered images are aligned (if automatic alignment fails, human supervision will be requested) and combined. Once the reduced images are generated, the pipeline asks the user to select stars of primary interest, and visually identify good sky regions inside the first image of that source. The pipeline will use triangular matching of the field stars identified using *sextractor* to automatically update the star and sky coordinates for all the subsequent images. These transformed coordinates are used to do standard aperture photometry, as well as PSF photometry using *daophot* IRAF binaries. The parameters for all these photometry steps are controlled in the configuration file. Final magnitude outputs of photometry are written to a machine and human readable table.

Spectroscopy procedure

The sixth block onwards in Figure 10.2 b) are specific to spectroscopy data reduction. An optional A-B, B-A subtraction is done if the user demands[2]. The spectrum is traced, 1-D extracted, and automatically wavelength calibrated by matching with argon lamp templates. Once the wavelength-calibrated spectra of the science target as well as a standard star are obtained, one can use the *Telluric Correction Tool* (see below) to remove telluric absorption lines from the spectra.

[2]It is not necessary, since TIRSPEC's slits are quite uniform and HCT does not offer a fast AB dithered observation mode. Hence, taking sky from both sides of the star suffices in case of the TIRSPEC data.

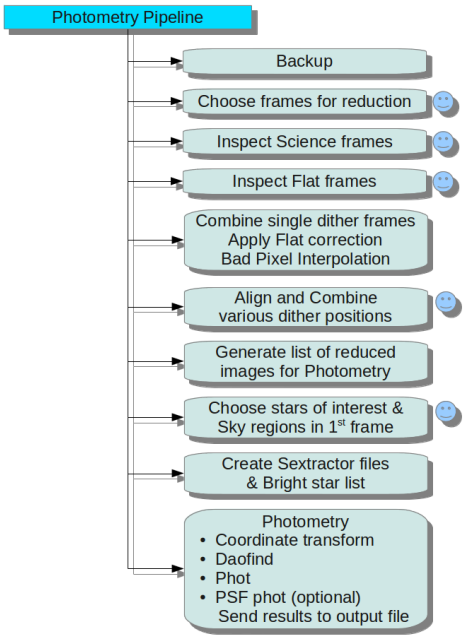

(a) Photometry

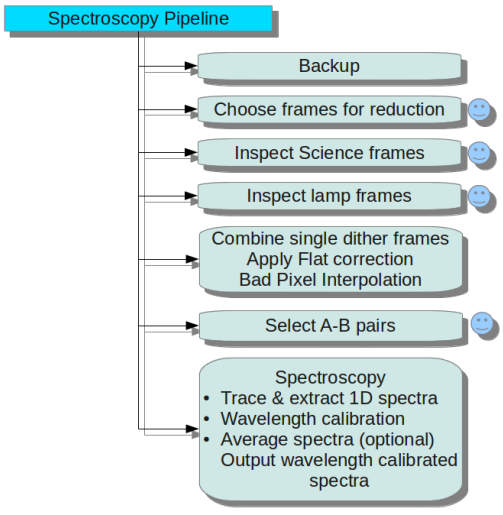

(b) Spectroscopy

FIGURE 10.2: Block diagrams of the Photometry and Spectroscopy pipelines. The blocks which have a human face smiley represent blocks which need some human supervision.

Telluric Correction Tool

Near-infrared spectra contain many telluric lines. They are removed by dividing with the spectrum of a spectroscopic near-infrared standard star, taken within a nearby airmass immediately before or after the target observation. Along with telluric lines, this step also removes the instrument response and outputs a continuum-corrected spectrum[3]. This step also helps in removing the fringes in the *K* band spectrum formed in the HAWAII-1 PACE array used in TIRSPEC. The *Telluric Correction Tool* is a fully interactive graphical software which removes the intrinsic stellar lines of the standard star, aligns it to the science star, and scales it before dividing the science star spectrum with it. Finally the tool applies black body temperature correction to output a continuum-corrected spectrum of the source. This continuum-corrected spectrum is finally scaled to the magnitude of the source star to obtain the flux-calibrated spectrum of the source. This fully interactive tool includes both, a deconvolution algorithm, as well as a simple Gaussian subtraction algorithm to remove stellar lines of the telluric standards. Figure 10.3 shows the paths one can choose through this interactive tool to do telluric correction.

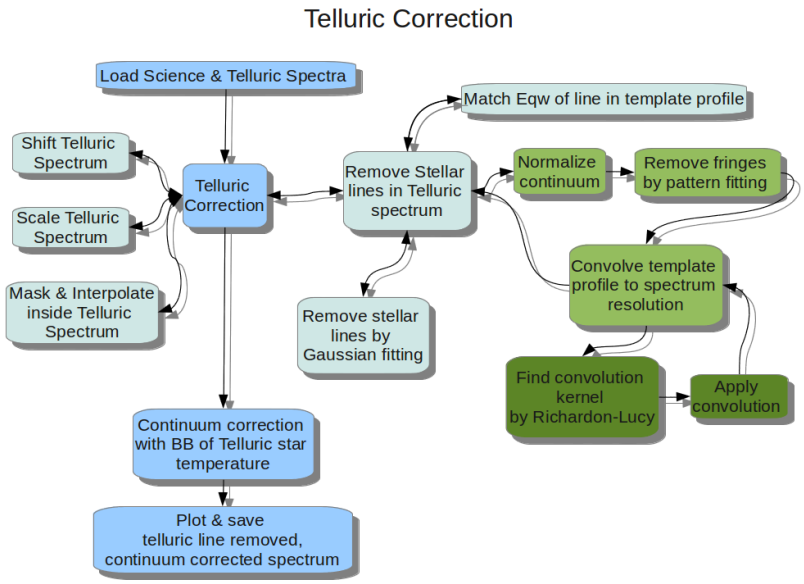

FIGURE 10.3: Block diagram of the fully interactive graphical Telluric Correction Tool. Various paths one could take through the blocks in this tool are represented by the arrows.

10.2 Optical Photo-spec Pipeline

For our MFES program, various optical spectrographs and imagers like HFOSC, IFOSC, and 512×512 ARIES camera were used (see Chapter 2).

[3]Provided the black-body temperature correction of the standard star is known.

Similar to near-infrared instruments, various optical instruments also have certain shared fundamental steps and a few instrument specific steps in the data reduction procedure. Optical Photo-spec Pipeline was designed by separating the instrument specific algorithms from the fundamental steps. The interface was designed to be same as the near-infrared instrument pipeline.

The first step in the pipeline is the standardisation of important header information required for reduction across various instruments into a log file[4]. The sequence of the data reduction routines needed for each instrument is also defined at the beginning. To add support for a new instrument, it is only necessary to update the instrument specific Python class in the source code. The rest of the reduction algorithms are all designed to be independent of the instrument.

After standardisation of the data, depending on the instrument, a selected chain of reduction routines are executed sequentially. The photometry and the spectroscopy steps are conceptually similar to the near-infrared flowchart presented in the previous section 10.1.2. Similar to the near-infrared pipeline, all the meta data is passed from one block to the next block via human readable text files to provide for more control in the running of the pipeline.

10.3 SALT-HRS reduction tool

We used the High Resolution Spectrograph (HRS) on 11 m SALT for obtaining high resolution (R ∼37000 & ∼12000) spectra of southern hemisphere sources in the MFES program. We were the first group to publish results using this instrument, and hence we had to develop our own SALT-HRS reduction tool to reduce the HRS data.

10.3.1 Implemented Procedure

In this subsection, I briefly outline the implemented high resolution spectrum extraction procedure. Apertures of the echelle frame are first traced by adaptive thresholding of the bright quartz flat spectrum. The flux in each aperture is then summed along the axis perpendicular to the dispersion axis. A small tilt of the slit with respect to this axis slightly degrades the resolution of the final collapsed 1-D spectrum. In order to perfectly match and align the emission lines in the sky spectrum and the target spectrum of each aperture, the tool scales sky spectrum before subtraction. The scaling factor is estimated using the flux of telluric emission line strengths in the object and the sky spectra. It also shifts along the dispersion axis to correct for any differential dispersion between the sky and the object spectra. Finally, wavelength calibration is done by identifying ThAr lines. For early epoch observations with HRS, where the ThAr arc spectrum was taken only through the sky fibre, our tool applies the shift correction obtained using atmospheric emission lines. The wavelength-calibrated spectrum is finally normalized with an iteratively fitted smooth continuum.

[4]To be safe, the pipeline will never edit the original data files or folders.

10.3.2 Code architecture experiment

The SALT-HRS reduction tool is written purely in Python, making use of *scikit-image* (Walt et al., 2014), *scipy* (Jones, Oliphant, Peterson, et al., 2001), *numpy* (Walt, Colbert, and Varoquaux, 2011) and *astropy* (Astropy Collaboration et al., 2013). Its design was an experiment to test the concept of combining the data reduction routines inside the data object itself. This architecture is fundamentally different from the previous pipelines, where a procedural programming architecture was followed, in which the pipeline is a sequence of routine calls which passes data in fits format as inputs and outputs.

The concept of incorporating data reduction methods into the data object, initially seemed to be an appealing idea to keep all the methods associated with a certain kind of data organised within itself. However, after implementation, I concluded that this architecture is not good for astronomy data reduction applications, for the following reasons.

- Astronomy data reduction is a chain of procedures, which evolves with time as new algorithms are written for different kinds of observations. However, the format of the data which is generated by the instrument is stable. When the reduction procedure is incorporated into the data object, any minor change in the reduction procedure percolates to a change in the data object, potentially making it incompatible with previous versions of reduced data.
- In practice, astronomy data pipelines often need to be interrupted and certain procedures bypassed or inserted for special cases. Mixing data and reduction procedure makes this really hard to manage.
- Since astronomy pipelines often need to be restarted from a certain step, this architecture introduces the unnecessary issues of keeping track of the state of the reduction done inside the data object. Any change in the reduction procedure could easily make the previous partially reduced data incompatible.

10.4 Status

All the pipelines developed for various instruments are publicly released under GNU GPL v3+ license. Codes are version controlled and hosted on Github pages, and they are being constantly updated and improved as more and more users provide feedback and suggestions. Almost all the parts of the pipelines are written in Python, using standard modules used by the astronomy community, like astropy[5], numpy[6], matplotlib[7] and PyRAF[8].

The modular implementation with inbuilt documentation designed to be reusable has enabled many other users to use them in their own programs or instrument pipelines.

[5] Astropy Collaboration et al., (2013)

[6] NumPy is the fundamental package for scientific computing with Python (Oliphant, 2007)

[7] Hunter, (2007)

[8] PyRAF is a product of the Space Telescope Science Institute, which is operated by AURA for NASA

The TIRSPEC near-infrared imaging and spectroscopy pipeline is heavily used by the user community of TIRSPEC. Several refereed publications have already been published using this pipeline.

The Optical Photo-spec Pipeline is also used by some of the user community of the optical instruments. Due to its versatile architecture, support for many new instrument are being implemented into the pipeline regularly.

The SALT-HRS reduction tool, is also used in several publications. However, it is not being further developed and in the near future the routines from this pipeline will be incorporated into PYHRS, which will be the official reduction tool (currently under development) for the SALT-HRS instrument.

Chapter 11

Conclusion

As part of my doctoral thesis work, I carried out a long-term multi-wavelength monitoring of FUors and EXors Sources (MFES program). The observations were carried out in optical, near-infrared, and radio wavelengths using primarily the 2 m class telescopes in India (HCT and IGO Telescope), 11 m SALT in South Africa, and GMRT in India. The data included hundreds of nights of observations spanning from 2008 to 2016.

In this chapter, the major results from this thesis work are summarised.

11.1 Part I : On episodic accretion and Outflows from YSOs

Bimodal classification of FUors and EXors is probably unreal

Our detailed characterisation of V899 Mon as well as V1647 Ori showed both these sources demonstrated a mixture of properties seen in classical FUors and EXors. Both these sources are still undergoing outburst and their timescales are more than EXors but less than classical FUors. Spectroscopically, they are more like EXors but a few characteristics are similar to FUors. Hence, we propose V1647 Ori and V899 Mon as a new intermediate class of eruptive variables. This family of episodic accretion outbursts probably has a "continuum" distribution and is not bimodal in nature.

Transition to short period quiescence between two outbursts of V899 Mon

Due to our continuous monitoring MFES program, for the first time in the family of eruptive variables, we could spectroscopically monitor the transition from the first outburst to a short period quiescence and back to the second outburst of V899 Mon. This gave significant insights on the temperature variations as well as the evolution of outflows during the transition phases of eruptive variables. We identified that the flux was reddest during the transition phase, which indicates the flux at the onset of the outburst was cooler than the stellar color temperature during the quiescent phase.

Inadequacy of disc instability models

We showed the long, second outburst seen in both V1647 Ori and V899 Mon cannot be explained by the 'S-curve' disc instability models like the thermal and magnetorotational instability models. Using the α-disc parametrisation of viscous disc, we proposed the likely scenarios in the inner disc region which could explain the observed time scales in the light curves.

Instability in magnetospheric accretion as the cause of short breaks

The disc instability models cannot explain the short period quiescence we observed in V1647 Ori and V899 Mon. Based on the time scales of the rise time and the duration of the second outburst, we showed that the mechanism needed to explain the short break between the first and the second outburst should be capable of temporarily pausing the accretion without fully draining the inner disc below a critical density (like the disc instability models do). The heavy outflows and large turbulence detected just before V899 Mon transitioned to quiescent phase seemed to indicate a highly dynamic unstable activity in the magnetospheric accretion. Comparing with the simulations of the instability in the magnetospheric accretion in the literature, we proposed this as the most consistent mechanism which can explain all the traits we observed during the transition phases. These mechanisms can pause the accretion temporarily without having to drain the disc and can easily resume as soon as the magnetic fields stabilise with a sharp rise in the light curve.

Direct detection of accretion - outflow correlation

From our V899 Mon observations, for the first time we could directly detect the outflows, traced by the P-Cygni profiles of Hα and Ca II IR triplet lines, disappearing below the detection limit when the accretion rate dropped during the quiescent phase. We also detected resumption of the outflows during the second accretion outburst. This confirms the accretion driven outflow models.

Detection of episodic magnetic reconnection winds in V1647 Ori

We detected short duration episodic (few weeks timescale) outflow winds in V1647 Ori, which is at an inclination angle of $\sim 61^o$. From our analysis, we proposed that these are likely to be magnetic reconnection winds.

First detection of magnetically accelerated polar winds

Our high resolution multi-epoch spectra of V899 Mon showed fast episodic winds in timescales of a few days. Such variations have never been reported in any young stars. Our analysis showed magnetically accelerated polar winds seen in simulations by Kurosawa and Romanova, (2012) and Romanova et al., (2009), which is a weak field case of the propeller-regime, is the most likely outflow driving mechanism. They can have the large velocity changes and the timescales we detected in the outflow from V899 Mon.

Hierarchical Bayesian model to constrain outburst frequency

We developed a framework for a powerful, flexible hierarchical Bayesian model which can be used to constrain the period of FUors and EXors outbursts using all the available multi-epoch, multi-wavelength photometric data of YSOs in the literature. Our simulations showed the model is powerful enough to constrain the outburst frequency much more than simple binomial model methods, and that they can also give quantitative probability on comparison between the outburst frequencies across different classes of YSOs. This is extremely fundamental to the study of the evolution of outbursts and its influence on

the protoplanetary disc as the system evolves. This model also enables us to constrain the decay timescale of FUors outbursts.

11.2 Part II : Instrumentation

In this section, the current status of the instruments and pipelines which were developed as part of this thesis are summarised.

TIFR Near Infrared Spectrometer and Imager (TIRSPEC)
After taking part in the development, I conducted repairs, upgrades and carried out detailed calibrations of TIRSPEC on HCT. The instrument has been released for astronomical observations from May 2014. It is currently heavily used by the community on 2 m HCT. It is the first public near-infrared spectrograph in the country. Several science results from local star formation to extra galactic studies have already been published by various groups using my calibrations and pipelines.

TIFR Near Infrared Imaging Camera - II (TIRCAM2)
After carrying out calibration of the upgraded TIRCAM2, it was extensively used for science observations from 2 m IGO telescope. Recently we have shifted TIRCAM2 to the largest telescope in India, the 3.6 m DOT in Nainital. TIRCAM2 is the only camera in the country which can image in the L′ band (3.6 μm).

100 cm TIFR Far-Infrared Balloon-borne Telescope
The wavelet filter signal processing I developed has enabled us to improve the pointing and aspect of the 100 cm TIFR Far-Infrared Balloon-borne Telescope while operating in fast un-chopped mode. We will be having our next balloon flight by the end of 2016. The pipeline for the FIR Fabry-Perot spectrometer on this telescope is also successfully implemented and it generates clean maps of 158 μm [C II] line emission as well as continuum.

Unified NIR and Optical Pipelines for multiple instruments
By separating out the instrument specific parts from the general algorithms of optical and near infrared data reduction, I developed two modular pipelines for NIR instruments and Optical instruments for reducing both photometry as well as spectroscopy data. These pipelines currently support more than five different instruments, and more instruments are incorporated as they are commissioned. Several science results have already been published in refereed journals by various groups using these pipelines.

11.3 Future work

We have demonstrated that the FUors and EXor systems are the best laboratories to test any accretion-outflow models. While it is possible to measure instantaneous outflows by carrying out high resolution optical spectroscopy, it is difficult to estimate the instantaneous accretion rates by using the line fluxes alone. Simultaneous long term X-ray observations along

with high-resolution optical and near-infrared spectroscopy will give a better understanding of the relationship between the accretion and the outflow mechanisms.

Continuing the long-term multi-wavelength monitoring of all the available FUors and EXors will provide more insights on the environmental effects of these episodic outbursts on the protoplanetary discs. Modelling the effect of the outbursts on the chemistry of the disc, snow-line, dust structure, etc., needs to be carried out for each source and can in principle be verified by conducting observations with ALMA[1].

The hierarchical Bayesian model, we have developed, shows very promising results in our simulations. Codes written for the model are directly applicable to the real data. Hence, the next step is to compile all the available multi-epoch, multi-wavelength photometric observations of the YSOs and to fit the model to them.

On the instrumentation side, lots of new exciting instruments are being developed in the country. The expertise from TIRSPEC, TIRCAM2, etc, will be invaluable for the next generation instruments we are currently developing at TIFR, namely TANSPEC[2] and IRSIS[3]. TIRSPEC can also be upgraded to the more modern H1RG detector array to keep the instrument competitive for the next decade.

[1] Atacama Large Millimeter Array
[2] TIFR-ARIES Near Infrared Spectrograph
[3] Infrared Spectroscopic Imaging Survey (satellite)

Appendix A

List of Sources in the MFES Program

List of sources in our long-term multi-wavelength monitoring program of FUors and EXors Sources (MFES). All the coordinates are in J2000.0 epoch.

Name	RA (hh mm ss)	Dec (dd mm ss)
OO ser	18 29 49.130	+01 16 20.65
IRAS 18341-0113	18 36 46.494	-01 10 41.57
V710 Cas	00 36 46.30	+63 28 54.1
V1515 Cyg	20 23 48.02	+42 12 25.8
PV Cep	20 45 53.943	+67 57 38.66
V2492 Cyg	20 51 26.184	+44 05 20.51
V2493 Cyg	20 58 17.025	+43 53 43.39
V2494 Cyg	20 58 21.093	+52 29 27.70
V2495 Cyg	21 00 25.38	+52 30 15.5
V1331 Cyg	21 01 09.210	+50 21 44.77
V1735 Cyg	21 47 20.66	+47 32 03.6
V733 Cep	22 53 33.26	+62 32 23.6
V1180 Cas	02 33 01.539	+72 43 26.92
V710 Cas	00 36 46.30	+63 28 54.1
IRAS 04376+5413	4 41 35.8	+54 19 20.0
NY Ori	5 35 36.0	-5 12 25
V1118 Ori	5 34 44.8	-5 33 42
V1143 Ori	5 38 03.9	-4 16 43
V2775 Ori	5 42 48.49	-08 16 34.74
FU Ori	5 45 22.36	+09 04 12.40
V1647 Ori	5 46 14.0	-00 05 40.1
V1184 Tau	5 47 03.8	+21 00 36
V899 Mon	6 09 19.3	-06 41 55.4
V900 Mon	6 57 22.224	-08 23 17.64

Bibliography

Ábrahám, P. et al. (2009). "Episodic formation of cometary material in the outburst of a young Sun-like star". en. In: *Nature* 459.7244, pp. 224–226. ISSN: 0028-0836. DOI: 10.1038/nature08004. URL: http://www.nature.com/nature/journal/v459/n7244/full/nature08004.html (visited on 03/18/2013).

Abrahám, P. et al. (2006). "First AU-scale observations of V1647 Orionis with VLTI/MIDI". In: *Astronomy and Astrophysics* 449.2, pp. 13–16.

Acosta-Pulido, J. A. et al. (2007a). "The 2004-2006 Outburst and Environment of V1647 Ori". en. In: *The Astronomical Journal* 133.5, p. 2020. ISSN: 1538-3881. DOI: 10.1086/512101. URL: http://iopscience.iop.org/1538-3881/133/5/2020 (visited on 05/15/2013).

— (2007b). "The 2004-2006 Outburst and Environment of V1647 Ori". en. In: *The Astronomical Journal* 133.5, p. 2020. ISSN: 1538-3881. DOI: 10.1086/512101. URL: http://iopscience.iop.org/1538-3881/133/5/2020.

Acosta-Pulido, Jose, Carlos Dominguez-Tagle, and Arturo Manchado (2003). "Characterization of the scientific grade Hawaii detector for LIRIS". In: ed. by Masanori Iye and Alan F. M. Moorwood. 00000, pp. 437–444. DOI: 10.1117/12.460314. URL: http://spie.org/Publications/Proceedings/Paper/10.1117/12.460314 (visited on 04/27/2014).

Alcalá, J. M. et al. (2014). "X-shooter spectroscopy of young stellar objects: IV. Accretion in low-mass stars and substellar objects in Lupus". In: *Astronomy & Astrophysics* 561, A2. ISSN: 0004-6361, 1432-0746. DOI: 10.1051/0004-6361/201322254. URL: http://www.aanda.org/10.1051/0004-6361/201322254 (visited on 01/13/2015).

André, Ph. et al. (2010). "From filamentary clouds to prestellar cores to the stellar IMF: Initial highlights from the *Herschel* Gould Belt Survey". In: *Astronomy and Astrophysics* 518, p. L102. ISSN: 0004-6361, 1432-0746. DOI: 10.1051/0004-6361/201014666. URL: http://www.aanda.org/10.1051/0004-6361/201014666 (visited on 03/30/2015).

Andrews, S. M, B. Rothberg, and T. Simon (2004). "Mid-Infrared and Submillimeter Observations of the Illuminating Source of MCNeil's Variable Nebula". In: *The Astrophysical Journal Letters* 610, p. L45.

Appenzeller, Immo and Claude Bertout (2013). "Inclination effects in T Tauri star spectra". In: *Astronomy & Astrophysics* 558, A83. ISSN: 0004-6361, 1432-0746. DOI: 10.1051/0004-6361/201322160. URL: http://www.aanda.org/10.1051/0004-6361/201322160 (visited on 02/03/2016).

Armitage, P. J., M. Livio, and J. E. Pringle (2001). "Episodic accretion in magnetically layered protoplanetary discs". In: 324, pp. 705–711. DOI: 10.1046/j.1365-8711.2001.04356.x. eprint: astro-ph/0101253.

Aspin, C. and B. Reipurth (2009). "V1647 Orionis: Optical Photometric and Spectroscopic Monitoring Through the 2003-2006 Outburst". In: *The Astronomical Journal* 138, p. 1137.

Aspin, C. et al. (2006). "The 1966-1967 Outburst of V1647 Orionis and the Appearance of McNeil's Nebula". In: *The Astronomical Journal* 132, p. 1298.

Aspin, C. et al. (2009). "V1647 Orionis: Reinvigorated Accretion and the Re-Appearance of McNeil's Nebula". In: *The Astrophysical Journal Letters* 692, p. L67.

Aspin, Colin (2011a). "The Continuing Outburst of V1647 Orionis: Winter/Spring 2011 Observations". en. In: *The Astronomical Journal* 142.4, p. 135. ISSN: 1538-3881. DOI: 10.1088/0004-6256/142/4/135. URL: http://iopscience.iop.org/1538-3881/142/4/135.

— (2011b). "V2492 Cygni: The Early Evolution of the 2010 Outburst". en. In: *The Astronomical Journal* 141.6, p. 196. ISSN: 1538-3881. DOI: 10.1088/0004-6256/141/6/196. URL: http://iopscience.iop.org/1538-3881/141/6/196 (visited on 01/30/2015).

Aspin, Colin, Tracy L. Beck, and Bo Reipurth (2008). "V1647 ORIONIS: ONE YEAR INTO QUIESCENCE". In: *The Astronomical Journal* 135.1, pp. 423–440. ISSN: 0004-6256, 1538-3881. DOI: 10.1088/0004-6256/135/1/423. URL: http://stacks.iop.org/1538-3881/135/i=1/a=423?key=crossref.954d6f4c03be6ae9036331bd0360495e.

Astropy Collaboration et al. (2013). "Astropy: A community Python package for astronomy". In: *Astronomy and Astrophysics* 558, p. 33. ISSN: 0004-6361. DOI: 10.1051/0004-6361/201322068. URL: http://adsabs.harvard.edu/abs/2013A%26A...558A..33A (visited on 04/30/2014).

Audard, M. et al. (2014). "Episodic Accretion in Young Stars". In: *Protostars and Planets VI*, pp. 387–410. DOI: 10.2458/azu_uapress_9780816531240-ch017. arXiv: 1401.3368 [astro-ph.SR].

Baraffe, I., E. Vorobyov, and G. Chabrier (2012). "Observed Luminosity Spread in Young Clusters and FU Ori Stars: A Unified Picture". en. In: *The Astrophysical Journal* 756.2, p. 118. ISSN: 0004-637X. DOI: 10.1088/0004-637X/756/2/118. URL: http://iopscience.iop.org/0004-637X/756/2/118 (visited on 03/19/2015).

Bell, K. R. and D. N. C. Lin (1994). "Using FU Orionis outbursts to constrain self-regulated protostellar disk models". In: *The Astrophysical Journal* 427, pp. 987–1004. ISSN: 0004-637X. DOI: 10.1086/174206. URL: http://adsabs.harvard.edu/abs/1994ApJ...427..987B (visited on 03/07/2015).

Bessell, M. S. and J. M. Brett (1988). "JHKLM photometry - Standard systems, passbands, and intrinsic colors". In: *Publications of the Astronomical Society of the Pacific* 100, pp. 1134–1151. ISSN: 0004-6280. DOI: 10.1086/132281. URL: http://adsabs.harvard.edu/abs/1988PASP..100.1134B (visited on 05/21/2013).

Blandford, R. D. and D. G. Payne (1982). "Hydromagnetic flows from accretion discs and the production of radio jets". en. In: *Monthly Notices of the Royal Astronomical Society* 199.4, pp. 883–903. ISSN: 0035-8711, 1365-2966. DOI: 10.1093/mnras/199.4.883. URL: http://mnras.oxfordjournals.org/content/199/4/883 (visited on 01/22/2016).

Blinova, A. A., M. M. Romanova, and R. V. E. Lovelace (2015). "Boundary between Stable and Unstable Regimes of Accretion. Ordered and

Chaotic Unstable Regimes". In: *arXiv:1501.01948 [astro-ph]*. URL: http://arxiv.org/abs/1501.01948 (visited on 03/06/2015).

Bolatto, Alberto D., Mark Wolfire, and Adam K. Leroy (2013). "The CO-to-H2 Conversion Factor". In: *Annual Review of Astronomy and Astrophysics* 51.1, pp. 207–268. DOI: 10.1146/annurev-astro-082812-140944. URL: http://dx.doi.org/10.1146/annurev-astro-082812-140944 (visited on 10/24/2016).

Boley, A. C. et al. (2006). "The Thermal Regulation of Gravitational Instabilities in Protoplanetary Disks. III. Simulations with Radiative Cooling and Realistic Opacities". In: 651, pp. 517–534. DOI: 10.1086/507478. eprint: astro-ph/0607112.

Bonnell, Ian and Pierre Bastien (1992). "Fragmentation of elongated cylindrical clouds. V - Dependence of mass ratios on initial conditions". In: *The Astrophysical Journal* 401, pp. 654–666. ISSN: 0004-637X. DOI: 10.1086/172093. URL: http://adsabs.harvard.edu/abs/1992ApJ...401..654B (visited on 05/15/2013).

Bouvier, J. et al. (2003). "Eclipses by circumstellar material in the TTauri star AA Tau - II. Evidence for non-stationary magnetospheric accretion". In: *Astronomy & Astrophysics* 409.1, p. 24. DOI: 10.1051/0004-6361:20030938.

Bramall, D. G. et al. (2010). "The SALT HRS spectrograph: final design, instrument capabilities, and operational modes". In: *Society of Photo-Optical Instrumentation Engineers (SPIE) Conference Series*. Vol. 7735. Society of Photo-Optical Instrumentation Engineers (SPIE) Conference Series, p. 4. DOI: 10.1117/12.856382.

Briceño, C. et al. (2004). "MCNeil's Nebula in Orion: The Outburst History". en. In: *The Astrophysical Journal Letters* 606.2, p. L123. ISSN: 1538-4357. DOI: 10.1086/421395. URL: http://iopscience.iop.org/1538-4357/606/2/L123 (visited on 05/15/2013).

Cardelli, Jason A., Geoffrey C. Clayton, and John S. Mathis (1989). "The relationship between infrared, optical, and ultraviolet extinction". In: *The Astrophysical Journal* 345, pp. 245–256. ISSN: 0004-637X. DOI: 10.1086/167900. URL: http://adsabs.harvard.edu/abs/1989ApJ...345..245C (visited on 11/11/2014).

Ciesla, Fred J. (2007). "Outward Transport of High-Temperature Materials Around the Midplane of the Solar Nebula". en. In: *Science* 318.5850, pp. 613–615. ISSN: 0036-8075, 1095-9203. DOI: 10.1126/science.1147273. URL: http://science.sciencemag.org/content/318/5850/613 (visited on 10/24/2016).

Cieza, Lucas A. et al. (2016). "Imaging the water snow-line during a protostellar outburst". en. In: *Nature* 535.7611, pp. 258–261. ISSN: 0028-0836. DOI: 10.1038/nature18612. URL: http://www.nature.com/nature/journal/v535/n7611/full/nature18612.html (visited on 07/14/2016).

Clarke, C. J. and D. Syer (1996). "Low-mass companions to T Tauri stars: a mechanism for rapid-rise FU Orionis outbursts". In: 278, pp. L23–L27. DOI: 10.1093/mnras/278.1.L23. eprint: astro-ph/9511030.

Connelley, Michael S. and Thomas P. Greene (2014). "Near-IR Spectroscopic Monitoring of Class I Protostars: Variability of Accretion and Wind Indicators". en. In: *The Astronomical Journal* 147.6, p. 125. ISSN: 1538-3881.

DOI: 10.1088/0004-6256/147/6/125. URL: http://stacks.iop.org/1538-3881/147/i=6/a=125 (visited on 01/22/2016).

Connelly, James N. et al. (2012). "The Absolute Chronology and Thermal Processing of Solids in the Solar Protoplanetary Disk". en. In: *Science* 338.6107, pp. 651–655. ISSN: 0036-8075, 1095-9203. DOI: 10.1126/science.1226919. URL: http://www.sciencemag.org/content/338/6107/651 (visited on 04/22/2015).

D'Angelo, Caroline R. and Hendrik C. Spruit (2010). "Episodic accretion on to strongly magnetic stars". en. In: *Monthly Notices of the Royal Astronomical Society* 406.2, pp. 1208–1219. ISSN: 0035-8711, 1365-2966. DOI: 10.1111/j.1365-2966.2010.16749.x. URL: http://mnras.oxfordjournals.org/content/406/2/1208 (visited on 03/06/2015).

Dokkum, Pieter G. van (2001). "Cosmic-Ray Rejection by Laplacian Edge Detection". In: *Publications of the Astronomical Society of the Pacific* 113.789, pp. 1420–1427. ISSN: 0004-6280. DOI: 10.1086/323894. URL: http://www.jstor.org/stable/10.1086/323894 (visited on 03/02/2015).

Dopita, A. (1978). "The Herbig-Haro objects in the GUM Nebula". In: *Astronomy and Astrophysics* 63, pp. 237–241. ISSN: 0004-6361. URL: http://adsabs.harvard.edu/abs/1978A%26A....63..237D (visited on 07/12/2016).

Dunham, Michael M. et al. (2008). "Identifying the Low-Luminosity Population of Embedded Protostars in the c2d Observations of Clouds and Cores". en. In: *The Astrophysical Journal Supplement Series* 179.1, p. 249. ISSN: 0067-0049. DOI: 10.1086/591085. URL: http://stacks.iop.org/0067-0049/179/i=1/a=249 (visited on 08/09/2016).

Evans II, Neal J. et al. (2009). "The Spitzer c2d Legacy Results: Star-Formation Rates and Efficiencies; Evolution and Lifetimes". en. In: *The Astrophysical Journal Supplement Series* 181.2, p. 321. ISSN: 0067-0049. DOI: 10.1088/0067-0049/181/2/321. URL: http://iopscience.iop.org/0067-0049/181/2/321 (visited on 03/25/2013).

Fedele, D. et al. (2007). "Optical and infrared properties of V1647 Orionis during the 2003–2006 outburst". In: *Astronomy and Astrophysics* 472.1, pp. 207–217. ISSN: 0004-6361, 1432-0746. DOI: 10.1051/0004-6361:20077725. URL: http://www.aanda.org/articles/aa/abs/2007/34/aa7725-07/aa7725-07.html.

Finger, Gert et al. (2000). "Performance of large-format HgCdTe and InSb arrays for low-background applications". In: vol. 4008, pp. 1280–1297. DOI: 10.1117/12.395445. URL: http://dx.doi.org/10.1117/12.395445.

Ghosh, S. K. (2010). "Infrared astronomy in India with balloons". In: *Astronomical Society of India Conference Series*. Vol. 1, pp. 167–170. URL: http://adsabs.harvard.edu/full/2010ASInC...1..167G (visited on 04/07/2016).

Ghosh, S. K. and M. B. Naik (1993). "A data acquisition system for the TIFR near-infrared camera". In: *Bulletin of the Astronomical Society of India* 21, pp. 485–487.

Ghosh, S. K. et al. (1988). "Far-infrared (120-300 micron) observations of the Carina Nebula". In: *The Astrophysical Journal* 330, p. 928. ISSN: 0004-637X. URL: http://adsabs.harvard.edu/abs/1988ApJ...330..928G (visited on 04/07/2016).

Greene, Thomas P. et al. (1994). "Further mid-infrared study of the rho Ophiuchi cloud young stellar population: Luminosities and masses of pre-main-sequence stars". In: *The Astrophysical Journal* 434, pp. 614–626. ISSN: 0004-637X. DOI: 10.1086/174763. URL: http://adsabs.harvard.edu/abs/1994ApJ...434..614G (visited on 05/04/2015).

Gullbring, Erik et al. (1998). "Disk Accretion Rates for T Tauri Stars". en. In: *The Astrophysical Journal* 492.1, p. 323. ISSN: 0004-637X. DOI: 10.1086/305032. URL: http://iopscience.iop.org/0004-637X/492/1/323 (visited on 03/13/2015).

Gutermuth, R. A. et al. (2009). "A Spitzer Survey of Young Stellar Clusters Within One Kiloparsec of the Sun: Cluster Core Extraction and Basic Structural Analysis". In: 184, pp. 18–83. DOI: 10.1088/0067-0049/184/1/18. arXiv: 0906.0201 [astro-ph.SR].

Hamaguchi, Kenji et al. (2012). "X-Raying the Beating Heart of a Newborn Star: Rotational Modulation of High-energy Radiation from V1647 Ori". en. In: *The Astrophysical Journal* 754.1, p. 32. ISSN: 0004-637X. DOI: 10.1088/0004-637X/754/1/32. URL: http://iopscience.iop.org/0004-637X/754/1/32 (visited on 05/15/2013).

Hamann, Fred (1994). "Emission-line studies of young stars. 4: The optical forbidden lines". In: *The Astrophysical Journal Supplement Series* 93, pp. 485–518. ISSN: 0067-0049. DOI: 10.1086/192064. URL: http://adsabs.harvard.edu/abs/1994ApJS...93..485H (visited on 05/15/2013).

Hamann, Fred and S. E. Persson (1992). "Emission-line studies of young stars. I - The T Tauri stars." In: *The Astrophysical Journal Supplement Series* 82, pp. 247–283. ISSN: 0067-0049. DOI: 10.1086/191715. URL: http://adsabs.harvard.edu/abs/1992ApJS...82..247H (visited on 05/15/2013).

Hartigan, Patrick, Suzan Edwards, and Louma Ghandour (1995). "Disk Accretion and Mass Loss from Young Stars". In: *The Astrophysical Journal* 452, p. 736. ISSN: 0004-637X. DOI: 10.1086/176344. URL: http://adsabs.harvard.edu/abs/1995ApJ...452..736H (visited on 01/10/2015).

Hartmann, L. (2009). *Accretion Processes in Star Formation: Second Edition*. Cambridge University Press.

Hartmann, Lee (1998). *Accretion Processes in Star Formation*. Cambridge Univ. Press, Cambridge. ISBN: 0521435072. URL: http://adsabs.harvard.edu/abs/1998apsf.book.....H (visited on 03/04/2015).

Hartmann, Lee and Scott J. Kenyon (1996). "The Fu Orionis Phenomenon". In: *Annual Review of Astronomy and Astrophysics* 34.1, pp. 207–240. DOI: 10.1146/annurev.astro.34.1.207. URL: http://www.annualreviews.org/doi/abs/10.1146/annurev.astro.34.1.207 (visited on 07/11/2013).

Hartmann, Lee, Zhaohuan Zhu, and Nuria Calvet (2011). "On Rapid Disk Accretion and Initial Conditions in Protostellar Evolution". In: *arXiv:1106.3343 [astro-ph]*. arXiv: 1106.3343. URL: http://arxiv.org/abs/1106.3343 (visited on 07/12/2016).

Herbig, G. H. (1977). "Eruptive phenomena in early stellar evolution". In: *Astrophysical Journal, Part 1, vol. 217, Nov. 1, 1977, p. 693-715.* URL: http://articles.adsabs.harvard.edu/cgi-bin/nph-iarticle_

query?1977ApJ...217..693H&defaultprint=YES&filetype=.pdf (visited on 01/17/2013).

Herbst, W. et al. (2007). "The Rotation of Young Low-Mass Stars and Brown Dwarfs". In: *Protostars and Planets V*, pp. 297–311. eprint: astro-ph/0603673.

Hillenbrand, Lynne A. and Krzysztof P. Findeisen (2015). "A Simple Calculation in Service of Constraining the Rate of FU Orionis Outburst Events from Photometric Monitoring Surveys". en. In: *The Astrophysical Journal* 808.1, p. 68. ISSN: 0004-637X. DOI: 10.1088/0004-637X/808/1/68. URL: http://stacks.iop.org/0004-637X/808/i=1/a=68 (visited on 11/19/2015).

Hillenbrand, Lynne A. et al. (2013). "Highly Variable Extinction and Accretion in the Jet-driving Class I-type Young Star PTF 10nvg (V2492 Cyg, IRAS 20496+4354)". en. In: *The Astronomical Journal* 145.3, p. 59. ISSN: 1538-3881. DOI: 10.1088/0004-6256/145/3/59. URL: http://stacks.iop.org/1538-3881/145/i=3/a=59 (visited on 01/27/2016).

Hodapp, K. W. et al. (1996). "The HAWAII Infrared Detector Arrays: testing and astronomical characterization of prototype and science-grade devices". In: *New Astronomy* 1.2. 00165, pp. 177–196. ISSN: 1384-1076. DOI: 10.1016/S1384-1076(96)00013-9. URL: http://www.sciencedirect.com/science/article/pii/S1384107696000139 (visited on 04/27/2014).

Hosokawa, Takashi, Stella S. R. Offner, and Mark R. Krumholz (2011). "On the Reliability of Stellar Ages and Age Spreads Inferred from Pre-main-sequence Evolutionary Models". en. In: *The Astrophysical Journal* 738.2, p. 140. ISSN: 0004-637X. DOI: 10.1088/0004-637X/738/2/140. URL: http://stacks.iop.org/0004-637X/738/i=2/a=140 (visited on 07/12/2016).

Hunt, L. K. et al. (1998). "Northern JHK Standard Stars for Array Detectors". en. In: *The Astronomical Journal* 115.6, p. 2594. ISSN: 1538-3881. DOI: 10.1086/300349. URL: http://iopscience.iop.org/1538-3881/115/6/2594 (visited on 05/15/2013).

Hunter, John D. (2007). "Matplotlib: A 2D Graphics Environment". In: *Computing in Science & Engineering* 9.3, pp. 90–95. ISSN: 1521-9615. DOI: 10.1109/MCSE.2007.55. URL: http://scitation.aip.org/content/aip/journal/cise/9/3/10.1109/MCSE.2007.55 (visited on 04/30/2014).

Ioannidis, G. and D. Froebrich (2012). "YSO jets in the Galactic plane from UWISH2 – II. Outflow luminosity and length distributions in Serpens and Aquila". en. In: *Monthly Notices of the Royal Astronomical Society* 425.2, pp. 1380–1393. ISSN: 1365-2966. DOI: 10.1111/j.1365-2966.2012.21556.x. URL: http://onlinelibrary.wiley.com/doi/10.1111/j.1365-2966.2012.21556.x/abstract (visited on 03/25/2013).

Irwin, J. and J. Bouvier (2009). "The rotational evolution of low-mass stars". In: *The Ages of Stars*. Ed. by E. E. Mamajek, D. R. Soderblom, and R. F. G. Wyse. Vol. 258. IAU Symposium, pp. 363–374. DOI: 10.1017/S1743921309032025.

Jones, Eric, Travis Oliphant, Pearu Peterson, et al. (2001). *SciPy: Open source scientific tools for Python*. [Online; accessed 2015-03-03]. URL: http://www.scipy.org/.

Kastner, J. H. et al. (2004). "An X-ray outburst from the rapidly accreting young star that illuminates McNeil's nebula". In: *Nature* 430.6998, pp. 429–431.

Kenyon, Scott J. et al. (1990). "An IRAS survey of the Taurus-Auriga molecular cloud". In: *The Astronomical Journal* 99, pp. 869–887. ISSN: 0004-6256. DOI: 10.1086/115380. URL: http://adsabs.harvard.edu/abs/1990AJ.....99..869K (visited on 07/13/2013).

Kley, W. and D. N. C. Lin (1999). "Evolution of FU Orionis Outbursts in Protostellar Disks". In: 518, pp. 833–847. DOI: 10.1086/307296.

Konigl, A. and R. E. Pudritz (2000). "Disk Winds and the Accretion-Outflow Connection". In: *Protostars and Planets IV*, p. 759. URL: http://adsabs.harvard.edu/abs/2000prpl.conf..759K (visited on 02/03/2016).

Kospal, A. et al. (2005). "The rapid fading of V1647 Orionis: the sudden end of a FUor-type eruption?" In: *Arxiv preprint astro-ph/0511733*.

Kóspál, á. et al. (2011). "NEAR-INFRARED SPECTROSCOPY OF EX Lupi IN OUTBURST". In: *The Astrophysical Journal* 736.1, p. 72. ISSN: 0004-637X, 1538-4357. DOI: 10.1088/0004-637X/736/1/72. URL: http://stacks.iop.org/0004-637X/736/i=1/a=72?key=crossref.cd1cd616453cf1228b5692d9af839923 (visited on 02/08/2015).

Kóspál, Á et al. (2013). "Exploring the circumstellar environment of the young eruptive star V2492 Cygni". en. In: *Astronomy & Astrophysics* 551, A62. ISSN: 0004-6361, 1432-0746. DOI: 10.1051/0004-6361/201220553. URL: http://dx.doi.org/10.1051/0004-6361/201220553 (visited on 10/08/2015).

Kraus, S. et al. (2016). "V346 Normae: first post-outburst observations of an FU Orionis star". en. In: *Monthly Notices of the Royal Astronomical Society: Letters* 462.1, pp. L61–L65. ISSN: 1745-3925, 1745-3933. DOI: 10.1093/mnrasl/slw126. URL: http://mnrasl.oxfordjournals.org/content/462/1/L61 (visited on 08/01/2016).

Kruschke, J. (2014). *Doing Bayesian Data Analysis: A Tutorial with R, JAGS, and Stan*. Elsevier Science. ISBN: 9780124059160. URL: https://books.google.co.in/books?id=FzvLAwAAQBAJ.

Kulkarni, A. K. and M. M. Romanova (2008). "Accretion to magnetized stars through the Rayleigh–Taylor instability: global 3D simulations". en. In: *Monthly Notices of the Royal Astronomical Society* 386.2, pp. 673–687. ISSN: 0035-8711, 1365-2966. DOI: 10.1111/j.1365-2966.2008.13094.x. URL: http://mnras.oxfordjournals.org/content/386/2/673 (visited on 03/06/2015).

Kun, M. (2008). "Early spectroscopy and photometry of the new outburst of V1647 Ori". In: *Information Bulletin on Variable Stars* 5850, p. 1. ISSN: 0374-0676. URL: http://adsabs.harvard.edu/abs/2008IBVS.5850....1K.

Kurosawa, Ryuichi and M. M. Romanova (2012). "Line formation in the inner winds of classical T Tauri stars: testing the conical-shell wind solution: Line profile models of the inner wind of CTTSs". en. In: *Monthly Notices of the Royal Astronomical Society* 426.4, pp. 2901–2916. ISSN: 00358711. DOI: 10.1111/j.1365-2966.2012.21853.x. URL: http://

mnras.oxfordjournals.org/cgi/doi/10.1111/j.1365-2966.2012.21853.x (visited on 02/03/2016).

Lada, CJ (1987). *Star Forming Regions (IAU Symp. 115), ed. M. Peimbert & J. Jugaku*.

Landolt, Arlo U. (1992). "UBVRI photometric standard stars in the magnitude range 11.5-16.0 around the celestial equator". In: *The Astronomical Journal* 104, pp. 340–371. ISSN: 0004-6256. DOI: 10.1086/116242. URL: http://adsabs.harvard.edu/abs/1992AJ....104..340L (visited on 12/11/2014).

Lee, Jeong-Eun et al. (2015). "High Resolution Optical and NIR Spectra of HBC 722". en. In: *The Astrophysical Journal* 807.1, p. 84. ISSN: 0004-637X. DOI: 10.1088/0004-637X/807/1/84. URL: http://stacks.iop.org/0004-637X/807/i=1/a=84 (visited on 01/22/2016).

Lii, Patrick, Marina Romanova, and Richard Lovelace (2012). "Magnetic launching and collimation of jets from the disc-magnetosphere boundary: 2.5D MHD simulations: Magnetic launching and collimation of jets". en. In: *Monthly Notices of the Royal Astronomical Society* 420.3, pp. 2020–2033. ISSN: 00358711. DOI: 10.1111/j.1365-2966.2011.20133.x. URL: http://mnras.oxfordjournals.org/cgi/doi/10.1111/j.1365-2966.2011.20133.x (visited on 02/04/2016).

Lodato, G. and C. J. Clarke (2004). "Massive planets in FU Orionis discs: implications for thermal instability models". In: *Monthly Notices of the Royal Astronomical Society* 353.3, pp. 841–852. ISSN: 00358711, 13652966. DOI: 10.1111/j.1365-2966.2004.08112.x. URL: http://doi.wiley.com/10.1111/j.1365-2966.2004.08112.x (visited on 07/24/2012).

Lombardi, M., J. Alves, and C. J. Lada (2011). "2MASS wide field extinction maps: IV. The Orion, Monoceros R2, Rosette, and Canis Major star forming regions". In: *Astronomy & Astrophysics* 535, A16. ISSN: 0004-6361, 1432-0746. DOI: 10.1051/0004-6361/201116915. URL: http://www.aanda.org/10.1051/0004-6361/201116915 (visited on 09/22/2014).

Lovelace, R. V. E. et al. (2002). "Poynting Jets from Accretion Disks". en. In: *The Astrophysical Journal* 572.1, p. 445. ISSN: 0004-637X. DOI: 10.1086/340292. URL: http://stacks.iop.org/0004-637X/572/i=1/a=445 (visited on 02/04/2016).

McGehee, P.M. et al. (2004). "The V1647 Ori (IRAS 05436-0007) Protostar and its environment". In: *Arxiv preprint astro-ph/0408308*.

McNeil, J. W., B. Reipurth, and K. Meech (2004). "IRAS 05436-0007". In: 8284.

Megeath, S. T. et al. (2012). "The Spitzer Space Telescope Survey of the Orion A and B Molecular Clouds. I. A Census of Dusty Young Stellar Objects and a Study of Their Mid-infrared Variability". In: 144, 192, p. 192. DOI: 10.1088/0004-6256/144/6/192. arXiv: 1209.3826.

Men'shchikov, A. et al. (2012). "A multi-scale, multi-wavelength source extraction method: *getsources*". In: *Astronomy & Astrophysics* 542, A81. ISSN: 0004-6361, 1432-0746. DOI: 10.1051/0004-6361/201218797. URL: http://www.aanda.org/10.1051/0004-6361/201218797 (visited on 01/25/2015).

Merle, T. et al. (2011). "A grid of non-local thermodynamic equilibrium corrections for magnesium and calcium in late-type giant and supergiant

stars: application to Gaia". In: *Monthly Notices of the Royal Astronomical Society*. URL: http://onlinelibrary.wiley.com/doi/10.1111/j.1365-2966.2011.19540.x/full.

Meyer, Michael R., Nuria Calvet, and Lynne A. Hillenbrand (1997). "Intrinsic Near-Infrared Excesses of T Tauri Stars: Understanding the Classical T Tauri Star Locus". In: *The Astronomical Journal* 114, pp. 288–300. ISSN: 0004-6256. DOI: 10.1086/118474. URL: http://adsabs.harvard.edu/abs/1997AJ....114..288M (visited on 03/06/2015).

Mookerjea, B. et al. (2003). "Mapping of large scale 158 [CII] line emission: Orion A". In: *Astronomy and Astrophysics* 404.2. 00000, pp. 569–578. ISSN: 0004-6361, 1432-0756. DOI: 10.1051/0004-6361:20030537. URL: http://www.edpsciences.org/10.1051/0004-6361:20030537 (visited on 04/18/2016).

Moran, J. M. (1983). "Radio Observations of Compact Sources Near Herbig-Haro Objects". In: 7, p. 95.

Mosoni, L. et al. (2013). "Dynamics during outburst: VLTI observations of the young eruptive star V1647 Ori during its 2003-2006 outburst". In: *Astronomy & Astrophysics* 552, A62. ISSN: 0004-6361, 1432-0746. DOI: 10.1051/0004-6361/201218770. URL: http://www.aanda.org/index.php?option=com_article&access=dkey&dkey=10.1051/0004-6361/201218770.

Muzerolle, J., L. Hartmann, and N. Calvet (1998). "Emission-Line Diagnostics of T Tauri Magnetospheric Accretion. I. Line Profile Observations". In: *The Astronomical Journal* 116, p. 455.

Naik, M. B. et al. (2012). "TIRCAM2: The TIFR Near Infrared Imaging Camera". In: *Bull. Astr. Soc. India* 40, pp. 531–545. URL: http://arxiv.org/abs/1211.5542 (visited on 05/15/2013).

Ninan, J. P., D. K. Ojha, and N. S. Philip (2016). "Episodic High-velocity Outflows from V899 Mon: A Constraint On The Outflow Mechanisms". en. In: *The Astrophysical Journal* 825.1, p. 65. ISSN: 0004-637X. DOI: 10.3847/0004-637X/825/1/65. URL: http://stacks.iop.org/0004-637X/825/i=1/a=65 (visited on 06/30/2016).

Ninan, J. P. et al. (2012). "V1647 Orionis". In: *Central Bureau Electronic Telegrams* 3164.

Ninan, J. P. et al. (2013a). "Dust formation in Nova Cephei 2013". In: *The Astronomer's Telegram* 5269, p. 1. URL: http://adsabs.harvard.edu/abs/2013ATel.5269....1N (visited on 11/12/2013).

Ninan, J. P. et al. (2013b). "Reappearance of McNeil's Nebula (V1647 Orionis) and its Outburst Environment". en. In: *The Astrophysical Journal* 778.2, p. 116. ISSN: 0004-637X. DOI: 10.1088/0004-637X/778/2/116. URL: http://iopscience.iop.org/0004-637X/778/2/116 (visited on 11/12/2013).

Ninan, J. P. et al. (2014). "TIRSPEC: TIFR Near Infrared Spectrometer and Imager". en. In: *Journal of Astronomical Instrumentation*, p. 1450006. ISSN: 2251-1717, 2251-1725. DOI: 10.1142/S2251171714500068. URL: http://www.worldscientific.com/doi/abs/10.1142/S2251171714500068 (visited on 11/20/2014).

Ninan, J. P. et al. (2015). "V899 Mon: An Outbursting Protostar with a Peculiar Light Curve, and Its Transition Phases". en. In: *The Astrophysical Journal* 815.1, p. 4. ISSN: 0004-637X. DOI: 10.1088/0004-637X/815/

1/4. URL: http://stacks.iop.org/0004-637X/815/i=1/a=4 (visited on 01/07/2016).

Nisini, B. et al. (1995). "Mass loss rates from HI infrared lines in Herbig Ae/Be stars." In: *Astronomy and Astrophysics* 302, p. 169. ISSN: 0004-6361. URL: http://adsabs.harvard.edu/abs/1995A%26A...302..169N (visited on 01/26/2015).

Ojha, D. K. et al. (2002). "First light observations with TIFR near-infrared camera." In: *Bulletin of the Astronomical Society of India* 30.

Ojha, D. K. et al. (2003). "Infrared L'band (lambda-cen- ~3.9 mu-m) observations with TIFR near-infrared camera (TIRCAM)." In: *Bulletin of the Astronomical Society of India* 31, pp. 467–470.

Ojha, D. K. et al. (2005). "V1647 Orionis (IRAS 05436-0007): A New Look at McNeil's Nebula". In: *PASJ* 57, p. 203. URL: http://arxiv.org/abs/astro-ph/0412455.

Ojha, D. K. et al. (2006). "Post-outburst phase of McNeil's nebula (V1647 Orionis)". In: *Monthly Notices of the Royal Astronomical Society* 368.2, pp. 825–836. ISSN: 0035-8711, 1365-2966. DOI: 10.1111/j.1365-2966.2006.10159.x. URL: http://doi.wiley.com/10.1111/j.1365-2966.2006.10159.x.

Ojha, D. K. et al. (2012). "TIFR Near Infrared Spectrometer and Imager (TIRSPEC)". In: *Astronomical Society of India Conference Series*. Vol. 4, p. 191. URL: http://adsabs.harvard.edu/abs/2012ASInC...4..191O (visited on 05/02/2014).

Oliphant, Travis E. (2007). "Python for Scientific Computing". In: *Computing in Science & Engineering* 9.3, pp. 10–20. ISSN: 1521-9615. DOI: 10.1109/MCSE.2007.58. URL: http://scitation.aip.org/content/aip/journal/cise/9/3/10.1109/MCSE.2007.58 (visited on 04/30/2014).

Orlando, Salvatore et al. (2011). "Mass accretion to young stars triggered by flaring activity in circumstellar discs". en. In: *Monthly Notices of the Royal Astronomical Society* 415.4, pp. 3380–3392. ISSN: 0035-8711, 1365-2966. DOI: 10.1111/j.1365-2966.2011.18954.x. URL: http://mnras.oxfordjournals.org/content/415/4/3380 (visited on 03/06/2015).

Osterbrock, D. E. and G. J. Ferland (2006). *Astrophysics of gaseous nebulae and active galactic nuclei*. CA: University Science Books.

Persson, S. E. et al. (1998). "A New System of Faint Near-Infrared Standard Stars". en. In: *The Astronomical Journal* 116.5. 00869, p. 2475. ISSN: 1538-3881. DOI: 10.1086/300607. URL: http://iopscience.iop.org/1538-3881/116/5/2475 (visited on 05/28/2014).

Petrov, P. P. et al. (2014). "Facing the wind of the pre-FUor V1331 Cyg". en. In: *Monthly Notices of the Royal Astronomical Society* 442.4, pp. 3643–3652. ISSN: 0035-8711, 1365-2966. DOI: 10.1093/mnras/stu1131. URL: http://mnras.oxfordjournals.org/content/442/4/3643 (visited on 01/23/2016).

Plunkett, Adele L. et al. (2015). "Episodic molecular outflow in the very young protostellar cluster Serpens South". en. In: *Nature* 527.7576, pp. 70–73. ISSN: 0028-0836. DOI: 10.1038/nature15702. URL: http://www.nature.com/nature/journal/v527/n7576/full/nature15702.html (visited on 11/09/2015).

Pringle, J. E. (1981). "Accretion discs in astrophysics". In: *Annual review of astronomy and astrophysics* 19, pp. 137–162. URL: http://adsabs.harvard.edu/full/1981ARA&A..19..137P.

Reipurth, B. and C. Aspin (2004). "IRAS 05436–0007 and the Emergence of MCNeil's Nebula". In: *The Astrophysical Journal Letters* 606, p. L119. URL: http://iopscience.iop.org/1538-4357/606/2/L119.

Reipurth, Bo and Colin Aspin (1997). "Infrared Spectroscopy of Herbig-Haro Energy Sources". In: *The Astronomical Journal* 114, p. 2700. ISSN: 0004-6256. DOI: 10.1086/118680. URL: http://adsabs.harvard.edu/abs/1997AJ....114.2700R (visited on 07/12/2016).

Rettig, T.W. et al. (2005). "CO Emission and Absorption toward V1647 Orionis (McNeil's Nebula)". In: *The Astrophysical Journal* 626, p. 245.

Rieke, G. H. and M. J. Lebofsky (1985). "The interstellar extinction law from 1 to 13 microns". In: *The Astrophysical Journal* 288, pp. 618–621. ISSN: 0004-637X. DOI: 10.1086/162827. URL: http://adsabs.harvard.edu/abs/1985ApJ...288..618R (visited on 11/11/2014).

Rieke, G.H. (2007). "Infrared Detector Arrays for Astronomy". In: *Annual Review of Astronomy and Astrophysics* 45.1, pp. 77–115. DOI: 10.1146/annurev.astro.44.051905.092436. URL: http://www.annualreviews.org/doi/abs/10.1146/annurev.astro.44.051905.092436 (visited on 11/13/2013).

Riopel, Martin et al. (2004). "An Optimized Data Acquisition System Without Reset Anomaly for the Hawaii and Hawaii-2 Arrays". In: *Scientific Detectors for Astronomy*. Ed. by Paola Amico, James W. Beletic, and Jenna E. Beletic. Astrophysics and Space Science Library. 00013. Springer Netherlands, pp. 453–458. ISBN: 978-1-4020-1788-9 978-1-4020-2527-3. URL: http://link.springer.com/chapter/10.1007/1-4020-2527-0_59 (visited on 04/27/2014).

Robberto, Massimo (2007). *Analysis of the sampling schemes for WFC3-IR*. Tech. rep. 00004, p. 12. URL: http://adsabs.harvard.edu/abs/2007wfc..rept...12R (visited on 04/27/2014).

Robitaille, Thomas P. et al. (2007). "Interpreting Spectral Energy Distributions from Young Stellar Objects. II. Fitting Observed SEDs Using a Large Grid of Precomputed Models". en. In: *The Astrophysical Journal Supplement Series* 169.2, p. 328. ISSN: 0067-0049. DOI: 10.1086/512039. URL: http://iopscience.iop.org/0067-0049/169/2/328 (visited on 06/30/2014).

Romanova, M. M. et al. (2009). "Launching of conical winds and axial jets from the discmagnetosphere boundary: axisymmetric and 3D simulations". en. In: *Monthly Notices of the Royal Astronomical Society* 399.4, pp. 1802–1828. ISSN: 00358711, 13652966. DOI: 10.1111/j.1365-2966.2009.15413.x. URL: http://mnras.oxfordjournals.org/cgi/doi/10.1111/j.1365-2966.2009.15413.x (visited on 02/04/2016).

Scholz, Alexander, Dirk Froebrich, and Kenneth Wood (2013). "A systematic survey for eruptive young stellar objects using mid-infrared photometry". en. In: *Monthly Notices of the Royal Astronomical Society* 430.4, pp. 2910–2922. ISSN: 0035-8711, 1365-2966. DOI: 10.1093/mnras/stt091. URL: http://mnras.oxfordjournals.org/content/430/4/2910 (visited on 04/19/2013).

Semkov, E. H. et al. (2013). "Photometric and spectroscopic variability of the FUor star V582 Aurigae". en. In: *Astronomy & Astrophysics* 556, A60. ISSN: 0004-6361, 1432-0746. DOI: 10.1051/0004-6361/201321732. URL: http://dx.doi.org/10.1051/0004-6361/201321732 (visited on 10/07/2015).

Shu, Frank et al. (1994). "Magnetocentrifugally driven flows from young stars and disks. 1: A generalized model". In: *The Astrophysical Journal* 429, pp. 781–796. ISSN: 0004-637X. DOI: 10.1086/174363. URL: http://adsabs.harvard.edu/abs/1994ApJ...429..781S (visited on 01/22/2016).

Shu, Frank H., Hsien Shang, and Typhoon Lee (1996). "Toward an Astrophysical Theory of Chondrites". en. In: *Science* 271.5255, pp. 1545–1552. ISSN: 0036-8075, 1095-9203. DOI: 10.1126/science.271.5255.1545. URL: http://science.sciencemag.org/content/271/5255/1545 (visited on 10/24/2016).

Siess, L., E. Dufour, and M. Forestini (2000). "An internet server for pre-main sequence tracks of low- and intermediate-mass stars". In: *Astronomy and Astrophysics* 358, pp. 593–599. ISSN: 0004-6361. URL: http://adsabs.harvard.edu/abs/2000A%26A...358..593S (visited on 01/26/2015).

Spitzer, L. (1978). *Physical processes in the interstellar medium*. DOI: 10.1002/9783527617722.

Srivastav, Shubham et al. (2016). "Optical and NIR observations of the nearby type Ia supernova SN 2014J". en. In: *Monthly Notices of the Royal Astronomical Society* 457.1. 00000, pp. 1000–1014. ISSN: 0035-8711, 1365-2966. DOI: 10.1093/mnras/stw039. URL: http://mnras.oxfordjournals.org/content/457/1/1000 (visited on 02/09/2016).

Stahler, S. W. and F. Palla (2005). *The Formation of Stars*. Wiley-VCH.

Stamatellos, Dimitris, Anthony P. Whitworth, and David A. Hubber (2011). "THE IMPORTANCE OF EPISODIC ACCRETION FOR LOW-MASS STAR FORMATION". In: *The Astrophysical Journal* 730.1, p. 32. ISSN: 0004-637X, 1538-4357. DOI: 10.1088/0004-637X/730/1/32. URL: http://stacks.iop.org/0004-637X/730/i=1/a=32?key=crossref.04b8fad827af77f099f32e872a7aa5ef (visited on 11/19/2015).

Swarup, G. et al. (1991). "The Giant Metre-Wave Radio Telescope". In: *Current Science, Vol. 60, NO.2/JAN25, P. 95, 1991* 60, p. 95. URL: http://adsabs.harvard.edu/abs/1991CuSc...60...95S (visited on 01/26/2015).

Tambovtseva, L. V., V. P. Grinin, and G. Weigelt (2014). "Hydrogen lines as a diagnostic tool for studying multicomponent emitting regions in hot young stars: magnetosphere, X-wind, and disk wind". In: *Astronomy & Astrophysics* 562, A104. ISSN: 0004-6361, 1432-0746. DOI: 10.1051/0004-6361/201322712. URL: http://www.aanda.org/10.1051/0004-6361/201322712 (visited on 01/23/2016).

Teets, W.K. et al. (2011). "X-ray Production by V1647 Ori During Optical Outbursts". In: *The Astrophysical Journal* 741, p. 83.

Terebey, S., F. H. Shu, and P. Cassen (1984). "The collapse of the cores of slowly rotating isothermal clouds". In: *The Astrophysical Journal* 286, pp. 529–551. ISSN: 0004-637X. DOI: 10.1086/162628. URL: http://adsabs.harvard.edu/abs/1984ApJ...286..529T (visited on 08/07/2016).

Ustyugova, G. V. et al. (2006). ""Propeller" Regime of Disk Accretion to Rapidly Rotating Stars". en. In: *The Astrophysical Journal* 646.1, p. 304. ISSN: 0004-637X. DOI: 10.1086/503379. URL: http://stacks.iop.org/0004-637X/646/i=1/a=304 (visited on 02/03/2016).

Vacca, W. D, M. C Cushing, and T. Simon (2004). "Near-infrared spectroscopy of McNeil's Nebula Object". In: *The Astrophysical Journal Letters* 609, p. L29.

Venkata Raman, V. et al. (2013). "Near-Infrared Monitoring and Modelling of V1647 Ori in its On-going 2008-12 Outburst Phase". In: *arXiv:1301.2110*. URL: http://arxiv.org/abs/1301.2110.

Vig, S. et al. (2006). "Post-outburst radio observation of the region around McNeil's nebula (V1647 Orionis)". In: *Astronomy and Astrophysics* 446.3, pp. 1021–1026. ISSN: 0004-6361, 1432-0756. DOI: 10.1051/0004-6361:20053403. URL: http://www.aanda.org/articles/aa/abs/2006/06/aa3403-05/aa3403-05.html.

Vorobyov, E. I. and S. Basu (2005). "The Origin of Episodic Accretion Bursts in the Early Stages of Star Formation". In: 633, pp. L137–L140. DOI: 10.1086/498303. eprint: astro-ph/0510014.

Vorobyov, Eduard I. and Shantanu Basu (2010). "The Burst Mode of Accretion and Disk Fragmentation in the Early Embedded Stages of Star Formation". en. In: *The Astrophysical Journal* 719.2, p. 1896. ISSN: 0004-637X. DOI: 10.1088/0004-637X/719/2/1896. URL: http://stacks.iop.org/0004-637X/719/i=2/a=1896 (visited on 07/31/2016).

Walt, Stéfan van der, S. Chris Colbert, and Gaël Varoquaux (2011). "The NumPy Array: A Structure for Efficient Numerical Computation". In: *Computing in Science & Engineering* 13.2, pp. 22–30. ISSN: 1521-9615. DOI: 10.1109/MCSE.2011.37. URL: http://scitation.aip.org/content/aip/journal/cise/13/2/10.1109/MCSE.2011.37 (visited on 03/03/2015).

Walt, Stéfan van der et al. (2014). "scikit-image: image processing in Python". en. In: *PeerJ* 2, e453. ISSN: 2167-8359. DOI: 10.7717/peerj.453. URL: https://peerj.com/articles/453 (visited on 03/03/2015).

Walter, Frederick M. et al. (2004). "V1647 Orionis (IRAS 05436-0007) in Outburst: The First Three Months". In: *The Astronomical Journal* 128, pp. 1872–1879. ISSN: 0004-6256. DOI: 10.1086/423703;. URL: http://adsabs.harvard.edu/abs/2004AJ....128.1872W.

Williams, Jonathan P. and Lucas A. Cieza (2011). "Protoplanetary Disks and Their Evolution". In: *Annual Review of Astronomy and Astrophysics* 49.1, pp. 67–117. DOI: 10.1146/annurev-astro-081710-102548.

Wils, P. et al. (2009). "IRAS 06068-0641 and IRAS 06068-0643". In: *Central Bureau Electronic Telegrams* 2033, p. 1.

Woolfson, M. M. (1993). "The Solar - Origin and Evolution". In: *Quarterly Journal of the Royal Astronomical Society* 34. ISSN: 0035-8738. URL: http://adsabs.harvard.edu/abs/1993QJRAS..34....1W (visited on 08/09/2016).

Wright, Edward L. et al. (2010). "The Wide-field Infrared Survey Explorer (WISE): Mission Description and Initial On-orbit Performance". en. In: *The Astronomical Journal* 140.6, p. 1868. ISSN: 1538-3881. DOI: 10.1088/0004-6256/140/6/1868. URL: http://iopscience.iop.org/1538-3881/140/6/1868 (visited on 03/05/2015).

Zanni, C. and J. Ferreira (2013). "MHD simulations of accretion onto a dipolar magnetosphere: II. Magnetospheric ejections and stellar spin-down".

In: *Astronomy & Astrophysics* 550, A99. ISSN: 0004-6361, 1432-0746. DOI: 10.1051/0004-6361/201220168. URL: http://www.aanda.org/10.1051/0004-6361/201220168 (visited on 02/03/2016).

Zhu, Zhaohuan, Lee Hartmann, and Charles Gammie (2010). "LONG-TERM EVOLUTION OF PROTOSTELLAR AND PROTOPLANETARY DISKS. II. LAYERED ACCRETION WITH INFALL". In: *The Astrophysical Journal* 713.2, pp. 1143–1158. ISSN: 0004-637X, 1538-4357. DOI: 10.1088/0004-637X/713/2/1143. URL: http://stacks.iop.org/0004-637X/713/i=2/a=1143?key=crossref.ce880de8485bebae77f198c9cb641cd3.

Zhu, Zhaohuan et al. (2009). "TWO-DIMENSIONAL SIMULATIONS OF FU ORIONIS DISK OUTBURSTS". In: *The Astrophysical Journal* 701.1, pp. 620–634. ISSN: 0004-637X, 1538-4357. DOI: 10.1088/0004-637X/701/1/620. URL: http://stacks.iop.org/0004-637X/701/i=1/a=620?key=crossref.4f81d145a616abde6e00bbbf460918e0 (visited on 08/18/2012).